High-throughput Single-Entity Analysis Methods: From Single-Cell Segmentation to Single-Molecule Force Measurements

Inaugural-Dissertation

to obtain the academic degree

Doctor rerum naturalium (Dr. rer. nat.)

submitted to the Department of Biology, Chemistry, Pharmacy

of Freie Universität Berlin

by

Yannic Kerkhoff

Berlin, October 2022

The following project was carried out within the research groups of Dr. Stephan Block and Prof. Dr. Petra Knaus from **January 2019** until **October 2022** at the Institute of Chemistry and Biochemistry of the Freie Universität Berlin.

First supervisor: Dr. Stephan Block

Institute of Chemistry and Biochemistry

Freie Universität Berlin

Arnimallee 22, 14195 Berlin

E-Mail: stephan.block@fu-berlin.de

Second supervisor: Prof. Dr. Petra Knaus

Institute of Chemistry and Biochemistry

Freie Universität Berlin

Thielallee 63, 14195 Berlin

E-Mail: petra.knaus@fu-berlin.de

Date of disputation: 20.02.2023

Acknowledgements

First of all, I would like to thank Dr. Stephan Block for giving me the opportunity to do this work in his group and for all his support throughout the years. The change from the world of cells to the world of molecules was not easy, but I learned a lot and I am happy to be able to bridge both worlds in the future. I would also like to thank Professor Dr. Petra Knaus, who agreed to mentor me as a second supervisor and to chair the committee. I always found the collaboration with her very pleasant and I also liked her, her group, and her research from the beginning.

Next, I would like to thank all Block group members. But especially Matthias Wallert, who is now no longer a member, but who kindly welcomed me from the beginning and integrated me into the group. I would like to thank Dr. Stefanie Wedepohl, Dr. Katharina Hugentobler, and Kevin Diestelhorst for fun conversations and lunch breaks as well as professional expertise and support in the lab.

Furthermore, I would like to thank all my other colleagues from other research groups who have become close friends over time. To name all of them would probably go beyond the limits of this work, but I would like to highlight a few in particular. First of all, I would like to thank Elisa Quaas, whom I like to call my better half. I have never met such a combination of joie de vivre, humor, and competence in one person. I consider Dr. Alexander Oehrl and Daniel Braatz from the Haag Group among the first who have transitioned from colleagues to friends to me. A great support after I moved to a new city. Then there is Alexander Schweigerdt from the Weinhart Group who has become one of my best friends here in Berlin. I would also like to thank Dr. Katharina Achazi, who was my first contact with Freie Universität and BioSupraMol and who brought the Block Group to my attention. I would also like to thank Dr. Wiebke Fischer, who is known by everyone as the good soul of the Haag Group and who competently takes personal care of every conceivable task.

Of course, I would also like to thank my family and long-time friends for their everlasting support. My parents Gerrit and Petra have always supported the curiosity of me and my sibling. For this I name exemplarily a whole basement room full of children discover and dinosaur books. Especially in such pandemic times, the weeks-long remote office in my parents' house was a real if unplanned joy that certainly spared me a lot of loneliness. Both my sibling Denny and my good friend Nora Fresman were welcome fellow sufferers, as we were all working on our doctoral theses at the same time. Furthermore, I would like to thank my two best friends, Jessica Ilenburg and Sascha Steffen, just for being there and especially for reminding me about the world outside of work and science. Of course, I would also like to thank all my friends from the Bielefeld biotechnology community, who always acted as friends and role models for me.

Finally, I would like to tell a personal story that I think is fundamental to this work. I still vividly remember my time at middle school (Realschule), where I had a really hard time because learning, concentration and discipline were not my strong points. This led to mediocre to poor grades, so I felt I was always in the shadow of my older sibling, who was at the high school (Gymnasium) and always had very good grades. I thought of myself as not being smart and always having bad grades, that's just how I was. But then we got a new class teacher, Birgit Schalk. I began the first German exam under her supervision

with the familiar fear of expecting a bad grade, and I feared the ridicule of the others as always. But it turned out differently. I got an A, the first ever. I thought it was a mistake, because of course I'm a bad student and only get bad grades. So, I went to her and asked if it was a mistake. She looked at my work and said, *"I see.... well, the form is not perfect yet, but I see the potential and that's why I decided to give you an A, as motivation."* That changed the way I looked at myself. *"There can be things hidden inside of you? Potential. Not there yet, but you can uncover it?"* After that, I worked hard to realize that potential. I got very good grades, excelled in my class, went to high school, and university, which eventually led to this thesis. I am convinced that without her warming words, I would never have believed that there was potential in me. Therefore, I dedicate this work to my class teacher and her memorable words:

„Die Form ist nicht perfekt, aber ich erkenne das Potential.“

Birgit Schalk

Declaration of honesty

Hereby I declare and confirm that this PhD thesis is entirely the result of my own work and that no other sources than those cited have been used. All annotations, which have been used from published or unpublished sources, are identified as such. The shown illustrations have been created by me, or have been marked with the corresponding references.

Berlin,

_____

Yannic Kerkhoff

October 2022

Table of contents

Zusammenfassung

Im Rahmen dieser Arbeit wurden neue mikroskopische Analysemethoden mit Einzelobjektauflösung und hohem Durchsatz entwickelt, welche von der zellulären bis zur molekularen Ebene die Untersuchung von Biomembran-assoziierten Interaktionen erlauben. Derzeit gibt es eine Vielzahl von Methoden zur Gewinnung quantitativer Informationen über zelluläre und molekulare Reaktionen auf äußere Reize, aber vielen von ihnen mangelt es entweder an hoher Empfindlichkeit oder an hohem Durchsatz. Die Kombination dieser beiden Aspekte ist entscheidend für die Untersuchung der schwachen, aber oft komplexen und multivalenten Wechselwirkungen, die an der Grenzfläche biologischer Membranen auftreten. Dazu gehören die Bindung von Krankheitserregern wie einigen Viren (z. B. Influenza- und Herpesviren, sowie SARS-CoV-2), die Transmembransignalwege wie ligandenbasierte Oligomerisierungsprozesse oder auch die Übertragung auf Zellen wirkender mechanischer Kräfte in biochemische Signale.

Ziel dieser Arbeit war es, die Limitierungen der derzeitigen Methoden zu überwinden, indem in vier verschiedenen Projekten neue Methoden mit einem noch nie dagewesenen Grad an Automatisierung, Sensitivität und Parallelisierung entwickelt und etabliert wurden. Alle Methoden basieren auf der Kombination von optischer (Video-)Mikroskopie, gefolgt von einer hoch verfeinerten Datenanalyse zur Untersuchung einzelner zellulärer und molekularer Objekte. Dies erlaubt die Erkennung seltener Ereignisse und die Identifizierung und Quantifizierung zellulärer und molekularer Populationen, die bei Ansätzen mit Ensemble-Mittelung verborgen bleiben würden.

Auf zellulärer Ebene wurden zwei Methoden für die Segmentierung von Einzelzellen und die zellweise Auslesung von Fluoreszenzreportersystemen entwickelt, hauptsächlich zur Untersuchung der Bindung und Hemmung der Bindung von Viren an Wirtszellen. Die Methode des ersten Projekts zeichnet sich durch einen hohen Automatisierungsgrad aus und bietet die Möglichkeit, automatisch geschätzte Analyseparameter (Hintergrundkorrektur, Segmentierungsempfindlichkeit und Fluoreszenz-Cutoff) zu verwenden, um den manuellen Aufwand für die Analyse von zellbasierten Infektionsassays zu verringern. Diese Methode wurde für das Screening der Hemmkraft auf der Grundlage des IC_{50}-Wertes verschiedener Virusbindungsinhibitoren verwendet. Durch die im zweiten Projekt verwendete Methode wurde die Empfindlichkeit der ersten Methode um eine Schätzung der Anzahl der an die Zellen gebundenen fluoreszierenden Nanopartikel, erweitert. Die Bildauflösung wurde so gewählt, dass viele Zellen parallel abgebildet werden können, was einerseits die Identifizierung der Heterogenität der Partikelbindung von Zelle zu Zelle ermöglicht, andererseits aber auch die fluoreszierenden Nanopartikel als unscharfe Intensitätsflecken sichtbar werden lässt. Während es dann nicht möglich ist, die einzelnen Nanopartikel bei solchen Auflösungen aufzulösen, wurde ein neuer Ansatz entwickelt und durch Simulationen validiert, um die Anzahl der fluoreszierenden Nanopartikel unterhalb der Auflösungsgrenze mit einer Genauigkeit von etwa 80 bis 100 % zu schätzen. Im dritten Projekt wurde ein Ansatz für die Analyse und Verfeinerung von zweidimensionalen Einzelpartikelverfolgungsexperimenten vorgestellt, der sich auf die Qualitätsbewertung der Trajektorien konzentriert, indem er einen Leitfaden für die Auswahl eines geeigneten maximalen Verknüpfungsabstands liefert. Dieser Tracking-Ansatz wurde im vierten Projekt verwendet, um die mechanischen Reaktionen kleiner Moleküle auf hydrodynamische Scherkräfte mit

einer Auflösung im sub-nm-Bereich zu quantifizieren. Hier ermöglichte die Kombination von TIRF-Mikroskopie, Mikrofluidik und Einzelpartikelverfolgung die Entwicklung einer neuen Einzelmolekül-Kraftspektroskopiemethode mit hoher Auflösung und Parallelisierungsmöglichkeiten. Diese Methode wurde durch die Quantifizierung der mechanischen Reaktion wohldefinierter PEG-Linker validiert und anschließend zur Untersuchung der Energiebarrieren der Dissoziation multivalenter Biotin-NeutrAvidin-Komplexe unter niedrigen (~ 1,5 bis 12 pN) statischen Kräften verwendet.

Zusammenfassend lässt sich sagen, dass diese Arbeit das Repertoire an geeigneten Methoden für die Hochdurchsatzuntersuchung der Eigenschaften und Wechselwirkungen von Zellen, Nanopartikeln und Molekülen mit Einzelobjektauflösung erweitert. In Zukunft werden die hier entwickelten Methoden zum Screening nach weiteren Virusbindungsinhibitoren, zur Untersuchung der Oligomerisierung von Membranrezeptoren auf Zellen und Modellmembranen und zur Quantifizierung der mechanischen Reaktion von krafttragenden Proteinen und Liganden-Rezeptor-Komplexen unter niedrigen Kraftbedingungen verwendet werden.

Abstract

This work is focused on the development of new microscopy-based analysis methods with single-entity resolution and high-throughput capabilities from the cellular to the molecular level to study biomembrane-associated interactions. Currently, there is a variety of methods available for obtaining quantitative information on cellular and molecular responses to external stimuli, but many of them lack either high sensitivity or high throughput. Yet, the combination of both aspects is critical for studying the weak but often complex and multivalent interactions at the interface of biological membranes. These interactions include binding of pathogens such as some viruses (e.g., influenza A virus, herpes simplex virus, and SARS-CoV-2), transmembrane signaling such as ligand-based oligomerization processes, and transduction of mechanical forces acting on cells.

The goal of this work was to overcome the shortcomings of current methods by developing and establishing new methods with unprecedented levels of automation, sensitivity, and parallelization. All methods are based on the combination of optical (video) microscopy followed by highly refined data analysis to study single cellular and molecular events, allowing the detection of rare events and the identification and quantification of cellular and molecular populations that would remain hidden in ensemble-averaging approaches.

This work comprises four different projects. At the cellular level, two methods have been developed for single-cell segmentation and cell-by-cell readout of fluorescence reporter systems, mainly to study binding and inhibition of binding of viruses to host cells. The method developed in the first project features a high degree of automation and automatic estimation of sufficient analysis parameters (background threshold, segmentation sensitivity, and fluorescence cutoff) to reduce the manual effort required for the analysis of cell-based infection assays. This method has been used for inhibition potency screening based on the IC_{50} value of various virus binding inhibitors. With the method used in the second project, the sensitivity of the first method is extended by providing an estimate of the number of fluorescent nanoparticles bound to the cells. The image resolution was chosen to allow many cells to be imaged in parallel. This allowed for the quantification of cell-to-cell heterogeneity of particle binding, at the expense of resolution of the individual fluorescent nanoparticles. To account for this, a new approach was developed and validated by simulations to estimate the number of fluorescent nanoparticles below the diffraction limit with an accuracy of about 80 to 100 %. In the third project, an approach for the analysis and refinement of two-dimensional single-particle tracking experiments was presented. It focused on the quality assessment of the derived tracks by providing a guide for the selection of an appropriate maximal linking distance. This tracking approach was used in the fourth project to quantify small molecule responses to hydrodynamic shear forces with sub-nm resolution. Here, the combination of TIRF microscopy, microfluidics, and single particle tracking enabled the development of a new single molecule force spectroscopy method with high resolution and parallelization capabilities. This method was validated by quantifying the mechanical response of well-defined PEG linkers and subsequently used to study the energy barriers of dissociation of multivalent biotin-NeutrAvidin complexes under low (~ 1.5 to 12 pN) static forces.

In summary, with this work, the repertoire of appropriate methods for high-throughput investigation of the properties and interactions of cells, nanoparticles, and molecules at single resolution is expanded. In the future, the methods developed here will be used to screen for additional virus binding inhibitors, to study the oligomerization of membrane receptors on cells and model membranes, and to quantify the mechanical response of force-bearing proteins and ligand-receptor complexes under low force conditions.

1. Introduction

Many biological processes and interactions involve the cell membrane, as it is the barrier between the interior of a cell (a living system) and its environment [1]. These systems are constantly interacting with each other, for example, in the approach and binding to the membrane of pathogens attempting to enter the cell [2] [3] [4], or in the sensing of external forces by the cell [5] [6] [7] during migration and proliferation.

Optical microscopy is a very versatile and widely used method for obtaining data and studying such processes. It allows imaging of e.g., tissue, single cells, and even nanoparticles or single labeled molecules. Using super-resolution microscopy methods [8], resolutions below the diffraction limit are achieved. However, systematic quantification of these image datasets can be quite challenging, as the size of the imaged targets can span many orders of magnitude [9]. Depending on the target, the data analysis steps to extract reliable information from the images can vary dramatically. For example, when quantifying a dense two-dimensional cellular monolayer, segmenting cells from the background and from each other is the most important analysis step to determine a cellular response to external stimuli with sufficient accuracy. Dense fluorescent nanoparticles (~ 1-100 nm in size [10]), on the other hand, cannot be segmented because the point-scattering function of their emitted light (~ 200 - 400 nm [11]) most likely represents them as diffraction-limited intensity spots when imaged with optical microscopy. An estimation of the number of such particles may therefore differ drastically from the actual number of particles present [12]. When analyzing single molecules that are even smaller than most nanoparticles (e.g., barrel-shaped green fluorescent protein (GFP) has a size of about 4x2 nm [13]), they cannot be structurally resolved by diffraction-limited optical microscopy, but only through interactions with their environment or attached probes (e.g., changes in intensity or motion). Subsequent data analysis must therefore be performed very carefully to obtain useful information. Molecular responses such as the stretching or unfolding of polymers and proteins due to applied forces are even smaller and may extend to the sub-nm range with extremely low signal-to-noise ratios. This requires an analysis of such systems in a high-throughput manner to obtain statistically meaningful data, making systematic analysis of such image-based experiments quite complicated and time-consuming. As a consequence, the development of new, fast, and accurate high-throughput analysis methods from the cellular to the molecular scale is essential.

Currently, there is a variety of methods available for segmentation of cells [14], quantification of fluorescent nanoparticles [15], and application of forces and readout of molecular responses by single-molecule force spectroscopy [16]. However, each of these approaches is currently limited, e.g., by the complexity of selecting appropriate analysis parameters (such as for cell segmentation), sensitivity, which is mainly constrained by physical limitations such as resolution limits (e.g., for fluorescent nanoparticles) or thermal fluctuations [17] (e.g., for single-molecule measurements), validation of the accuracy of the results obtained, and a lack of high-throughput capabilities in general.

In this work, the aforementioned problems are addressed by establishing new multiscale single-analysis methods combining optical (video) microscopy, refined image data analysis, result validation by simulations, and (in the case of single-molecule force spectroscopy) microfluidics. The methods established

here are tested on well-studied model systems to demonstrate their precision and potential for high-throughput screening. Through this validation it was shown that they are excellent tools for further biomembrane-associated interaction studies.

2. Theoretical background

In the following chapter the basics and details necessary to understand the scope of this work and assess its relevance in comparison to the current state of the art are described.

First, the biological processes are highlighted, for which new sensitive and high-throughput methods must be developed (2.1 Biomembrane associated interactions). It is then explained in which systems (2.2 Native, hybrid, and artificial systems) and how the data of this work was generated (2.3 Optical microscopy methods), analyzed (2.4 Multiscale image quantification), and why a single-entity resolution was necessary for its interpretation (2.5 Ensemble versus single-entity analysis). Afterwards, the current state of the art of single-molecule force measurement methods and their limitations will be presented (2.6 Single-molecule force measurements) and how these limitations can be overcome by the establishment of a new microfluidics-based approach (2.7 Microfluidic shear force applications).

2.1 Biomembrane associated interactions

The biological membrane of cells consists of a complex mixture of different lipids, proteins, and carbohydrates [18] [19] [20]. All components interact with each other [21] [22] and allow both a separation [1] from, and communication with the cellular environment [23]. Relevant interactions at these biological interfaces include host-agent interactions, such as infections with viruses [2] [3] [4] and bacteria [24] as well as signaling across the cell membrane such as seen in mechanosensing [5] [6] [7] and BMP-signaling [25] [26] [27] [28], which will be investigated using the methods developed in this work.

2.1.1 Pathogen and host cell interactions

For a pathogen like a virus to infect a host cell, a binding to its target needs to be established (Figure 1). For many viruses, this first step in the infection process is often mediated by a transient binding to heparan sulfate protruding from the cell membrane [29] [30]. This brings the virus in spatial vicinity to its specific cellular receptor e.g., the angiotensin converting enzyme 2 (ACE2) in case of SARS-CoV-2 [31]. This is a multivalent process which needs many parallel binding events [32] for successful internalization. However, this infection process can be prevented by the usage of virus infection inhibitors like heparin [33] [34] [35], which have a higher binding affinity to the virus surface proteins than those proteins have to their respective cellular receptors [36]. The development of such virus inhibitors is of great interest, which is highlighted by the current SARS-CoV-2 pandemic [37], and thus developments and improvements in methods to screen the potency of virus inhibitors like in [38] are always in need and therefore a major objective of this work (see 4.1 A fast open-source Fiji-macro to quantify virus infection and transfection on single-cell level by fluorescence microscopy and 4.2 Bridging cellular- and nanoscale: Accurate quantification of clustered nanoparticles on monolayered confocal imaged cells).

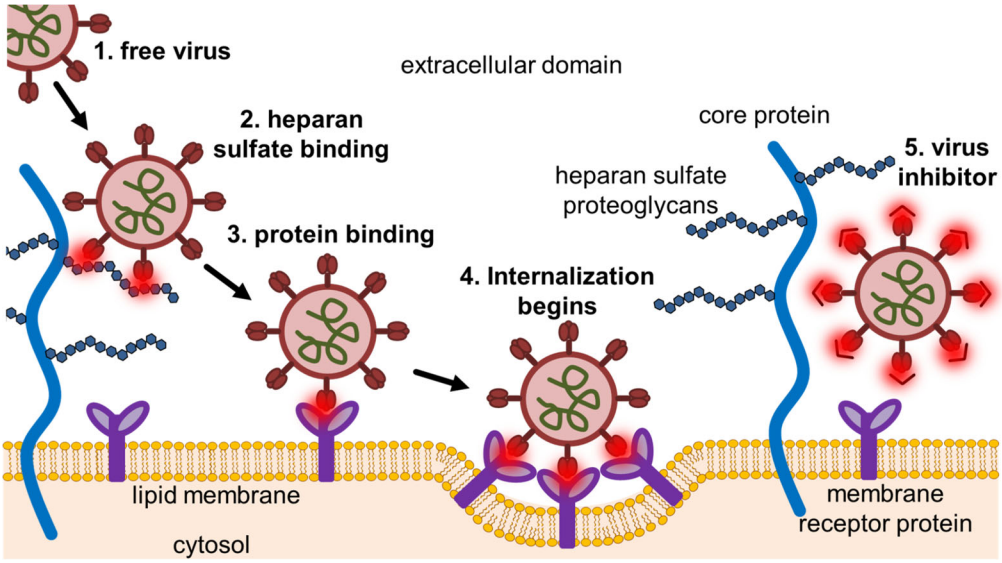

Figure 1: Schematic overview of virus, host cell, and inhibitor interactions. The free viruses (1) first bind to heparan sulfate (2) near the cell membrane. They then bind their specific cellular receptors (3, e.g., ACE2 [31], SA [39], HVEM [3]). This induces the cell entry (4) which will then lead to replication inside the cell (not shown). Specific virus inhibitors (5) have higher affinity to the virus proteins than the virus proteins have to their cellular receptors and thus inhibit binding and entry of the virus. Interactions are visualized in glowing red.

A similar pathogen-related biomembrane interaction process is the multivalent monosialotetrahexosyl-ganglioside (GM1) binding of the exotoxin (cholera toxin) secreted by the bacterium *Vibrio cholerae*. Cholera toxin consists of two subunits (A and B), where the pentameric subunit B is responsible for binding to the cell membrane by acquisition of GM1 (Figure 2) on intestinal cells [24]. Subunit A mediates a toxic effect due to the formation of membrane pores by conformational changes [40], resulting in watery diarrhea and, if untreated, likely death of patients infected with *V. cholerae*.

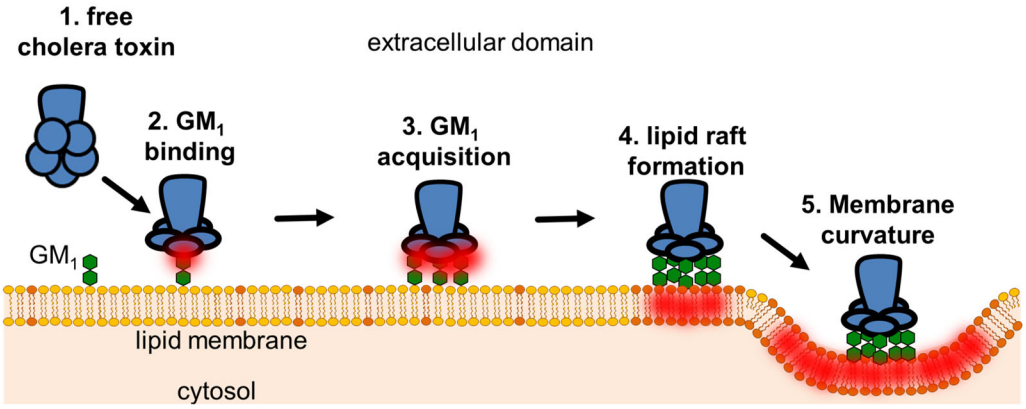

Figure 2: Interactions of cholera toxin with the cell membrane. The free cholera toxin (1) can multivalently bind GM1 (2) at the cell surface. As the cholera toxins subunit B is a pentamer, it can acquire more GM1 (3), to enhance the binding to the cell surface. The acquisition of several GM1 induces a lipid raft formation (4) which induces a membrane curvature (5).

However, the GM1 acquisition of the nontoxic subunit B also leads to a phase separation in lipid membranes, stabilizing ordered membrane domains (lipid raft formation). This induces a membrane curvature [41], which makes cholera toxin subunit B (CTxB) an interesting biophysical tool for the investigation of membrane structure and dynamics, as well as the assembly of nanodomains [42] and was therefore used as a model system in this work (see 7.1.1 Multivalent GM1 binding of choleratoxin subunit B).

2.1.2 Transmembrane signaling

In addition to the study of pathogen-host interactions (as described above), the diverse spectrum of biomembrane-associated interactions related to transmembrane signaling is also of great scientific importance. This is true for basic research, e.g., in the field of mechanobiology [43] [44] [45], as well as for investigation (and possible treatment) of diseases caused by erroneous cellular signaling, such as fibrodysplasia ossificans progressive (FOP) [46].

The bone morphogenetic protein (BMP) signaling pathway (Figure 3) is such a well-studied and biologically highly relevant transmembrane signaling cascade. Extracellular release of BMPs leads to an oligomerization of transmembrane type I and type II BMP-receptors, resulting in the regulation of gene expression as the signal is led down to the nucleus [47]. The vast amount BMP-signaling related protein-families (i.e., receptors, ligands, coreceptors, and corepressors) leads to complex regulation patterns regarding embryonic development and tissue differentiation [48], as well as cardiovascular [49], gastrointestinal [50], and neurological [51] diseases, just to name a few. As BMP signaling depends on receptor-ligand interactions (leading to oligomerization), quantification of these membrane-associated mobility properties (such as in [52], e.g., by single-particle tracking (SPT) [53]) allows for detailed investigation and thus understanding of this complex molecular interaction network (see 4.3 Analysis and refinement of 2D single-particle tracking experiments and 7.1.2 Hybrid lipid bilayer formation).

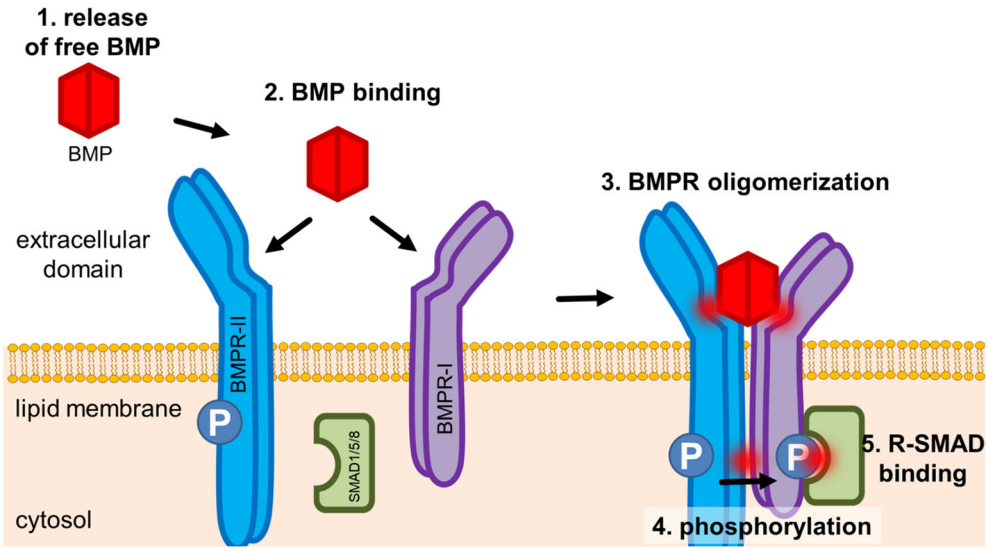

Figure 3: Overview of the BMP signaling pathway. For cell signaling, BMPs can be released (1) which bind their corresponding type II and type I receptors (2). This leads to an oligomerization of the BMPRs (3) which allows for a phosphorylation of the type I receptor (4). This then leads to a phosphorylation of R-SMADs (5), starting an intracellular signaling cascade.

Another interesting example of transmembrane signaling is the talin-vinculin mediated mechanotransduction of cellular force sensing at the extracellular matrix interface (Figure 4). Here, cells are attached to the extracellular matrix by focal adhesion, containing different proteins (like fibronectin) which are attached via the cell membrane by integrins to talin and the cytoskeleton (i.e., actin filaments) [54]. A tensile force acting on the actin filaments (e.g., by cell migration) is transmitted to talin, whose unfolding reveals vinculin binding sites [55] [56]. The binding of vinculin then stabilizes the unfolded conformation of

talin [57], leading to a signaling cascade that enables the cell to sense mechanical forces by converting them into biochemical signals [58] [59] [60]. The force-dependent unfolding of talin has been intensively studied in the past [6] [56] [57] [61] [62] [63]. However, it is known that the R3-domain of talin unfolds at forces below 5 pN and intermediate unfolding states [64] are expected to occur at even lower forces. Methods that allow for the application of forces in such low to sub-pN range in high-throughput manner have yet to be developed and thus are one of the main scopes of this work (see 4.4 Microfluidics-based force spectroscopy enables to perform high-throughput force measurements with sub-nm resolution and sub-pN sensitivity).

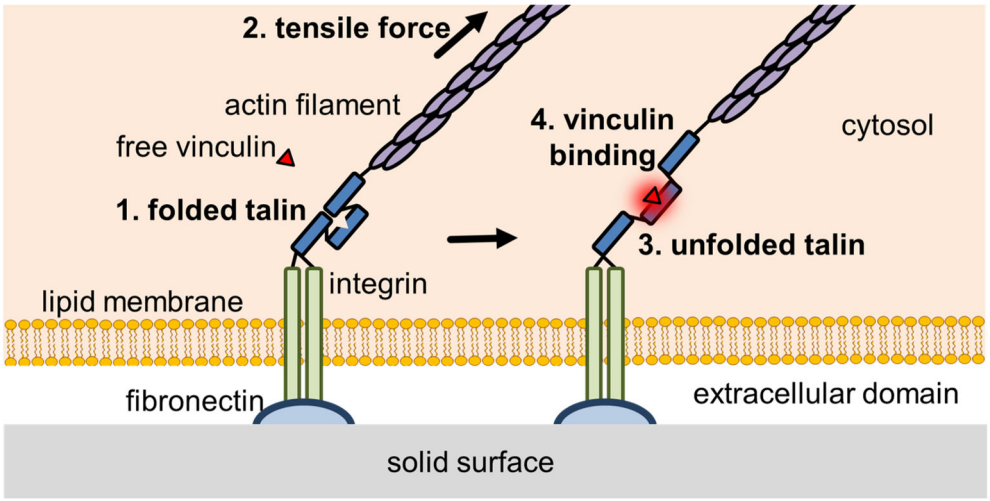

Figure 4: Talin-related interactions for cellular force sensing. The cell is connected to a solid surface by fibronectin, integrin, folded talin, and actin filaments (1). A tensile force acting on the actin filaments (2, e.g., by cell locomotion) can then lead to a force-dependent unfolding of talin (3) revealing vinculin binding sites. The vinculin can then bind to these sites (4) starting an intracellular signaling cascade.

2.2 Native, hybrid, and artificial systems

To study the biomembrane associated interactions mentioned above, different possible systems with varying complexity can be used and are described in this chapter (Figure 5). Performing cell-based assays (like virus infection assays [65]) ensures that the generated data reflects the real *in vivo* or approximated *in vitro* processes, as the interactions take place in their native cellular environment (Figure 5a). However, probing the intrinsic molecular characteristics of specific targets (like transmembrane receptors [52]) in the native cell membrane can be challenging, due to the vast amount of native cell membrane components interacting with each other, sometimes interfering with the target [66] [67]. To reduce the complexity of the system (yet keeping some native environmental conditions), it is possible to transfer molecular targets (like lipids or receptors) into a hybrid system, as demonstrated in [68] and also as part of this thesis (see 7.1.2 Hybrid lipid bilayer formation). Here, native cell membrane vesicles were prepared and fused with synthetic lipid vesicles on a glass surface, building a simplified hybrid model membrane (Figure 5b) containing native membrane material [69] [70]. Synthetic vesicles can also be used without any native material, instead incorporating purified proteins, lipids, or other receptors, providing a synthetic membrane model (Figure 5c, top) to study interactions like by virus binding assays [71] or the multivalent binding of CTxB to GM1 [72] (see 7.1.1 Multivalent GM1 binding of choleratoxin subunit B).

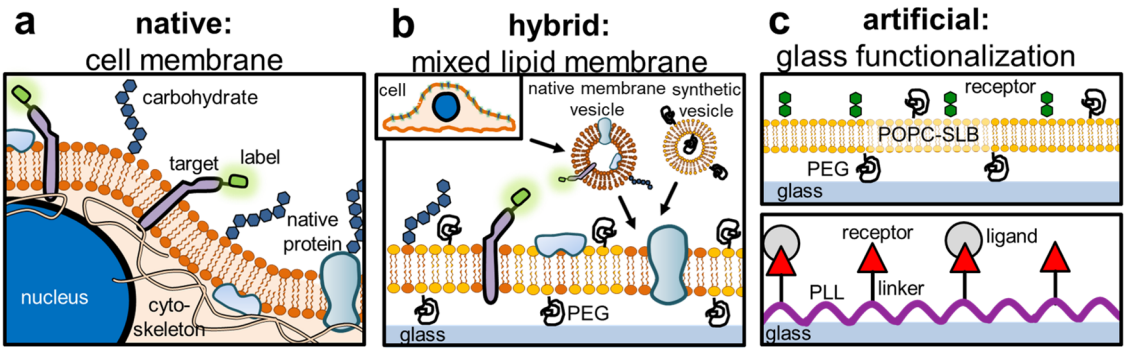

Figure 5: Comparison of native, hybrid, and artificial systems for probing membrane associated interactions. Molecular targets like transmembrane receptors can be labeled and investigated in their native environments, i.e. the cell membrane (a). Here they show their natural interactions but the complexity of diverse membrane components (e.g., other proteins, lipid mixture, carbohydrates, cytoskeleton, etc.) can complicate the analysis of the target. To simplify the analysis of the target, it can be integrated into a hybrid system (b; by fusing native membrane vesicles (NMVs) with synthetic lipid vesicles on glass slides). This reduces the amount of other membrane components interacting with the target. The simplest system to study membrane interactions is an artificial glass functionalization (c). This can be for example a supported lipid bilayer containing synthetic lipids like phosphatidylcholine (POPC), polyethylene glycol (PEG), and a specific receptor like GM1 (top) or a glass coating of poly-L-lysine (PLL) with attached receptors allowing for binding studies of their ligands (bottom).

The simplest artificial system to study protein interactions and properties is glass functionalization without any lipid material (Figure 5c, bottom). Here the target receptors are immobilized on an interface (e.g., by PLL [73]), allowing for binding studies with their ligands [74] or as a setup for force-spectroscopy methods like AFM [56] or the surface linking in microfluidic channels (see 4.4 Microfluidics-based force spectroscopy enables to perform high-throughput force measurements with sub-nm resolution and sub-pN sensitivity).

2.3 Optical microscopy methods

For the methods developed in this work, optical (video) microscopy was chosen for data generation because it is a widely used and versatile method for investigation and data collection in various fields of life sciences [75]. It allows for studying various qualitative and quantitative biological processes *in vitro*, and is also the basis for many laboratory assays, from cellular to molecular scale [76]. The three fluorescence-based optical microscopy techniques and their properties used in this work are thus described in the following.

2.3.1 Widefield fluorescence microscopy

Fluorescence is a process in which a fluorophore absorbs light of a specific wavelength and then emits light of a longer wavelength [77]. In widefield fluorescence microscopy (WFM), the entire sample volume is illuminated by a light source (often a light emitting diode (LED)), resulting in fluorescence emission from the target (Figure 6a). The emitted light of longer wavelength is then captured by a digital camera (sometimes also a charge-coupled device (CCD)), allowing for rapid imaging of a relatively large field of view (Figure 6b). Sine WFM allows for fast imaging of relatively large samples, it has high-throughput imaging capabilities needed for rapid screening of various samples, such as image-based screening for viral infection inhibitors [38] (see 4.1 A fast open-source Fiji-macro to quantify virus infection and transfection on single-cell level by fluorescence microscopy).

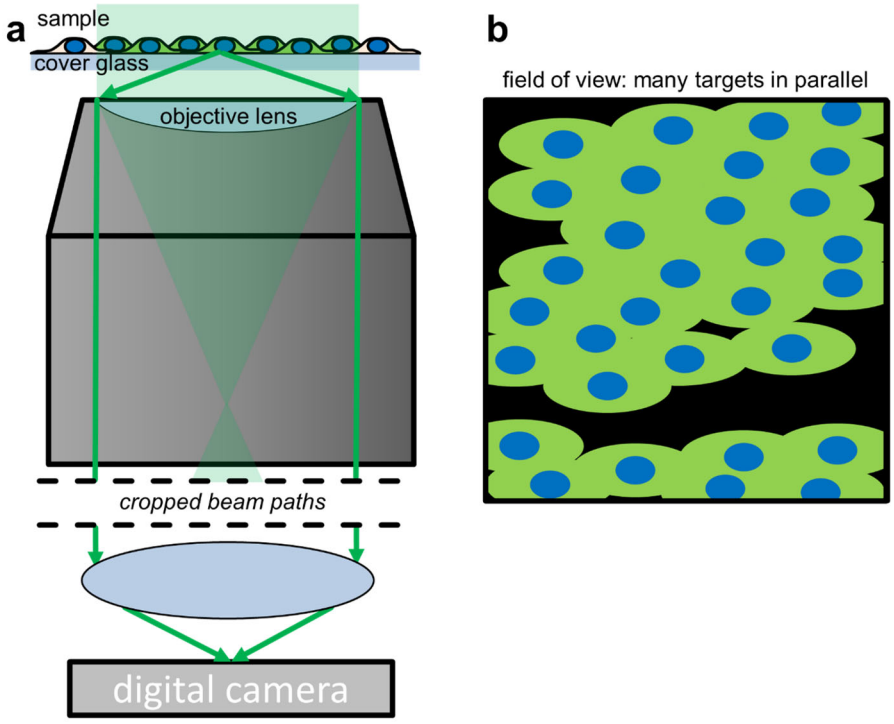

Figure 6: In widefield fluorescence microscopy a relatively large field of view (e.g., several hundred micrometers) can be imaged by a digital camera (a), which allows for a fast imaging of many fluorescent targets in parallel (b, i.e., monolayered green fluorescent protein (GFP)-expressing cells). While this is a microscopy method with high-throughput potential, it gives no information about the z-position of fluorescent targets.

Compared to confocal laser scanning microscopy (CLSM), WFM does not provide information about z-position of the fluorescence probe [78] [79] and the actual resolution is reduced by background fluorescence. Since the entire sample is illuminated, areas above and below the focal plane will also be detected by the camera. Therefore, the emission wavelengths of a fluorophore may be obscured by this background fluorescence, resulting in a decreased signal-to-noise ratio and achievable resolution [78] [79].

2.3.2 Confocal laser scanning microscopy

In a confocal laser scanning microscope, the sample is illuminated by a laser beam, and the emitted fluorescence light is focused through a pinhole and sensed by a photon detector such as photoelectron multiplier tubes (PMTs), avalanche photodetectors (APDs), or the so-called hybrid detectors [80] [79]. This allows for a user-selected, precise illumination and imaging of specific sample regions, without illuminating the whole sample volume (Figure 7a). CLSM offers many advantages over conventional widefield microscopy for cell imaging, providing depth-of-field control and the ability to create serial optical sections of thick samples. This eliminates much of the out-of-focus or background fluorescence, resulting in higher resolution [80] [79], which makes CLSM the method of choice in many life science fields. The higher image quality comes with the drawback that the imaging process also needs notably more time, limiting its high-throughput capabilities. However, as CLMS can resolve the position of a fluorescent target in the sample (Figure 7b), it allows the study of position-dependent processes, such as the differentiation of binding or uptake of nanoparticles (e.g., viruses) on cells [81] (see 4.2 Bridging cellular- and nanoscale: Accurate quantification of clustered nanoparticles on monolayered confocal imaged cells).

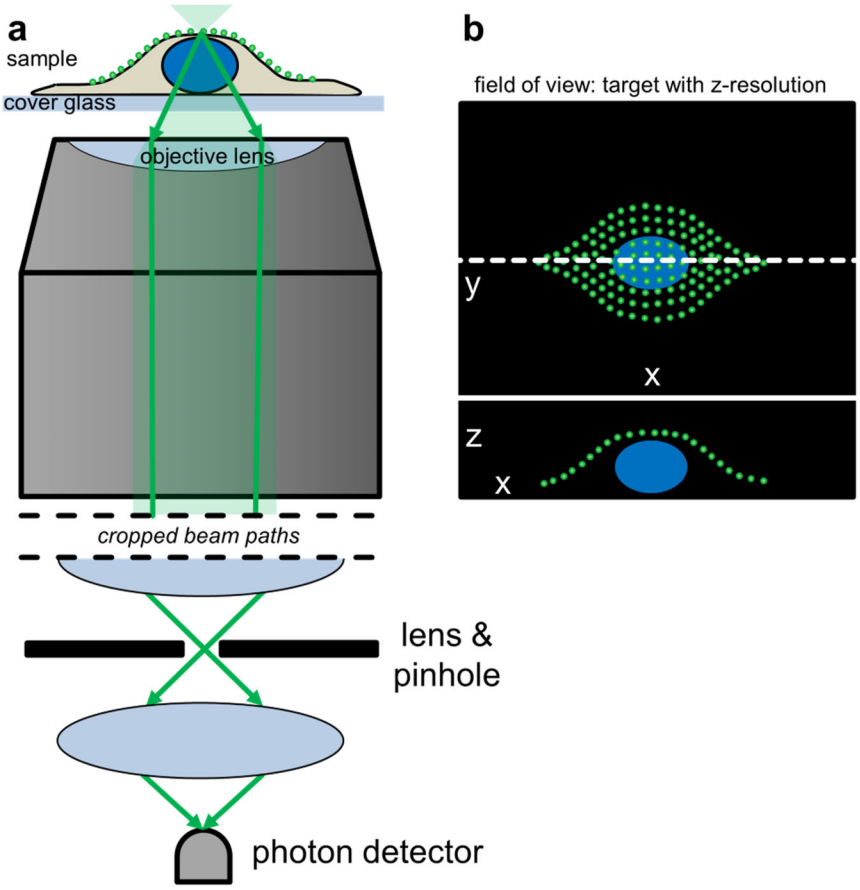

Figure 7: Compared to widefield microscopy, confocal laser scanning microscopy requires significantly more time for imaging because the image is generated by a photon detector through a pinhole (a). However, this enables precise scanning of the sample also in the z-direction, e.g., to determine whether fluorescent probes accumulate intracellularly or on the cell surface (b).

2.3.3 Total internal reflection fluorescence microscopy

Total internal reflection fluorescence (TIRF) microscopy is a highly specialized method of optical microscopy as it combines the advantages of WFM and CLSM. In most cases the sample is illuminated with a laser (sometimes also a lamp or a LED) and the images are captured by a digital camera, which enables rapid image acquisition. However, since the light beam is directed at the sample surface at a specific angle, resulting in total internal reflection and the development of an evanescent wave, only targets up to about 150 nm above the interface are illuminated (Figure 8a) [82] [83] [84]. The resulting captured image will thus only show fluorescent targets near the interface (Figure 8b). This ability to resolve the distance to the interface on nanometer scale, while keeping fast imaging capabilities, makes TIRF microscopy a valuable tool for the investigation of fast and delicate molecular interactions at interfaces, like tracking of mobile membrane components [85], transient virus binding events [71], and to track force-dependent molecular responses (see 4.4 Microfluidics-based force spectroscopy enables to perform high-throughput force measurements with sub-nm resolution and sub-pN sensitivity). This versatile imaging method has already been used in microfluidic setups to study the flow dependent forces acting on nanoparticles [86], in order to characterize DNA-bearing polymer particles [87], and to study *in situ* precipitation [88]. It is thus one of the main imaging methods used in this work.

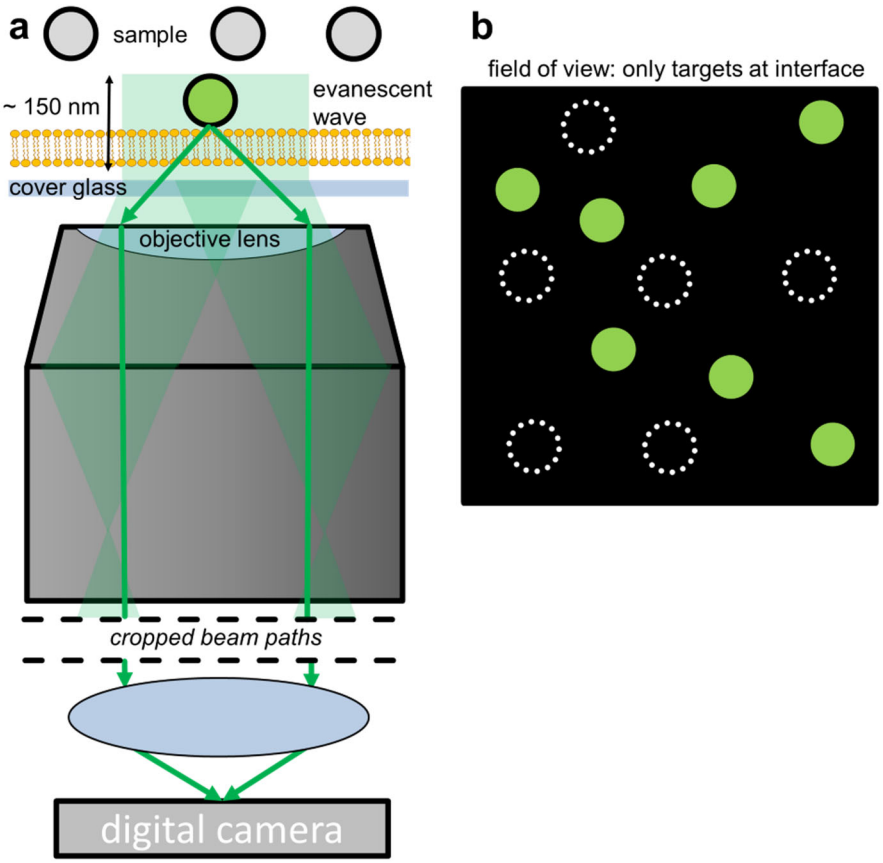

Figure 8: In TIRF microscopy, the illumination beam is led to the sample in a specific angle, which leads to a total reflection and the formation of an evanescent wave, exciting only probes up to 150 nanometers near the interface (a). As the image is mostly created with a digital camera, it has a high-throughput potential to analyZe target interactions near the sample interface (b).

2.4 Multiscale image quantification

After the generation of image data by optical (video) microscopy as described above, the next important step is to derive quantitative information from this raw data [89]. This is done by image analysis (or image quantification), in which various mathematical algorithms are systematically applied to the image data (often in high throughput), with respect to the target to be analyzed. Since there are different types of raw image data (e.g., in terms of spatial and temporal resolution), these algorithms (or analysis steps) must be carefully chosen. The following describes the multiscale image quantification approaches used in this work, to extract image-based quantitative information with single-cell, single-nanoparticle, and single-molecule resolution.

2.4.1 Single-cell analysis

To extract information about individual cells from a microscopy image showing a two-dimensional cellular monolayer, in principle three basic steps [90] are necessary (Figure 9a). If the cells are not fully confluent, the first step is to separate the cells from the background of the image (Figure 9b). This is usually done by selecting an intensity threshold [91] for the pixel values of the image, where the background intensity (empty space) is below the selected threshold and the cell bodies or nuclei (depending on the coloring) are above the threshold. If the cells are also touching, they must then be segmented. A very effective method for this is the seeded watershed algorithm [92]. This requires identifying the cell centers

(Figure 9c, second step) by extracting the local intensity maxima of the image (which is usually done based on nuclear staining). Then, the watershed algorithm segments the cell centers (Figure 9d) based on the distance between the maxima and the intensity profile above the threshold (third step). In most cases, this leads to a decent estimation of the outline of the nuclei or cell bodies.

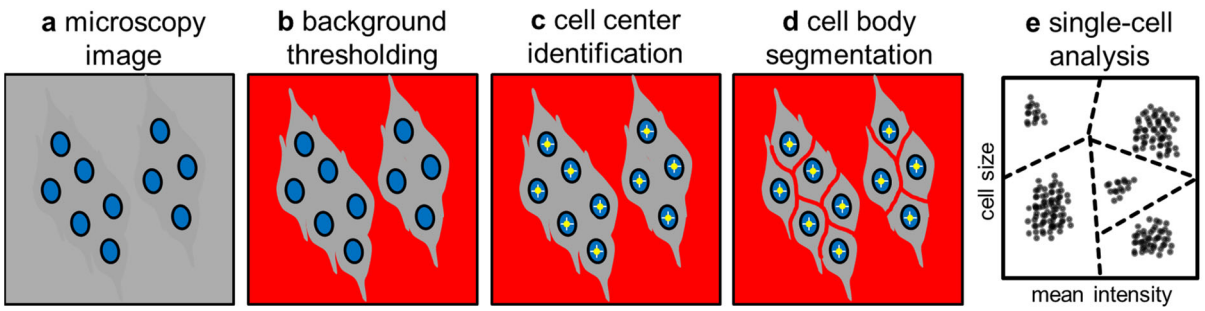

Figure 9: Overview of basic steps for image-based single-cell analysis. Firstly, the cells on the microscopy images (a) must be separated from the background (b) which is mostly done by intensity thresholding. The cell centers must then be detected (c, in most of the cases by nuclei staining) and then different algorithms (e.g., watershed) can be used to segment the cell bodies (d). Then, single-cell values like size, position, shape, and intensity can be quantified and plotted (e) to identify distinct cellular populations.

The segmented cells can be analyzed using specialized software tools (such as Fiji's Particle Analyzer [93]), which provide information such as size, fluorescence intensity, shape, orientation, and position for each individual cell, allowing identification of cell populations (Figure 9e) and quantification of condition-dependent effects [38].

2.4.2 Single-nanoparticle quantification

The overall fluorescence signal of a cell can be based on different reporter systems, resulting in an uniformly distributed fluorescence signal within the cell (e.g., due to GFP expression), but also in an inhomogeneous fluorescence distribution with local intensity maxima (e.g., due to clustered fluorescent nanoparticles such as labeled viruses). The quantification of the binding of such nanoparticles to cells is a very important method to study the interactions of biological relevant nanoparticles and cells, e.g., to study the uptake of medical nanoparticles [94] [95] [96] or the binding of viruses on cells [97] [98] [99]. In contrast to cells which are several tens of micrometer in size and can be easily imaged by current optical microscopy methods, nanoparticles (NPs) are between 1 to 100 nanometers in size [10], and thus below the diffraction limit of optical microscopy methods. Since the size of fluorescent nanoparticles and the point spread function (PSF) of their emitted light are close to the pixel size (about 60 - 300 nm [79]) of classical optical microscopy methods, alternative analysis steps have to be performed to obtain quantitative image-based information from them. The main challenge is that images of fluorescent nanoparticles associated with cells are very pixelated (Figure 10a) when pixel sizes of about 300 nm are used and therefore it is not possible to easily distinguish whether a fluorescent event (local intensity maximum) is a single nanoparticle or an agglomeration (or cluster) with an unknown number of particles [15]. To obtain an estimate of the total number of fluorescent NPs contained in an image (or region of interest (ROI) such as a cell), it is recommended to consider the intensity distribution of the image.

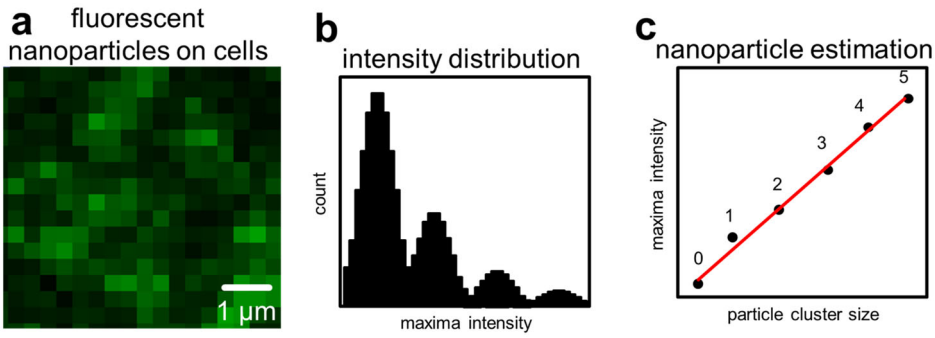

Figure 10: Nanoparticle quantification near the diffraction limit. Images of nanoparticles on cells (a) can be very pixelated (at pixel sizes at about 300 nm). If more than one particle can be accumulated within one pixel, an intensity histogram may reveal distinct intensity peaks (b). These peaks can then be attributed to the number of particles clustered together, allowing for a correlation of particle cluster size and intensity (c), which can be used to convert the fluorescence signal into a nanoparticle number.

If the fluorescent nanoparticles are not too densely packed and their intensity is relatively homogeneous, the intensity distribution of the ROI can reveal distinctive peaks (Figure 10b) that may represent the underlying number of fluorescent NPs in vicinity [100] that cannot be resolved individually [100]. This allows for a correlation (Figure 10c) of the intensity and particle cluster size, allowing to estimate the total number of NPs, even below the resolution limit of the microscopy method. However, these estimations are not always accurate, as previous studies showed that the number of NP events derived from optical microscopy is underestimated by a factor of ten when compared with the total NP number received by transmission electron microscopy (TEM) [12]. A precise validation of the intensity-based estimation is thus crucial to derive reliable results. Also, methods of analyzing fluorescent nanoparticles and cells in parallel with optical microscopy are mostly focused on single-cells, lacking the high-throughput capability of analyzing many cells in parallel to assess cell-to-cell heterogeneity in particle binding.

2.4.3 Single-particle tracking

In addition to image-based quantification of static nanoparticles, it is also possible to obtain quantitative information about dynamic systems by SPT [53] of image series obtained by video microscopy (Figure 11). Similar to single-cell analysis, it is important here to first separate the targets from the image background by intensity thresholding and then to localize the target center with localization accuracy below the diffraction limit, which can be achieved by applying two-dimensional fits (e.g., Gaussian maximum-likelihood estimator) to the intensity profile [101] [102]. After identifying the target centers for all images in the time series, these positions must be linked on an image-by-image basis. To accomplish this, most linking algorithms link nanoparticles across adjacent frames by calculating the distances between the "current" position of one nanoparticle and that of all nanoparticles in the subsequent frame, often taking into account a maximum linking distance [103]. This is done frame-by-frame for all nanoparticles. In this way, the time-dependent motion of the particles is represented by a single-particle trajectory (or track) that contains important information such as the diffusion coefficient as well as the diffusion mode (Brownian or anomalous diffusion [104] [105]). The diffusion mode provides information on whether the particles moved undisturbed by external factors (Brownian motion), or whether they were hindered by diffusion barriers [106] (subdiffusion) or under the influence of an external force [107] (superdiffusion). The diffusion coefficient D also contains information about the viscosity η of the surrounding medium and

the hydrodynamic radius *r* (approximately the size) of the tracked particle, as indicated by the Stokes-Einstein equation, which is valid for simple fluids:

$$D = \frac{k_B T}{6\pi\eta r} \qquad \text{Equation 1}$$

The relationship between the hydrodynamic radius of a particle in a lipid bilayer with solid support and its diffusion coefficient is described by the Evans-Sackmann model [108]. Basically, the model states that the larger the hydrodynamic radius of a particle in a two-dimensional fluid system, the lower its diffusion coefficient. Thus, if the size of a tracked object has changed during the time series (for example due to oligomerization of individual particles or decay of an oligomer) this can be detected via changes in the diffusion coefficient [109].

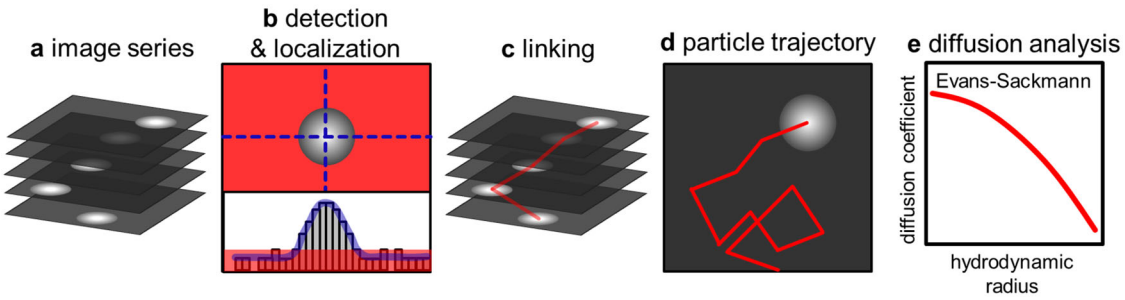

Figure 11: Overview of the basic steps of single particle tracking. A microscope-derived image series (a) is processed by detecting and localizing (b) the different PSFs of the target particles. The particle centers are linked image-wise (c), resulting in a time-resolved particle track (d). The diffusion coefficient derived from the particle track correlates with the hydrodynamic radius of the particles and is described by the Evans-Sackmann model (e) for 2D solid-support fluid systems.

However, these diffusion transition processes may be very rare events in an ensemble of many molecules and therefore difficult to detect or completely obscured if only the average response of all particles analyzed in parallel is investigated. It is therefore recommended that single entity methods be used for analysis.

2.5 Ensemble versus single-entity analysis

As described earlier, dynamic biological processes such as cellular or molecular responses to external stimuli can be analyzed using optical microscopy image series, e.g., by quantifying fluorescence intensities or diffusion coefficients. Although it is possible to do this using ensemble measurements, in which the average response of all detected targets is recorded (e.g., fluorescence or diffusion shift for the entire image), performing these analyses on a single-entity basis provides more information [110] [111] [112] and often describes the effect under investigation more realistically. For example, an ensemble measurement at the cellular level would be the fluorescence quantification of GFP-transfected cells under different transfection conditions using a plate reader. Here, it would be possible to identify more efficient transfection conditions based on the fluorescence signal, but a potential cytopathic effect of the transfection agents used would not be detected. Also, if subpopulations of the targets are present, they will likely not be accurately described by ensemble analysis. The mean intensity of a dark and a bright cellular population will deliver an average value, that is not representative for the real effect, as indicated

by the position of the mean line of the black boxplot in Figure 12a, which is located at an intensity value, not shown by one cell. Only the mean and standard deviation of the separated single-cell populations (green box plots) accurately describes the real behavior of the cells. At the molecular level, FRAP measurements of labeled membrane proteins before and after inducing oligomerization might show a general shift in diffusion coefficient [113] but do not allow identification of specific oligomerization states [114]. The black box plot of Figure 12b shows that the same mean and standard deviation of the diffusion coefficient of two different oligomerization histograms (top: valency of 2; bottom: valency of 3) would be derived.

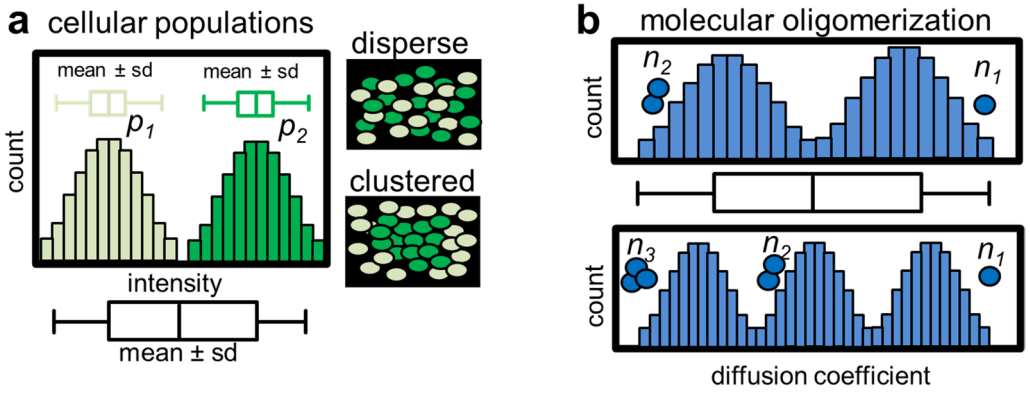

Figure 12: Importance of single-entity analysis compared to ensemble analysis. Microscopy images showing fluorescent cells are best described using a single cell analysis approach (a). In this example, an intensity histogram shows two different cell populations characterized by low (p_1) and high (p_2) intensity. The means and standard deviation (indicated by the green boxplots above the histogram peaks) of the two populations describe reality better than an ensemble analysis (indicated by the black boxplot below the x-axis), which analyses only the mean and standard deviations of the entire image fluorescence. An ensemble approach would also not be able to quantify the position of the cells, whereas a single-cell approach would be able to clarify whether the fluorescent cells appear disperesed or clustered on the images. Similarly, an ensemble approach would not be able to quantify different molecular oligomerisation states based on diffusion coefficient (b). Here, two diffusion coefficient histograms show two (top; n_1 and n_2) and three (bottom; n_1, n_2, and n_3) oligomerization states. However, an ensemble analysis (indicated by the black boxplot between the graphs) would yield the same mean and standard deviation in both cases, so that the different oligomerization states could not be resolved.

Using a single-entity analysis approach thus allows precise quantification of different target populations, identification of rare events, and provides more data points for the statistical analysis required to test small-scale effects. In addition to identifying these distinct populations, the single-entity approach also allows us to localize them and distinguish whether these populations are influenced by local microenvironmental conditions. For example, at the cellular level, this could reveal the presence of infectious plaques [115] if virus-infected cells show a fluorescent signal and cluster in certain areas of the image. At the molecular level, localization of labeled and tracked lipids with different diffusion coefficients may reveal the presence of nanodomains in the lipid membrane if these lipid populations cluster in certain regions on the image [116] [117].

However, to reliably identify those populations by single-entity analysis, the sample size and readout signal must be high enough, as otherwise those populations cannot be resolved and are obscured by data variance and measuring noise. In principle, to reliably identify local maxima in histograms as real peaks (populations) a specific minimal peak to valley ratio is needed [118] [119] (Figure 13a). Otherwise measuring noise, random effects, or binning artifacts [120] can be misinterpreted as populations (Figure

13b). In case of low-throughput analysis, it is therefore recommended to describe the readout as mean and standard deviation to avoid misinterpretation of pseudo peaks.

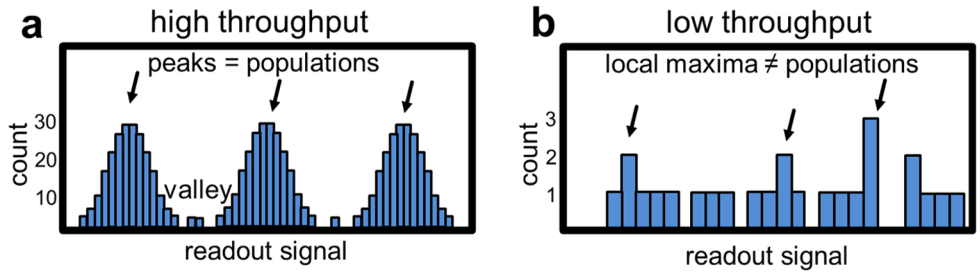

Figure 13: High-throughput analysis is required to reliably quantify different target populations. Only if high throughput data (a) is generated and plotted, the presence of distinct target populations can be assessed. The readout signal histogram of an experiment that only provides low throughput data (b) is not able to quantify or show the presence of different target populations.

It is therefore crucial to use high-throughput analysis methods [121] [111] to gain necessary readout and sample sizes for single-entity based identification of cellular and molecular populations. Such high-throughput approaches for the cellular scale were already described above (see 2.4.1 Single-cell analysis) however other techniques are needed to identify single-entity based populations on a molecular scale.

2.6 Single-molecule force measurements

The ability to study single molecules is a very powerful biophysical tool for many fields in life sciences, as it allows for the determination of the very soft intrinsic molecular target properties whose interactions ultimately lead to the formation of very complex systems such as cells. Many of these properties are related to forces, and thus various methods have been developed to measure single-molecule forces that allow for the study of the energy landscape [122], e.g., in protein (un)folding, receptor-ligand complexes, or the general mechanical properties of biopolymers. In the following, the three most prominent methods of single-molecule force spectroscopy [16] as well as their advantages and limitations are introduced.

2.6.1 Atomic force microscopy

Atomic force microscopy (AFM) is a single-molecule spectroscopy method, where an atomically sharp tip is mounted on a soft cantilever spring which is brought in vicinity to the sample. It allows for imaging of any flat solid surface, without the need for surface preparation, in vacuum, air, and liquids. To do this, a laser beam is sensing the cantilever's deflection (as it has a lower spring constant than the effective spring between two atoms) while a piezoelectric system moves the sample beneath the cantilever tip [123] [124] [125] [126]. AFM was often used in material science and physics to image the atomic structure of different materials like graphene or metal oxides. However, in recent years, is has also become a tool in biology, as it is possible to image the morphology, stiffness, and viscosity of cells (Figure 14a) [127] [128]. This allows for the atomic imaging of the cell surface topography, revealing e.g., nanodomains [129] [130] [131] [90] [90] which could not be resolved by optical microscopy techniques. Besides the imaging of a surface with atomic resolution, it is also possible to functionalize the cantilever tip, allowing for a direct binding of the tip to a molecular target (Figure 14b). With the cantilever bound to the target, a force

(10 - 10^4 pN [16]) can be applied to it and the stretching and rupture of the target can be monitored by yielding force-extension curves. As the target molecules are too small to be observed, it is very important to avoid and identify force-extension-curves (FECs) of unspecific binding events. To do so, proteins with known unfolding patterns can be integrated into a multi-protein construct as references (p_{r1} and p_{r2} in Figure 14b). The construct also contains the target protein (p_t) whose unfolding will be investigated. The FECs will show a characteristic saw tooth shaped pattern (Figure 14c), where the patterns of the reference proteins can be used as an indicator for a specific binding event, allowing for the exclusion of all unspecific binding events from further analysis.

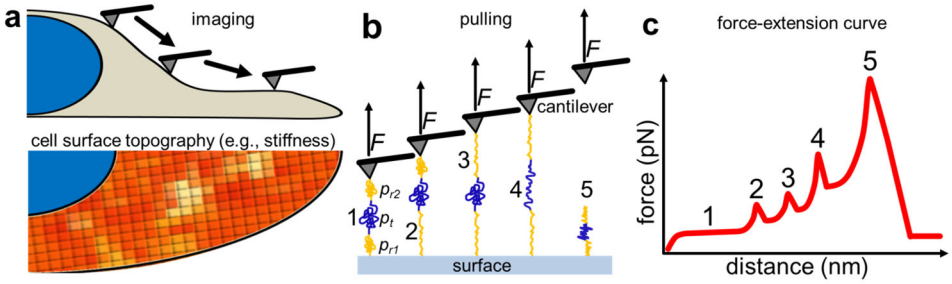

Figure 14: Overview of atomic force microscopy applications. The cantilever can screen the surface topography of biological membranes to investigate mechanical properties like the position-dependent surface stiffness of a cell membrane (a). By direct contact and pulling the target (b), the mechanical response of a target (e.g., a folded protein-construct) can be assessed. Therefore a reference protein (p_{r1}) is attached to a surface and a second reference protein (p_{r2}) is attached to a cantilever. Located between the two reference proteins is the target protein (p_t), which will be investigated. As the cantilever applies a force (F) on the proteins, the whole construct is stretched (1). First, the two reference proteins will unfold (2, 3) and afterwards the target protein will unfold (4) before the whole construct rips from the cantilever (5). This leads to a specific saw-tooth pattern in the force-extension curve (c).

AFM thus provides a direct way for measuring the binding and unbinding forces between various biomolecules like receptor-ligand complexes [132] [133]. This probing of the energy landscape of folded proteins is especially interesting for proteins which are cellular mechanosensors, like talin. Here, AFM was used to unfold the rod domains of talin and proved that each of the thirteen domains unfolds hierarchically at specific forces in the range of 10 to 40 pN [63], allowing the cell to sense subtle forces e.g., at locomotion. As this example shows how useful AFM as a single-molecule force spectroscopy method is, it has some limitations which must be overcome to expand the variety of biomolecular targets. That is that AFM lacks the capability of parallelization at low loading rates, as only one molecule at a time can be investigated [134]. This lack of parallelization limits the derived sample size especially in the regime of low loading rates making it difficult to yield statistically strong results for very weak effects at the low to sub pN and nm range. Also, the detection is ultimately limited by thermal fluctuations of the cantilever [134]. Therefore, the force exerted on the tip by spontaneous thermal fluctuations at room temperature (k_BT = 4.1 pN nm [17]) determines the minimal measurable force (which is also a problem with optical and magnetic tweezers, as discussed below).

2.6.2 Optical tweezers

Another single-molecule force spectroscopy method, able to apply lower forces (0.1 – 100 pN [16]) than AFM on molecular targets is called optical tweezers (OT). In this setup, a dielectric bead is hold in an optical trap, as light carries momentum, and thus any illuminated object experiences a force (Figure

15a). A bead placed in a weakly-focused laser beam will experience a net force towards the beam center, as the gradient of light intensity will exert different forces on the bead sides. This allows for the trapping of nano- and microbeads in Gaussian-profile lasers [135] [136]. OT is very versatile as it can apply forces in a wide pN range with sub-nm resolved three-dimensional measurement of the bead displacement [16]. If a trapped bead is linked to an immobilized target molecule and the laser then displaced, it is possible to translate the forces acting on the bead to the target to perform force measurements (Figure 15b). Again, the measurement of the displacement of the beam in the optical trap, and the force needed to induce this displacement, yield force-extension curves (Figure 15c) providing information about the mechanical properties of the target.

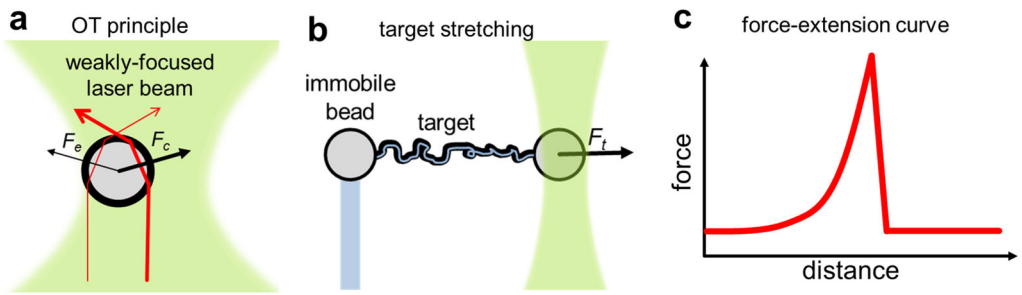

Figure 15: Overview of optical tweezers-based force measurements. Light passing through a transparent bead is refracted and bent, exerting force onto it. Near a weakly-focused laser beam (a), the bead is drawn from the edge (F_e) of the beam toward the beam center (F_c). A bead trapped in OT and attached to an immobilized target (b) will exert a force (F_t) on the target if the light source is moved. Monitoring of the position of the light source and the force applied to move it results in a force-extension curve (c) of the target.

This method was used to probe the mechanical properties of DNA [137], receptor-ligand complexes [138] [139], and even for tracking the movement of motor proteins [140]. OT measurements can be performed in artificial systems, where the target was immobilized on a functionalized glass surface, as well as on cells [139]. Interestingly it is also possible to hold whole cells [141], organelles within cells [142], and lipid vesicles [143] in the optical trap. Despite this versatility, OT also has some limitations and drawbacks mainly based on the used light trap. A disadvantage is the low parallelizability of the OTs. In most setups, only one or two optical traps can be used to capture particles and manipulate molecules. Holographic optical tweezers [144] are able to parallelize several optical traps by splitting a laser beam into several single beams. While this allows a certain degree of parallelization, the application remains limited to tens rather than hundreds of particles. The light beam will also trap all small dielectric particles (sometimes many in parallel) reducing the specificity and single-molecule aspect of this technique. Furthermore, the light of the optical trap can lead to photodamage of the sample, and will also heat up the local environment of the target, which will lead, e.g., to increasing enzyme activity or lower viscosity of the medium around the target.

2.6.3 Magnetic tweezers

Magnet tweezers (MT) is very similar to optical tweezers, since it also applies an external force is to a micrometer sized (magnetic) bead, but the source of the force is a magnetic field gradient [145] (Figure 16a), thus preventing drawbacks like sample heating or photodamage and making it very selective for the magnetic probe. MT also has a very broad force range (10^{-3} - 100 pN [16]) and can not only stretch

but also rotate the sample, making it very interesting for the study of rotary proteins [146] [147]. As the magnetic force is applied in a noninvasive way, MT can be used in complex and sensible environments like with magnetic beads inside cells [148] and biopolymer networks [149]. Recently, the MT setup was also used to apply lateral forces on fluorescent magnetic nanoparticles linked to the membrane of living cells (Figure 16b), allowing for the manipulation of surface proteins [150] and the probing for diffusion barriers (cytoskeleton) beneath the cell membrane [151].

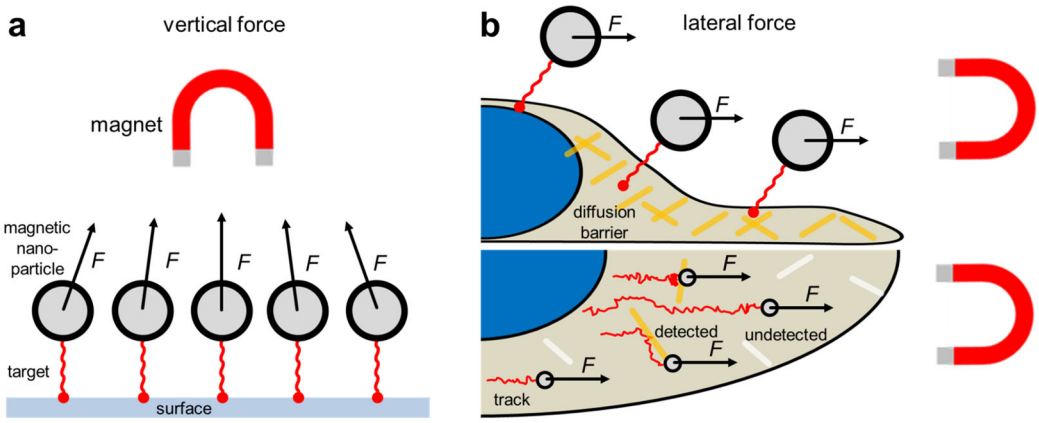

Figure 16: Magnetic tweezers applications for force investigations. A magnet above a sample of magnetic nanoparticles attached to a surface by linkers can apply vertical forces on many targets in parallel (a). This setup can also be used to apply lateral forces on magnetic nanoparticles (e.g. on cell membranes) to probe for diffusion barriers (b).

The drawbacks of MT are that using a permanent magnet configuration lacks the manipulation ability of other techniques and that the generated force falls off rapidly with displacement away from the magnet. Although there are experimental setups for parallelized magnetic tweezers [152] (allowing for parallel investigation of 400+ targets), the force gradient of the magnetic field will always lead to a target position dependent bias of the applied force. An alternative approach to apply forces on micro- and nanoparticles is the usage of hydrodynamics-based flow profiles instead of a magnetic field, which allow for a high degree of parallelization and flexibility in the applied force range.

2.7 Microfluidic shear force applications

In the last two decades, a new approach of single-molecular force applications emerged, namely the use of microfluidics-based hydrodynamic shear forces. Here, one end of a target molecule is immobilized at a solid (e.g., glass) or fluid (e.g., lipid bilayer) surface in a microfluidic channel and the other end is linked to a small bead. A bulk flow in the channel then exerts a force to the bead due to Stokes drift [153] and this force is then translated to the target. Tracking the position of the bead with optical microscopy allows then for a precise determination of the force-response of the target. As the flow will be ubiquitous in the system, many targets can be analyzed in parallel, while the sample size is only limited by the target density and the size of the imaged FoV. The following section gives an overview of the current state of the art of microfluidics based force applications and how this principle will be used to develop a new shear force based single-molecule force spectroscopy method with high-throughput capabilities, overcoming limitations of current methods.

2.7.1 Hydrodynamic force measurements

The basic setup for hydrodynamic-based single-molecule force measurements, is a microfluidic chip mounted on an optical microscope (Figure 17a). A bulk flow of the liquid in the microfluidic channel has a parabolic velocity profile, as friction with the channel walls will decrease the flow velocity, leading to the highest velocity being present in the channel center (Figure 17b). Suspended nanoparticles (or beads) inside the flow channel will experience shear gradient lift force (F_{LS}) and a wall-induced lift force (F_{LW}), based on their position in the channel [154]. When immobilizing the nanoparticle to the surface by a single molecular linker (Figure 17c), the force applied to the nanoparticle (F_{NP}) will be translated to the target (F_t). Knowing the architecture of the microfluidic channel and the parabolic flow velocity profile, it is possible to calculate the forces acting on the nanoparticle, based on the applied flow [155] [156]. Here it must be noted that a geometrical model regarding the angle (θ) of the NP and the target must be taken into account, to calculate the exact force that will be translated from the NP to the target:

$$F_t = F_{NP} cos\theta \qquad \text{Equation 2}$$

The flow-based forces acting on the target can range from sub-pN to several hundred pN force [156, 86]. Precise tracking of the nanoparticle displacement and calculating the flow based acting force, allows then for the extraction of the mechanical properties of the target through force-extension curves.

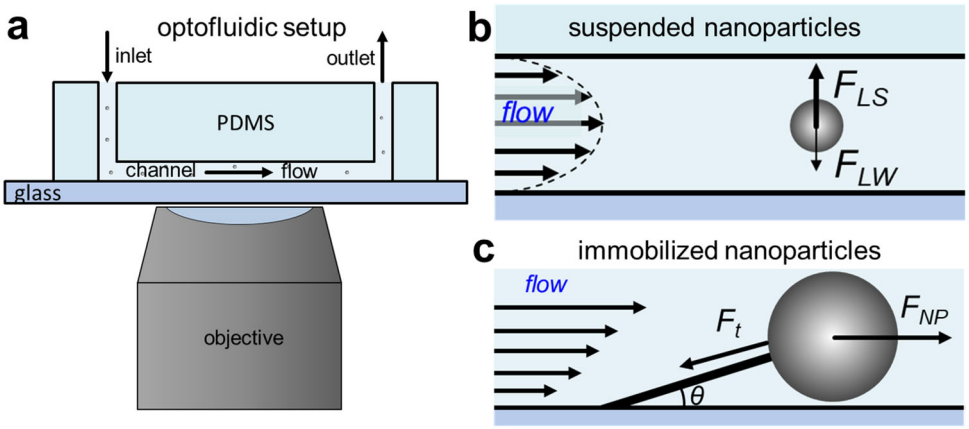

Figure 17: Overview of the usage of microfluidics to apply forces on nanoparticles. A PDMS microfluidic chip with a flow channel is attached to a glass surface and mounted on a microscope (a). The parabolic shaped flow velocity profile applies a shear gradient lift force (F_{LS}) and a wall-induced lift force (F_{LW}) on suspended nanoparticles (b). The nanoparticles can also be immobilized at the glass surface (c) to apply flow dependent forces (F_{NP}) on the target (F_t), allowing for the assessment of the mechanical response of the linker.

This technique was already used in the past, for example to quantify the streptavidin-biotin bond rupture force [155], determine the sequence dependence of the rate of DNA digestion by λ exonuclease [157], to characterize the effect of primase activity on DNA fork progression [158] [159], to monitor the kinetics of loop growth and leading-strand synthesis by replisomes [160], and to collect force-dependent motility parameters of cytoskeletal motors [161]. Despite the high versatility of this method, one of the limitations is that the forces acting on the target are derived by theoretical assumptions about the velocity profile of the flow and thus are only estimates of the real acting force. In addition, probes in the size range of approximately 1 - 10 µm have generally been used up to now. This reduces the parallelizability and leads to the preferred investigation of relatively long systems such as DNA.

2.7.2 Two-dimensional flow nanometry

While in the previous cases the flow-dependent force acting on the target was mostly estimated from the parabolic shaped flow profile, the following technique (2D flow nanometry [86]) allowed for a precise quantification of the acting forces and thus a force calibration (similar to Liang *et al.* [156]) of the used microfluidic channel architecture (Figure 18). Here it was experimentally proven that the torque near the microfluidic walls is neglectable, as the parabolic flow profile collapses here, since no turbulent flow can occur at the bead and the Reynolds number is therefore 0. In this setup, gold nanoparticles were linked to a SLB in a microfluidic channel on a TIRF microscope to study their movement by SPT. The bulk flow in the channel acted a shear force on the particles (Figure 18a) resulting in a movement in flow direction. When tracked (Figure 18b) the movement of the particles showed a directed motion in flow direction and a random motion perpendicular to the flow (Figure 18c). These two movement patterns were split, allowing for the determination of the velocity in flow direction (Figure 18d, v_x) and the diffusion coefficient of the linker (Figure 18e, D_y). As D_y is dominated by the friction of the linker in the SLB, and v_x scales with the applied flow and the particle radius (r), it is possible to calculate the shear force (F_s) acting on the particle, based on the Einstein-Smoluchowski relation [162]:

$$D_y = k_B T \frac{v_x}{F_s} \qquad \text{Equation 3}$$

This is based on the fluctuation-dissipation theorem, which states that the shear force that generates directional NP motion also generates dissipation/friction in the SLB [163].

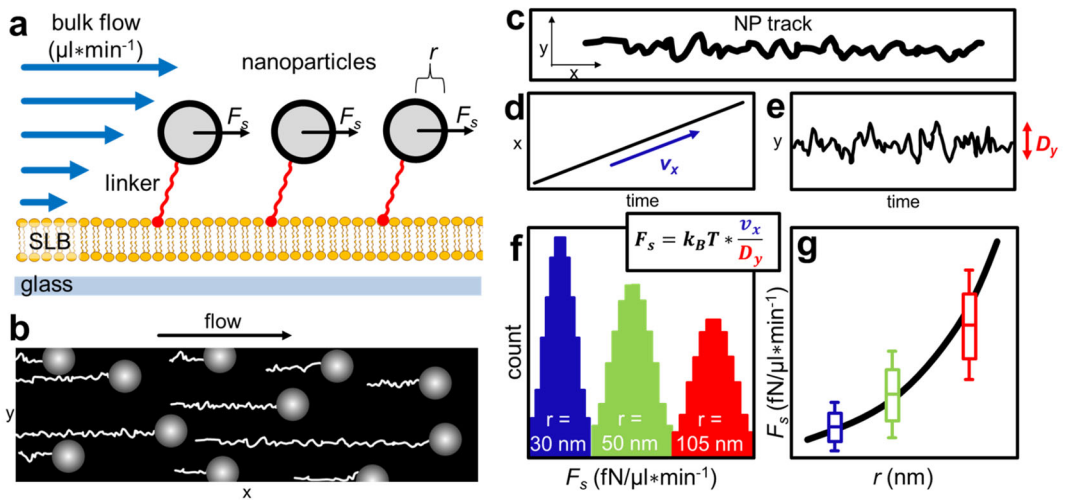

Figure 18: Two-dimensional flow nanometry allows for precise force-calibration of a microfluidic channel architecture. Nanoparticles linked to a SLP in a microfluidic channel experience a specific shear force (F_S) dependent on their hydrodynamic radius (r) and the applied bulk flow (a). The movement of the particles in flow direction (b) results in particle tracks (c) which movement can be split in the velocity in flow direction (v_x; d) and the diffusion coefficient of the linker (D_y; e). The Einstein–Smoluchowski relation then allows for the calcultion of the shear force acting on a nanoparticle with a specific hydrodynamic radius (r; f). Plotting the shear force acting on the particles (F_S) against their hydrodynamic radius (r) allows for quantification of the relation of the flow dependent shear force acting on nanoparticles of specific sizes (g).

In short, the greater the shear force F_s is due to flow rate or particle size, the faster the particle's movement in flow direction $v_{x,}$ while the diffusion coefficient D_y remains constant, unless the shear force influences the interactions with the membrane. The values of v_x and D_y can both be quantified by tracking the particle movement. With this relation, the shear force acting on particles of different sizes was calculated (Figure 18f) and with this information the specific microfluidic channel system could be calibrated, by determining the relation of the shear force acting on a particle depending on its size (Figure 18g).

The force calibration based on 2D flow nanometry allows to precisely calculate the force F_s acting on a NP of the size r in a given microfluidic channel architecture at a specific flow rate f. For the microfluidic channel system used by Block *et al.* [86] (width: 150 µm; height: 100 µm) this would be, a shear force of 11.5 fN/µl*min^{-1} for a 200 nm sized nanoparticle. A molecular target linked to the channel surface and to such a 200 nm sized bead would experience a shear force of roughly 0.1 pN at a flow of 10 µl/min or 17.3 pN at 1500 µl/min. In a system with a stable surface linking, a geometrical model regarding the angle of the NP and displacement of the target (Equation 2) must be taken into account to calculate the precise acting forces translated to the target. However, the aforementioned force range shows that a microfluidic-based force spectroscopy method would be able to probe molecular targets in the low to sub pN range, while still retain a high-throughput character, due to the homogeneously distributed flow-induced shear force.

3. Scientific goals

The problem with current image-based quantification methods is that they often lack either high throughput or sensitivity, as it is very difficult to address both aspects simultaneously. This is true, for example, for the analysis of cellular images, which are often only qualitatively examined or for which special training is required to find appropriate analysis parameters (such as intensity thresholds or size cutoffs), but also for the precise quantification of nanoparticles, whether they are static (e.g., bound to cells) or used as probes in a dynamic setup (e.g., tracking of membrane receptors or microprobes in force spectroscopy techniques). Therefore, the aim of this work is the development of new high-throughput yet very sensitive methods able to quantify cellular and molecular populations and responses, with single-entity resolution. These methods are based on the high versatility and resolution, which optical microscopy with subsequent refined data analysis can achieve. While imaging of cells is already established for many biochemical assays [164] [165], the systematic quantification of these images with single-cell resolution is not. Optical microscopy also allows for the quantification of fluorescent nanoparticles (like vesicles, viruses, or medical nanocarriers) on the cellular level [100], but doing so in high throughput with sufficient precision is not a laboratory routine yet. Furthermore, optical video microscopy bears an even higher potential (compared to the analysis of static images) as the analysis of image-based time series (e.g., the tracking of proteins or lipids on cells) can give information about otherwise invisible domains [166] [167] on cell membranes or the oligomerization state of transmembrane receptors [52]. Block *et al.* [86] showed that optical video microscopy in combination with a microfluidic setup and single-particle tracking, is even able to analyze the shear-force dependent movement of nanobeads with a precise spatial resolution in the nanometer range while still analyzing many targets in parallel.

One aim of this thesis is to develop a single-cell analysis method to quantify the number of virus-infected and -uninfected cells under treatment with virus-binding inhibitors in different concentrations. To be efficient, the method must not only be precise (yielding single-cell information, qualitatively comparable to manual analysis), but also fast (1-2 seconds per image), and fully automated, to make it easy to use even for untrained personnel. Furthermore, this approach should be expanded to even be able to quantify single fluorescent viruses (nanoparticles) on single cells to allow for a deeper understanding of the binding and binding inhibition processes of viruses and host cells. Here, it is crucial to image several tens of cells in parallel, to probe for cell-to-cell heterogeneity in virus binding, which will lead to a sub-diffractive clustering of the targets and thus the need for precise reconstruction of the number of bound particles, which must be carefully validated. Beside the quantification of static nanoparticles, dynamic processes on the nanoscale should additionally be investigated by optical video microscopy with subsequent single-particle tracking. For this, the quality of established SPT setups must first be assessed and refined, so that molecular responses can be quantified, which are below the diffraction limit of optical microscopy. If successful, this should be combined with a microfluidic setup to allow for the application of low forces in the pN range to single immobilized molecular targets like polymers and proteins. Due to the high resolution and parallelization capability of such a system, it is expected to enable the probing of force responses and energy landscapes of single-molecules and molecule complexes with unprecedented sensitivity.

To conclude, the following scientific goals and hypothesis will be addressed in this thesis: (I) It is possible to perform a fully automated high-throughput segmentation of 2D cellular monolayers with subsequent identification of cellular populations based on fluorescence. (II) Cells and fluorescent NPs can precisely be quantified in parallel even at resolutions where clustered NPs cannot be resolved individually. (III) SPT can resolve molecular responses (such as oligomerization processes) on cells as well as in artificial systems. (VI) Microfluidics can apply low to sub-pN forces on single-molecule targets and the combination of optical video microscopy and SPT is able to precisely resolve the mechanical molecular response in high-throughput manner.

These hypotheses were addressed in four projects. In the first project, a fully automatic Fiji-macro for the segmentation of 2D cellular monolayers was developed, which was able to determine the fluorescent and non-fluorescent cellular populations under inhibitor treatment with different concentrations, allowing for the quantification of the IC_{50} value of virus-inhibitors. The second project regarded the establishment of an imaging and analysis workflow, enabling the segmentation of confocal imaged cells and quantification of the number of bound sub-diffractive fluorescent virus-like particles (VLPs) in high precision (validated by simulations), which revealed cell-to-cell heterogeneity in particle binding. In the third project, an approach for the refinement of SPT experiments was introduced, which was used to quantify the oligomerization grade of membrane associated proteins and the displacement of fluorescent beads used in project four. Here, a new highly sensitive microfluidics based single-molecule force spectroscopy method was established, used for analyzing the mechanical response of PEG-linkers and the third rod domain of the protein talin, as well as for probing the energy barriers of the biotin-NeutrAvidin complex.

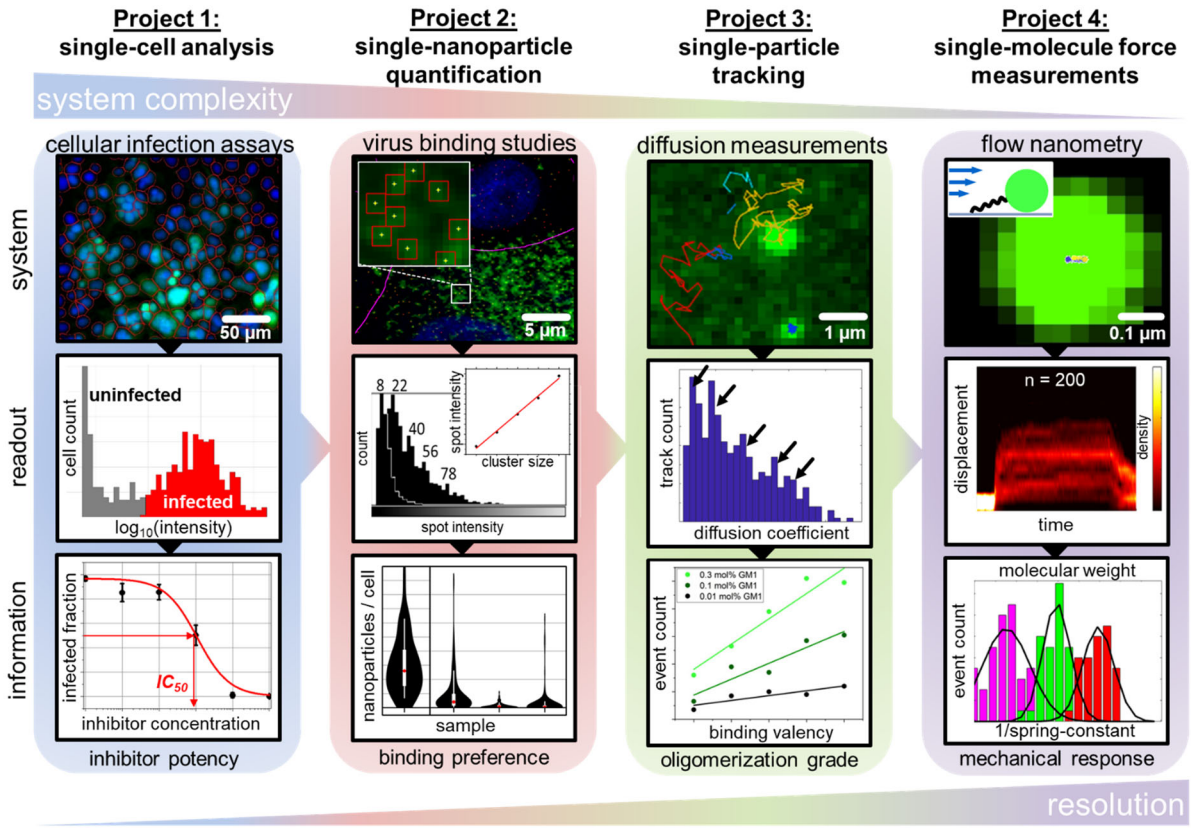

Figure 19: Overview of the subprojects included in this thesis. First, a single-cell analysis method (project 1) was developed to quantify the fraction of virus infected cells under inhibitor treatment to determine the inhibitor potency based on its IC_{50} value. Next, the single-cell segmentation method was extended with the quantification of sub-diffractive nanoparticles (project 2), allowing to perform binding studies of virus-like particles with single-cell resolution. Refined single-particle tracking (project 3) was then used to analyze dynamic membrane-associated interactions like BMPR oligomerization and multivalent GM1 binding of CTxB. The single-particle tracking was then combined with microfluidics (project 4) to perform high-troughput single-molecule force measurements to probe the mechanical response of polymers, proteins, and receptor-ligand complexes.

4. Publications

In this chapter all published articles and submitted manuscripts are listed and the contribution of the authors are stated.

4.1 A fast open-source Fiji-macro to quantify virus infection and transfection on single-cell level by fluorescence microscopy

---

Yannic Kerkhoff, Stefanie Wedepohl, Chuanxiong Nie, Vahid Ahmadi, Rainer Haag, and Stephan Block

MethodsX 9, 101834 (**2022**)

DOI: https://doi.org/10.1016/j.mex.2022.101834

Short summary

In this work an automatic single-cell segmentation method was implemented to quantify the fluorescent fraction of widefield and confocal imaged cellular monolayers (Figure 20). It was used to screen the infection inhibition potency of heparin mimicking polymers against HSV-1 infection, showing virustatic and virucidal effects [168].

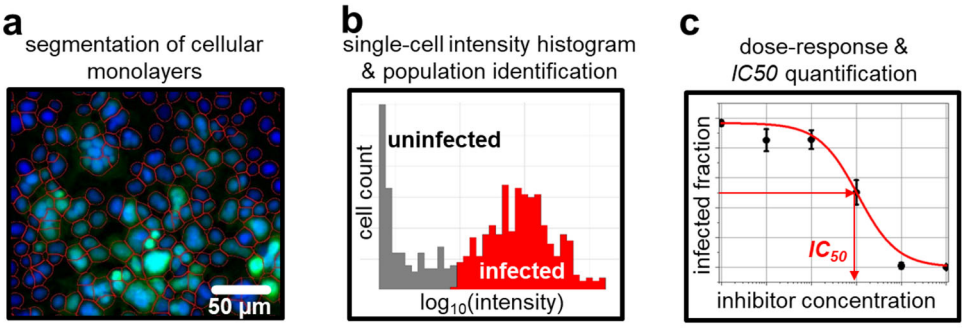

Figure 20: Widefield imaged cellular monolayers were automatically segmented (a) and the single-cell intensity was plotted in a logarithmic scale to determine the infected fraction (b). Plotting the infected fraction against the applied inhibitor concentration allowed for the determination of the inhibitos IC_{50} value.

Author contributions

Yannic Kerkhoff developed and validated the software, performed all image analysis, prepared all figures and wrote the original draft. Chuanxiong Nie performed all virus infection and inhibition assays. Stefanie Wedepohl performed all experiments for the transfection series and cell mixing validation series. Vahid Ahmadi prepared and provided inhibitors. Rainer Haag and Stephan Block were responsible for supervision, reviewing, and editing of the draft.

MethodsX 9 (2022) 101834

Contents lists available at ScienceDirect

MethodsX

journal homepage: www.elsevier.com/locate/mex

Method Article

A fast open-source Fiji-macro to quantify virus infection and transfection on single-cell level by fluorescence microscopy

Yannic Kerkhoff*, Stefanie Wedepohl, Chuanxiong Nie, Vahid Ahmadi, Rainer Haag, Stephan Block*

Institute of Chemistry and Biochemistry, Freie Universität Berlin, Berlin, Germany

A B S T R A C T

The ability to automatically analyze large quantities of image data is a valuable tool for many biochemical assays, as it rapidly provides reliable data. Here, we describe a fast and robust Fiji macro for the analysis of cellular fluorescence microscopy images with single-cell resolution. The macro presented here was validated by successful reconstruction of fluorescent and non-fluorescent cell mixing ratios (for fluorescence fractions ranging between 0 and 100%) and applied to quantify the efficiency of transfection and virus infection inhibition. It performed well compared with manually obtained image quantification data. Its use is not limited to the cases shown here but is applicable for most monolayered cellular assays with nuclei staining. We provide a detailed description of how the macro works and how it is applied to image data. It can be downloaded free of charge and may be used by and modified according to the needs of the user.

- Rapid, simple, and reproducible segmentation of eukaryotic cells in confluent cellular assays
- Open-source software for use without technical or computational expertise
- Single-cell analysis allows identification and quantification of virus infected cell populations and infection inhibition

A R T I C L E I N F O

Method name: Single-cell fluorescence quantification (SCFQ) macro

Keywords: Automatic cell segmentation, Single-cell analysis, Quantitative fluorescence microscopy, Infection inhibition, Transfection efficiency

Article history: Received 3 June 2022; Accepted 22 August 2022; Available online 2 September 2022

* Corresponding authors.
E-mail addresses: ykerkhoff@zedat.fu-berlin.de (Y. Kerkhoff), stephan.block@fu-berlin.de (S. Block).

https://doi.org/10.1016/j.mex.2022.101834

Specifications table

Subject area;	
More specific subject area;	Automatic single-cell segmentation
Name of your method;	Single-cell fluorescence quantification (SCFQ) macro
Name and reference of original method;	*NA*
Resource availability;	Fiji is freely available (https://imagej.net/software/fiji/downloads). The macro (S7), a tutorial video (S8) and widefield images from the cell mixing experiment (S9) are provided as free separate supplementary materials

Introduction

Cellular infection assays are a widely used laboratory method to probe the infectivity of viruses as well as to test potential virus infection inhibitors [1], and proved to be highly valuable especially in times like the current SARS-CoV-2 pandemic [2]. Many infection assays can be analyzed by imaging an infected cell culture using optical microscopy, by staining of the cell nuclei (*e.g.*, using Hoechst 33342) and by using a fluorescent marker (*e.g.*, GFP expression [3]) or immunostaining of viral proteins [4]. To show a general effect of infection or infection inhibition, the acquired images are often examined only qualitatively. However, an image series of different experimental conditions (*e.g.*, treatment with different inhibitor concentrations) can also provide quantitative information [5] (*e.g.*, the inhibitor potency based on the IC_{50} value) if one is able to extract this information from the image series. In recent years, several open-source software solutions have been developed that allow to extract image-based fluorescence information with single-cell resolution [6–12]. Each of these software solutions have different analysis strategies and aim for different fluorescence readouts. For example, QuantIF [9] and FNMM [11] aim for the colocalization of the nucleus staining with another fluorescence signal. FluoQ [6] and PiQSARS [12] are tailored for time-lapse-based experiments, while Cytokit [8] is specialized in correlating single-cell parameters with spatial information (for details see Supplemental Materials Section S6: Image analysis software overview). However, as most software is highly specialized for specific tasks, the software solutions mentioned above may not necessarily meet the needs of all users. This is due to the high variability of experimental setups (*e.g.*, the microscopy method, magnification, cell type, and cell density used) and read-outs (*e.g.*, fluorescence source, intensity, and fraction) used by the community. To address this, we developed and validated a versatile, easy-to-use and open-source Fiji macro [13] that is capable of quantifying transfection, viral infection, or inhibition of viral infection by evaluating intensity distributions at the level of individual cells in monolayered cellular assays. The macro was optimized to perform on a wide range of cell densities and fluorescent cell fractions for different cell lines as well as experimental and microscopy setups. It requires only three input parameters (addressing background signal, cell density, and marker intensity) and allows for fast batch analysis with detailed single-cell information. Besides fluorescence, the position, size, and circularity of each detected cell is saved in a data table, which allows, *e.g.*, for the localization of fluorescent and non-fluorescent cells within the sample. It contains an automatic correction of background fluorescence and provides a segmentation overlay and visualization of cell populations for easy manual inspection of the analysis output.

Fig. 1 shows an overview of our approach for quantifying fluorescent cell populations. First, images of a cell monolayer with stained nuclei and another fluorescent marker (dependent on the experimental setup) are acquired (Fig. 1A, D, G, J). The cells are automatically segmented (Fig. 1B, E, H, K) and the fluorescent marker intensity is quantified for each cell individually, enabling to discriminate between different populations (recognizable as two peaks or one peak with a tail in Fig. 1C, F, I, L) across the cell ensemble.

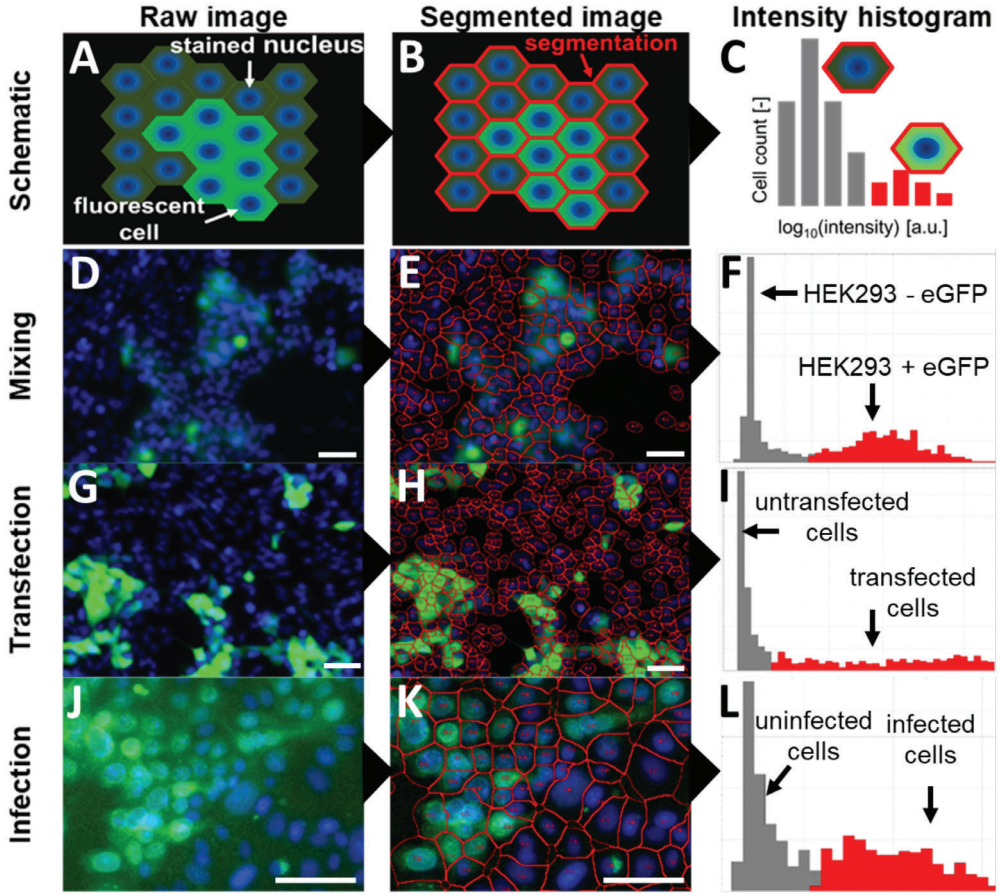

Fig. 1. Concept overview (scale bars = 50 µm) of the single-cell fluorescence quantification procedure. The raw images (A, D, G, J) consist of two-dimensional cell monolayers, in which the nuclei of all cells have been stained (blue), while only a fraction of the cells shows a fluorescent signal of a fluorescent marker (green). Individual cells are identified based on their nucleus (centers), segmented by a watershed algorithm (red lines, B, E, H, K), and separated from empty (cell-free) areas by their intrinsic autofluorescence signal. Calculating $\log_{10}$ intensity histograms (C, F, I, L) of the observed single-cell fluorescence values typically reveals two populations, which correspond to fluorescent (red) and non-fluorescent cells (gray) observed in the image.

Method details

Cell transfection and mixing

10^4 human embryonic kidney cells (HEK293, #ACC 305, Leibnitz Institute DSMZ – German Collection of Microorganisms and Cell Cultures GmbH) per well were seeded in full medium (DMEM supplemented with 10% FBS (#P04-04500 and #P30-3031, PAN Biotech Germany), 0.1 g/L streptomycin sulfate and 0.065 g/L penicillin G potassium (#1852,0100 and #A1837,0100, BioChemica Germany)) into 96 well plates and incubated over night at 37 °C and 5% CO_2. On the next day, transfection complexes were formed and added to the cells as follows: 0.1 µg plasmid DNA (pEGFP-N3, Clontech) was diluted in 10 µL 150 mM NaCl solution (saline) and 0.1 to 0.6 µg of PEI (25 kDa branched, #408727, Sigma-Aldrich) was diluted in 10 µL of saline separately. The PEI dilutions were added to the DNA dilutions under vigorous mixing for 5–10 s and incubated for 15 min at room temperature

afterwards. The cell culture supernatant was replaced with 100 µL/well fresh medium and 20 µL/well of transfection complexes were added. After incubation for 48 h at 37 °C and 5% CO_2, cell nuclei were stained with Hoechst 33342 (1 µg/mL in medium, #H1399, Thermo Fisher Scientific) for 10 min at 37 °C. The cell culture supernatant was replaced with fresh medium and cells in the plates were imaged with a 10x objective (A-plan 10x/0.25 Ph1, #441031-9910, Zeiss; FOV: 895.26 µm x 670.80 µm) on a Zeiss Axio Observer Z1 widefield fluorescence microscope equipped with an Illuminator HXP 120C, Colibri LED light sources 400, 530 and 625 nm, and an AxioCam MRm monochrome CCD camera. The ZEN software was used for image acquisition with the default GFP, DAPI or phase contrast settings using filter sets 38 (GFP: excitation 450–490 nm, emission 500–550 nm) and 49 (DAPI: excitation 335–383 nm, emission 420–470 nm). The confocal images of Fig. 3B were taken with a 20x objective (20x/0.75 HC PL APO CS2 Imm Corr (oil, water, glycerol) WD 0.68 mm, #11506343, Leica Microsystems; FOV: 581.82 µm x 581.82 µm) with oil immersion on a Leica SP8 system based on a DMI6000CSB microscope, which is equipped with diode (405 and 561 nm), argon (458, 488, and 514 nm) and a HeNe (633 nm) laser as well as two PMTs and two HyDs (high sensitivity Hybrid Detectors). The LAS X software was used for image acquisition with the Leica presets for DAPI (excitation 405 nm, emission 430–550 nm, HyD) and GFP (excitation 488 nm, emission 503–603 nm, PMT).

For the validation experiment (Fig. 3), a HEK293 cell line (stably transfected with pEGFP-N3 and showing 100% eGFP expression after clonal selection under 0.4 mg/mL geneticin) was mixed with non-transfected (non-fluorescent) HEK293 cells at different ratios and seeded into a µ-slide 8-well (#80826, ibidi; 300 µL/well at 4×10^5 cells/mL). After overnight incubation, cell nuclei were stained with Hoechst 33342 and images were acquired as described above.

Virus infection assay

African green monkey kidney epithelial cells (Vero) were seeded in 12 well plates (#83.3921.005, SARSTEDT AG & Co. KG, Germany) at a density of 2×10^5 cells per well. At 90% confluency, the cells were first incubated with unfractionated heparin (#375095, Calbiochem, Germany) at different concentrations for 1 h. Then herpes simplex virus type 1 having the gene for green fluorescent protein (GFP) integrated into its genome (HSV-1_GFP) was added at a multiplicity of infection (MOI) of 0.1 for 48 h. Cell nuclei were labelled by Hoechst 33342 (1 µg/mL in medium, #H1399, Thermo Fisher Scientific) for 10 min at room temperature and the cells were fixed by 1% formaldehyde (#1039992055, Sigma-Aldrich) for 30 min. After being washed with PBS, the cells were imaged using widefield epifluorescence microscopy as mentioned above (2.1), in which infected cells showed green fluorescence due to GFP expression.

Analysis macro

Fig. 2 shows the basic steps for using the single-cell analysis macro presented in this work. All images to be analyzed must be collected in one input folder, which may contain several subfolders (*e.g.*, different inhibitor concentrations etc.). One output folder should be prepared, which will store all results generated by the macro. The macro is opened in Fiji [13] (which is an open-source distribution of ImageJ [14]) and started by pressing *Run*. The user then selects the input and output folder as well as the data format (without a ".") of the input images (*e.g.*, lif, czi, tif) and defines, which channels contain the nucleus staining and the fluorescent marker signal, respectively (additional channels will be ignored). Afterwards, the user choses analysis parameters that are connected to the background threshold (denoted by β in the following), the segmentation sensitivity ω, and the intensity cutoff value α (for details see Supplemental Materials Section S4: Parameter optimization). These parameters can be optimized iteratively by repeating the analysis using revised parameters. For the initial analysis iteration, default parameters are implemented in the macro, which can be used in most cases. Alternatively, automatically estimated analysis parameters can also be used on demand (for details see Supplemental Materials Section S5: Automatic parameter estimation). The macro then automatically analyzes all selected images (taking approximately 1–2 s per image for a personal computer equipped with a CPU having a clock speed of 2.5 GHz, 2 cores, and 8 GB of RAM) and saves for each analyzed

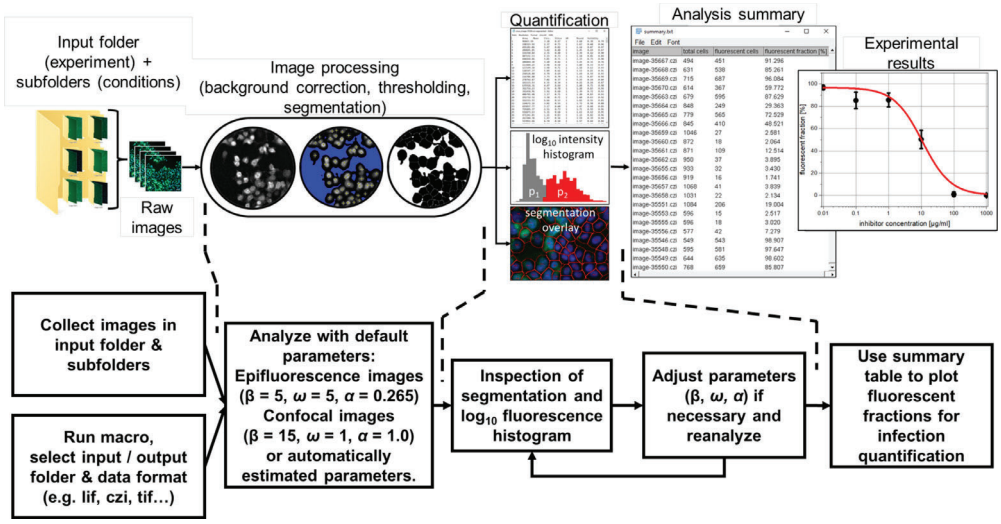

Fig. 2. Usage flowchart of the analysis macro. All images in a user-selected input folder (and all subfolders) are automatically analyzed using default or automatically estimated analysis parameters (for details see Supplemental Materials Section S5: Automatic parameter estimation). The segmentation overlays and infection histograms are saved in a user-selected output folder. The analysis parameters can be adjusted after manual inspection of the analysis results in order to refine the analysis process until the segmentation overlay and intensity histograms show reasonable results.

image the obtained segmentation overlay, the $\log_{10}$ histogram of the extracted cell intensity, a data table collecting various single-cell parameters (*e.g.*, area, mean intensity, x- and y-position, circularity, …) and a summary table to the output folder. The analysis workflow is also shown and explained further detail in a tutorial video (see Supplemental Materials Section S8).

To get a first impression on the validity of the parameters chosen for analysis, it is recommended to analyze either one image with two equally represented populations (non-fluorescent and fluorescent) or two images, in which most cells either exhibit fluorescence or not, which serve as positive and negative controls. A manual inspection of the segmentation overlay and the $\log_{10}$ intensity histogram of these images allows to check if analysis parameters need to be adjusted (see Supplemental Materials Section S4 for a guide for parameter optimization). The analysis can then be revised several times until the outcome of the segmentation and intensity analysis is acceptable for the user. Afterwards, the summary table (which contains the image titles, total cell number, and fluorescent cell number) can be used to quantify the property of interest, *e.g.*, transfection efficiencies or infection inhibition effects (for details see Supplemental Materials Section S1: Image processing steps).

Method validation

The method implemented in the macro was validated by mixing an eGFP expressing HEK293 cell line with non-transfected HEK293 cells at different mixing ratios. Fig. 3A and B show representative images for three mixing ratios (0, 40 or 50, and 100% eGFP expressing cells; obtained using either widefield or confocal microscopy) as well as the results of the segmentation and the corresponding $\log_{10}$ intensity histograms obtained using the macro. For both imaging modalities, we observed a linear correlation between the determined and the input fluorescent fraction (Fig. 3C; widefield: $R^2 = 0.95$, slope $= 0.94 \pm 0.06$; confocal: $R^2 = 0.98$, slope $= 0.94 \pm 0.05$), indicating that the macro reliably determines the correct ratio of fluorescent and non-fluorescent cells. Only the widefield measurements having an input fraction of 30% and 70% of eGFP expressing cells showed a statistically significant deviation from the expected trend. However, these deviations were also present in the images and are therefore not due to a failure of the analysis macro. These deviations are attributed

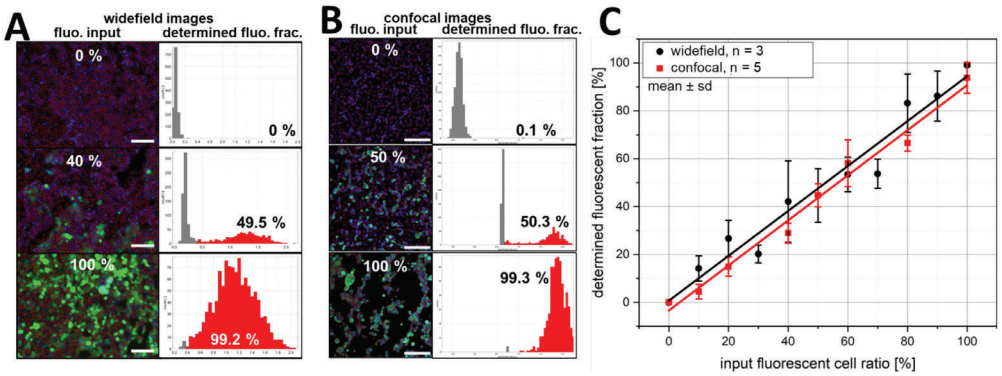

Fig. 3. Validation by cell mixing. Two HEK293 cell populations, either expressing eGFP or not, were mixed at different ratios and three to five images per ratio were quantified using the analysis macro. Panels A and B show three representative microscopic images (scale bars = 150 µm), which were obtained using either widefield (A) or confocal microscopy (B), as well as the result of the segmentation process (red contours in the images) and the corresponding single-cell $\log_{10}$ intensity histograms. The fraction of fluorescent cells is indicated in the microscopy images (input values, defined by the mixing process) and histograms (extracted by single-cell analysis), respectively. For both imaging modalities a high correlation between input and determined fluorescent fraction is observed (panel C; widefield: $R^2 = 0.95$, slope = 0.94 ± 0.06; confocal: $R^2 = 0.98$, slope = 0.94 ± 0.05). The images of the widefield mixing series are provided in the Supplemental Materials Section (S9) so that the macro (with possible modifications) can be tested by the user. Sufficient analysis parameters are $\beta = 15$; $\omega = 5$; $\alpha = 0.4$.

to minor manual errors in the initial cell mixing and random fluctuations in the number of cells that can be imaged in one field of view, as well as cells which have low expression levels [15].

Use cases

Quantification of transfection efficiencies

After successful validation, we applied the analysis macro to quantify the transfection efficiency of HEK293 cells, which were transiently transfected with eGFP for different transfection conditions (*i.e.*, for DNA:PEI ratios ranging from 1:1 to 1:6 and for a total amount of DNA:PEI complexes ranging from 0.1 to 0.7 µg). Fig. 4A shows three representative images corresponding to DNA:PEI ratios of 1:5, 1:3 and 1:1 (0.4 µg DNA:PEI complexes) as well as the obtained segmentation and corresponding $\log_{10}$ intensity histogram. For this series, the highest fluorescent fraction was observed for a DNA:PEI ratio of 1:3 (51%), so that an optimal transfection efficiency could be seen at this condition. The total number of observed cells decreased with decreasing DNA:PEI ratio, which is attributed to the well-known cytotoxic effect exhibited by PEI at higher concentrations (see Fig. S3 in the Supplemental Materials Section S3 - Plate reader validation) [16]. Hence, optimal transfection requires to find a balance between the DNA:PEI ratio (transfection efficiency) and the total PEI concentration (cytotoxicity).

To this end, we made use of the high-throughput capability of the macro and visualized the determined transfected cells (Fig. 4B) and transfected fraction for all tested conditions (Fig. 4C) as heat maps. A considerable amount of transfection (> 35%) was observed for DNA:PEI ratios ranging between 1:2 and 1:4 at a total amount of DNA:PEI complexes ranging between 0.2 and 0.5 µg. At lower ratios and amounts, less transfection was found, which indicates that the amounts of plasmid DNA or transfection reagent were too low. At higher ratios and amounts, the transfection efficiency was also reduced, which is again attributed to the cytotoxic effect of PEI at higher concentrations [16]. The highest fraction of transfected cells (75.4%) was found at a DNA:PEI ratio of 1:2 and a total amount of DNA:PEI complexes of 0.5 µg, which marks the optimal transfection condition in this setup if the transfected fraction is considered the key marker for transfection efficiency. Considering also

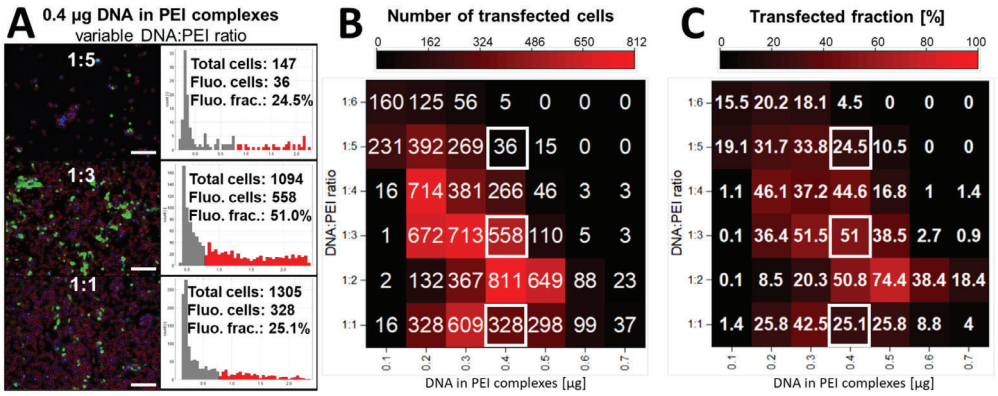

Fig. 4. Quantification of transfection efficiencies of DNA:PEI complexes. HEK293 cells were transiently transfected with eGFP by PEI using different amounts of plasmid DNA (0.1–0.7 µg) and mixing ratios of DNA and PEI (1:1 – 1:6). Panel A shows three representative microscopic images of cells treated with 0.4 µg of DNA:PEI complexes (using DNA:PEI ratios of 1:5, 1:3, and 1:1 as indicated in the images) as well as the segmentation and corresponding single-cell $\log_{10}$ intensity histograms (scale bars = 150 µm). Panels B and C show heat maps that visualize the total number of transfected cells (B) or fraction of transfected cells in% (C), respectively. The three conditions shown in Panel A are marked with white squares in the heat maps. One image per condition was analyzed.

cytotoxicity, the best balance between transfection efficiency and cytotoxic effects is observed at a DNA:PEI ratio of 1:2 and a total amount of DNA:PEI complexes of 0.4 µg.

Quantification of viral infection

In another use case, the analysis macro was used to automatically determine the fraction of Vero cells that had been infected with a variant of the herpes simplex virus 1 (HSV-1_GFP), which causes infected cells to exhibit green fluorescence due to GFP expression. Six images of infected cells that vary in their cell densities (approximately 650 to 1050 cells per image) and values of the infected fraction (approximately 2 to 90%) were chosen and analyzed manually (Fig. 5A) as well as with the analysis macro (Fig. 5B), which allowed to correlate automatically and manually obtained results (Fig. 5C). Cells were manually identified and counted based on their nucleus staining and their perinuclear space was inspected for green fluorescence to identify infected cells.

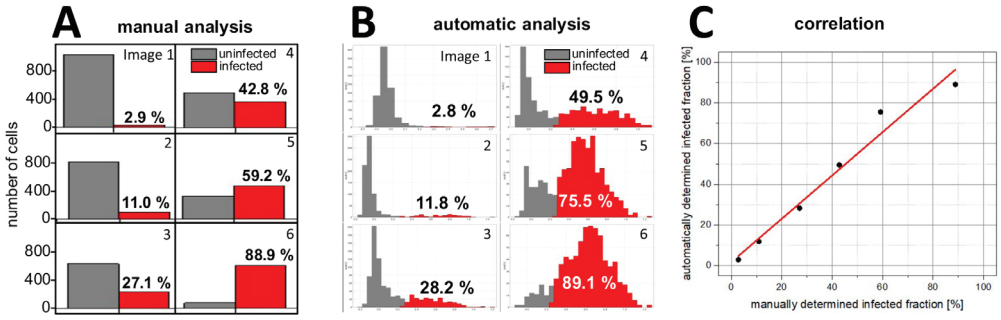

Fig. 5. Comparison of manual and automatic quantification of the fraction of Vero cells that had been infected with a GFP-equipped herpes simplex virus 1 (HSV-1_GFP). Panel A and B show the fractions of uninfected (gray) and infected (red) cells as determined from six microscopic images. The values were derived by manual cell counting (A) or the single-cell $\log_{10}$ intensity histograms of the automatic analysis (B), respectively. The manually and automatically determined infected fractions show a very high correlation (R^2 = 0.97, slope = 1.03).

Similar to the validation using transfected HEK cells, we found a linear correlation (R^2 = 0.97, slope = 1.03, Fig. 5C) between the manually and automatically determined fraction of infected cells. This indicates that both approaches give essentially identical results, with manual inspection being far more time-consuming than using the macro and providing no further information about fluorescence intensity distributions.

Quantification of virus infection inhibition

In addition to mere quantification of viral infection, our analysis macro can also be applied to quantify the efficiency of virus binding inhibitors [17]. This is demonstrated in Fig. 6, which summarizes the results of inhibition experiments, in which Vero cells were treated with heparin as inhibitor at different concentrations (0.01–1000 µg/mL) and infected with HSV-1_GFP. Fig. 6A shows six representative images and the corresponding $\log_{10}$ intensity histograms, in which the fluorescent (infected) cell fraction is indicated in red. The inhibitory effect of heparin can clearly be seen in the images, as well as in the $\log_{10}$ intensity histograms.

Fig. 6B shows the impact of the heparin concentration on mean value and standard deviation of the fluorescent (infected) cell fraction, which were calculated from four image replicates done for each concentration. This data allowed to determine the IC_{50} value (8.6 ± 1.3 µg/mL ~ 573.3 ± 86.7 nM (M_W ~ 15.000 ± 2.000 Da) of heparin inhibition, which was quantified by fitting the observed inhibition curve using the Langmuir-type inhibition model:

$$f_{inf} = \frac{1}{1 + \frac{c_{inh}}{IC_{50}}} \tag{1}$$

In this equation, f_{inf} denotes the fraction of infected cells, which is observed at an inhibitor concentration c_{inh}, while IC_{50} give the half maximal inhibitory concentration (*i.e.*, the inhibitor concentration, at which 50% of infection inhibition is observed). The determined IC_{50} value is in the range of previously reported IC_{50} values obtained by plaque reduction assays performed with Vero cells and similar HSV-1 variants (6–10 µg/mL [18], 240–380 nM [19]).

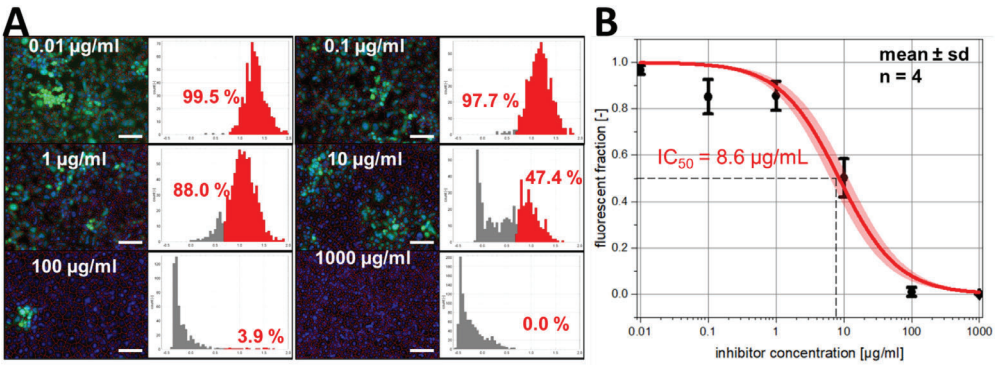

Fig. 6. Quantification of the efficiency of heparin in inhibiting HSV-1_GFP infection of Vero cells. Panel A shows six representative images (corresponding to applied heparin concentrations of 0.01–1000 µg/mL as indicated; scale bars = 150 µm) together with the result of the segmentation and the corresponding single-cell $\log_{10}$ intensity histograms. The population of infected cells is shown in red in the histograms. The fraction of infected cells decreases with increasing heparin concentration (B), which is well described by a Langmuir-type inhibition model (solid line; red area indicates 95% confidence interval).

Discussion

In this work, we described the development, validation, and application of a fast and robust Fiji macro offering an automated fluorescence quantification with single-cell resolution. To ensure the versatility of the macro, it employs a watershed-based segmentation [20], which allows for thresholding of empty spaces without cells and avoids splitting of nuclei in cell-dense areas. This makes the macro applicable over a wide range of cell coverage (*i.e.*, for samples with low as well

as high cell coverage). As not only the area of the nucleus is analyzed but the entire cell body (based on its autofluorescence signal), the macro can quantify fluorescence signals of the nucleus and the cytoplasmic area. We validated the macro for a wide range of fractions of fluorescent cells (between 0 and 99%), which makes it applicable to a broad spectrum of fluorescence images. We observed excellent agreement with manual image analysis when quantifying the fraction of transfected or virus-infected cells. Hence, the macro can be used to screen transfection efficiencies under different conditions as well as to quantify inhibition of virus infection of cells treated with virus inhibitors (providing the IC_{50} value of the inhibition process based on a quantification with single-cell resolution).

So far, the macro has been applied successfully on data derived using different cell lines (Vero, HEK293, HeLa), imaging techniques (widefield and confocal fluorescence microscopy) and labeling strategies (GFP transfection, virus protein surface staining), which demonstrates its feasibility. However, the user should be aware of the limitations of the method: The data quality is highly dependent on a sufficient segmentation based on staining of cell nuclei. If not all cell nuclei are sufficiently stained, the macro will not be able to correctly recognize them as cells and the resulting fraction of fluorescent cells will be incorrect. If cells are not in a monolayer and therefore overlap, the segmentation quality is reduced and nuclei in lower positions are excluded from the analysis, which causes a bias in the quantified populations. Also, shifts of the background intensity can cause a shift of the non-fluorescent cellular population in the $\log_{10}$ intensity histograms, which can lead to misclassification if the intensity cutoff is not carefully adjusted. Manual verification of the segmentation overlay and the $\log_{10}$ intensity histogram for each new experiment and condition is therefore recommended.

Conclusion

Quantitative analysis of image data is a valuable complement to qualitative visual inspection for obtaining information about biological processes. The segmentation and analysis macro developed in this work provides a suitable tool for rapid quantification of fluorescence at the single-cell level, *e.g.*, for a quantification of cellular transfection, infection, or infection inhibition. It is based entirely on open-source components (contained in the Fiji package [13]) and allows to obtain accurate information with high throughput. The macro provided here (see Supplemental Material Section S7) performed well when validated by comparison with manually obtained image quantification data as well as in experiments, in which fluorescent and non-fluorescent cells were mixed in known ratios. The application of the macro presented is not limited to the use cases shown here; it is intended to be applicable for most monolayered cellular assays using nuclei staining and fluorescence as readout. As a Fiji macro, it is freely available and can be used and modified according to the users needs.

Declaration of Competing Interest

The authors declare that they have no known competing financial interests or personal relationships that could have appeared to influence the work reported in this paper.

The authors declare the following financial interests/personal relationships which may be considered as potential competing interests:

CRediT authorship contribution statement

Yannic Kerkhoff: Methodology, Software, Validation, Formal analysis, Investigation, Data curation, Writing – original draft. **Stefanie Wedepohl:** Investigation. **Chuanxiong Nie:** Investigation. **Vahid Ahmadi:** Resources. **Rainer Haag:** Supervision, Writing – review & editing. **Stephan Block:** Supervision, Writing – review & editing.

Acknowledgments

This work was Funded by the Deutsche Forschungsgemeinschaft (DFG, German Research Foundation) - Project ID 431232613 - SFB 1449; BL1514/1. As well as the Corona Virus Pre-Exploration

Project of the Berlin University Alliance. We gratefully acknowledge assistance from the Core Facility BioSupraMol supported by the DFG . We also thank Prof. Benedikt Kaufer for providing lab space for the HSV-1 experiments.

Supplementary materials

Supplementary material associated with this article can be found, in the online version, at doi:10.1016/j.mex.2022.101834.

References

[1] F. Georgi, F. Kuttler, L. Murer, V. Andriasyan, R. Witte, A. Yakimovich, G. Turcatti, U. Greber, A high-content image-based drug screen of clinical compounds against cell transmission of adenovirus, Sci. Data 7 (2020), doi:10.1038/s41597-020-00604-0.
[2] N. Zhu, D. Zhang, W. Wang, X. Li, B. Yang, J. Song, X. Zhao, B. Huang, W. Shi, R. Lu, P. Niu, F. Zhan, X. Ma, D. Wang, W. Xu, G. Wu, G. Gao, W. Tan, A novel coronavirus from patients with pneumonia in China, N. Engl. J. Med. 382 (2019) 727–733 2020.
[3] G. Elliott, P. O'Hare, Live-cell analysis of a green fluorescent protein-tagged herpes simplex virus infection, J. Virol. 73 (1999) 4110–4119.
[4] P. Gardner, J. MacQuillin, M. Grandien, Rapid Virus Diagnosis; Application of Immunofluorescence, Butterworths, London (U.A.), 1980.
[5] J. Caicedo, S. Cooper, F. Heigwer, S. Warchal, P. Qiu, C. Molnar, A. Vasilevich, J. Barry, H. Bansal, O. Kraus, M. Wawer, L. Paavolainen, M. Herrmann, M. Rohban, J. Hung, H. Hennig, J. Concannon, I. Smith, P. Clemons, S. Singh, P. Rees, P. Horvath, R. Linington, A. Carpenter, Data-analysis strategies for image-based cell profiling, Nat. Methods 14 (2017) 849–863.
[6] F. Stein, M. Kress, S. Reither, A. Piljić, C. Schultz, FluoQ: a tool for rapid analysis of multiparameter fluorescence imaging data applied to oscillatory events, ACS Chem. Biol. 8 (2013) 1862–1868.
[7] S. Culley, G. Towers, D. Selwood, R. Henriques, J. Grove, Infection counter: automated quantification of *in vitro* virus replication by fluorescence microscopy, Viruses 8 (2016) 201.
[8] E. Czech, B. Aksoy, P. Aksoy, J. Hammerbacher, Cytokit: a single-cell analysis toolkit for high dimensional fluorescent microscopy imaging, BMC Bioinf. 20 (2019) 488.
[9] L. Handala, T. Fiore, Y. Rouillé, F. Helle, QuantIF: an ImageJ macro to automatically determine the percentage of infected cells after immunofluorescence, Viruses 11 (2019) 165.
[10] A. Chumakova, M. Hitomi, E. Sulman, J. Lathia, High-throughput automated single-cell imaging analysis reveals dynamics of glioblastoma stem cell population during state transition, Cytom. Part A 95 (2019) 290–301.
[11] J. Peterson, M. DeRuiter, Fluorescent Nuclei Measurements Macro (FNMM), a tool for automated cell quantification in ImageJ, Softw. Impacts 6 (2020) 100030.
[12] E. Lévy, F. Jaffrézic, D. Laloë, H. Rezaei, M. Huang, V. Béringue, D. Martin, L. Vernis, PiQSARS: a pipeline for quantitative and statistical analyses of ratiometric fluorescent biosensors, MethodsX 7 (2020) 101034.
[13] J. Schindelin, I. Arganda-Carreras, E. Frise, V. Kaynig, M. Longair, T. Pietzsch, S. Preibisch, C. Rueden, S. Saalfeld, B. Schmid, J. Tinevez, D. White, V. Hartenstein, K. Eliceiri, P. Tomancak, A. Cardona, Fiji: an open-source platform for biological-image analysis, Nat. Methods 9 (2012) 676–682.
[14] C. Schneider, W. Rasband, K. Eliceiri, NIH Image to ImageJ: 25 years of image analysis, Nat. Methods 9 (2012) 671–675.
[15] M. Krishnan, J. Park, F. Cao, D. Wang, R. Paulmurugan, J. Tseng, M. Gonzalgo, S. Gambhir, J. Wu, Effects of epigenetic modulation on reporter gene expression: implications for stem cell imaging, FASEB J. 20 (2005) 106–108.
[16] O. Boussif, F. Lezoualc'h, M. Zanta, M. Mergny, D. Scherman, B. Demeneix, J. Behr, A versatile vector for gene and oligonucleotide transfer into cells in culture and *in vivo*: polyethylenimine, Proc. Natl. Acad. Sci. 92 (1995) 7297–7301.
[17] V. Ahmadi, C. Nie, E. Mohammadifar, K. Achazi, S. Wedepohl, Y. Kerkhoff, S. Block, K. Osterrieder, R. Haag, One-pot gram-scale synthesis of virucidal heparin-mimicking polymers as HSV-1 inhibitors, Chem. Commun. 57 (2021) 11948–11951.
[18] B. Herold, S. Gerber, B. Belval, A. Siston, N. Shulman, Differences in the susceptibility of herpes simplex virus types 1 and 2 to modified heparin compounds suggest serotype differences in viral entry, J. Virol. 70 (1996) 3461–3469.
[19] D. Pinna, P. Oreste, T. Coradin, A. Kajaste-Rudnitski, S. Ghezzi, G. Zoppetti, A. Rotola, R. Argnani, G. Poli, R. Manservigi, E. Vicenzi, Inhibition of herpes simplex virus types 1 and 2 *in vitro* infection by sulfated derivatives of escherichia coli K5 polysaccharide, Antimicrob. Agents Chemother. 52 (2008) 3078–3084.
[20] L. Shafarenko, M. Petrou, J. Kittler, Automatic watershed segmentation of randomly textured color images, IEEE Trans. Image Process. 6 (1997) 1530–1544.

Supplementary material

S1 Image processing steps

The main part of the macro consists of image processing steps (Fig. S1), which make the images accessible for a single-cell analysis based on Fiji's *Particle Analyzer*. Fig. S1A shows a representative fluorescence image of HSV-1_GFP infected Vero cells (green), while cell nuclei are stained with Hoechst 33342 (blue). Non-infected cells barely show green fluorescence, but can be detected based on the nucleus staining. The blue and the green channels were color balanced (saturation of 0.35 % of pixels) to make the effect clearly visible to the naked eye. Infected cells can be identified by their bright green fluorescence. Also, a strong, inhomogeneous green background signal is present. To obtain quantitative information, the images are processed as follows:

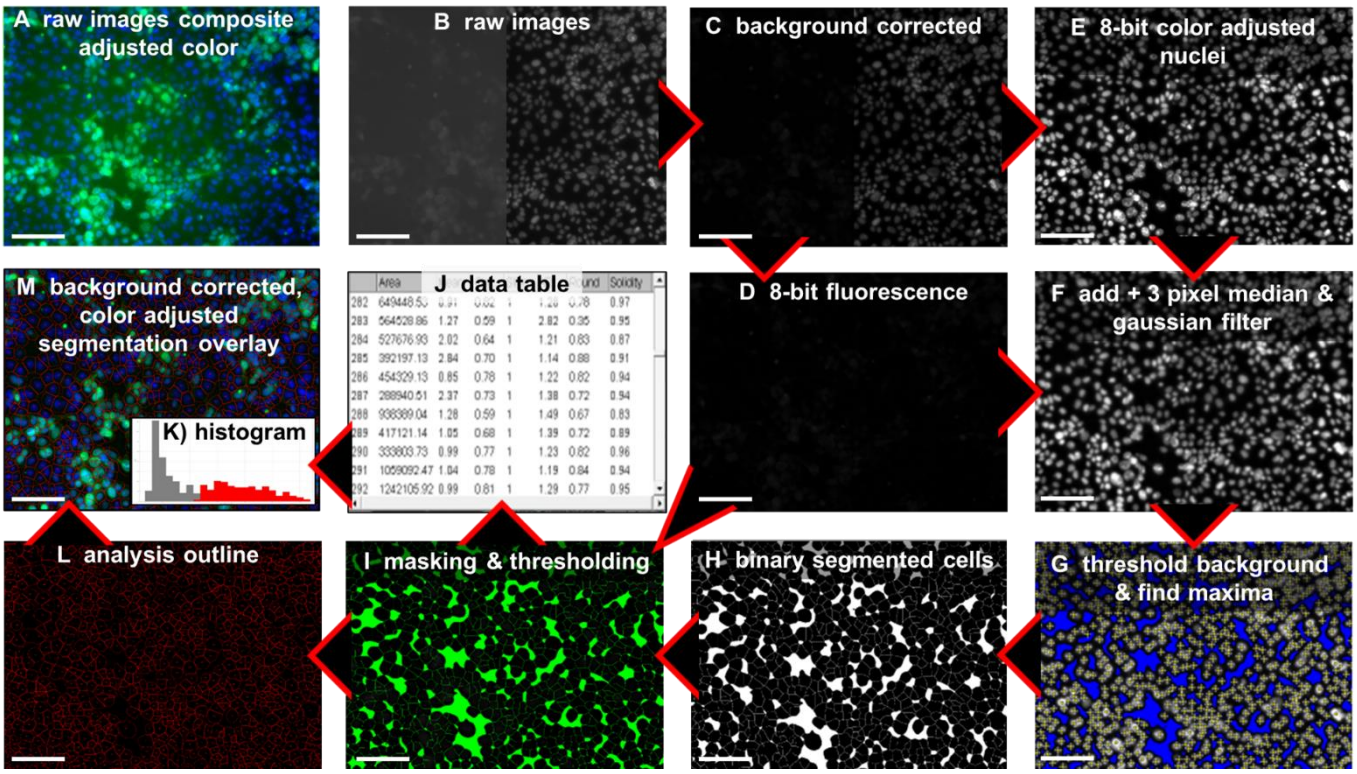

Fig. S1. Overview of the image processing steps (all scale bars = 150 µm). Panel A shows a representative color balanced composite fluorescence image of HSV-1_GFP infected (green) Vero cells with stained nuclei (blue). Panel B shows the raw images (left: GFP; right: nuclei) represented in gray values. Both channels are background corrected, using the rolling ball function with a 100-pixel radius (Panel C), converted to 8-bit format and split (Panel D and E). The nuclei channel is additionally color balanced. The fluorescence and nuclei channels are combined and a median and a Gaussian filter (both with a 3-pixel radius) are applied (Panel F). The background of the resulting image is thresholded (blue) and local intensity maxima (yellow) are detected (Panel G). Afterwards, the cells are segmented by a watershed-based segmentation and the resulting image is binarized (Panel H). The binarized image with the segmented cells is used as a mask on the 8-bit image of the green channel (Panel I) and the single-cell data is derived by the *Particle Analyzer* of Fiji (Panel J). Panel K shows the $\log_{10}$ intensity histogram indicating the population of dark (gray) and fluorescent cells (red) as determined from the single-cell data. The red outlines of analyzed cells, which are also delivered by the Particle Analyzer (Panel L), are overlaid with the background corrected and color balanced green and blue channels (Panel M).

First, the background of the green and blue channel is corrected by applying a rolling ball subtraction with a 100-pixel radius to remove illumination artifacts and inhomogeneities, which, especially in the green channel, would cause problems in the analysis. Afterwards, both image channels are converted to 8-bit resolution and split. The intensity of the nuclei channel is color balanced (saturation of 2 % of pixels) to make them more accessible for the identification of intensity maxima. The green channel is duplicated and added to the blue channel. A median and a Gaussian filter (3-pixel radius) are applied on the resulting image to remove noise pixels and minor inhomogeneities. The background is then thresholded with the beforehand chosen background threshold parameter β and nuclei are identified with the *Find Maxima* function with the prominence of the beforehand chosen segmentation sensitivity ω, which uses a

watershed-based (Ref. 1) segmentation. The resulting binary image with the segmented particles is then inverted and used as a mask overlaid to the 8-bit fluorescence channel. The *Particle Analyzer* function is then called to generate the single-cell data from the segmented cells and the resulting data table is stored as a csv-file in the output folder. The mean intensity of the cells is then plotted as a $\log_{10}$ intensity histogram, in which the population above the intensity cutoff α is indicated in red. The name of the image file, the total cell number, the number of fluorescent cells, and the resulting fluorescent fraction (in %) is then added to the summary table, which is saved as a csv-file in the output folder. The outline of the analyzed particles is overlaid as red contours on the background corrected, color balanced green and blue channel. The histogram is stitched to the segmentation overlay and saved as a single png-file in the output folder.

S2 Validation by cell mixing studies

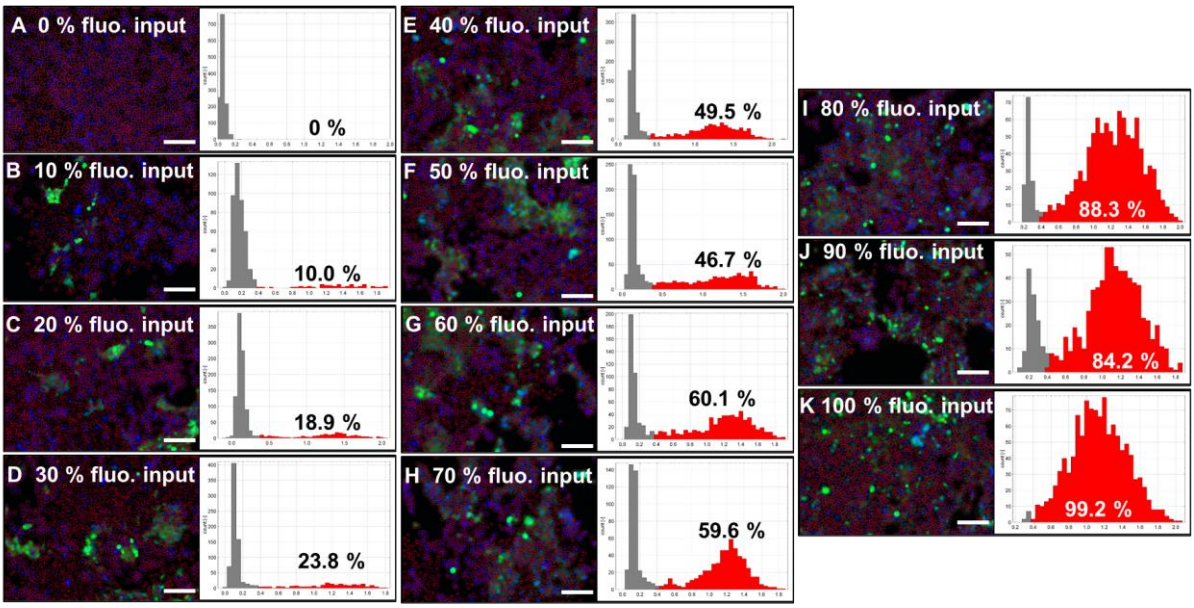

Fig. S2. Summary of all measurements of the mixing validation experiment (see Fig. 3 in the main manuscript). Shown are representative widefield images (scale bars = 150 µm) as well as the result of the segmentation process (red contours in the images) and the corresponding single-cell $\log_{10}$ intensity histograms. The fraction of fluorescent cells is indicated in the microscopy images (input values, defined by the mixing process) and histograms (extracted by single-cell analysis), respectively.

S3 Validation using plate reader measurements

To validate the results obtained from the Fiji macro using an established system, the transfection series was also analyzed based on fluorescence data measured with a plate reader. Fig. S3 shows the results of the image analysis (Panels A to C) compared to the results obtained by a plate reader (Panels D to F). The number of detected cells (Fig. S3A) and fluorescence signal of the Hoechst staining (Fig. S3D) show a very similar pattern across the wells. In general, the number of cells decrease with increasing PEI concentration, which is attributed to toxicity. However, the cell number is slightly increased when 0.2 µg DNA was complexed with PEI at a ratio of 1:2 and 0.3 µg DNA was complexed with PEI at a ratio of 1:3, which is attributed to the cell attachment promoting feature of PEI (Ref. 2). In this experiment, an unusually high intensity of the Hoechst signal was found in the plate reader experiment at the condition of 0.2 µg complexes with a DNA:PEI ratio of 1:1, but not in the corresponding single-cell measurement. This could be due to a local cell aggregation or contamination that causes a misrepresentation of the total cell number by mere average fluorescence in a well plate and demonstrates the advantage of single-cell image analysis, in which aggregates or artifacts in the field of view can be identified easily. The number of fluorescent cells (Fig. S3B) determined by the macro as well as the GFP fluorescence signal (Fig. S3E) determined by the plate reader showed a very similar pattern as well. Both indicated optimal transfection efficiencies at DNA:PEI ratios ranging between 1:2 to 1:3 and at a total amount of DNA:PEI complexes of about 0.4 to 0.5

µg. The highest transfection efficiency is found at a DNA:PEI ratio of 1:2 and a total amount of DNA:PEI complexes of 0.4 µg if the total number of fluorescent cells (n = 811) is considered as a key marker. When the fluorescent fraction (Fig. S3C) is chosen as a key marker, optimal transfection efficiency is reached at a DNA:PEI ratio of 1:2 and a total amount of DNA:PEI complexes of 0.5 µg (74.4 %).

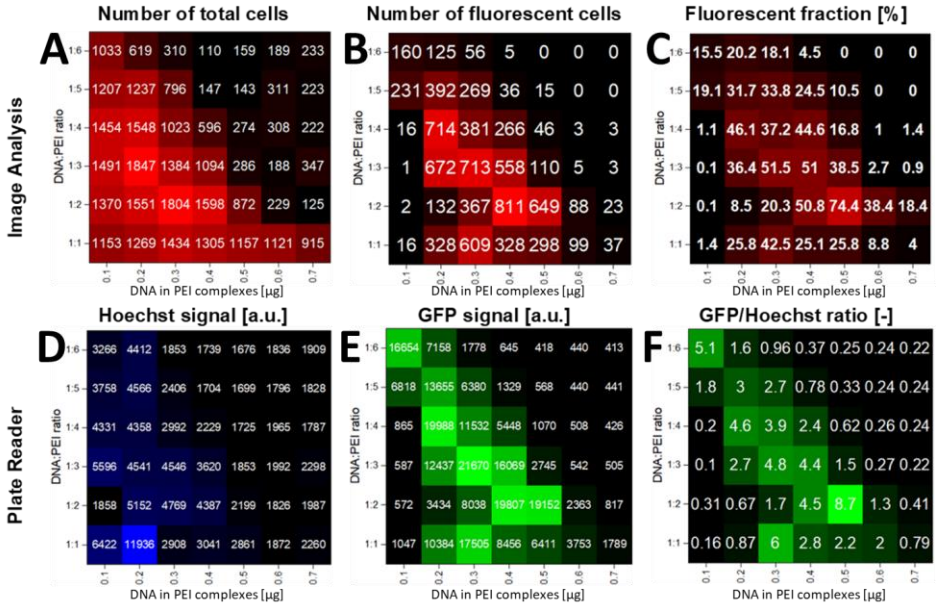

Fig. S3. Comparison of the results of the single-cell image analysis with plate reader measurements. Shown are heat maps of HEK293 transfection series derived by the single-cell image analysis (top row) and a plate reader measurement (bottom row), respectively. The heat maps visualize the total number of cells (Panels A and D), the total number of fluorescent cells (B, E) and the fraction of fluorescent cells (C, F), which were either derived directly by single-cell counting (A - C) or estimated by the intensity of the corresponding dye (D: Hoechst, E: GFP, F: GFP/Hoechst fluorescence ratio).

S4 Guide to optimize the analysis parameters

Fig. S4 shows a guideline to optimize the analysis parameters β (background intensity threshold), ω (cellular segmentation sensitivity) and α (fluorescence intensity cutoff) by manual inspection of the segmentation overlay (for β and ω) and of the $\log_{10}$ intensity histogram (for α).

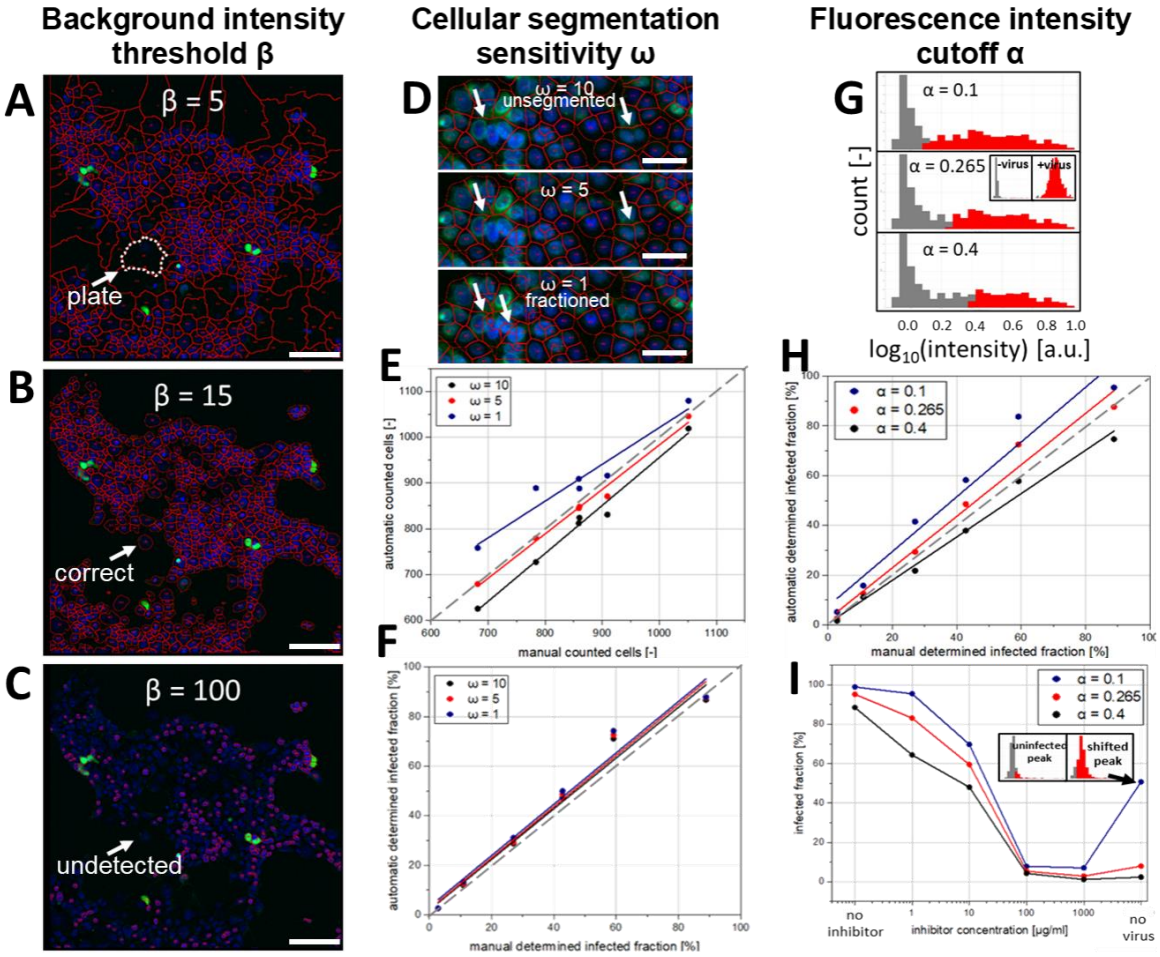

Fig. S4. Guidelines for the analysis parameter optimization. Panels A to C show the influence of three different values of the background threshold parameter (β) on the segmentation of eGFP-transfected HEK293 cells (scale bars = 100 µm). A β of 5 is too low and the background is not correctly thresholded. Cells in confluence are well segmented, while cells on the edges are mis-segmented, causing big parts of empty areas to be regarded as cell bodies. A β of 15 thresholds the background correctly and the cells are well segmented. A β of 100 is far too large, as only the brightest nuclei centers are identified and all others are thresholded with the background. Panels D to F show a comparison of manual and automatic cell counting and classification at different segmentation sensitivities (ω) using HSV-1 infected Vero cells. Panel D shows a crop of an infection assay image with cell segmentation using low (ω = 10), medium (ω = 5), and high (ω = 1) sensitivity (scale bars = 50 µm). Panel E shows the impact of the segmentation sensitivity on the automatically determined cell number. At a low sensitivity (black), the R^2 is 0.98 and the difference from the manual counted cells is -6.2 ± 2.3 %. At a medium sensitivity (red), the R^2 is 0.99 and the difference from the manual counted cells is -1.5 ± 1.4 %. At a high sensitivity (blue), the R^2 is 0.93 and the difference from the manual counted cells is 6.2 ± 5.0 %. Panel F shows the influence of different segmentation sensitivities (ω) at constant intensity cutoff (α) on the determined infected fraction. All sensitivities show a high correlation of R^2 ~ 0.97 and a minor deviation from the manual determined infected fraction (difference = -3.6 ± 5.4 %). Panels G to I show a comparison of the influence of different intensity cutoffs (α) used to determine the infected fraction in HSV-1_GFP infected Vero cells treated with an inhibitor (17). Panel G shows a $\log_{10}$ intensity histogram of an image, in which approximately half of the cells were infected, and highlights the impact of three different intensity cutoff values (α = 0.1, 0.265, and 0.4) on the assignment into infected (red) and non-infected cells (gray). The inset in the middle gives two additional histograms, which indicate the intensity distributions of non-infected and highly infected cells and enabled to determine the appropriate cutoff of 0.265. Panel H shows the impact of the intensity cutoff α on the determined fraction of infected cells. A cutoff value of 0.1 (blue) is too low and leads to overestimation of the infected fraction by 11.3 ± 8.3 %. A cutoff value of 0.265 (red) generates only a minor overestimation of 3.5 ± 5.3 % and is therefore appropriate. A cutoff value of 0.4 (black) is too high as the infected fraction is now underestimated by about -4.5 ± 5.3 %. All cutoffs show a high correlation of R^2 > 0.94. Panel I shows the influence of the cutoff based determined infected fractions (mean of four images) of an inhibition experiment. All cutoff values show an inhibition effect with increasing inhibitor concentration. A cutoff value of 0.4 (black) underestimates the fraction of infected cells, while a value of 0.1 (red) causes the infected fraction to be overestimated and misclassifies some uninfected cells as infected as the intensity histogram is slightly shifted to higher intensities (small histograms), which distorts the mean infected fraction for the non-infected control.

The background threshold parameter β is the intensity below which empty spaces of the image should be excluded from the analysis, while areas above this intensity should contain nuclei as well as

(auto)fluorescence signal from cells. It plays a minor role if the whole image is densely covered with cells, but becomes important when cells are on the edge of cell clusters. Fig. S4A-C shows how different background threshold parameters influence the cell segmentation of eGFP-expressing HEK293 cells. In the representative image shown in Fig. S4A, a β of 5 was too low, and thus the empty area of the image was not thresholded and cells on the edge of the cluster were not correctly segmented. Such giant edge cells had a highly reduced mean intensity, as the low background intensity is present in a major area of the mis-segmented cell and thus cells with a bright fluorescence signal were not recognized as such. A β value of 15 was appropriate, as the background is successfully thresholded from the cells and the cells at the center and the edge of the cluster were sufficiently segmented. Larger β values (*e.g.*, 100) were too high and many cells with dim nuclei were excluded from the analysis, which generated a bias in the quantification of the fraction of transfected cells. While the determination of a suitable threshold parameter β is very important for the analysis quality, the segmentation overlay makes it easy to identify inappropriate values and allows for a straightforward adjustment.

To determine the reliability of the automatic analysis with respect to a manual evaluation, six images with different cell densities (approximately 650 to 1050 cells per image) and degree of infection (approximately 2 to 90 %) were chosen and manually analyzed (Fig. S4D-F). For this, cells were counted by hand using the nucleus staining and infected cells were identified by visual inspection of the green infection signal in their cytoplasm. The manually derived data was regarded as a reference and plotted against the result of the macro using three different segmentation sensitivities ω to check for correlation (R^2). For all chosen ω, the segmentation was in general successful, but at ω value of 10 some cells remained unsegmented in clusters, while at ω of 1 some cells became fragmented. However, these differences were hard to see by the naked eye even with the segmentation overlay. Fig. S4E shows the influence of ω more clearly. A ω value of 5 (red) showed the best correlation and agreement with the manually determined cell number with just a slight underestimation by about -1.5 %. A high ω value (black) and thus low sensitivity underestimated the number of cells (-6.5 % for ω = 10). A low ω value (blue) and thus high sensitivity overestimated the number of cells due to fragmentation (6.2 % for ω = 1). However, Fig. S4F shows that the accurate segmentation of cells, at least with the three tested ω values, was not that important to gain reliable results. All tested segmentation sensitivities showed very similar correlations (R^2 ~ 0.97) and only minor difference (underestimation of ~ -3.6 %) to the manually determined fraction of infected cells. As long as the majority of cells are correctly segmented, some fragmented or clustered cells seemed not to bias the resulting fraction of infected cells.

However, Fig. S4G-I shows that the determination of a suitable value of the intensity cutoff α is crucial to get reliable infection and inhibition data. Fig. S4G shows three $\log_{10}$ intensity histograms of an image, in which approximately half of the cells were infected (resulting in a bimodal infection histogram), and three different values of the intensity cutoff α (0.1, 0.265, 0.4) applied. The intensity cutoff value of α = 0.265 was determined by a positive and negative control experiment, where either no or a high virus titer was applied to the cells. This led to images, in which either none or nearly all cells were infected. The infection histograms of those images showed distinguishable histograms were with α < 0.265 nearly no cells were identified as infected (~ 3 %) and with α > 0.265 nearly all cells were identified as infected (~ 98 %). An α value of 0.265 is thus the correct parameter value of this measurement. The other cutoff values of 0.1 and 0.4 led to an overestimation and underestimation of fraction of infected cells, respectively. Fig. S4H shows the effect of the three different intensity cutoff values on the automatic determination of the infected fraction, which is plotted against the manually determined infected fraction. All cutoff values showed a high correlation (R^2 > 0.94) but also the expected overestimation of infection (11.3 %) in case of α = 0.1 and the underestimation (-4.5 %) for α = 0.4. The intensity cutoff α should therefore be chosen very carefully and evaluated throughout the analysis process in order to avoid a bias of the automatically determined fraction of infected cells. However, Fig. S4I shows that the inhibitory effect can still be resolved (if present), even if slightly inappropriate intensity cutoff values are used. When the intensity cutoff α was too low (0.1, blue) some uninfected cells were misclassified as infected, as seen in the mean infected fraction of cells without

virus infection. We attribute this to low, but in this case important, changes in autofluorescence and background, shifting the $\log_{10}$ intensity histogram slightly but above the intensity cutoff of 0.1. However, this artifact was obvious and if recognized either the intensity cutoff should be increased generally or the images which lead to this artifact should be analyzed separately with an increased intensity cutoff or be excluded from further analysis.

S5 Automatic parameter estimation

In addition to the manual selection and optimization of the analysis parameters, there is also the option to use automatically estimated analysis parameters. Fig. S5A shows the analysis parameters dialog box with the checked option “use automatic parameters”. If this option is chosen, the three analysis parameters are estimated by the equations (2) – (4). These estimations are based on standard values which were found matching for many widefield and confocal images and are additionally scaled with the intensity distribution of the current image to be analyzed. While this automatic option performed well in most of the cases presented here, the general performance of the automatically estimated parameters cannot be guaranteed and depends on the particulars of the experiment.

The automatic background intensity threshold β_{auto} is estimated by the equation:

$$\beta_{\mathrm{auto}} = 5 + mean(Int_{nuc+fluo} < 10) \quad (2)$$

so that there is at least a background intensity threshold of five, with the mean intensity of the pixels with an intensity of ten or less (of the image with the saturated nuclei and the added fluorescence, Fig. S1F) added to it. The range of this estimation for the cases tested was between ~ 5 and ~ 15.

The automatic segmentation sensitivity ω_{auto} is estimated by

$$\omega_{auto} = 0.5 + \frac{50}{mean(Int_{nuc+fluo})}. \quad (3)$$

This equation follows the idea that the presence of more, and presumably, dense nuclei in the image leads to a higher mean intensity and hence requires a more sensitive segmentation. The range of this estimation was between ~ 0.5 and ~ 5.5 for the cases tested.

The automatic intensity cutoff parameter α_{auto} is estimated by

$$\alpha_{auto} = \log_{10}(1 + mean(Int_{fluo} < 5)). \quad (4)$$

In this case, the intensity cutoff parameter scales directly with the background fluorescence from the fluorescence reporter channel (without nuclei signal), estimated by the mean intensity of all pixels with an intensity of 5 or lower. The range of this estimated parameter was between 0.2 and 1.1 for most images tested. Figure S5B and C show an example of the scaling of the automatic intensity cutoff parameter α_{auto}. Two images from the same experiment performed under the same imaging conditions, showed different grades of background intensity (Fig. S5B: Log_{10} intensity of the non-fluorescent population at ~ 0.15. Fig. S5C: non-fluorescent population at ~ 0.3.) The automatically estimated intensity cutoff (α_{auto}) scales accordingly and is shifted from ~ 0.4 in Fig. S5B to ~ 0.55 in Figure S5C.

As validation of the estimation quality, the widefield cell mixing image series (Supplemental Materials Section S9) was analyzed with automatically and manually chosen parameters and the analysis results showed a high correlation (R^2 = 0.99 for validation images obtained using widefield microscopy, see Fig. S5D; R^2 = 0.98 for validation images obtained using confocal microscopy). This shows, that the automatically estimated analysis parameters can be used for both widefield and confocal images.

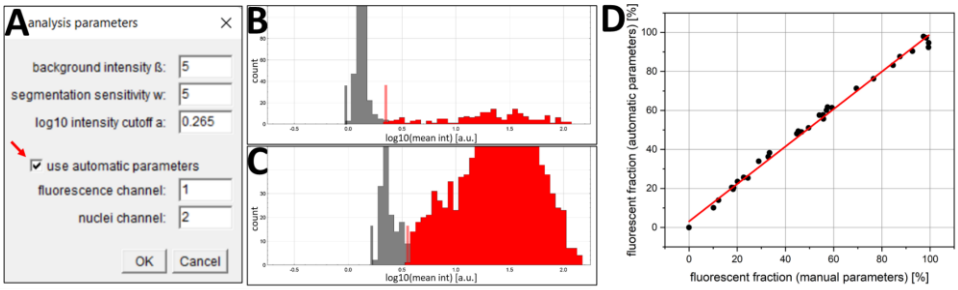

Figure S5: Overview of the option for automatically estimated analysis parameters. Panel A shows the analysis parameter dialog box with the selected checkbox “use automatic parameters”. Panel B and C show the log_{10} intensity histograms of two images. One having a non-fluorescent population around 0.15 (B), leading to an automatically estimated intensity cutoff (α_{auto}) of ~ 0.4. The other histogram (C) has its non-fluorescent population shifted to ~ 0.3, which is accounted by an automatic shift of the intensity cutoff (αauto) to ~ 0.55. If this shift would not have been regarded in C, a significant fraction of the non-fluorescent population would have been misclassified as fluorescent. Panel D shows that the fractions of fluorescent cells, which were determined using manually and automatically chosen analysis parameters, show an excellent correlation (R^2 = 0.99, slope = 0.96).

S6 Image analysis software overview

Table S1: Overview of the cited image analysis software (6-12). In columns 1 to 4, the short name of the software as well as the first author, the journal and the year of publication are given, respectively. Column 5 (Source(s)) lists the additional programs/software packages needed to run the analysis software. Column 6 (Scope and properties) gives a brief description of the software specialties. Columns 7 to 10 indicate whether the software is suitable for 2D, 3D, time-lapse and batch processing.

Method short name	Author	Journal	Year	Source(s)	Scope and properties	2D	3D	time	batch
SCFQ	Kerkhoff *et al.*	MethodsX, this work	2022	Fiji	High-throughput single-cell fluorescence quantification (SCFQ) of 2D images of **cell monolayers** applicable for **varying cell density (up to confluence) and fluorescence distribution**. Watershed-based nuclei segmentation. Three analysis parameters must be chosen with the **option for an automatic parameter estimation.**	x			x
PiQSARS	Lévy *et al.*	MethodsX	2020	Fiji, RStudio, MATLAB	**Time-lapse focused** fluorescence microscopy analysis. Performs best at relatively low cell densities of 300 – 500 cells per cm^2.	x		x	x
FNMM	Peterson *et al.*	Software Impacts	2020	Fiji	Quantification of **nuclei area with and without colocalization with fluorescence** signal. Two analysis parameters (2x threshold) are needed. Performs best at relatively low cell densities.	x			
HASCIA	Chumakova *et al.*	Cytometry Part A	2019	ImageJ, Fiji, R, Shiny	**Quantitative assessment of protein expression** with single-cell resolution. Processing in ImageJ, data analysis in web application. Fluorescence assessment is based on nuclei mask. **Shading images needed** for every microscope/camera setup. Six analysis parameters must be chosen (2x threshold, 2x size, 2x circularity).	x			x
QuantIF	Handala *et al.*	Viruses	2019	ImageJ	**Counting nuclei** with and without **colocalization with fluorescence** signal. No quantification of fluorescence intensity. Three threshold parameters must be chosen.	x			x
Cytokit	Czech *et al.*	BMC Bioinformatics	2019	Python	Collection of open-source tools for quantifying and analyzing **properties of individual cells** in large fluorescent microscopy datasets with **spatial information**.	x			x
Infection Counter	Culley *et al.*	Viruses	2016	ImageJ	**Voronoi based nuclei segmentation** and fluorescence measurement to **quantify infection status**. Validated in infection fraction range up to 10 % infected cells.	x			
FluoQ	Stein *et al.*	ACS Chemical Biology	2013	ImageJ, R	**Multiparameter fluorescence** image analysis applied to **oscillatory events** with **subsequent statistical analysis** of measured parameters in R. Only few input parameters needed. Cell **segmentation not based on nuclei** staining but on fluorescence reporter.	x		x	x

S7 Macro-script

S8 Video tutorial

S9 Widefield cell mixing image series

References

1. L. Shafarenko, M. Petrou, J. Kittler, Automatic watershed segmentation of randomly textured color images, IEEE Transactions on Image Processing 6, 1530-1544 (1997).
2. A. Vancha, S. Govindaraju, K. Parsa, M. Jasti, M. González-García, R. Ballestero, Use of polyethyleneimine polymer in cell culture as attachment factor and lipofection enhancer, BMC Biotechnology 4, 23 (2004).

4.2 Bridging cellular- and nanoscale: Accurate quantification of clustered nanoparticles on monolayered confocal imaged cells

---

Yannic Kerkhoff, Chuanxiong Nie, Stefanie Wedepohl, and Katharina Hugentobler

In manuscript.

DOI: N/A

Short summary

In this work a method was developed for single-cell segmentation of confocal imaged monolayered cells, with subsequent quantification of single-nanoparticles bound to the cell surface (Figure 21). An early version of this method was used to quantify the binding of SARS-CoV-2 on Vero E6 cells, showing that negatively charged polysulfates can inhibit binding and uptake of the virus particles [169].

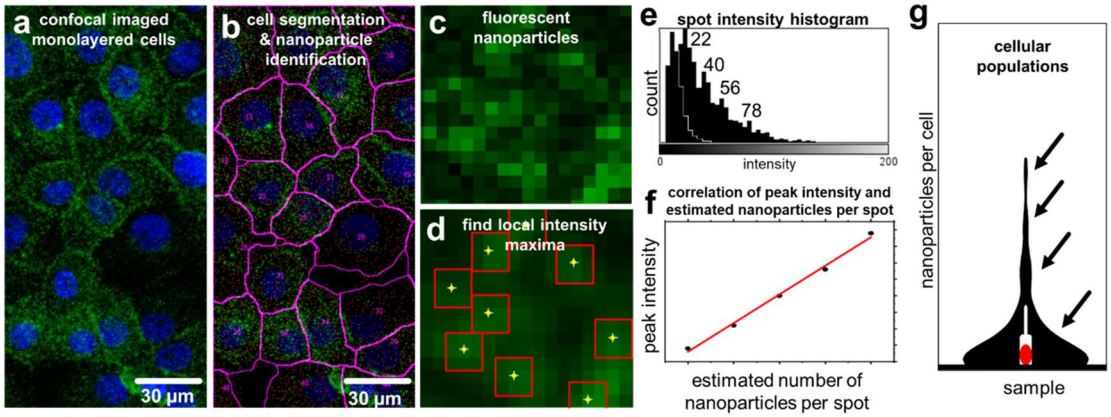

Figure 21: Confocal imaged monolayered cells (a) were segmented (b) and the intensity of surface bound sub-diffractive fluorescent nanoparticles (c + d) was quantified. Distinct intensity peaks (e) could be correlated with the number of clustered nanoparticles (f) allowing for quantification of nanoparticle binding with single-cell resolution (g).

Author contributions

Yannic Kerkhoff developed and validated the software, performed all image analysis, prepared all figures and wrote the original draft. Chuanxiong Nie performed all assays with virus like liposomes. Stefanie Wedepohl performed validation experiments with polysterene-beads. Katharina Hugentobler prepared and provided virus like liposomes.

Manuscript

Bridging cellular- and nanoscale: Accurate quantification of clustered nanoparticles on monolayered confocal imaged cells

Yannic Kerkhoff,*[a] Chuanxiong Nie,[a] Stefanie Wedepohl[a], and Katharina Hugentobler[a]

[a]*Freie Universität Berlin, Institute of Chemistry and Biochemistry, Berlin, Germany*

Abstract

Interactions between biological nanoparticles and cells are fundamental natural processes, ranging from intracellular vesicle transport and infection of cells by viruses to treatment of diseases by medical nanocarriers. Studying the binding and internalization of fluorescent nanoparticles by cells is challenging due to the size differences between the nanometer-sized particles and cells. While nanometer-sized particles range below the ~ 200 nm resolution limit of optical microscopy, cells are typically several micrometers in size. Although it is possible to resolve individual nanoparticles using high-resolution microscopy, these methods are limited by the small field of view and long acquisition times compared to conventional optical microscopy techniques such as confocal laser scanning microscopy. This makes it very difficult to detect and quantify cellular heterogeneity in terms of nanoparticle interactions, as this requires a sample size of at least hundreds of cells. In this work, we present an imaging and analysis approach based on confocal laser scanning microscopy with subsequent intensity correlation, with the aim to bridge the gap between the cellular- and nanoscale. We show that at a pixel size of about 400 nm, dozens of cells can be imaged, segmented, and analyzed in parallel, and that the number of bound fluorescent nanoparticles per cell can be accurately estimated using low-pass filtered local intensity maxima followed by intensity-agglomeration correlation. Using simulated images of fluorescent nanoparticles with different densities and resolutions, we demonstrate that the estimation accuracy is in the range of about 80 to 100 %, for nanoparticle densities up to 3.4 particles per μm^2. We used this to quantify the total number of virus-like particles with or without the SARS-CoV-2 spike protein bound to Vero E6 and A549 cells, showing heterogeneities in binding between individual cells. We are confident that the workflow presented here represents a valuable contribution to the quantification of nanoparticles based on optical microscopy and will enable the systematic detection of cellular binding heterogeneities.

Keywords: *Single-cell segmentation, fluorescent nanoparticle quantification, confocal image analysis, intensity-agglomeration correlation, particle density simulations*

**Corresponding author*

Email address: ykerkhoff@zedat.fu-berlin.de (Yannic Kerkhoff)

Introduction

Understanding the interactions of biological nanoparticles (NPs) and cells is very important [1], as they occur in many native and artificial forms like cellular lipid vesicles for intracellular transport [2] [3], medical nanocarriers for drug delivery [4] [5] [6] [7], or viruses [8] [9] [10]. Due to the small size of nanoparticles (1 - 100 nm [11]) and their size difference to cells (i.e., a 60 µm sized cell is 600 times larger than a 100 nm sized nanoparticle), imaging, quantifying, and localizing NPs with optical microscopy is very challenging [12]. As the size of fluorescent nanoparticles is below the diffraction limit of conventional optical microscopy methods (~ 200 nm in the lateral dimensions and 500 – 900 nm in the axial dimensions [13] [14] [15], depending on the wavelength of the light and the numerical aperture of the lens), NPs in vicinity cannot be resolved individually and prevent discrimination between single particles and small agglomerates, which are likely to form in biological medium [16]. Several techniques of high-resolution optical microscopy, like stimulated emission depletion microscopy (STED) [17], photoactivated localization microscopy (PALM) [18], or stochastic optical reconstruction microscopy (STORM) [19], and digital image restoration after confocal laser scanning microscopy (CLSM) [20] were developed to tackle this challenge. However, it is known that cells in a cell population, be it tissue (*in vivo*) or cells in a culture dish (*in vitro*), do not always behave in the same way. This cell-to-cell heterogeneity [21] [22] is strongly influenced by the cell-cycle [23] but also based on epigenetics [24], natural variation due to mutation [25], or the microenvironment of the cells [26]. To identify and probe these cellular heterogeneities and identify rare events, it is important to yield data from many cells (hundreds to thousands) in high throughput. The cellular heterogeneity also influences the binding and internalization of nanoparticles [27] [28] [29], e.g., due to differences in membrane composition [30] [31] [32] [33]. The use of high-resolution imaging to quantify NPs, however, strongly counteracts any high throughput approach to identify and quantify the heterogenous cellular populations, as higher resolutions means a smaller field of view and thus a smaller sample size of imaged cells. To circumvent this, it is possible to image the cells with the nanoparticles at lower resolution and try to estimate the number of fluorescent nanoparticles by their intensity signal [34] or using flow cytometry [35]. However, this estimation is not always accurate [36] [37] and difficult to validate (manually or automatically) as the nanoparticles are not resolved in the raw images. While there are already analysis methods available to quantify the absolute number of fluorescent nanoparticles in cells [38] [39] [40], they often lack the high-throughput or single-cell capabilities needed to resolve cellular heterogeneity.

To solve this problem, we present a CLSM-based imaging and analysis workflow where many cells are imaged and segmented in parallel, and the number of fluorescent nanoparticles can precisely be estimated by the fluorescence profile for each cell individually by the identification of local intensity maxima and the subsequent use of a low-pass filter. The intensity-based estimated number of fluorescent nanoparticles was validated by simulated synthetic images of nanoparticles, showing high accuracies of 90 to 100 % for the tested conditions. This is of high relevance, as previous studies showed that the number of NP events derived from optical microscopy is underestimated by a factor of ten when compared with the total NP number received by transmission electron microscopy (TEM) [41]. We used this method to quantify the cell-to-cell heterogeneity of virus-like particle (VLPs) binding to different cell lines, which could in the future be used as a platform for virus-host interaction studies. All analysis steps

are combined in a single Fiji [42] macro, allowing for the high-throughput identification and quantification of cellular heterogeneity in nanoparticle binding with high precision. The VLPs and polystyrene beads with a size of approximately 200 nm used in this work are intended to serve as a comparison to viruses, which are generally considered as viral nanoparticles (VNPs) [43].

Experimental section

Sample preparation and imaging

Lipids soy phosphatidylcholine (PC), soy phosphatidylethanolamine (PE) and soy phosphatidylinositol (PI; all lipids Avanti Polar Lipids, Alabaster, AL, USA) were stored as stock solutions in $CHCl_3$. Lipids were mixed in a PC:PE:PI = 45:45:10 wt % ratio and 0.1 wt % Atto-565-dope (ATTO-Tec, Siegen, Germany) was added. Lipids were then dried extensively (nitrogen flow and subsequent removal of residual $CHCl_3$ on a membrane pump for > 1.5 h). The dried lipids were resuspended in HEPES buffer (20 mM, pH 7.5, supplemented with 150 mM NaCl) to yield a final lipid concentration of 1.6 mg/ mL and subjected to 4 cycles of vortexing, snap-freezing in liquid N_2, and thawing in water at room temperature. The preparation was stored at −20 °C until further use.

For the preparation of virus like particles (VLPs) the lipid preparation (45 µL) was thawed and loaded in a mini extruder (Avanti Polar Lipids, Alabaster, AL, USA), and extruded 31× (200 nm Whatman PC filter). The extruded lipids were mixed in an Eppendorf tube with 20 wt % cholate solution (0.54 µL), Spike-protein solution (CUBE Biotech, Monheim, Germany, c = 0.84 mg/mL; 4.19 µL), and HEPES buffer (0.28 µL) to yield a protein-liposome mixture with a nominal concentration ratio of 20 Spike-proteins per liposome. As a control, “empty” liposomes were generated by adding the corresponding amount of buffer instead of protein. After overnight dialysis (14 kDa dialysis membrane) in 100 mL HEPES buffer, liposomes were flash frozen and stored at -80°C until further use.

HEK293 cells (Leibnitz Institute DSMZ – German Collection of Microorganisms and Cell Cultures GmbH) per well were seeded in full medium (DMEM (#9007.1, Roth) supplemented with 10 % FBS (#10270-106, Thermo Fisher Scientific) and 1 % penicillin/streptomycin (P4333-100ML, Sigma Aldrich/Merck) into a µ-slide 8-well (ibidi; 300 µL/well at 4 × 10^5 cells/mL) slide and incubated over night at 37 °C and 5 % CO_2. The next day, cell nuclei were stained with Hoechst 33342 (1 µg/mL in medium, Thermo Fisher Scientific) for 10 min at 37 °C. The cell culture supernatant was replaced with fresh medium and cells were imaged with a 63x objective (HC PL APO CS2 63x/1.40 OIL, FOV 184.52 µm x 184.52 µm) with oil immersion on a Leica SP8 system based on a DMI6000CSB microscope equipped with diode (405 and 561 nm), argon (458, 488, and 514 nm) and a HeNe (633 nm) laser as well as two PMTs and two HyDs (high sensitivity hybrid detectors). The LAS X software was used for image acquisition (channel 1: excitation 405 nm, emission 421–483 nm, HyD, channel 3: excitation 488, emission 500-550 nm, PMT) of z-stacks of 41 images in 0.5 µm intervals.

For the binding of VLPs on different cells, Vero E6 and A549 cells were seeded into a µ-slide 8-well plate (ibidi; 200 µL/well, approx. 10^5 cells per well) and cultured for 2 days to form a confluent cell layer. Afterwards, cells were washed with PBS and the cell nuclei were stained as described above. The cells were fixed with 3.7 % formaldehyde for 10 min and blocked with 5 % BSA for 30 min. The VLPs were diluted in 2.5 % BSA and incubated with the cells at RT for 45 min. Finally, the cells were washed with

PBS 3 times and z-stacks of 5 to 14 images in 1 µm intervals images were taken with the image acquisition presets for mCherry (excitation 552 nm, emission 559–789 nm, PMT).

For validation experiments, 200 nm sized fluorescent polystyrene beads (Thermo Fisher Scientific) were imaged on glass with a Nikon fluorescence microscope with 100x objective (NA 1.45) with a pixel size of 65 nm, using a dichroic filter set consisting of a 482 nm excitation filter (18 nm bandwidth), 495 nm dichroic filter, and a 520 nm emission filter (28 nm bandwidth).

Results and discussion

Image processing steps

The basic image processing steps needed for parallel single-cell segmentation and single-nanoparticle quantification are shown in Figure 1. First, the z-stack of the channel containing the nuclei staining (Figure 1a) is converted to a 2D image, by accumulating the intensity of all images (Figure 1b). The 2D image is duplicated and the nuclei are prepared for analysis by applying a Gaussian filter with a radius of 5 pixels (both images) to smooth the intensity profile. For one of the duplicated images, 35 % of all pixels are saturated, revealing the autofluorescence of the cells which allows for an estimation of the outline of the cell bodies (Figure 1c). Both images are merged, the background intensity is thresholded, and the local maxima are identified (Figure 1d). The local maxima (corresponding to the nuclei) are used as seeds in a watershed-segmentation [44] [45] and thus represent the centers of the cells to be segmented. The thresholded background is excluded from segmentation. The resulting segmented objects (Figure 1e) are a good approximation for the cells and are used to generate the region of interests (ROIs) for the analysis of the nanoparticles.

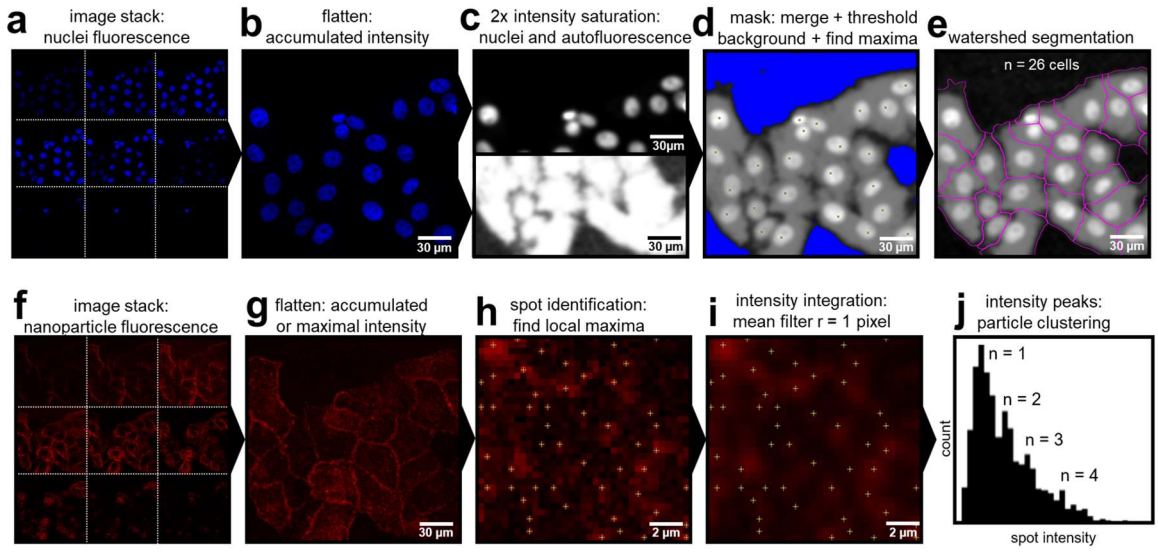

Figure 1: Image processing steps for parallel single-cell segmentation (a-e) and single-nanoparticle quantification (f-j). The intensity of all images of the nuclei channel (a) is accumulated and converted to one 2D image (b). The 2D image is duplicated allowing for intensity saturation for the nuclei and the autofluorescence of the cell body (c). The images of the nuclei and the cell bodies are merged, the background is thresholded and the local maxima are identified (d) allowing for a seeded watershed-based segmentation (e). The intensity of all images of the fluorescent nanoparticles (f) is transformed into a 2D image (g). The local maxima are identified (h) and a mean filter with a radius of 1 pixel is applied (i). The intensity histogram of the filtered maxima reveals distinct peaks if particle clustering is occurrent (j).

Analogous to the nuclei channel, also the channel containing the fluorescent nanoparticles (Figure 1f) is flattened (Figure 1g). Here, it is recommended to use the maximal intensity for each pixel position of the stack. If the intensity of the nanoparticles on the stacks is saturated, the intensity of each pixel position is summarized in a 32-bit format and then reconverted to a 16-bit format to remove the saturation. The ROIs of the cell bodies derived from the single-cell segmentation are overlayed with the flattened nanoparticle image which allows for the identification of the local intensity maxima (Figure 1h) for each cell individually. Subsequently, a mean filter with a radius of 1 pixel is applied (Figure 1i) acting as a low-pass filter [46]. This is done to account for the intensity of the pixels surrounding the original local maxima, which reduces pixelation artifacts in the intensity profile. The intensity of each local maximum after mean filtering is assessed and plotted as a histogram (Figure 1j). If clustered nanoparticles (more than one NP per pixel) are present, distinct peaks are revealed in this step. The first peak of the resulting histogram represents the population with the lowest intensity. This may be either the background intensity (if present), or the intensity of local maxima containing a single fluorescent nanoparticle, or alternatively the smallest cluster (e.g., agglomeration of 2 NPs) present in the images. The distance (intensity-wise) of the peaks should be consistent and in the range of the of intensity of the center of the first peak. While the nanoparticle aggregates cannot be resolved in the images, a precise estimation of the number of nanoparticles present in the sample is obtained after low pass filtering. All analysis steps are automated and wrapped up in a Fiji macro, allowing for high-throughput analysis.

Validation of intensity peaks

The assumption that the peaks in the intensity histogram represent the cluster sizes of multiple sub-diffractive nanoparticles within a single pixel was validated in the following. Imaging of 200 nm sized fluorescent polystyrene beads with a pixel size of 65 nm allows for a manual identification and counting of nanoparticles. The beads which are mostly individually present, sometimes form small aggregates with sizes of two to six beads. To use this for validation of the intensity peaks, the images were binned to an effective pixel size of 390 nm (Figure 2a), which is close to the used confocal image pixel size of 180 to 360 nm. This leads to images with a resolution in the typical range for CLSM. The local maxima of the binned images were identified and the image was mean filtered (Figure 2b) as previously described. The intensity histogram (Figure 2c) showed distinct peaks, where the first peak has its center at an intensity of 10 a.u., with subsequent peaks approximately every 10 a.u. of intensity. This shows that the local intensity maximum of a single bead after mean filtering is about 10 arbitrary units. The number of beads per spot (local intensity maxima) was estimated and plotted against the intensity of the peak centers (Figure 2d), showing a linear correlation with a slope of 8.4±0.2 a.u. and an R^2 of 0.99. This prediction of the number of beads per spot by intensity analysis, was tested by extracting the intensity of local maxima from a crop of the binned bead image (390 nm pixel size, Figure 2e) and manual inspection and comparison with the same region of the original image (65 nm pixel size, Figure 2f). The binned and filtered image crop showed six intensity spots with intensites of 11 to 12, implying the presence of single fluorescent beads, one spot with a local intensity maximum of 21, implying two clustered beads, and one spot with a local maximum of 50 a.u., implying five to six clustered beads. Manual inspection of the unbinned image, confirmed that the intensity-based prediction of the number of clustered beads was correct.

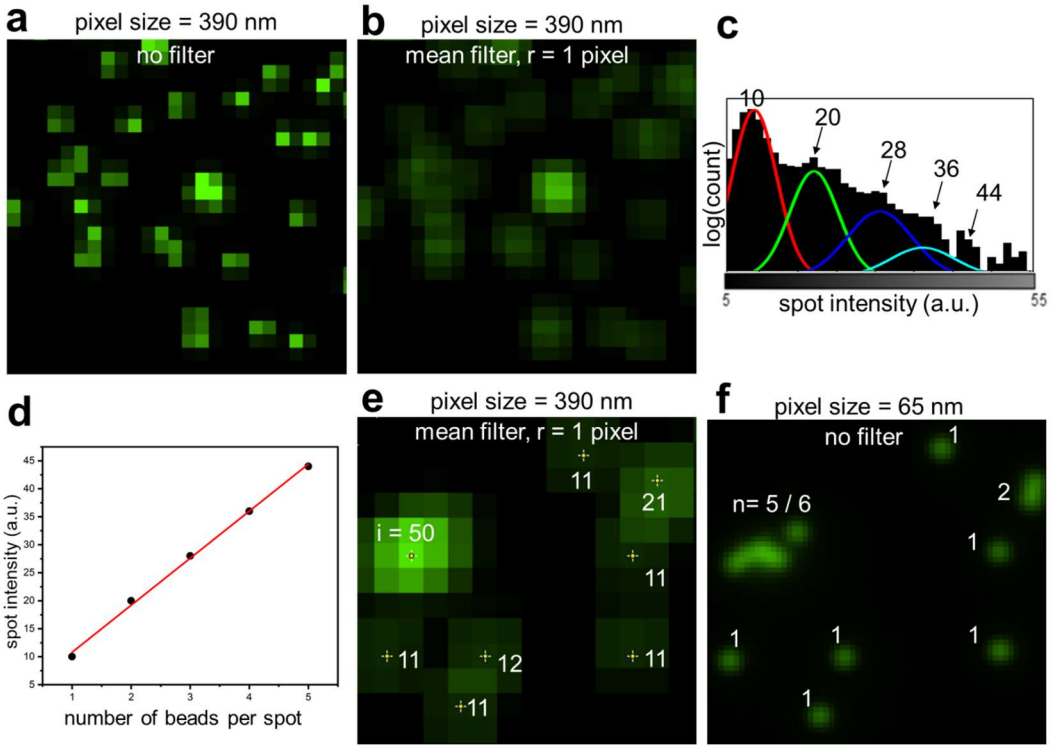

Figure 2: Validation of the intensity correlation by 200 nm sized fluorescent polystyrene beads on glass, imaged with a pixel size of 65 nm. Images of fluorescent beads with a pixel size of 65 nm were binned to an effective pixel size of 390 nm (a), making them comparable to the resolution of confocal images. The application of the mean filter with a radius of 1 pixel (b) reduces the intensity variance of the point-spread function (PSF) of the beads. The histogram (c) of the intensity of the mean filtered beads of panel b shows overlapping peaks (Gaussian fits for four peaks and arrows with intensity). The first peak with an intensity of 10 a.u. is estimated to represent single beads in one pixel. For each peak, the number of underlaying clustered nanoparticles is estimated and plotted against the intensity of the peak centers (d), showing a linear correlation (slope = 8.4±0.2 a.u., R^2 = 0.99). The intensity of the local maxima of mean filtered beads is represented in panel e. Six local maxima with an intensity of 11 to 12 a.u. are present, as well as one maximum with 21 a.u. and one with 50 a.u. respectively. The same region of e is shown in panel f with the original pixel size of 65 nm, allowing for manual identification and counting of the beads number n, showing the presence of six single beads, one cluster of two beads and one cluster of five to six beads, as implied by the intensity analysis of panels d and e.

Intensity correlation for nanobead- and VLP-clusters on cells

200 nm sized fluorescent polystyrene beads were incubated on HEK293 cells and imaged using CLSM (Figure 3a) to test whether the observed intensity peaks and the linear correlation of intensity and estimated cluster-size of the validation experiments are still valid for z-stacks in a cellular environment. Manual inspection revealed the presence of many aggregates and an x,z-projection showed that the beads covered the cell bodies (Figure 3a, arrow 2). The prominent bead aggregates of the image are also represented in the intensity histogram by nine distinct peaks (Figure 3b). The first peak center is located at an intensity of about 22 a.u., with subsequent peaks in approximately 11 a.u. steps, which indicates that the first peak already represents clusters of two beads. This is also supported by the linear correlation of the estimated number of beads per spot and the peak center intensity (Figure 3c) as the fit has a slope of 10.4 ± 0.1. The images of the VLPs incubated on Vero E6 cells (Figure 3d) are similar to the ones of beads on HEK cells, however due to blocking of unspecific binding, the VLPs are only covering the cell membrane, but not the glass surface. A line was placed on the x,y-projection of the image, crossing four cells, where three cells (1, 3, 4) showed many bound VLPs, but one cell (2) showed nearly none, which can also be seen in the x,z-projection. The intensity histogram of the spots (Figure 3e) shows four peaks, each separated by about 22 a.u. of intensity, which is also supported by a linear

correlation (slope = 17.4±0.8) of the estimated number of VLPs per spot and the peak center intensity (Figure 3f). The slope of the linear fit was later used to calculate the number of underlaying fluorescent nanoparticles based on the intensity of the detected spots.

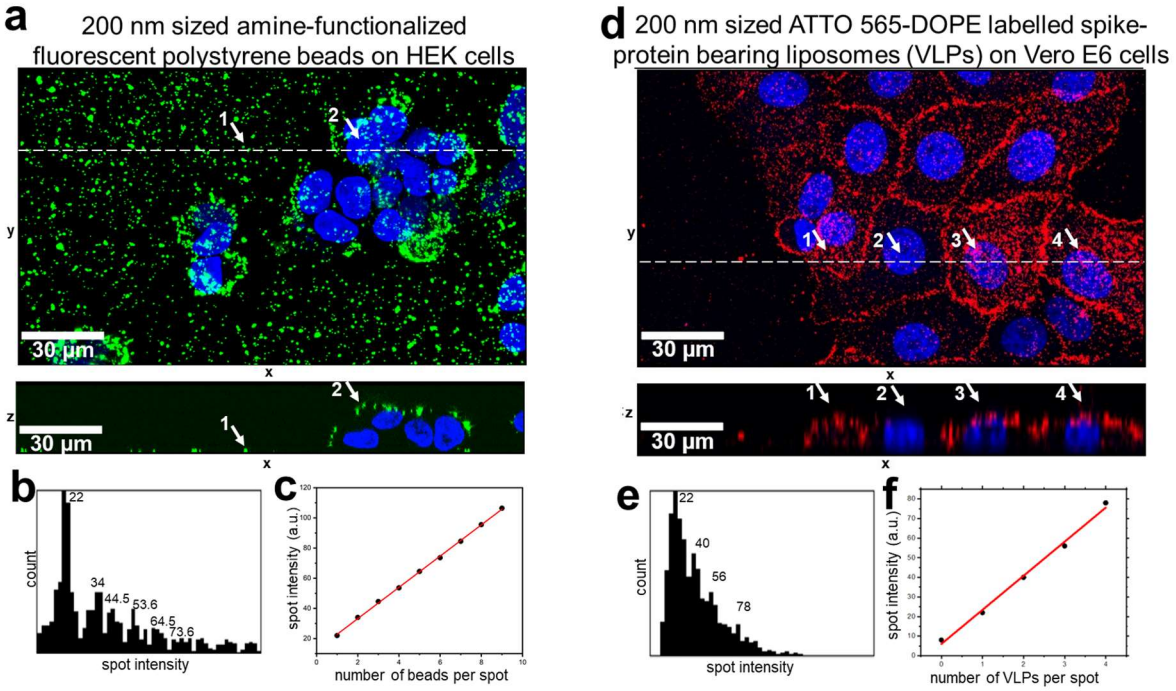

Figure 3: The correlation of intensity with nanoparticle cluster size was performed for polystyrene beads on HEK cells (180 nm pixel size) and VLPs on Vero E6 cells (360 nm pixel size). The amine-functionalized beads showed an unspecific adherence on the cover glass (a, arrow 1) and on the cell membrane (a, arrow 2), as well as a high degree of aggregation. The intensity histogram of the beads (b) showed many distinct peaks, confirming the presence of many bead clusters of different sizes. Plotting of the estimated number of beads per spot and the intensity of their corresponding peak centers, showed a linear correlation (slope = 10.4 ± 0.1, R^2 = 0.99). The ATTO-labelled VLPs showed binding to the cell membrane (d, cells 1, 3, 4) but no binding to the glass surface. Interestingly, the cells showed a high degree of heterogeneity regarding the amount of bound VLPs, where some cells had only very few VLPs bound to them (d, cell 2). Similar to panels b and c, the intensity histogram showed distinct peaks (e) and a linear correlation (f) of the estimated number of VLPs per spot and spot intensity (slope = 17.4 ± 0.8, R^2 = 0.99).

Resolution and density dependent particle quantification accuracy

To test the accuracy of intensity correlation-based particle estimation, synthetic images containing different densities of fluorescent nanoparticles (0.2, 1.1, 3.4, and 5.6 NPs/µm^2) were simulated (Figure 4a) and analyzed with the method presented in this work. The synthetic images were 1028x1028 pixels in size with a pixel size of 65 nm. The images contained 1000, 5000, 15000, and 25000 simulated NPs (half-maximum PSF width of 320 nm) respectively and were binned 10 times in 65 nm intervals to assess the NP estimation accuracy for four densities and eleven resolutions. The estimated number of NPs for each density and resolution was divided by the known input number of simulated NPs (Figure 4b). For a density of 0.2 NPs/µm^2 the mean ratio is about 108 ± 4 %, with a slight tendency towards overestimation with increasing pixel size. At 65 nm pixel size the estimation accuracy is 100 % while at a pixel size of 650 nm it is increased to 113 %.

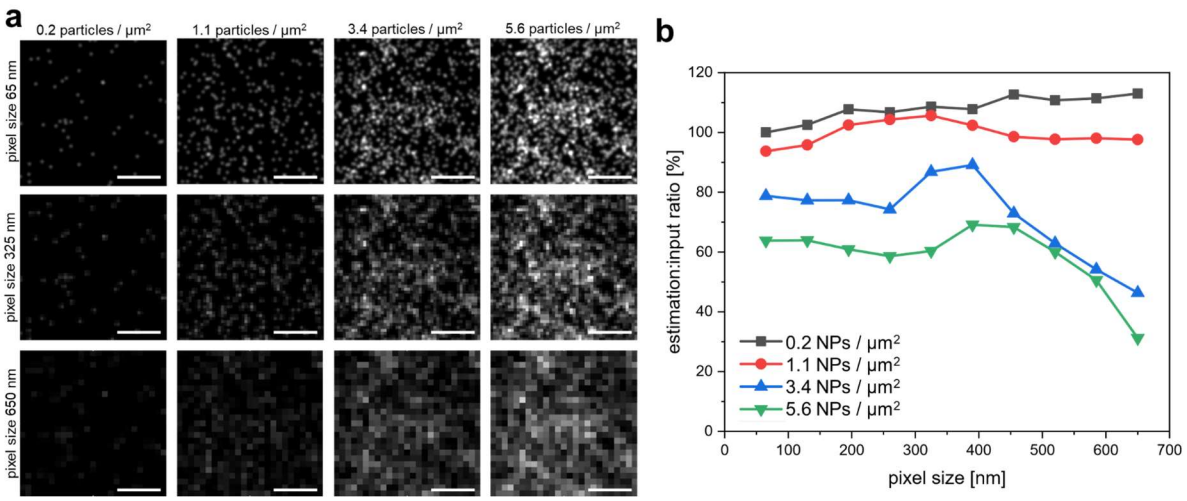

Figure 4: Simulation and analysis of fluorescent nanoparticles at different densities and resolutions (scale bars = 5 µm). Images with different densities of nanoparticles (0.2 to 5.6 particles per µm^2) were simulated and binned to pixel sizes of 65 to 650 nm in 65 nm intervals (a). The images were analyzed, and the ratio of estimated particles compared to the simulated ground truth was plotted for each pixel size (b). The ratio for the two lower densities is around 100 % with a light tendency for overestimation. The estimated ratio of the higher densities is 60 and 90 % until pixel sizes of 455 nm are exceeded.

For a density of 1.1 NPs/µm^2 the overall estimation ratio for all pixel sizes is 99 ± 4 %. In this case however, there is a local maximum of 106 % at a pixel size of 325 nm, while at 65 and 650 nm there are underestimations with 94 and 98 % respectively. Despite these minor deviations from the known number of simulated particles, the simulation shows that for all pixel sizes the estimated number of particles is valid for densities up to 1.1 NPs/µm^2. For higher densities (3.4 to 5.6 NPs/µm^2) the estimation accuracy drops dramatically and shows a more complex dependency on the resolution. For a density of 3.4 NPs/µm^2 with pixel sizes up to 455 nm, the estimation ratio is about 80 ± 6 %, showing that there is a general underestimation due to the high particle density. For lower resolution, the ratio decreases further until 46 % at a pixel size of 650 nm. This trend is also present for a density of 5.6 NPs/µm^2. For pixel sizes up to 455 nm the particle number is underestimated with a ratio of 60 ± 4 %, with further reduction down to 31 % at a pixel size of 650 nm.

The simulation experiment of Figure 4 gives a good impression of the accuracy and the limits of the sub-diffractive nanoparticle estimation method presented here. The simulation implicates that at low particle densities (up to 1.1 NPs/µm^2) the pixel size can be extended beyond 650 nm to enlarge the confocal imaged field of view and get a higher number of imaged cells (and thus stronger statistics), while maintaining the capability of a highly accurate estimation of the nanoparticles bound to the cells. At relatively high densities (3.4 NPs/µm^2 and beyond) the pixel size should not exceed 455 nm, and that the number of estimated particles is likely underestimated by 20 to 40 %. This calls for careful interpretation of data gained/obtained under these conditions / with these parameter settings.

Heterogenous binding of VLPs on Vero E6 and A549 cells

As a proof of concept, the method of parallel single-cell and single-nanoparticle quantification presented in this work was eventually used to quantify the heterogenous binding of VLPs on Vero E6 and A549 cells (Figure 5). Fluorescent VLPs with and without the reconstituted SARS-CoV-2 spike-protein were incubated on Vero E6 and A549 cells in different concentrations (1, 0.1, 0.01 nM lipid content). Vero E6

cells are very accessible for viral infection [47] [48] [49] as they abundantly express the angiotensin-converting enzyme 2 (ACE2) receptor [50] which also mediates the cell entry of SARS-CoV-2 [51]. This leads to a specific binding of the spike-protein bearing VLPs (Figure 5a). At a lipid content of 1 nM of the spike-protein bearing VLPs, the median of bound particles per cells is 260. When the amount of incubated VLPs was reduced to 0.1 nM, the median of bound particles was also reduced approximately by a factor of about ten to 21 VLPs/cell which shows that the binding is concentration dependent. This trend continues to the lowest concentration of 0.01 nM, where the median was further reduced to 4. This is close to the number of detected particles in the control (median at 2 particles/cell) where no VLPs were incubated and thus only unspecific autofluorescence and noise events are identified. There is no concentration dependent trend in bound VLPs per cell visible when the VLPs were not bearing the SARS-CoV-2 spike-protein, which shows that the binding events at concentrations of 1 and 0.1 nM are specific and mediated by the spike-protein. While the concentration dependent binding of the VLPs is also present for A549 cells, there is no difference in the amount of bound VLPs with or without spike protein. This means that the binding events detected here are not specifically mediated by the spike-protein but other effects like lipid-lipid interactions of the cell membrane and the VLPs [52].

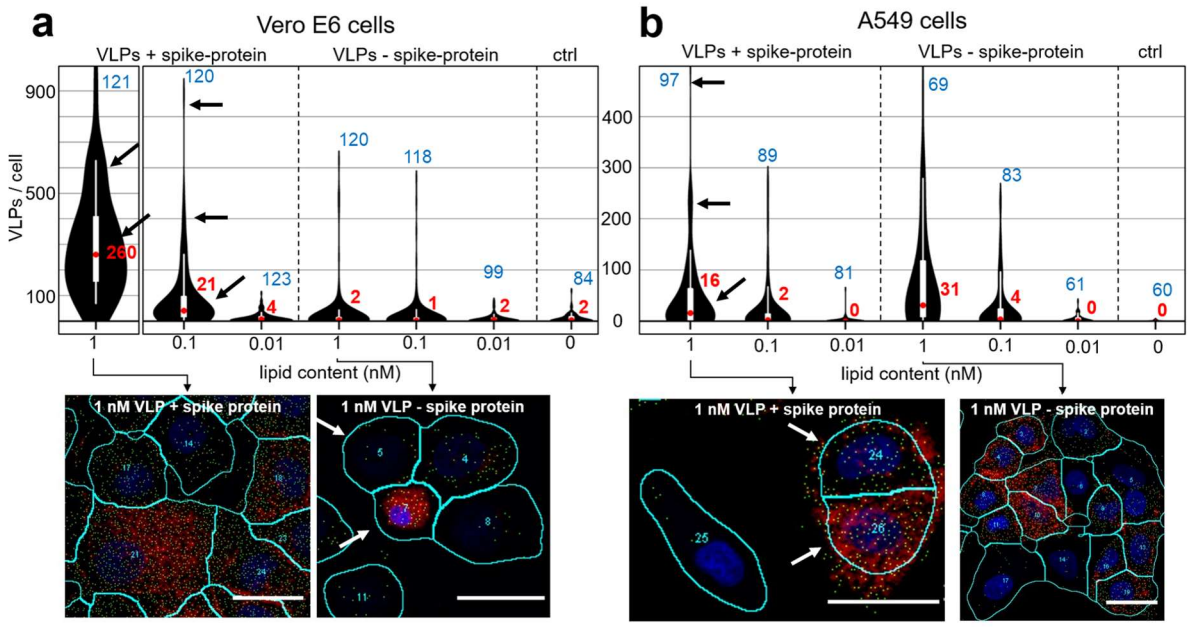

Figure 5: Quantification of VLPs with or without the SARS-CoV-2 spike protein to Vero E6 and A549 cells (scale bars = 30 µm).. The number of bound VLPs per cell are represented as violin plots (black) with the median is shown in red with the 25,75 percentile and 10,90 whiskers as box plots (white). Cellular populations are indicated by black arrows in the violin plots. The total number of analyzed cells per condition is shown in blue near the top of the violin plots The number of VLPs bearing the spike-protein show a concentration dependent binding to the Vero E6 cells (a, top) while this effect is not present for VLPs without the protein. The distribution of bound VLPs per cell is relatively broad, which is also seen by the cell-to-cell heterogeneity of VLP binding in the microscopy images (a, bottom). For the A549 cells, the concentration dependent number of bound VLPs (b, top) is much less prominent compared to Vero E6 cells, and there seems to be no difference between VLPs with and without the spike protein. However, cell-to-cell heterogeneity in the number of bound VLPs is still present and represented in the plots as well as in the images (b, bottom).

The accuracy of these analyses can be assessed by the results of the simulation described earlier (Figure 4b). The pixel size of the cell images is 360 nm, which is close to the simulated images with a binning of 6 (390 nm). The area of the analyzed cells varies between approximately 625 µm^2 for small cells (e.g., shortly after division) and 2500 µm^2 for big cells (e.g., shortly before division). The maximal

detected number of VLPs per cell was 1866, for the sample of the spike-protein bearing VLPs at a concentration of 1 nM on Vero E6 cells. This leads to a maximal particle density between 3.0 and 0.7 particles per cell. The simulation results for these densities at a pixel size of about 390 nm imply that the ratio of the number of estimated and real particles is in the range of 90 to 105 %. At the particle densities tested in Figure 5, no strong biases due to resolution or density are expected. The light overestimation at low densities additionally helps to explain the presence of the few particles in the control measurements which were detected additionally to events based on noise and autofluorescence.

The comparison of the median of bound VLPs per cell for all samples confirms that the binding of VLPs is specific for Vero E6 cells and mediated by the presence SARS-CoV-2 spike-protein, consistent with literature [51]. However, the true strength of the method proposed in the present work is the ability to generate single-cell information on particle binding, which allows for the assessment of cell-to-cell heterogeneity, as shown by the presence of local maxima in the violin plots (Figure 5a) and the confocal images (Figure 5b). As the heterogeneity of VLP binding is present in both cell lines and for VLPs with and without the spike-protein, this effect does not seem to be a specific property of the spike-protein but of the cells. The reason for this is yet unknown, as the effect seems to be independent of cell morphology. The Vero E6 images of Figure 5a (bottom) for example show heterogeneity (e.g., cell 21 vs cell 17) in bound spike-protein bearing VLPs for confluent healthy cells, while the VLPs without spike protein also show an extreme degree of heterogeneity for cell of inconspicuous morphology (cell 4, 5, and 8) and cells that seem to be apoptotic or shortly before division (cell 7). For the A549 cells Figure 5a, bottom, for example, the spike-protein bearing VLPs show a high degree of binding heterogeneity even for freshly divided cells (cell 24 and 26).

Conclusion

In summary, we presented an imaging and analysis approach to bridge the multicellular- and nanoscale, using the correlation of intensities peaks and clustered nanoparticles of CLSM imaged cells. We showed that the number sub-diffractive fluorescent nanoparticles can be precisely estimated from local intensity profiles, even beyond pixel sizes of 400 nm, which allows for imaging of relatively large fields of view. It is therefore possible to get single-cell results of bound nanoparticles for dozens of cells in parallel. This allows for the probing of cell-to-cell heterogeneities. While super-resolution microscopy may yield more accurate results (especially for extremely dense particles) than the method presented here, simulations imply that accuracies of 90 to 100 % can be attained with our approach. The intensity-based particle estimation of confocal imaged cells thus allows for high-throughput yet precise screening of cells, which would not be possible with super-resolution microscopy. All analysis steps are implemented in a single open-source Fiji-macro, making the screening of single-nanoparticle binding on single-cell level freely available to the scientific community.

Author Contributions

Yannic Kerkhoff: Methodology, Software, Validation, Formal analysis, Experiments, Writing – original draft. **Chuanxiong Nie:** Experiments. **Stefanie Wedepohl:** Experiments. **Katharina Hugentobler:** Experiments.

Conflicts of interest

There are no conflicts to declare.

Acknowledgements

This work was funded by the Deutsche Forschungsgemeinschaft (DFG, German Research Foundation) - Project ID 431232613 - SFB 1449; SFB 1078; BL1514/1. As well as the Corona Virus Pre-Exploration Project of the Berlin University Alliance. We gratefully acknowledge assistance from the Core Facility BioSupraMol supported by the DFG.

References

[1] L. Shang, K. Nienhaus and G. Nienhaus, „Engineered Nanoparticles Interacting With Cells: Size Matters," Journal of Nanobiotechnology, 12 (1), 2014.

[2] T. Iversen, T. Skotland and K. Sandvig, „Endocytosis And Intracellular Transport Of Nanoparticles: Present Knowledge And Need For Future Studies," Nano Today, 6 (2), pp. 176-185, 2011.

[3] M. Liu, Q. Li, L. Liang, J. Li, K. Wang, J. Li, M. Lv, N. Chen, H. Song, J. Lee, J. Shi, L. Wang, R. Lal and C. Fan, „Real-Time Visualization Of Clustering And Intracellular Transport Of Gold Nanoparticles By Correlative Imaging," Nature Communications, 8 (1), 2017.

[4] K. Cho, X. Wang, S. Nie, Z. Chen and D. Shin, „Therapeutic Nanoparticles For Drug Delivery In Cancer," Clinical Cancer Research, 14 (5), pp. 1310-1316, 2008.

[5] A. Wilczewska, K. Niemirowicz, K. Markiewicz and H. Car, „Nanoparticles As Drug Delivery Systems," Pharmacological Reports, 64 (5), pp. 1020-1037, 2012.

[6] P. Couvreur, „Nanoparticles In Drug Delivery: Past, Present And Future," Advanced Drug Delivery Reviews, 65 (1), pp. 21-23, 2013.

[7] M. Mitchell, M. Billingsley, R. Haley, M. Wechsler, N. Peppas and R. Langer, „Engineering Precision Nanoparticles For Drug Delivery," Nature Reviews Drug Discovery, 20 (2), pp. 101-124, 2020.

[8] G. Seisenberger, M. Ried, T. Endreß, H. Büning, M. Hallek and C. Bräuchle, „Real-Time Single-Molecule Imaging Of The Infection Pathway Of An Adeno-Associated Virus," Science, 294 (5548), pp. 1929-1932, 2001.

[9] B. Brandenburg and X. Zhuang, „Virus Trafficking – Learning From Single-Virus Tracking," Nature Reviews Microbiology, 5 (3), pp. 197-208, 2007.

[10] S. Liu, Z. Wang, H. Xie, A. Liu, D. Lamb and D. Pang, „Single-Virus Tracking: From Imaging Methodologies To Virological Applications," Chemical Reviews, 120 (3), pp. 1936-1979, 2020.

[11] M. Vert, Y. Doi, K. Hellwich, M. Hess, P. Hodge, P. Kubisa, M. Rinaudo and F. Schué, „Terminology For Biorelated Polymers And Applications (IUPAC Recommendations 2012)," Pure and Applied Chemistry, 84 (2), pp. 377-410, 2012.

[12] W. Wang, „Imaging The Chemical Activity Of Single Nanoparticles With Optical Microscopy," Chemical Society Reviews, 47 (7), pp. 2485-2508, 2018.

[13] M. Born, Principles of Optics, UK: Cambridge University Press, 2002.

[14] J. Pawley, Handbook of Biological Confocal Microscopy, New York: Springer, 2006.

[15] N. Ji, H. Shroff, H. Zhong and E. Betzig, „Advances In The Speed And Resolution Of Light Microscopy," Current Opinion in Neurobiology, 18 (6), pp. 605-616, 2008.

[16] W. Stark, „Nanoparticles In Biological Systems," Angewandte Chemie International Edition, 50 (6), pp. 1242-1258, 2011.

[17] S. Hell and J. Wichmann, „Breaking The Diffraction Resolution Limit By Stimulated Emission: Stimulated-Emission-Depletion Fluorescence Microscopy," Optics Letters, 19 (11), p. 780, 1994.

[18] E. Betzig, G. Patterson, R. Sougrat, O. Lindwasser, S. Olenych, J. Bonifacino, M. Davidson, J. Lippincott-Schwartz and H. Hess, „Imaging Intracellular Fluorescent Proteins At Nanometer Resolution," Science, 313 (5793), pp. 1642-1645, 2006.

[19] M. Rust, M. Bates and X. Zhuang, „Sub-Diffraction-Limit Imaging By Stochastic Optical Reconstruction Microscopy (STORM)," Nature Methods, 3 (10), pp. 793-796, 2006.

[20] H. Voort and K. Strasters, „Restoration Of Confocal Images For Quantitative Image Analysis," Journal of Microscopy, 178 (2), pp. 165-181, 1995.

[21] S. Altschuler and L. Wu, „Cellular Heterogeneity: Do Differences Make A Difference?," Cell, 141 (4), pp. 559-563, 2010.

[22] N. Komin and A. Skupin, „How To Address Cellular Heterogeneity By Distribution Biology," Current Opinion in Systems Biology, 3, pp. 154-160, 2017.

[23] Q. Nguyen, S. Lukowski, H. Chiu, A. Senabouth, T. Bruxner, A. Christ, N. Palpant and J. Powell, „Single-Cell RNA-Seq Of Human Induced Pluripotent Stem Cells Reveals Cellular Heterogeneity And Cell State Transitions Between Subpopulations," Genome Research, 28 (7), pp. 1053-1066, 2018.

[24] B. Carter and K. Zhao, „The Epigenetic Basis Of Cellular Heterogeneity," Nature Reviews Genetics, 22 (4), pp. 235-250, 2020.

[25] V. Almendro, A. Marusyk and K. Polyak, „Cellular Heterogeneity And Molecular Evolution In Cancer," Annual Review of Pathology: Mechanisms of Disease, 8 (1), pp. 277-302, 2013.

[26] F. Bocci, L. Gearhart-Serna, M. Boareto, M. Ribeiro, E. Ben-Jacob, G. Devi, H. Levine, J. Onuchic and M. Jolly, „Toward Understanding Cancer Stem Cell Heterogeneity In The Tumor Microenvironment," Proceedings of the National Academy of Sciences, 116 (1), pp. 148-157, 2018.

[27] K. Douglas, C. Piccirillo and M. Tabrizian, „Cell Line-Dependent Internalization Pathways And Intracellular Trafficking Determine Transfection Efficiency Of Nanoparticle Vectors," European Journal of Pharmaceutics and Biopharmaceutics, 68 (3), pp. 676-687, 2008.

[28] A. Verma and F. Stellacci, „Effect Of Surface Properties On Nanoparticle-Cell Interactions," Small, 6 (1), pp. 12-21, 2010.

[29] C. Fleischer and C. Payne, „Nanoparticle–Cell Interactions: Molecular Structure Of The Protein Corona And Cellular Outcomes," Accounts of Chemical Research, 47 (8), pp. 2651-2659, 2014.

[30] C. Peetla, S. Vijayaraghavalu and V. Labhasetwar, „Biophysics Of Cell Membrane Lipids In Cancer Drug Resistance: Implications For Drug Transport And Drug Delivery With Nanoparticles," Advanced Drug Delivery Reviews, 65 (13-14), pp. 1686-1698, 2013.

[31] E. Shin, Y. Li, U. Kumar, H. Sureka, X. Zhang and C. Payne, „Membrane Potential Mediates The Cellular Binding Of Nanoparticles," Nanoscale, 5 (13), p. 5879, 2013.

[32] K. Chen and G. Bothun, „Nanoparticles Meet Cell Membranes: Probing Nonspecific Interactions Using Model Membranes," Environmental Science & Technology, 48 (2), pp. 873-880, 2013.

[33] E. Melby, C. Allen, I. Foreman-Ortiz, E. Caudill, T. Kuech, A. Vartanian, X. Zhang, C. Murphy, R. Hernandez and J. Pedersen, „Peripheral Membrane Proteins Facilitate Nanoparticle Binding At Lipid Bilayer Interfaces," Langmuir, 34 (36), pp. 10793-1080, 2018.

[34] B. Andreiuk, A. Reisch, M. Lindecker, G. Follain, N. Peyriéras, J. Goetz and A. Klymchenko, „Fluorescent Polymer Nanoparticles For Cell Barcoding In Vitro And In Vivo," Small, 13 (38), p. 1582, 2017.

[35] H. Suzuki, T. Toyooka and Y. Ibuki, „Simple And Easy Method To Evaluate Uptake Potential Of Nanoparticles In Mammalian Cells Using A Flow Cytometric Light Scatter Analysis," Environmental Science & Technology, 41 (8), pp. 3018-3024, 2007.

[36] J. Waters, „Accuracy And Precision In Quantitative Fluorescence Microscopy," Journal of Cell Biology, 185 (7), pp. 1135-1148, 2009.

[37] E. Dmitrienko, O. Naumova, B. Fomin, M. Kupryushkin, A. Volkova, N. Amirkhanov, D. Semenov, I. Pyshnaya and D. Pyshnyi, „Surface Modification Of SOI-FET Sensors For Label-Free And Specific Detection Of Short RNA Analyte," Nanomedicine, 11 (16), pp. 2073-2082, 2016.

[38] A. Torrano, J. Blechinger, C. Osseforth, C. Argyo, A. Reller, T. Bein, J. Michaelis and C. Bräuchle, „A Fast Analysis Method To Quantify Nanoparticle Uptake On A Single Cell Level," Nanomedicine, 8 (11), pp. 1815-1828, 2013.

[39] J. Unciti-Broceta, V. Cano-Cortés, P. Altea-Manzano, S. Pernagallo, J. Díaz-Mochón and R. Sánchez-Martín, „ Number Of Nanoparticles Per Cell Through A Spectrophotometric Method - A Key Parameter To Assess Nanoparticle-Based Cellular Assays," Scientific Reports, 5 (1), 2015.

[40] H. Peuschel, T. Ruckelshausen, C. Cavelius and A. Kraegeloh, „Quantification Of Internalized Silica Nanoparticles Via STED Microscopy," BioMed Research International, 2015, pp. 1-16, 2015.

[41] B. Rothen-Rutishauser, D. Kuhn, Z. Ali, M. Gasser, F. Amin, W. Parak, D. Vanhecke, A. Fink, P. Gehr and C. Brandenberger, „Quantification Of Gold Nanoparticle Cell Uptake Under Controlled Biological Conditions And Adequate Resolution," Nanomedicine, 9 (5), pp. 607-621, 2014.

[42] J. Schindelin, I. Arganda-Carreras, E. Frise, V. Kaynig, M. Longair, T. Pietzsch, S. Preibisch, C. Rueden, S. Saalfeld, B. Schmid, J. Tinevez, D. White, V. Hartenstein, K. Eliceiri, P. Tomancak and A. Cardona, „Fiji: An Open-Source Platform For Biological-Image Analysis," Nature Methods, 9 (7), pp. 676-682, 2012.

[43] J. Pokorski and N. Steinmetz, „The Art Of Engineering Viral Nanoparticles," Molecular Pharmaceutics, 8 (1), pp. 29-43, 2010.

[44] S. Beucher, „The Watershed Transformation Applied to Image Segmentation Scanning," Scanning Microscopy, 6 (28), 1992.

[45] E. Bengtsson, C. Wählby and J. Lindblad, „Robust Cell Image Segmentation Methods," Pattern recognition adn image analysis, 14 (2), 2004.

[46] A. Makandar and B. Halalli, „Image Enhancement Techniques Using Highpass And Lowpass Filters," International Journal of Computer Applications, 109 (14), pp. 21-27, 2015.

[47] M. Temonen, O. Vapalahti, H. Holthofer, M. Brummer-Korvenkontio, A. Vaheri and H. Lankinen, „Susceptibility Of Human Cells To Puumala Virus Infection," Journal of General Virology, 74 (3), pp. 515-518, 1993.

[48] Z. Qinfen, C. Jinming, H. Xiaojun, Z. Huanying, H. Jicheng, F. Ling, L. Kunpeng and Z. Jingqiang, „The Life Cycle Of SARS Coronavirus In Vero E6 Cells," Journal of Medical Virology, 73 (3), pp. 332-337, 2004.

[49] N. Ogando, T. Dalebout, J. Zevenhoven-Dobbe, R. Limpens, Y. van der Meer, L. Caly, J. Druce, J. de Vries, M. Kikkert, M. Bárcena, I. Sidorov and E. Snijder, „SARS-Coronavirus-2 Replication In Vero E6 Cells: Replication Kinetics, Rapid Adaptation And Cytopathology," Journal of General Virology, 101 (9), pp. 925-940, 2020.

[50] W. Li, M. Moore, N. Vasilieva, J. Sui, S. Wong, M. Berne, M. Somasundaran, J. Sullivan, K. Luzuriaga, T. Greenough, H. Choe and M. Farzan, „Angiotensin-Converting Enzyme 2 Is A Functional Receptor For The SARS Coronavirus," Nature, 426 (6965), pp. 450-454, 2003.

[51] M. Hoffmann, H. Kleine-Weber, S. Schroeder, N. Krüger, T. Herrler, S. Erichsen, T. Schiergens, G. Herrler, N. Wu, A. Nitsche, M. Müller, C. Drosten and S. Pöhlmann, „SARS-Cov-2 Cell Entry Depends On ACE2 And TMPRSS2 And Is Blocked By A Clinically Proven Protease Inhibitor," Cell, 181 (2), pp. 271-280.e8, 2020.

[52] L. Stamatatos, R. Leventis, M. Zuckermann and J. Silvius, „Interactions Of Cationic Lipid Vesicles With Negatively Charged Phospholipid Vesicles And Biological Membranes," Biochemistry, 27 (11), pp. 3917-3925, 1988.

4.3 Analysis and refinement of 2D single-particle tracking experiments

---

Yannic Kerkhoff and Stephan Block

Biointerphases 15, 021201 (**2020**)

DOI: https://doi.org/10.1116/1.5140087

Short summary

This work gives an overview of the analysis steps needed for two-dimensional single-particle tracking experiments and offers refinement solutions for the assessment of the maximum linking distance to ensure optimal tracking quality (Figure 22). This refined SPT was used to track CTxB on synthetic GM1-containing POPC SLBs showing its pentameric GM1 binding valency (see Appendix 7.1.1 Multivalent GM1 binding of choleratoxin subunit B) and to quantify the BMP2 induced immobilization of BMPR2 on endothelia tip-cells [170]. It was also used to track IAVs binding on hybrid lipid bilayers [171] containing red blood cell membrane material (see Appendix 7.1.2 Hybrid lipid bilayer formation) and to track fluorescent beads in a microfluidic setup allowing for single molecule force measurements (see Publications 4.4 A new microfluidics-based force spectroscopy method applying lateral piconewton forces on single molecules with sub-nanometer resolution in high-throughput).

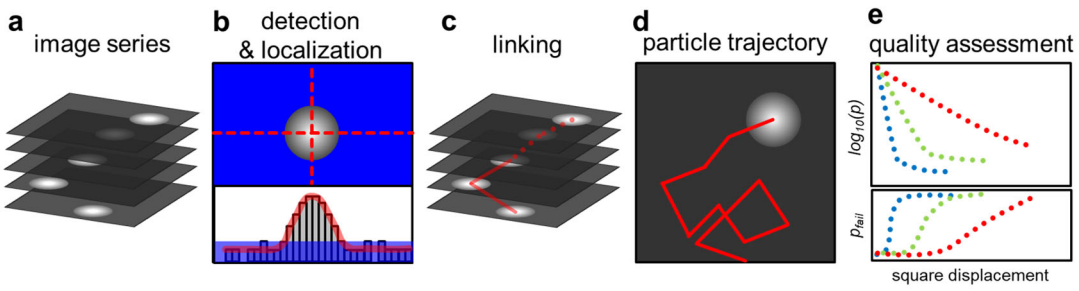

Figure 22: A recorded image series containing the PSFs of nanoparticles (a) can be analyzed by detection and localization of the PSFs centers (b) and linking them frame-wise (c) yielding single-particle trajectories (d). The quality of these single-particle tracks can then be assessed by evaluating the probability linking errors depending on the square displacement distribution (e).

Author contributions

Yannic Kerkhoff outlined a structure for the work, performed analysis, prepared figures, tables, and schemes, and wrote a major part of manuscript. Stephan Block was responsible for supervision, implementation of most equations, writing part of the manuscript, reviewing, and editing of the draft.

Biointerphases
A Journal of Biomaterials and Biological Interfaces

TUTORIAL

avs.scitation.org/journal/bip

Analysis and refinement of 2D single-particle tracking experiments

Cite as: Biointerphases 15, 021201 (2020); doi: 10.1116/1.5140087
Submitted: 26 November 2019 · Accepted: 5 February 2020 ·
Published Online: 5 March 2020

Yannic Kerkhoff and Stephan Block[a)]

AFFILIATIONS

Department of Chemistry and Biochemistry, Emmy-Noether Group "Bionanointerfaces," Freie Universität Berlin, Takustr. 3, 14195 Berlin, Germany

Note: This paper is part of the Special Topic Collection on Early Career Investigators.
[a)]**Author to whom correspondence should be addressed:** stephan.block@fu-berlin.de

ABSTRACT

In recent decades, single particle tracking (SPT) has been developed into a sophisticated analytical approach involving complex instruments and data analysis schemes to extract information from time-resolved particle trajectories. Very often, mobility-related properties are extracted from these particle trajectories, as they often contain information about local interactions experienced by the particles while moving through the sample. This tutorial aims to provide a comprehensive overview about the accuracies that can be achieved when extracting mobility-related properties from 2D particle trajectories and how these accuracies depend on experimental parameters. Proper interpretation of SPT data requires an assessment of whether the obtained accuracies are sufficient to resolve the effect under investigation. This is demonstrated by calculating mean square displacement curves that show an apparent super- or subdiffusive behavior due to poor measurement statistics instead of the presence of true anomalous diffusion. Furthermore, the refinement of parameters involved in the design or analysis of SPT experiments is discussed and an approach is proposed in which square displacement distributions are inspected to evaluate the quality of SPT data and to extract information about the maximum distance over which particles should be tracked during the linking process.

I. INTRODUCTION

In 1827, Robert Brown used optical microscopy to follow the motion of single particles suspended in water, which exhibited a random motion that was less pronounced for larger particles.[1] Although current technologies offer far more sophisticated approaches to perform and analyze such experiments, the basic concept of using single particle tracking (SPT) is mainly unchanged and relies on the use of microscopic approaches to track the motion of single particles, allowing particle information to be extracted from time-resolved trajectories. Nevertheless, technological developments in recent decades allowed us to expand the scope of SPT enormously, which is (in the context of life science) currently covering the range between single molecules (nanometer scale) up to eukaryotic cells (submillimeter scale) that move within tissue.[2,3] Current instrumentation is sensitive enough to resolve single molecules, regardless of whether the molecule is labeled with dyes or whether label-free detection schemes are used.[4,5] The application of high-speed cameras currently enables tracking with microsecond temporal resolution.[6] Advanced microscopy setups allow for imaging beyond the diffraction limit or to obtain three-dimensional (3D) maps of cellular distributions within tissue and how these distributions change over time.[7,8]

In parallel to these instrumental developments, the analysis of SPT experiments also experienced strong improvements. While early experiments had to be tracked manually, a variety of different software packages is now available, all of which allow for analyzing SPT experiments in an automatic or semiautomatic fashion.[9] Furthermore, sophisticated data analysis schemes were developed, involving, for example, statistical inference, Markov modeling, or Monte Carlo methods, in order to increase the accuracy and/or reliability of extracting properties from particle trajectories.

Due to the high relevance in life sciences, a large number of review articles are currently available,[9–14] each of which typically focusses on a particular aspect of SPT. Nevertheless, recent modeling of the SPT measurement process allowed for deriving limits for the accuracy, with which mobility-related properties can be extracted from SPT experiments. These works form a basis for refining the parameters used when measuring, analyzing, and assessing the quality of SPT experiments, yet a comprehensive overview of their

Biointerphases
A Journal of Biomaterials and Biological Interfaces
TUTORIAL
avs.scitation.org/journal/bip

main results is still lacking. It is, therefore, the aim of this tutorial to briefly introduce the technical aspects of SPT, followed by a comprehensive overview of accuracies, with which particles can be localized and their motion be quantified. Afterward, this tutorial will discuss how distributions derived from SPT experiments can be used to evaluate the quality of SPT data and provide guidance, and how SPT experiments and their analysis can be refined. All these considerations will be restricted, as detailed in Sec. II, to tracking the motion of nanometer-size particles that move within or close to two-dimensional (2D) interfaces.

II. TECHNICAL CONSIDERATIONS

A. Typical examples of systems of interest (of this tutorial)

Particle tracking has been successfully applied to a variety of different systems, ranging from tracking the 2D motion of single lipids in well-defined, synthetic lipid bilayers up to the motion of cells within entire 3D organoids and embryos.[3,10,15–18] Depending on the complexity of the system of interest, different methodological approaches are needed to perform the tracking experiment and to analyze the obtained data.[11,12,19–21] In order to provide a coherent framework, this tutorial will focus on tracking experiments of single, nanometer-sized molecules (such as lipids, proteins, etc.) and particles [such as viruses, (proteo-)liposomes, exosomes, etc.] that move in or at lipid membranes (such as supported or free standing lipid bilayers, cell membranes, or membrane-coated nanochannels; Fig. 1).

Although this may appear as a strong limitation, this class of SPT experiments allows us to investigate a large variety of biologically relevant questions, such as probing interactions arising between membranes and (i) proteins (e.g., during signaling), (ii) viruses (e.g., virus entry and egress), or (iii) particles (e.g., endocytosis, drug delivery), to name a few examples.[17,22–28] This class includes, for example, tracking the motion of single lipids and membrane proteins (and complexes) [Fig. 1(a)], which have been incorporated into fully synthetic (supported or freestanding) bilayers or expressed in the plasma membrane of a living cell (Figs. 1(c) and 1(d)]. But it also includes, for example, the tracking of viruses [Fig. 1(b)] that bind to receptors or attachment factors incorporated in synthetic or native lipid bilayers or that have been confined in nanometer-sized channels for certain analytical purposes [Fig. 1(e)]. Although these (exemplary) systems differ notably in their properties on a molecular scale, it will turn out that their motion can be assessed by conceptually similar measurement settings and analysis methods. Therefore, in the following, we refer to tracking of nanoparticles in general, regardless of whether the tracked object is a lipid, protein, or virus.

B. Instrumentation

Tracking the motion of nanoparticles with sufficient spatial resolution typically relies on the application of high-magnification

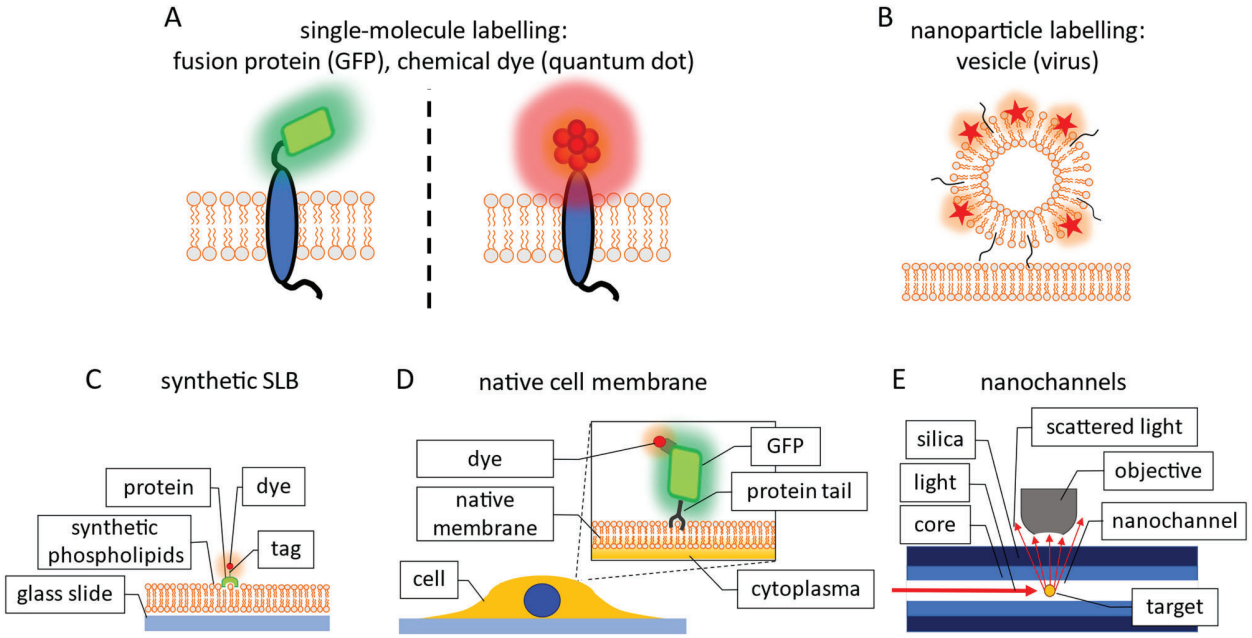

FIG. 1. Schematic overview of typical systems investigated in 2D tracking of single nanoparticles, which can be either categorized based on the type of tracked nanoparticle [(a) and (b)] or the experimental setting, in which its motion is recorded [(c)–(e)]: (a) membrane proteins, being labeled by fusion proteins (e.g., green fluorescent protein (GFP) and red fluorescent protein (RFP)), organic dyes, or quantum dots; (b) fluorescently labeled supramolecular complexes, such as (proteo-)liposomes or viruses interacting with (ligand- or receptor-containing) lipid bilayers. (c)–(e) The motion of such nanoparticles may be tracked at synthetic lipid bilayers (providing a well-defined environment), at cell membranes (providing a native environment), or within nanochannels (confining the nanoparticle motion for analytical purposes).

Biointerphases
A Journal of Biomaterials and Biological Interfaces
TUTORIAL
avs.scitation.org/journal/bip

microscopes in order to image the nanoparticle positions in the sample over time, leading to the recording of "particle tracking movies" that allow for further data analysis.[11,12,29] In most cases, fluorescence microscopes are used (Fig. 2), in which the nanoparticles are labeled by a single or multiple dyes [cf. Figs. 1(a) and 1(b)] and the microscope is operated so that only the (Stokes-shifted) emission of the dye is recorded, yielding high contrasts between the signal (dye) and the background (e.g., elastically scattered light). In general, two different implementations are widely used, wide-field [WFM; Fig. 2(a)] and confocal (laser scanning) microscopes [CLSM; Fig. 2(b)], which mainly differ in the image generation.[11]

In wide-field microscopy, the objective is used to project the image of the sample onto a camera, which in principle allows a complete snapshot of the imaged sample to be obtained at once (in contrast the CLSM in which the image is generated by a scanning process). Typically, EMCCD (electron-multiplying charge-coupled device) or sCMOS (scientific complementary metal oxide semiconductor) cameras are used to digitalize the image. These camera types differ in their photon conversion and readout electronics and generate, therefore, different noise characteristics in the recorded images.[30,31] EMCCD cameras are often superior for very dim (low quantum efficiency) dyes that require very long exposure times ($\gg$100 ms), while sCMOS cameras are often the better choice for brighter dyes (moderate to large quantum efficiency) that can be imaged with shorter exposure times. Both types of cameras can track single (dye) molecules.[2,32]

In contrast to WFM, the optical path of CLSMs is complemented by a pinhole, which ensures that the sample is probed only within a (diffraction-limited) spot.[11,12] As the sample is imaged point-wise, CLSMs are typically equipped with photon detectors such as photoelectron multiplier tubes, avalanche photodetectors, or the so-called hybrid detectors. To record (2D or 3D) spatially resolved images, the spot is scanned over the sample, typically lowering the temporal resolution of CLSM in comparison to WFM. The presence of the pinhole ensures that only light emitted within a diffraction-limited spot contributes to the measured signal, which effectively rejects photons being emitted outside of the focal plane (lowering, for example, the background signal in extended samples).[11,12] Furthermore, the distance at which two nanoparticles can still be unambiguously distinguished is decreased, thereby increasing the lateral resolution in the recorded images. Therefore, the use of WFM or CLSM may be advantageous, depending on the scope of the measurement. Recording particle tracking movies requiring large field of views and high temporal resolution typically benefit from using WFM, while suppression of off-focus fluorescence (e.g., originating from dyes being out of the focal plane) or the capability to probe the sample at different depths requires to use a CLSM.

These optical setups can be complemented by additional components yielding more complex settings that are able to improve the measurement quality in certain measurement scenarios. For motions or interactions that occur only at a certain plane in space (e.g., viruses that interact with a supported lipid bilayer), the usage of total internal reflection fluorescence microscopy (TIRFM) can offer advantages.[33] TIRFM can be applied if the refractive index of the sample is lower than that of the mounting substrate, which is

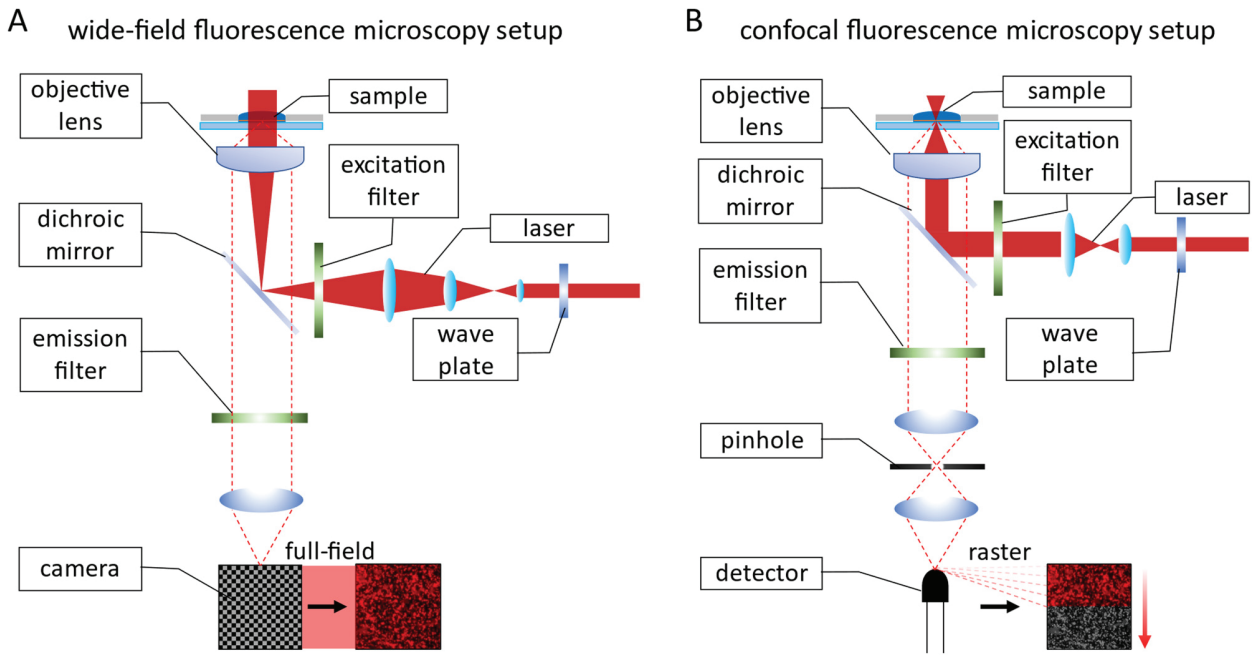

FIG. 2. Scheme of microscope setups commonly employed for 2D SPT: (a) WFM and (b) CLSM.

Biointerphases
A Journal of Biomaterials and Biological Interfaces
TUTORIAL
avs.scitation.org/journal/bip

fulfilled for most biological samples on glass substrates. In this case, the excitation light path is changed in such a way that the light hits the sample at the critical angle of total internal reflection (TIR) and the excitation light will, therefore, show total internal reflection at the substrate-sample interface. Although most of the irradiated light will be reflected under TIR conditions, this process also creates an evanescent wave at the interface, the intensity of which decays exponentially with increasing distance from the interface, limiting the excitation light to remain within close proximity to the interface (typically ~100–200 nm).[34] Hence, only dyes being close to the interface will be excited, which improves the signal-to-noise ratio (SNR) when probing processes occurring at interfaces.

Furthermore, recent developments rely on scattering instead of fluorescence in order to track the motion of nanoparticles without introducing dye-based labels.[35–37] In most of such implementations, the molecules of interest are labeled by optically dense nanoparticles (e.g., gold nanoparticles) that strongly scatter the incident light and can be either detected in a dark field configuration (i.e., the labeling nanoparticles are illuminated perpendicular to the readout light path) or by probing the backscattered light (e.g., in the iSCAT configuration). As the labeling nanoparticle is not bleached by the imaging process, it is possible to apply high illumination intensities, offering very high temporal and spatial resolution in the tracking process.[35,38] Nevertheless, as any label may disturb the motion/interactions of the nanoparticle of interest, current research increasingly focusses on label-free methods.[5,39]

Regardless of which optical setting and readout method are used in such experiments, each microscope has its resolution limit, below which two isolated nanoparticles cannot be unambiguously resolved anymore. This means that it is *a priori* impossible to distinguish if a spot in the image is created by a single nanoparticle or by multiple nanoparticles having separations below the resolution limit.[7] For CLSMs, the lateral resolution limit can be estimated by

$$\sigma_{\mathrm{res}} \approx \lambda/(2 \cdot \mathrm{NA}), \tag{1}$$

with λ denoting the wavelength of the light used and NA the numerical aperture of the objective.[40] This typically yields resolutions on the order of 200–250 nm for CLSMs, while slightly larger values are observed for WFMs. The intensity distribution of single nanoparticles on the detector can be approximated by[40]

$$I(x, y) = \frac{I_0}{2\pi\sigma_{\mathrm{PSF}}^2} \cdot \exp\left(-\frac{[x - x_0]^2 + [y - y_0]^2}{2 \cdot \sigma_{\mathrm{PSF}}^2}\right). \tag{2}$$

Here, I_0 denotes the intensity of the nanoparticle, x_0 and y_0 its center position in the image, σ_{PSF} the spot size of the nanoparticle (in the image), and $I(x, y)$ the intensity at the position (x, y) that is caused by the nanoparticle. For nanoparticles being much smaller than σ_{res}, the nanoparticle spot size σ_{PSF} is given by σ_{res} and is in this case representative for the resolution limit of the microscope, but not the true nanoparticle size anymore. This function is, therefore, often denoted as a point spread function (PSF), as it shows how the intensity of a point emitter will be distributed in the microscopic image. The optical resolution can be improved by more advanced measurement schemes (super-resolution microscopy) and values ranging between 50 and 100 nm are frequently reported,[7] though much higher resolutions have been demonstrated for dedicated systems.[41]

However, it should be emphasized that Eq. (1) indicates the minimum distance, at which two nanoparticles can still be unambiguously distinguished in the image. This is not to be confused with the question, how precise a single, isolated nanoparticle can be localized within an image. We will show in Sec. II C 2 that these are two completely different questions and that localization accuracies on the nanometer scale are possible even for nanoparticle spot sizes being on the order of multiple 100 nm.

C. General aspects of single particle tracking

After the motion of the nanoparticles has been captured, the resulting image series must be further processed to obtain information about the actual nanoparticle motion. Figure 3 shows on a very conceptual level the three main steps involved in all single particle tracking analyses: Detection of the nanoparticles, localization of the nanoparticle center positions, and linking the nanoparticles across the frames of the recorded tracking movie. In the past, a variety of different algorithms were proposed and implemented to solve these tasks. Detailed information on the underlying concepts and the performance of the different implementations are given in a couple of recent reviews.[9,14,29,42] These studies have shown that certain implementations offer advantages in certain experimental settings and that there is no single implementation that performs best in all possible settings. Therefore, these references can be used as guidelines to decide which SPT implementation may be the best choice for the system investigated, and we will give only a general overview in Subsections II C 1–II C 3.

1. Detection

The analysis always starts with the detection of the nanoparticles, which must be distinguished from the background signal. The background is mainly generated by the detector's readout noise and by background fluorescence (e.g., off-focus dyes or autofluorescence of the materials used) and can, therefore, contain random and systematic components. Different strategies have been proposed in the past, including the usage of centroid algorithms (after thresholding), difference of Gaussian filter segmenters, spatiotemporal filters, or a search for local intensity maxima.[9,14] In order to differentiate between noise and a true detection event, all these approaches typically require to define an intensity cutoff value, which has to be exceeded by the event to be counted as a true event. Additionally, most implementations also require an estimated value of the nanoparticle (spot) size, in order to differentiate if two closely separated events belong to one and the same or to two independent nanoparticles. Both parameters are commonly determined by visual inspection of the SPT movies. Certain algorithms may require additional parameters, such as the time period (i.e., the number of frames) used when applying temporal filters. Different detection strategies can differ in their performance (e.g., positive/negative detection rates, etc.) as comprehensively evaluated in Refs. 9 and 14. Such differences are typically negligible for bright nanoparticles but can become pronounced for dim ones.

Biointerphases
A Journal of Biomaterials and Biological Interfaces
TUTORIAL
avs.scitation.org/journal/bip

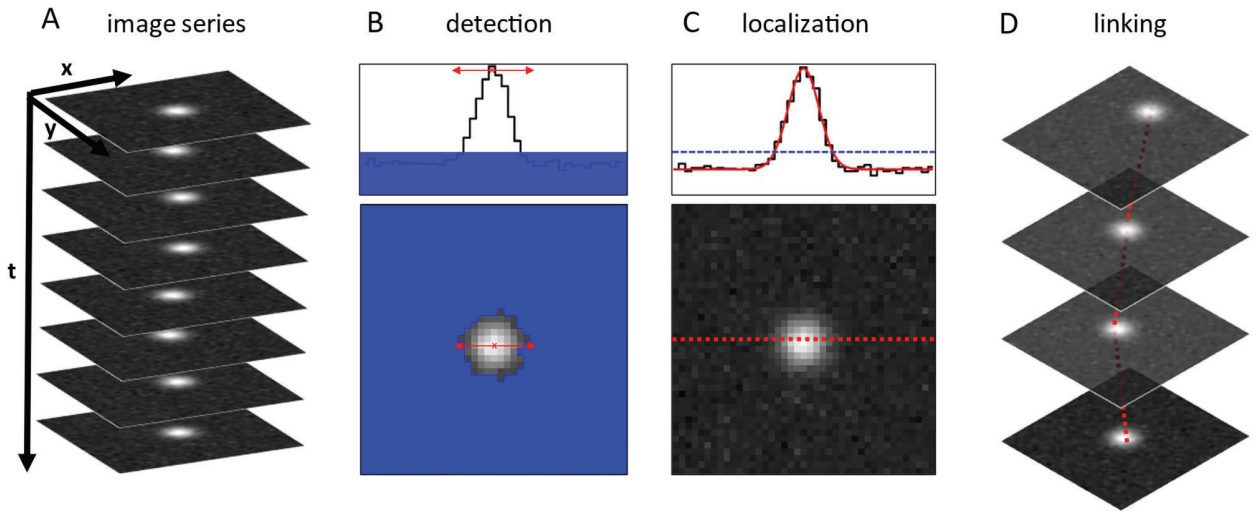

FIG. 3. Fundamental data analysis steps of 2D SPT: (a) Recording an image series at specific time intervals, containing the intensity distributions of the imaged nanoparticles; (b) detecting the nanoparticles in each frame of the image series; (c) localizing nanoparticle center positions based on localizing the center of the respective intensity distribution (typically yielding localization accuracies below the diffraction limit); (d) linking of nanoparticle center positions across consecutive time frames, yielding time-dependent nanoparticle trajectories.

Choosing an appropriate intensity threshold value is often challenging for nanoparticles with only few and/or dim dyes (low quantum yield), having intensities that are often close to the background noise. For such dim nanoparticles, it is necessary to choose a detection threshold being close to the background signal, which may create a notable false detection rate. Even if this false detection rate is as low as 0.003% (e.g., when choosing a threshold value being 4 standard deviations above the average background signal), this apparently small percentage can still end up in 50–500 falsely detected events in each frame, as current sCMOS and CCD camera sensors provide between 1 and 16×10^6 pixels. Hence, tracking very dim nanoparticles often requires the introduction of additional measures allowing to distinguish noise from true events, which can be, for example, the quality when fitting the PSF function to the detected spot.

This shows that the ratio of nanoparticle intensity to the magnitude of intensity fluctuations (due to noise) is an important property in the SPT analysis. This ratio is often denoted as SNR,

$$\mathrm{SNR} = \frac{I_0}{\sigma_{\mathrm{noise}}}, \tag{3}$$

in which σ_{noise} is the standard deviation of all noise processes (i.e., $\sigma^2_{\mathrm{noise}} = \sigma^2_{\mathrm{back}} + \sigma^2_{\mathrm{photon}} + \ldots$, typically including the standard deviation of the background noise σ^2_{back} and the one of the photon noise of the fluorescence emission $\sigma^2_{\mathrm{photon}}$).[43]

2. Localization

The next step after detecting the particles of interest is the determination of their center position in the image, a process that is sometimes denoted as subpixel localization as it often provides localization accuracies being below the size of a single pixel (and therefore often even below the diffraction limit). This process is sometimes included in the detection process, for example, in many centroid algorithms, while other implementations provide a dedicated subpixel localization step in order to improve the accuracy. Over the past few decades, many approaches have been introduced, including unweighted and weighted centroid algorithms, Gaussian maximum-likelihood estimator (MLE) or least mean squares (LMS) fitting applied to the nanoparticle intensity profiles and approaches employing the radial symmetry or Fourier transformations,[43–45] most of which have been evaluated in recent works.[9,14,46] These evaluations generally show that the localization error Δr, which is the deviation between the true, (x_0, y_0), and the extracted position, (x, y), according to $\Delta r^2 = (x - x_0)^2 + (y - y_0)^2$, strongly depends on the SNR. Thomson *et al.*,[43] for example, calculated the average localization error of Gaussian LMS fits to be

$$\sigma^2_{\mathrm{pos,LMS}} = \frac{\sigma^2_{\mathrm{PSF}} + a^2/12}{I_0} + \frac{8\pi\sigma^4_{\mathrm{PSF}}\sigma^2_{\mathrm{back}}}{a^2 I_0^2}, \tag{4}$$

with a denoting the size of a pixel in the image. A related, but more general, equation is given by the Cramér–Rao lower bound (CRLB), which reads for Gaussian intensity profiles,

$$\sigma^2_{\mathrm{pos,CRLB}} = \Gamma \cdot \frac{\sigma^2_{\mathrm{PSF}} + a^2/12}{I_0}\left(1 + 4\cdot\tau + \sqrt{\frac{2\cdot\tau}{1+4\cdot\tau}}\right), \tag{5}$$

Biointerphases
A Journal of Biomaterials and Biological Interfaces
TUTORIAL
avs.scitation.org/journal/bip

with $\tau = \frac{2\pi(\sigma_{PSF}^2 + a^2/12)\cdot\sigma_{back}^2}{a^2 I_0}$ and the excess noise factor Γ (=2 for EMCCD cameras).[47,48]

The CRLB is often regarded to indicate the lowest localization error achievable for the particular experiment.[14,49] Evaluation of localization approaches by analyzing synthetic SPT data (simulating a random 2D motion of multiple nanoparticles in the presence of well-defined noise sources) confirmed that most implementations are able to reach the limit given by Eq. (5), except for centroid algorithms that often yield a notably lower localization accuracy and may provide a quick, first estimate of the nanoparticle center.[43,45] Although Gaussian MLE, Gaussian LMS, and approaches employing radial symmetry or Fourier transformations are often comparable in terms of localization accuracy, they differ significantly in their processing speed, with Gaussian MLE and especially Gaussian LMS being computationally more expensive than radial symmetry- or Fourier-based approaches.[44,45]

In general, good fluorophores may yield on average as many as 10^5 photons before they break down due to photobleaching. Therefore, a single fluorophore can theoretically be tracked to a precision of 65 nm over 100 frames, or 20 nm over 10 frames, in the absence of background noise. To optimize measurements for single fluorophore localization and tracking, it is crucial to maximize the detected fluorescence and minimize the measurement noise, i.e., to maximize the achieved SNR.[43] Higher accuracies can be reached when tracking brighter nanoparticles, which are, for example, labeled by multiple dyes. This allows us to yield localization accuracies on the order of 10 nm over hundreds of frames.[50] The highest accuracies have been reported when using dye-labeled beads or scattering approaches that are able to operate at very high illumination intensities and yield localization accuracies on the order of 1 nm.[27,51]

3. Linking

In order to extract the motion of single nanoparticles in the form of trajectories, their center positions have to be linked between adjacent frames of the tracking movie. This is a very critical step in the analysis, as errors done in the linking process can have a high impact on the information that will be extracted afterward. Blinking of the dye, a drifting focal plane, and merging or splitting of trajectories make a robust connection of particles in successive frames challenging and thus numerous tracking algorithms have been developed to tackle these challenges.[9] In general, most linking algorithms connect nanoparticles across adjacent frames by calculating for each nanoparticle the distances between the "current" nanoparticle position and the one of all nanoparticles of the subsequent frame.[29] In the conceptually simplest implementation, nanoparticles would be linked across adjacent frames, which show the lowest displacement between the frames, i.e., the algorithm would identify a nanoparticle in the subsequent frame by identifying the nanoparticle that has the smallest distance from the initial nanoparticle position. This straightforward ("nearest-neighbor linking") approach exhibits a good performance, if the nanoparticle movement between adjacent frames is small in comparison to the average nanoparticle distance, i.e., if the nanoparticle density is fairly low, but creates a notable proportion of linking errors for high nanoparticle densities (cf. Sec. IV C).[9,52]

Since it is not always possible to operate at low to moderate nanoparticle densities, e.g., when tracking membrane proteins in live cells, more complex linking algorithms have been developed that optimize the linking process based on the application of certain statistical measures or filters to the linking data. Examples include nearest-neighbor linking in combination with local or global optimization of the extracted nanoparticle displacement distributions, multiple hypothesis tracking, combinatorial optimization, or the application of Kalman filtering.[9,29,42] Of particular interest for tracking of dense nanoparticle distributions are approaches in which nanoparticle detection and linking are iteratively coupled, such as the implementation introduced by Sergé *et al.*[53] In this work, a detection and linking method suitable for high particle densities was implemented, which involved the iterative deflation of detected peaks in order to detect smaller (and otherwise hidden) peaks. Successive linking, which includes local and past statistical information of the trajectories, resolves possible conflicts due to very close particles or blinking and allows us to study the diffusion of single nanoparticles at very high densities. Such approaches can also provide a more robust linking in comparison to nearest-neighbor linking for nanoparticles that show pronounced directionality in their motion, e.g., for viruses that are actively transported along the plasma membrane or for biological nanoparticles moving on top of bilayers or within nanochannels under the action of a shear flow.[9,54]

Irrespective of the complexity of the linking algorithm used, the user typically has to define at least a distance threshold, above which a linking step is considered "unphysical" as the distance between the nanoparticle positions (in adjacent frames) is considered to be too large to be achievable within the available time period. This threshold is often chosen by visual inspection of the extracted nanoparticle trajectories or estimated based on assumptions of the investigated system. If the nanoparticles perform a predominantly random motion, we will show in Sec. IV C how this threshold can be extracted from experimental data.

III. ANALYSIS OF 2D SPT DATA

The overarching aim when tracking the motion of single nanoparticles is always to obtain information about certain nanoparticle properties. Analysis of the nanoparticle trajectory typically allows us to gain information about the type of the nanoparticle motion (random versus directed, normal versus anomalous diffusion, mobility within certain compartments), which will be the topic of Sec. III A and III B. Additional information, such as the hydrodynamic size of the nanoparticle, its loading with a certain compound, or its interaction strength with the underlying bilayer membrane, can also be extracted as illustrated in Secs. III B and III C.

As SPT provides information on single trajectories, all these analysis schemes can, in principle, be performed on the level of single nanoparticles, allowing us to extract the distribution of the property of interest within the nanoparticle ensemble probed. It should be stressed, however, that the value of a particular property can only be extracted with a certain accuracy and that the achievable accuracy can be very low for short trajectories. Hence, in SPT experiments that yield rather short nanoparticle trajectories, an analysis of the trajectories on the single nanoparticle level may be counterproductive, suggesting analysis schemes on the ensemble-averaged level.

Biointerphases
A Journal of Biomaterials and Biological Interfaces
TUTORIAL
avs.scitation.org/journal/bip

It is the scope of this section to introduce different single nanoparticle and ensemble-averaged analysis schemes, to give the limits in the achievable accuracies (if known), and to provide guidance when choosing between analysis schemes.

A. Random motion of nanoparticles

The most obvious property to extract from a single trajectory is the type of motion as nanoparticles can show different moving behaviors at biointerphases. In the absence of a net force, their motion is purely random, following either Brownian or anomalous diffusion,[16,55] while in the presence of a net force, a directed motion can superimpose on this diffusion, leading to complex motions combining deterministic and stochastic contributions.[50]

1. General aspects of diffusion measurements

In the absence of net forces, the nanoparticles are expected to perform a random motion [Fig. 4(a)], which can be quantified in terms of the distance between the start and end point and the average or maximum distance traveled from the start point.[56] For a random motion, in which the individual "steps" (frame-to-frame displacements) are not correlated but random events (Brownian motion), a mathematical treatment shows that the calculation of the mean square displacement (MSD) allows us to extract the diffusion coefficient D of this motion.[1,57] By definition, the MSD of a particular track $[x(t), y(t)]$ at a given lag time Δt is calculated by first calculating the square displacements of trajectory positions that are separated in time by Δt, e.g.,

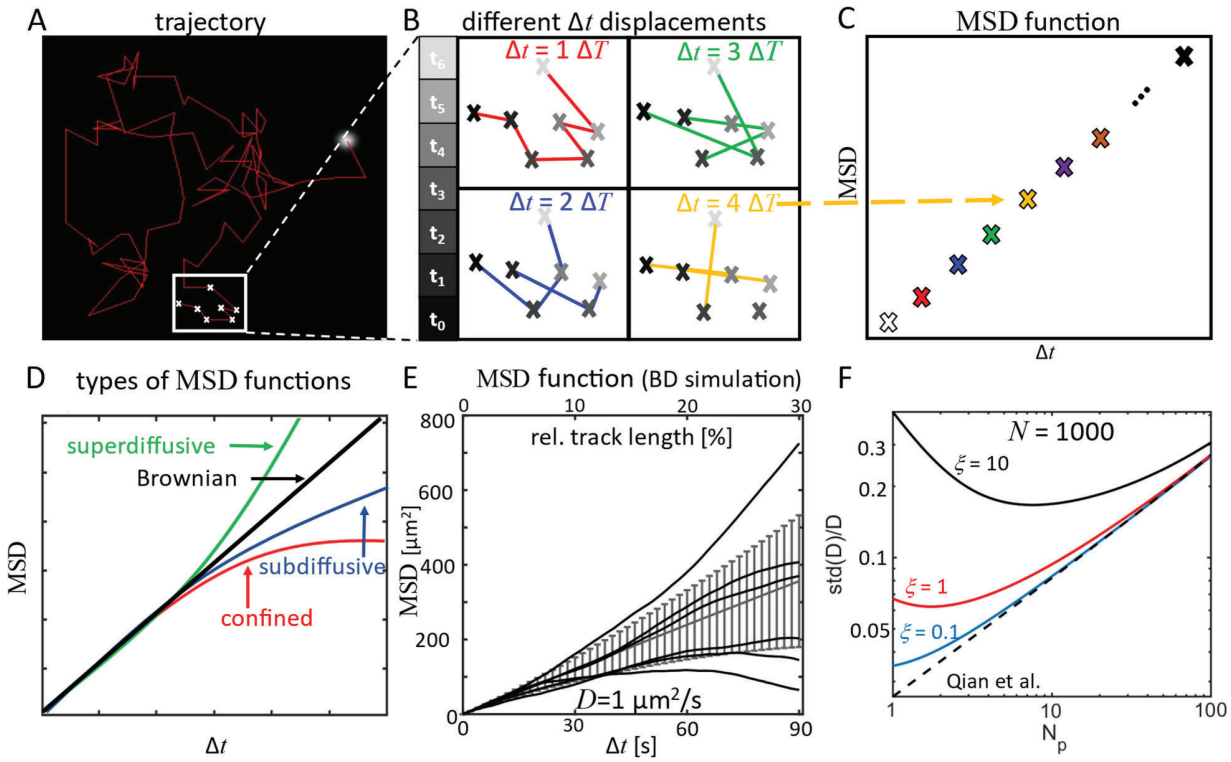

FIG. 4. MSD analysis of 2D SPT trajectories. Panel (a) shows a typical SPT trajectory (trace), for which the nanoparticle center positions have been marked for the first seven frames (white crosses). Panel (b) shows the extraction of displacements for four different lag times (Δt) ranging between $\Delta t = \Delta T$ and $\Delta t = 4\Delta T$ for the first seven frames ($t = 0$ to $t = 6\Delta T$). (c) For each lag time, several displacements can be extracted, allowing to calculate a MSD in dependence of the lag time Δt, yielding for this exemplary curve to a linear MSD(Δt) function. (d) Such linear MSD functions (black) are indicative for a random (Brownian) motion. In practice, deviations from this linear relationship can be observed. The corresponding nanoparticles are then denoted to be superdiffusive, subdiffusive, or confined nanoparticles (as indicated by the arrows). It should be noted, however, that resolving these different types of MSD functions requires sufficient measurement statistics. This is demonstrated in panel (e), which shows MSD functions that have been extracted from simulated SPT trajectories, i.e., for trajectories that have been generated by a Brownian dynamics simulation, treating the nanoparticles as perfect random walkers ($D = 1\ \mu m^2/s$, $N = 1500$ frames, $\Delta T = 0.2$ s). When analyzing MSD functions on the level of single trajectories (black lines), the mean square displacements can only be extracted within a certain accuracy [given by Eqs. (8) and (10) in the main text], which typically decreases with increasing lag time [see also panel (f)]. This is reflected by deviations from the linear increase, yielding apparent sub- or superdiffusive behavior for lag times exceeding 10% of the total trajectory length, although all simulated nanoparticles are perfect random walkers. Lag times exceeding this threshold can be extracted by switching the analysis from the single trajectory level (black traces) to the ensemble level [gray trace with errorbars indicating average value and standard deviation of the MSD(Δt) values of all simulated trajectories], restoring the linear increase in MSD(Δt). (f) Accuracy in the extraction of diffusion coefficients D for trajectories covering $N = 1000$ frames and using lag times up to $\Delta t_{max} = N_p \cdot \Delta T$. Shown are the results of Eq. (8) (dashed line) and Eq. (10) (solid lines) for different values of the normalized localization accuracy ξ.

Biointerphases
A Journal of Biomaterials and Biological Interfaces
TUTORIAL
avs.scitation.org/journal/bip

$SD = (x(t+\Delta t) - x(t))^2 + (y(t+\Delta t) - y(t))^2$, followed by calculating the average value of all obtained square displacements (SD). For an ideal 2D Brownian motion, the MSD function increases linearly with Δt according to

$$\mathrm{MSD}(\Delta t) = <\mathrm{SD}(\Delta t)> = 4 \cdot D \cdot \Delta t \tag{6}$$

allowing to extract the diffusion coefficient D from the slope of the MSD(Δt) function [Figs. 4(b) and 4(c)].[57,58] In practice, deviations from this linear behavior have been observed and a motion is denoted to follow anomalous diffusion if the MSD function shows a nonlinear dependence of Δt.[12] For example, motion confined within a certain area and subdiffusive motion create MSD functions that scale weaker than linear with Δt, while the presence of directed components in the motion create a scaling that is stronger than linear [Fig. 4(d)]. Hence, the inspection of the MSD function enables us to characterize the mode of motion of the corresponding object by inspection of the resulting MSD(Δt) curve.[10] The observation of anomalous diffusion of nanoparticles is intriguing and connected with the hope to learn more about the interactions experienced by the nanoparticle. It can be explained by obstruction and binding regarding the effect of initial conditions, energy barriers, and escape probabilities on lateral diffusion. Also, the diffusion can be dependent on the molecules position in the cell due to heterogeneities on the local cell diffusivities. This leads to effects like population splitting into fast and slow diffusers as well as trapping based on the initial position of the particles.[59]

We will now discuss how MSD functions can be extracted from single trajectories and which accuracy can be achieved when extracting diffusion coefficients from such MSD functions. In practice, MSD functions are often extracted by calculating the displacements of all data pairs that are separated by Δt,

$$\mathrm{MSD}(\Delta t) = \frac{1}{N - N_p} \cdot \sum_{i=1+N_p}^{N} (x(i) - x(i - N_p))^2 + (y(i) - y(i - N_p))^2, \tag{7}$$

a procedure that is often denoted as internal averaging.[57,58] In Eq. (7), the trajectory (covering N frames) has been parameterized via the frame number i and the lag time Δt is evaluated at multiples of time interval ΔT between two subsequent frames, $\Delta t = N_p \cdot \Delta T$. Hence, the parameter N_p corresponds to a lag "time" in terms of a frame displacement, with the lowest possible lag time, $\Delta t = \Delta T$, being achieved for $N_p = 1$ (and the largest one for $N_p = N$). This procedure allows for obtaining good estimates for the MSD function for short lag times ($N_p \ll N$), but suffers from the fact that for large lag times, the calculated displacements become statistically increasingly correlated, causing apparent deviations from Eq. (6) even for Brownian motion.[58] The accuracy in the determination of D in the absence of localization noise (i.e., for ultimate accuracy in the determination of the nanoparticle's center position, $\sigma^2_{\mathrm{pos}} \to 0$) is given by[57,58]

$$\frac{\mathrm{std}(D)}{D} = \sqrt{\frac{2}{3} \cdot \frac{N_p}{N - N_p}}. \tag{8}$$

In this equation, which is valid only for $N_p \ll N$, measurement error is expressed as the standard deviation of the extracted D values, std(D), i.e., 68% of the extracted D values will be located in the interval $D \pm \mathrm{std}(D)$. It gives the measurement error that is caused by the random nature of the motion and is, therefore, a lower limit for the accuracy in the extraction of D values, as additional errors, e.g., due to a finite localization accuracy, will always increase the measurement error. Furthermore, it shows the counterintuitive behavior that std(D) increases with N_p, i.e., that a linear fit to the MSD function has the highest accuracy for the shortest lag time possible ($N_p = 1 \to \Delta t = \Delta T$), which is a consequence of the fact that the square displacements observed for a Brownian motion exhibit a broad distribution according to probability distribution:[60]

$$p(\mathrm{SD}) = \frac{1}{\mathrm{MSD}} \cdot \exp\left(-\frac{\mathrm{SD}}{\mathrm{MSD}}\right) = \frac{1}{4 \cdot D \cdot \Delta t} \cdot \exp\left(-\frac{\mathrm{SD}}{4 \cdot D \cdot \Delta t}\right). \tag{9}$$

This is illustrated in Fig. 4(e) showing representative MSD functions of several trajectories that have been calculated using a Brownian dynamics simulation (i.e., for an ideal Brownian motion in the absence of localization error). Even though all trajectories have been calculated using the same diffusion coefficient of 1 μm^2/s, there is notable spread at lag times exceeding 30 s. This spread increases with increasing lag time, as indicated by the error bars in Fig. 4(e) and as expected by Eq. (8), showing that the highest accuracy is indeed obtained when using the smallest possible tag time. This figure also illustrates the fact that MSD functions extracted from single trajectories can deviate from the linear relationship given by Eq. (6) even for ideal Brownian motion, if too large lag times are used in the extraction of the MSD function.[58] Hence, some of the MSD functions in Fig. 4(e) apparently show sub- and superdiffusive behavior, despite the fact that the ideal Brownian motion was simulated. It is important to keep in mind that due to the (commonly used) internal averaging procedure, the extracted square displacements become statistically increasingly correlated at larger lag times, as noted by Saxton *et al.*,[58] so that the MSD values of a single trajectory do not randomly fluctuate around the true MSD value but rather form a smooth curve below or above the theoretically expected MSD curve. This is in fact a feature of the single trajectory resolution, as the linear dependence of Δt is regained if a sufficient number of these MSD functions is averaged [gray trace in Fig. 4(e)]. This example shows that it is not meaningful to use too large lag times in the calculation of MSD functions from single trajectories. In order to remain in the "linear" part of such MSD functions, the largest lag time, Δt_{max}, used in the analysis should not exceed 10% of the total trajectory time, $\Delta t_{\mathrm{max}} = 0.1 \cdot N \cdot \Delta T \to N_p \leq N/10$, which is of particular importance when probing nanoparticles showing truly anomalous diffusion. If lag times being larger than 10% of the total trajectory time have to be evaluated, it is necessary to analyze the data on the ensemble-averaged level in

Biointerphases
A Journal of Biomaterials and Biological Interfaces
TUTORIAL
avs.scitation.org/journal/bip

order to achieve sufficient measurement statistic at these large lag times.

Nevertheless, with respect to the measurement accuracy of D, Eq. (8) shows that in the absence of localization noise, there is no benefit in calculating the MSD at lag times exceeding ΔT, as this does not improve the accuracy in the determination of the square displacements but reduces the number of data pairs entering into the averaging process. This situation changes for finite localization accuracy, i.e., in the presence of a localization error σ_{pos}, the accuracy in D extraction reads for $N_p \leq K = N - N_p$

$$\frac{\text{std}(D)}{D} = \sqrt{\frac{1}{6 \cdot N_p \cdot K^2}(4N_p^2 \cdot K + 2K - N_p^3 + N_p) + \frac{1}{K} \cdot \left(2 \cdot \xi + \left(1 + \frac{1}{2}\left(1 - \frac{N_p}{K}\right)\right) \cdot \frac{\xi^2}{N_p^2}\right)}, \tag{10}$$

in which ξ denotes the ratio $\xi = \sigma_{\text{pos}}^2/(D \cdot \Delta T)$.[61,62] This equation contains Eq. (8) in the limit $\xi \to 0$ (i.e., negligible localization noise with respect to the mean square displacement observed between adjacent frames: $D \cdot \Delta T \gg \sigma_{\text{pos}}^2$) but also contains an additional contribution that increases with decreasing N_p, so that std(D) exhibits a minimum value at a certain lag time if the motion of the nanoparticle between subsequent frames is comparable or below the localization accuracy. In this case, the MSD function should be calculated at least up to this lag time [Fig. 4(f)] and the fit to the MSD function should be extended by an offset parameter in order to correctly account for the errors done in the MSD calculation due to finite localization accuracy,[63]

$$\text{MSD}(\Delta t) = 4 \cdot D \cdot \Delta t + 4 \cdot \sigma_{\text{pos}}^2. \tag{11}$$

These considerations show that the accuracy in the extraction of D is mainly limited by a finite length of trajectories and by the localization error. It has been shown that MLEs and (optimized) least squares fits are able to approach the theoretical limits given in Eqs. (8) and (10),[62] and hence that the achievable accuracy can, in principle, be estimated based on the knowledge of the diffusion coefficient D and experimental parameters like frame rate $1/\Delta T$ and localization noise σ_{pos}, allowing to optimize the experimental settings and the analysis parameters. In general, high accuracies can be achieved if the nanoparticle can be tracked over a long period of time ($N \gg N_p$), while short tracks (e.g., due to bleaching or transient interactions with the interface) generally lead to lower accuracies.

If it is not possible to obtain sufficiently long trajectories to achieve the desired accuracy in D (e.g., due to experimental restrictions such as bleaching), it is often necessary to switch the analysis from the single trajectory to the ensemble level. In this way, the accuracy as predicted by Eqs. (8) and (10) is improved as the averaging process includes a larger amount of displacement data, but the capability of analyzing the motion of a particular nanoparticle of interest is lost. This is always of advantage if the tracked nanoparticles are very similar in their D values, i.e., if only a single or very few subpopulations are present in the D distribution, while unambiguous analysis of very heterogeneous distributions is typically very challenging on the ensemble level. Such ensemble approaches include the extraction of SD or jump distance distributions from all tracks,[16,64] which allow us to extract the underlying diffusion coefficient by fitting the theoretically expected distributions to the measured ones, leading to information about the D distribution of the ensemble. More sophisticated approaches use statistical measures on the derived distributions, such as the application of Bayesian approaches or hidden Markov models or combinations of both.[65–67] These approaches have been shown to be very powerful tools, in particular, for very short trajectories, for which a conventional MSD analysis has a very low accuracy. It has been demonstrated that such sophisticated modeling approaches allow, for example, to combine the information from thousands of short single-molecule trajectories to identify and quantify diffusive states and the state transition rates. Statistical criteria can be used to determine the underlying model parameters and the number of diffusive states from the observed data, i.e., to identify the minimum number of subpopulations needed to explain the extracted displacement distributions.[67]

Irrespective of D value distributions being extracted on the single nanoparticle or ensemble level, it has been shown that motion blurring of the nanoparticle spot in the image creates a bias in the analysis of diffusion coefficients.[68] This motion blurring effect is caused by the finite camera integration time ΔT_{exp}, during which the nanoparticles are still able to move, leading to a spatial average of their intensity profiles during camera exposure. This bias has been comprehensively analyzed by MSD-based D value extractions and can be characterized by a motion blur coefficient R, which considers the temporal illumination profile of the camera during the imaging process.[68] For homogeneous illumination during an exposure period $\Delta T_{\text{exp}} \leq \Delta T$, R is given by

$$R = \Delta T_{\text{exp}}/(6 \cdot \Delta T), \tag{12}$$

and is therefore 1/6 for full exposure ($\Delta T_{\text{exp}} = \Delta T$). The bias in the D extraction can then be expressed by

$$\text{MSD}(\Delta t = N_p \cdot \Delta T) = 4 \cdot D \cdot \Delta T \cdot (N_p - 2 \cdot R) + 4 \cdot \sigma_{\text{pos}}^2. \tag{13}$$

Hence, when using full exposure ($\Delta T_{\text{exp}} = \Delta T$) and the lowest possible lag time ($N_p = 1$), which are typical parameters when tracking dim and fast moving nanoparticles (e.g., single lipids or membrane proteins), the slope of the MSD function becomes, due to motional blur, underestimated by a factor of 2/3.

Biointerphases
A Journal of Biomaterials and Biological Interfaces
TUTORIAL
avs.scitation.org/journal/bip

2. Time-resolved diffusion coefficients

In processes in which the diffusion coefficient D can vary over time, a time-resolved extraction of D is often very desirable, yielding D as a function of the measurement time t. This can be achieved, in principle, by an MSD subtrajectory analysis, in which only a fraction of the entire trajectory is used for the MSD analysis, yielding a D value for the part of the trajectory analyzed, and the time-resolved D value is obtained by shifting this fraction along the entire trajectory. This can be achieved, for example, using a rolling window approach, which regards only N_W successional positions of the nanoparticle trajectory that start at the frame N_a and yield a D value at the time $(N_a + N_W/2) \cdot \Delta T$.[50,69] $D(t)$ can then be extracted by applying this procedure to N_a values ranging between 1 and $N - N_W$. Knowing the experimental parameters, Eqs. (8) and (10) can be used to estimate the achievable accuracy in extracting D and hence to identify transitions between different mobility states (i.e., distinct D values) if the observed change in $D(t)$ is significantly larger than the expected fluctuation in D.[69] Furthermore, if the difference in D values (of certain mobility states) are known, Eqs. (8) and (10) can also be used to determine the lower limit in N_W, i.e., the minimum size of the window that is needed to resolve transitions between mobility states in a single trajectory.

It is apparent that this type of analysis is only reasonable for $N \gg N_W$ so that the extraction of time-resolved diffusion coefficients $D(t)$ typically requires long trajectories. This has been successfully demonstrated for nanoparticles that are permanently (yet mobile) linked to bionanointerfaces[50,69] or when using microscopy approaches, such as iSCAT, that offer acquisition rates on the order of multiple 100 kHz.[6,69] These studies have demonstrated that monitoring temporal changes in the motion of the nanoparticle allows us to extract information about the local interaction of the nanoparticle with its environment.[22]

In general, the diffusion coefficient of a nanoparticle depends on the size of its interaction area with the membrane and the fluidity of the membrane.[70–72] If the interaction area is kept constant, for example, by probing the motion of single lipids or membrane proteins within the bilayer, the nanoparticle acts as a probe that reports local changes in the fluidity of the surrounding bilayer. This has been used, for example, to map the spatial distribution of lipid domains in bilayers exhibiting coexistence of different lipid phases.[6] On the other hand, when using homogenous, fluid-phase bilayers, changes in the nanoparticle's diffusion coefficient are indicative of changes in its interaction with the membrane.[73] This has been demonstrated using nanoparticles that are able to form multiple interactions in parallel (so-called multivalent interaction) to lipids within a supported lipid bilayer, for which the diffusion coefficient of the nanoparticle–lipid complex decreases with increasing number of bound lipids.[69] It should be noted, however, that for suspended bilayers, a much weaker dependence of the number of bound lipids on the diffusion coefficient is expected according to the Saffman–Delbrück model, so that mobility-based quantifications of binding stoichiometries become more challenging.[70,71]

Furthermore, the presence of localized interactions can manifest itself by transient sticking or spatial confinement of nanoparticles, allowing to probe such interactions by monitoring changes in the nanoparticle diffusion profile.[22] Examples for such localized interactions include interleaflet interactions occurring between lipids of the upper and lower leaflet of the bilayer (e.g., pinning) or confinement of membrane proteins in small membrane patches according to the picket fences model of the plasma membrane.[15,17] Different statistical means have been introduced in the past in order to determine whether certain parts of a trajectory display a statically significant change in the diffusion and in the type of motion (normal, anomalous, and confined).[74] Even more sophisticated approaches compare the experimental data to simulations (e.g., Monte Carlo-based) of the expected diffusive behavior, in order to arrive at a model that is as complex as needed to properly describe the experimental data. Such approaches have been used to analyze particle movement in plasma membranes regarding Brownian or anomalous diffusion and transient binding to slowly diffusing structures even if no analytical theory is predefined.[75]

B. Directional motions

The presence of a net force acting on nanoparticles will typically manifest itself by the generation of a drift component in the nanoparticle motion, leading to a directed nanoparticle motion.[50] In general, this directed motion will superimpose with the random nanoparticle motion (due to diffusion) leading to complex motions containing stochastic (diffusion) and deterministic (drift) contributions. Although directional motions are often observed, for example, in nanoparticle transport into and within cells, an analysis of this type of motion has typically been limited to rather artificial systems, which had, in comparison to experiments on live cells, the advantage that the origin of the acting force is unambiguously known. In these measurements, nanoparticles have been linked to fluid-phase lipid bilayers using self-assembly of DNA constructs, receptor–ligand interactions, or electrostatic forces, and a directed component in the motion of the bilayer-linked nanoparticles has been induced by the application of a shear flow (generating a hydrodynamic shear force), electrophoretic effects (using charged nanoparticles), or magnetic forces (using magnetic nanoparticles).[50,76–78]

For nanoparticles that show Brownian diffusion while being bilayer-linked, the resulting motion is the sum of the random (diffusion-induced) and deterministic (force-induced) components, and this complex motion can be unambiguously decomposed into its random and deterministic components again.[50] Interestingly, a theoretical treatment of the problem reveals that both components are linked by the Einstein–Smoluchowski equation, stating that drift velocity v, achieved by the nanoparticle upon action of the force F, and nanoparticle's diffusion coefficient D are different measures of the nanoparticle mobility μ, which can be calculated either using v,

$$\mu = v/F, \tag{14}$$

or using D

$$\mu = D/(k_B \cdot T), \tag{15}$$

in which k_B denotes Boltzmann's constant and T is the absolute temperature.[79] As both properties, D and v, can be independently

Biointerphases
A Journal of Biomaterials and Biological Interfaces
TUTORIAL
avs.scitation.org/journal/bip

extracted from a single nanoparticle trajectory, application of the ratio of Eqs. (14) and (15) yields

$$F = k_B \cdot T \cdot v/D, \tag{16}$$

and therefore allows us to unambiguously extract the force acting on any tracked nanoparticle.[50] This is a very fundamental equation and shows that in principle the trajectory is already sufficient to determine the acting force, i.e., further knowledge about the microscopic details of the nanoparticle is not necessary to extract this force. In order to relate the measured force to a particular nanoparticle property, knowledge of the force generating process is necessary. For example, if a shear flow generates the directed motion of the nanoparticles, the hydrodynamic size of the nanoparticles can be extracted from the measured force, provided that the flow conditions are known. This has been achieved, e.g., by hydrodynamic modeling or calibration measurements (with nanoparticles of well-defined sizes), allowing us to determine the hydrodynamic size of a tracked nanoparticle with accuracies down to a few nanometers.[50,77] Nevertheless, as the underlying equations are very fundamental, this type of analysis is not restricted to hydrodynamic shear forces, but can be applied to any type of force acting on nanoparticles, provided that the linkage strategy used ensures nanoparticle mobility.

C. Interaction rates: Equilibrium fluctuation analysis

Besides measuring mobility-related properties, SPT trajectories also allows for extracting information about how long a particular nanoparticle remains bound to the interface (its residence time) and how many nanoparticles bind to the interface within a certain period of time. This capability is exploited in the so-called equilibrium fluctuation analysis, in which the transient interaction of nanoparticles with an interface is monitored.[80,81] Using interface-sensitive microscopy approaches, such as TIRF microscopy, it is possible to image only those nanoparticles that are in very close vicinity to the interface (typically <100–200 nm), while unbound nanoparticles (dissolved in the bulk phase) are not recorded in the images.[33] This allows for probing the fraction of nanoparticles that are bound to the interface under equilibrium conditions, i.e., under conditions at which the detachment of interface-bound nanoparticles is in equilibrium with the attachment of unbound nanoparticles to the interface.[24,25]

Both processes, i.e., the detachment of interface-bound nanoparticles and the attachment of unbound nanoparticles, can be independently quantified from SPT trajectories, yielding information about the nanoparticle attachment rate and the distribution of nanoparticles' residence times (see Ref. 25 for details of the analysis). For monovalent interactions, the attachment rate is proportional to the on-rate of the interaction and, in principle, the on-rate can be determined from such measurement, provided that the receptor density at the interface is known.[25] Furthermore, if the dissociation of a monovalent interaction is a random process, it can be shown that the residence time distribution follows an exponential decay, the decay rate of which is the off-rate of the interaction.[80] This shows that for monovalent interactions, the off-rate is directly extractable from the SPT data, while determination of the on-rate requires additional knowledge such as the bulk nanoparticle concentration and receptor density at the interface. This approach has been successfully applied to various interactions, for example, the hybridization-dehybridization equilibrium of DNA or the interaction of G protein-coupled receptors (GPCRs) with their ligands.[80,82]

For multivalent interactions, however, also the extraction of off-rates becomes complex, as the off-rate typically shows a complex dependence of the number of single interactions (=valency) acting in parallel to form the multivalent interaction.[24–26] Hence, the nanoparticle residence time strongly depends on the valency of the particular interaction, typically generating broad distributions of the measured residence times, which cannot be directly translated into an off-rate. Recently, it has been shown for nanoparticles interacting with lipid-bound receptors/attachment factor embedded in fluid-phase supported lipid bilayers that restricting the extraction of residence time distributions to nanoparticles of similar average diffusion coefficient yielded residence time distribution showing an exponential decay, allowing to extract nanoparticle off-rates in dependence of the nanoparticle diffusion coefficient.[26] As the nanoparticle mobility decreases with increasing linking valency (i.e., number of bound lipids), this D-dependent off-rate can, in principle, be translated into a valency-dependent off-rate, provided that the relationship connecting diffusion coefficient and valency is known.[69]

These examples demonstrate that probing the equilibrium between interface-bound and unbound nanoparticles with single nanoparticle resolution is very beneficial when investigating very weak interactions (dissociation constants $K_D \geq 1\,\mu$M), such as carbohydrate-carbohydrate interactions or carbohydrate-protein interactions (e.g., virus-receptor interaction), as these interactions are often only transiently formed and challenging to quantify using ensemble-averaging or bulk approaches.[26,83]

D. Further examples

SPT has, in addition to the above mentioned examples, been used to extract a multitude of different information about the tracked nanoparticles. Often, the (fluorescence/scattering) intensity of the nanoparticles is used as additional readout, yielding information of certain nanoparticle properties (depending on the particular measurement setting used). If the intensity is created by a scattering process, it contains information about the refractive index contrast (arising between nanoparticle and its surrounding) but also about nanoparticle size or distance to the interface.[39,51] A similar situation is observed when measuring nanoparticle fluorescence intensities, which can contain information about the nanoparticle size or the amount of a particular component within the nanoparticle,[50] depending on if the entire particle or only a particular component has been labeled by the dye. Using different dyes for different nanoparticle species allows us to probe interactions between these species based on a colocalization analysis, which has proved to be a very powerful tool to probe interactions between membrane proteins in live cells.[84]

IV. REFINEMENT AND OPTIMIZATION OF 2D SPT EXPERIMENTS

After introducing into the instrumentation needed for conducting 2D SPT experiments and discussing which quantities can

Biointerphases
A Journal of Biomaterials and Biological Interfaces
TUTORIAL
avs.scitation.org/journal/bip

be extracted (with which accuracy), we will now discuss how parameters related to the measurement or analysis of SPT experiments can be refined in order to improve the data quality and how the quality of SPT data can be quantitatively assessed.

A. General considerations

In general, the properties of the sample of interest will typically determine which parameter values ("settings") have to be chosen for the measurement and the analysis of the SPT data, in order to achieve the desired accuracies. In this context, it is reasonable to classify nanoparticles according to their brightness (e.g., bright nanoparticles yielding large SNRs versus dim ones yielding low SNRs), their mobility (e.g., fast moving/diffusing nanoparticles versus immobile ones), and their mode of binding (e.g., firmly attached nanoparticles versus transiently binding ones). Furthermore, it is important to specify which nanoparticle property is to be extracted. Some nanoparticle properties can, in principle, be extracted from a single data point (e.g., the nanoparticle intensity), though the accuracy of this process will generally increase with longer trajectories. However, most parameters will require that the length of the trajectory exceeds a certain threshold value in order to achieve a specified accuracy in the extraction of this parameter.

This holds true in particular for the extraction of diffusion-related properties, such as the diffusion coefficient, the type of diffusion, etc., as the randomness of the motion creates broad distributions requiring a significant amount of data points in order to achieve reasonable accuracies. For diffusion coefficients, Eqs. (8) and (10) can be used to estimate this minimum length of the trajectories in dependence of the required accuracy. If time-resolved diffusion coefficients are to be extracted, this minimum length corresponds to the size of the window used to extract the D value, so that the desired length of the trajectory needs to be much larger.

For extraction of the type of diffusion (Brownian versus anomalous) on the level of single trajectories, it was shown in Sec. III A 1 that the lag time used in the calculation of the MSD function (via the internal averaging procedure) should not exceed 10% of the total duration of the trajectory, as otherwise notable deviations from the linear increase can be observed even for Brownian diffusion. As the extracted MSD function needs to provide at least ~5 data points to allow for a meaningful fit of normal or anomalous diffusion models, it is apparent that the analyzed trajectories should cover at least ~50 frames for such type of analysis.

If the nanoparticle shows transient binding to the interface or if the property of interest changes within a certain period of time Δt_{lim}, this minimum length of the trajectory, N_{min}, has to be achieved within Δt_{lim}, which formulates a constraint on the minimum acquisition rate of the measurement: $1/\Delta T > N_{\mathrm{min}}/\Delta t_{\mathrm{lim}}$.

B. Imaging settings

If this acquisition rate $N_{\mathrm{min}}/\Delta t_{\mathrm{lim}}$ can be achieved depends strongly on the brightness of the nanoparticles. This rate also introduces a constraint on the exposure/dwell time of the detector, which cannot exceed $\Delta T_{\mathrm{exp}} \leq \Delta t_{\mathrm{lim}}/N_{\mathrm{min}}$ in order to allow for the desired acquisition rate. The measurement can be performed at this rate, if the nanoparticle intensity, emitted during the time span $\Delta t_{\mathrm{lim}}/N_{\mathrm{min}}$, is sufficiently large to achieve reasonable SNRs. Large nanoparticles, such as liposomes and certain viruses, can carry large amount of dyes and can often be made as bright as necessary, so that the acquisition rate $N_{\mathrm{min}}/\Delta t_{\mathrm{lim}}$ becomes rather limited by the speed of the camera/detector than the nanoparticle brightness.

Smaller structures, such as single proteins, typically carry only a few or even a single dye and are much dimmer than large nanoparticles. In this case, a balance between the desired acquisition rate $N_{\mathrm{min}}/\Delta t_{\mathrm{lim}}$ and the achieved SNR has to be found, as increasing the acquisition rate decreases the achieved SNR (due to the involved decrease in exposure/dwell time). The SNR has, however, a strong impact on the localization accuracy [cf. Eqs. (4) and (5)] and the reliability of the linking process. Using a high acquisition rate may, in principle, provide the desired temporal resolution but will likely result in poor SNRs for dim nanoparticles and thus a poor quality of the SPT data.

As the recorded nanoparticle intensity depends on several, user-accessible parameters (such as the magnification and numerical aperture of the used objective, the excitation intensity applied to the sample, and the exposure time of the camera/the dwell time of the detector), there are several options to balance the acquisition rate and SNR. An obvious option is to increase the excitation intensity applied to the sample. This will also increase the bleaching rate of the dye, thus reducing the time span in which the nanoparticles can be tracked. It is common practice to choose, if possible, an excitation intensity at which the bleaching is weak on the time scales needed to perform the experiment.

For camera-based systems, the SNR can be improved by a hardware-based reduction of the pixel resolution (binning). In this process, the physical size of the pixels is increased by pooling the readout values of neighboring pixels. In a 2×2 binning, for example, four pixels (two horizontal and two vertical ones) are grouped together, so that the pixel size is increased by a factor of 2 and total number of pixels of the sensor is reduced by a factor of 4. This procedure has the advantage that the binned pixel now contains the sum of the intensity of four pixels, while the intensity noise shows a much weaker increase, so that the SNR typically increases. EMCCD-based cameras may achieve a better improvement than sCMOS-based cameras due to differences in the implementation of the binning process. This procedure may allow us to approach the desired acquisition rate, as it increases the SNR without increasing the exposure time. Nevertheless, the effective pixel size increases with binning, which, according to Eqs. (4) and (5), decreases the localization accuracy. This is compensated by the increase in SNR to a certain extent, but its impact on the data can only be assessed by evaluating the SPT data.

C. Choosing appropriate distance cutoff values and particle densities

Nearest-neighbor linking schemes typically require to define a distance cutoff value R_{max} in order to decide, above which distance a linking step is considered to be too large. This cutoff value, therefore, prevents that independent trajectories become connected by the linking algorithm, which is otherwise very likely to occur in samples in which the nanoparticle density changes over time, and is thus an important parameter of the analysis. Choosing a too

Biointerphases
A Journal of Biomaterials and Biological Interfaces
TUTORIAL
avs.scitation.org/journal/bip

small cutoff value will segment the trajectories, causing an underestimation of the diffusion coefficient, while a too large value will merge independent trajectories, introducing an overestimation of the diffusion coefficient.

This distance cutoff value R_{max} is often determined by visual inspection of the tracking result, i.e., linking is performed by an estimated cutoff value, followed by visual comparison of the extracted trajectories with the measured tracking movie and, if necessary, a refinement of the cutoff value until good agreement is reached. It should be noted that the obtained trajectories should always be compared with the tracking movie, as it is often challenging to judge on the quality of the analysis by inspecting only the extracted trajectories. Nevertheless, this procedure depends on a visual judgment of the user and choosing the distance cutoff based on a statistical measure would be desirable. Wieser and Schütz[52] introduced, for example, a method, in which this cutoff value is varied within a certain range and the nanoparticle diffusion coefficients are determined in dependence of the cutoff value. They observed for relatively low cutoff values that D increases with increasing cutoff value, until a saturation of D is observed after exceeding a threshold value for the distance cutoff. Wieser and Schütz,[52] therefore, suggest to use a cutoff value in the analysis, at which D saturates.

Motivated by these considerations, we would like to suggest a refined approach to determine suitable values for the distance cutoff R_{max}. The behavior observed by Wieser and Schütz[52] can be well understood, if the distribution of the square displacements is taken into account, which decays exponentially according to Eq. (9). Hence, choosing a too small distance cutoff will reject all linking steps having large square displacements and therefore distort this distribution, leading to an underestimation of the associated D value,

$$\frac{D_{meas}}{D} = \frac{[1-\exp(-\chi)\cdot(1+\chi)]}{1-\exp(-\chi)} \quad \text{with} \quad \chi = \frac{R_{max}^2}{4\cdot D\cdot \Delta T}, \tag{17}$$

in which we defined the parameter χ as the ratio of the square of the distance cutoff value R_{max} and the nanoparticle MSD observed between subsequent frames. As pointed out by Wieser and Schütz, in order to have a negligible bias (underestimation) of D, R_{max} should exceed $\sqrt{4\cdot D\cdot \Delta T}$ by a factor of ~2.5, i.e., χ should be larger than ~6.

If such large cutoff value can be achieved depends on the SPT data and, hence, reasonable values for R_{max} should be extracted from the experiment. Interestingly, due to the exponential decay, large square displacements are much less often observed than small ones so that a good approximation of the square displacement distribution can be directly extracted from the SPT data even when using unphysically large R_{max} values. This is demonstrated in Fig. 5, in which SPT movies have been generated by Brownian dynamics simulations using well-defined values for the nanoparticle diffusion coefficients and densities (as indicated in the figures), followed by an SPT analysis using a very high distance cutoff ($R_{max} \sim 200$ pixels). Afterward, the distributions of the square displacements of all linking steps have been generated, showing in general an exponential decay as expected from Eq. (9). However, such distributions often show a tail at large square displacements, which indicates observation frequencies of square displacements that are much larger than expected based on Eq. (9). A comparison of the true (BD simulated) trajectories with the one extracted from the linking [Figs. 5(a)–5(c), bottom] allows for extracting the fraction of wrongly linked steps and indicates that these events are mainly created by linking errors, being introduced by using a too large distance cutoff.

Hence, an extracted square displacements distribution can typically be divided into a region, which decays exponentially and a tail distribution that shows only a weak dependence of the square displacement. We observed this feature not only for synthetic SPT data but, in general, when extracting square displacement distributions from SPT experiments. As the tail distribution is mainly created by linking errors [which is mathematically indicated by the deviation from Eq. (9) and demonstrated in Fig. 5 based on a comparison of known and extracted trajectories], there is no point in using a distance cutoff value being located within the tail distribution. Hence, the square displacement at which the transition from the exponential decay into the tail distribution occurs gives the largest reasonable value for the distance cutoff R_{max} (=square root of the square displacement) that can be used in the linking process, providing a statistical mean to extract the distance cutoff value from SPT data. This procedure works very well for nanoparticle ensembles having narrow D value distributions, while broad D distributions create complex square displacement distributions, in which it can be challenging to resolve the transition from the exponential decay into the tail distribution. In such a case, it is necessary to validate the choice of the distance cutoff value by visual comparison as described above.

In addition to this, an inspection of the square displacement distribution also allows us to evaluate the quality of the linking process. In Fig. 5(a), the frequency of the tail distribution is very low in comparison to the exponential decay, so that the number of linking steps lost when applying the refined distance cutoff value is negligible (i.e., segmentation of the trajectories is practically absent). The situation is different in Fig. 5(b), in which the frequency of the tail distribution is comparable to that of the exponential decay (squares and triangles). Such pronounced tail distributions are observed in SPT experiments, for example, if the nanoparticle density is too large (the threshold value of which depends on the nanoparticle mobility) or if there is a notable number of falsely detected nanoparticles, i.e., of background pixels having intensities above the detection threshold due to noise. In this case, a notable fraction of linking steps will be lost when applying the refined distance cutoff value, leading to a notable segmentation of the trajectories.

Interestingly, the impact of this segmentation can be directly extracted from the square displacement distribution. In Fig. 5(b), the green trace (triangles) starts to deviate from the exponential decay at a relative frequency of 2% [$\log_{10}(2\%) = -1.7$], which corresponds to a χ value of $\chi = -\log_e(2\%) = 3.9$. Inserting this value into Eq. (17) indicates that the extracted D value will be underestimated by a factor of 0.92. This is a low bias but indicates that the exponentially decay in the square displacement distribution should cover at least ~2 orders of magnitude, as elsewise a notable bias in the extraction of D will be experienced. In comparison, the red

Biointerphases
A Journal of Biomaterials and Biological Interfaces
TUTORIAL
avs.scitation.org/journal/bip

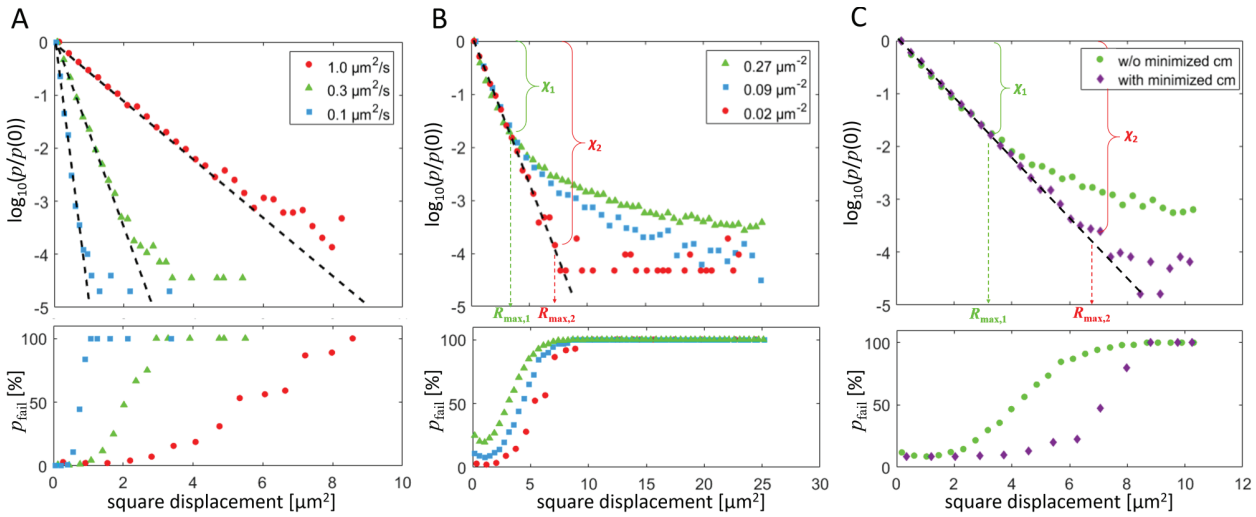

FIG. 5. Top row shows probability distributions $p(SD)$, indicating the probability to observe a step having a certain SD between subsequent frames. These square displacement distributions were extracted from simulated nanoparticles trajectories exhibiting a well-defined Brownian motion (BD simulation; $\Delta T = 0.2$ s) and were normalized to the probability at zero square displacement, $p(0)$. Comparing the simulated trajectories with the ones extracted using SPT allows us to calculate the fraction of errors done during the linking process and hence the probability that two nanoparticles are wrongly linked during the SPT analysis. These probabilities are shown in the bottom row in terms of the percentage $p_{fail}(SD)$ of wrong links in dependence of the square displacement. The distributions have been calculated (a) for three different D values [as indicated in panel (a); nanoparticle density = 0.02 μm^{-2}], (b) for different nanoparticle densities [as indicated in panel (b); $D = 1\,\mu m^2/s$], and (c) using two different linking algorithms, either relying only on the nearest-neighbor distance [full circles in (c)] or using additional statistical means during the linking process [minimization of a cost matrix according to Ref. 85; implemented in the trackmate (Ref. 86) plugin of IMAGEJ (Ref. 85); diamonds in panel (c)]. The $p(SD)$ distributions typically show an exponential decay (dashed line), the decay length of which is, according to Eq. (9), the mean square displacement observed between subsequent frames. Nevertheless, all $p(SD)$ distributions exhibit a tail distribution at larger SD values, which deviates from the exponential decay and is associated with linking errors (as evidenced by the increase in the percentage of wrong links, p_{fail}). The parameter χ (defined in Sec. IV C) can be directly extracted from these semilogarithmic plots by taking the distance indicated by the brackets in panel (b) and (c) multiplied by the factor 2.3 [$= \log_e(10)$] in order to account for the base 10 used in the semilogarithmic plots.

trace (full circles) in Fig. 5(b) shows the result of the same simulation, but using a lower nanoparticle density, and starts to deviate from the exponential decay at a relative frequency of 10^{-4}. This corresponds to $\chi = -\log_e(10^{-4}) = 9.2$, so that the bias in D due to segmentation (<1%) can be completely neglected.

This example shows that inspecting the square displacement distribution allows us to directly evaluate, to which extent the linking process will be able to reconstruct the Brownian motion and if processes are present that disturb this reconstruction. If the tail distribution is caused by intensity noise, its contribution can be reduced by choosing a larger intensity threshold (if this does not exclude the dim nanoparticles from the analysis), by application of spatial filters prior to the detection process, or by software-based binning. If the tail distribution is caused by a too large nanoparticle density, linking algorithms should be used that employ additional statistical means (see Sec. III C 3), which tend to perform better at higher densities than algorithms that rely only on the nanoparticle distance between subsequent frames [Fig. 5(c)]. Nevertheless, the same SPT experiment would yield a higher linking quality, if it could be repeated at a reduced nanoparticle density. This option is, however, not always possible.

If the nanoparticle density can be modified, it should be noted that its optimal value depends on the nanoparticle mobility. Jaqaman and Danuser suggested, for example, that in order for the nearest-neighbor linking scheme to perform well, the ratio of the average frame-to-frame displacement to the average nearest-neighbor distance within the frame should be much lower than 0.5. A similar value of ~0.3 is indicated by Wieser *et al.*,[52,87] which suggests to have only a single nanoparticle within the area $\sim 40 \cdot D \cdot \Delta T$. Hence, when tracking nanoparticles with $D = 1\,\mu m^2/s$ at an acquisition rate of $1/\Delta T = 10$ fps, this results in a surface coverage of having one nanoparticle each of $4\,\mu m^2$. If it is necessary to extract very long trajectories, this area should be even larger, as long trajectories always have a certain number of very large steps [cf. Eq. (8)], the linking of which can become challenging if their value approaches the average nearest-neighbor distance.

V. CONCLUSION

Over the past few decades, developments in instrumentation and data analysis schemes have allowed us to extend the range of applicability of SPT and to increase the number of properties that can be extracted from SPT-derived trajectories. Nevertheless, a central aspect in most SPT experiments is the extraction of mobility-related properties, such as the type of motion or diffusion coefficient for random particle motion, as these properties often contain information about local interactions experienced by the tracked particle. Such information can be extracted from SPT

Biointerphases
A Journal of Biomaterials and Biological Interfaces
TUTORIAL
avs.scitation.org/journal/bip

trajectories only within a certain accuracy, the lower limit of which has been theoretically derived for several properties such as the accuracy in localizing the center position of a particle and the accuracy in extracting diffusion coefficients or drift velocities from SPT trajectories. The aim of this tutorial is to provide a comprehensive overview of such limits, forming a basis for the refinement of parameters used in measurement and analysis of SPT experiments, and to show some of the intrinsic limitations when extracting mobility-related issues which, if unaccounted for, lead to misinterpretation of SPT data. It is also shown that inspection of the square displacement distribution yields information about the maximum distance that should be used in the linking process (connecting particles across subsequent frames), which is a crucial parameter in an SPT analysis. All this information can be used to evaluate the quality of the SPT data and to decide if parameters of the measurement or analysis should be refined.

ACKNOWLEDGMENTS

This work was funded by the Focus Area Nanoscale (Freie Universität Berlin) and the German Science Foundation (Project No. BL1514/1 and project A6 within the No. CRC 765).

The authors declare no competing financial interest.

REFERENCES

[1]Robert Brown, Philos. Mag. **4**, 161 (1828).
[2]A. Yildiz, J. N. Forkey, S. A. McKinney, T. Ha, Y. E. Goldman, and P. R. Selvin, Science **300**, 2061 (2003).
[3]P. J. Keller, A. D. Schmidt, J. Wittbrodt, and E. H. K. Stelzer, Science **322**, 1065 (2008).
[4]T. Klein, S. Proppert, and M. Sauer, Histochem. Cell Biol. **141**, 561 (2014).
[5]G. Young *et al.*, Science **360**, 423 (2018).
[6]H. M. Wu, Y. H. Lin, T. C. Yen, and C. L. Hsieh, Sci. Rep. **6**, 20542 (2016).
[7]L. Schermelleh, A. Ferrand, T. Huser, C. Eggeling, M. Sauer, O. Biehlmaier, and G. P. C. Drummen, Nat. Cell Biol. **21**, 72 (2019).
[8]S. Even-Ram and K. M. Yamada, Curr. Opin. Cell Biol. **17**, 524 (2005).
[9]N. Chenouard *et al.*, Nat. Methods **11**, 281 (2014).
[10]M. J. Saxton and K. Jacobson, Annu. Rev. Biophys. Biomol. **26**, 373 (1997).
[11]N. Ruthardt, D. C. Lamb, and C. Bräuchle, Mol. Ther. **19**, 1199 (2011).
[12]C. Manzo and M. F. Garcia-Parajo, Rep. Prog. Phys. **78**, 124601 (2015).
[13]H. Shen, L. J. Tauzin, R. Baiyasi, W. Wang, N. Moringo, B. Shuang, and C. F. Landes, Chem. Rev. **117**, 7331 (2017).
[14]A. Small and S. Stahlheber, Nat. Methods **11**, 267 (2014).
[15]K. M. Spillane, J. Ortega-Arroyo, G. de Wit, C. Eggeling, H. Ewers, M. I. Wallace, and P. Kukura, Nano Lett. **14**, 5390 (2014).
[16]G. J. Schütz, H. Schindler, and T. Schmidt, Biophys. J. **73**, 1073 (1997).
[17]C. Dietrich, B. Yang, T. Fujiwara, A. Kusumi, and K. Jacobson, Biophys. J. **82**, 274 (2002).
[18]M. J. Pittet and R. Weissleder, Cell **147**, 983 (2011).
[19]A. Gahlmann and W. E. Moerner, Nat. Rev. Microbiol. **12**, 9 (2014).
[20]L. Cognet, C. Leduc, and B. Lounis, Curr. Opin. Chem. Biol. **20**, 78 (2014).
[21]M. Weber and J. Huisken, Curr. Opin. Genet. Dev. **21**, 566 (2011).
[22]R. W. Taylor, R. G. Mahmoodabadi, V. Rauschenberger, A. Giessl, A. Schambony, and V. Sandoghdar, Nat. Photonics **13**, 480 (2019).
[23]J. D. Knight, M. G. Lerner, J. G. Marcano-Velázquez, R. W. Pastor, and J. J. Falke, Biophys. J. **99**, 2879 (2010).
[24]D. W. Lee, H. L. Hsu, K. B. Bacon, and S. Daniel, PLoS One **11**, e0163437 (2016).
[25]M. Bally, A. Gunnarsson, L. Svensson, G. Larson, V. P. Zhdanov, and F. Höök, Phys. Rev. Lett. **107**, 188103 (2011).
[26]M. Müller, D. Lauster, H. H. K. Wildenauer, A. Herrmann, and S. Block, Nano Lett. **19**, 1875 (2019).
[27]P. Kukura, H. Ewers, C. Müller, A. Renn, A. Helenius, and V. Sandoghdar, Nat. Methods **6**, 923 (2009).
[28]K. de Bruin, N. Ruthardt, K. von Gersdorff, R. Bausinger, E. Wagner, M. Ogris, and C. Bräuchle, Mol. Ther. **15**, 1297 (2007).
[29]E. Meijering, O. Dzyubachyk, and I. Smal, Methods Enzymol. **504**, 183 (2012).
[30]M. S. Robbins and B. J. Hadwen, IEEE Trans. Electron. Devices **50**, 1227 (2003).
[31]F. Long, S. Q. Zeng, and Z. L. Huang, Opt. Express **20**, 17741 (2012).
[32]M. J. Lang, P. M. Fordyce, A. M. Engh, K. C. Neuman, and S. M. Block, Nat. Methods **1**, 133 (2004).
[33]D. Axelrod, J. Cell Biol. **89**, 141 (1981).
[34]D. Axelrod, Traffic **2**, 764 (2001).
[35]J. Ortega-Arroyo and P. Kukura, Phys. Chem. Chem. Phys. **14**, 15625 (2012).
[36]A. Lundgren, B. J. Fast, S. Block, B. Agnarsson, E. Reimhult, A. Gunnarsson, and F. Höök, Nano Lett. **18**, 381 (2018).
[37]S. Faez, Y. Lahini, S. Weidlich, R. F. Garmann, K. Wondraczek, M. Zeisberger, M. A. Schmidt, M. Orrit, and V. N. Manoharan, ACS Nano **9**, 12349 (2015).
[38]H. M. Wu, Y. H. Lin, T. C. Yen, and C. L. Hsieh, Sci. Rep. **6**, 20542 (2016).
[39]G. de Wit, J. S. H. Danial, P. Kukura, and M. I. Wallace, Proc. Natl. Acad. Sci. U.S.A. **112**, 12299 (2015).
[40]B. Zhang, J. Zerubia, and J. C. Olivo-Marin, Appl. Opt. **46**, 1819 (2007).
[41]F. Gottfert, C. A. Wurm, V. Mueller, S. Berning, V. C. Cordes, A. Honigmann, and S. W. Hell, Biophys. J. **105**, L01 (2013).
[42]D. Sage, H. Kirshner, T. Pengo, N. Stuurman, J. Min, S. Manley, and M. Unser, Nat. Methods **12**, 717 (2015).
[43]R. E. Thompson, D. R. Larson, and W. W. Webb, Biophys. J. **82**, 2775 (2002).
[44]R. Parthasarathy, Nat. Methods **9**, 724 (2012).
[45]K. J. A. Martens, A. N. Bader, S. Baas, B. Rieger, and J. Hohlbein, J. Chem. Phys. **148**, 123311 (2018).
[46]M. K. Cheezum, W. F. Walker, and W. H. Guilford, Biophys. J. **81**, 2378 (2001).
[47]B. Rieger and S. Stallinga, Chemphyschem **15**, 664 (2014).
[48]M. Lindén, V. Ćurić, E. Amselem, and J. Elf, Nat. Commun. **8**, 15115 (2017).
[49]C. S. Smith, N. Joseph, B. Rieger, and K. A. Lidke, Nat. Methods **7**, 373 (2010).
[50]S. Block, B. J. Fast, A. Lundgren, V. P. Zhdanov, and F. Höök, Nat. Commun. **7**, 12956 (2016).
[51]R. W. Taylor and V. Sandoghdar, Nano Lett. **19**, 4827 (2019).
[52]S. Wieser and G. J. Schütz, Methods **46**, 131 (2008).
[53]A. Sergé, N. Bertaux, H. Rigneault, and D. Marguet, Nat. Methods **5**, 687 (2008).
[54]R. Friedrich, S. Block, M. Alizadehheidari, S. Heider, J. Fritzsche, E. K. Esbjörner, F. Westerlund, and M. Bally, Lab Chip **17**, 830 (2017).
[55]R. Metzler, J. H. Jeon, and A. G. Cherstvy, Biochim Biophys Acta Biomembr **1858**, 2451 (2016).
[56]J. B. Beltman, A. F. M. Marée, and R. J. de Boer, Nat. Rev. Immunol. **9**, 789 (2009).
[57]H. Qian, M. P. Sheetz, and E. L. Elson, Biophys. J. **60**, 910 (1991).
[58]M. J. Saxton, Biophys. J. **72**, 1744 (1997).
[59]A. G. Cherstvy and R. Metzler, Phys. Chem. Chem. Phys. **15**, 20220 (2013).
[60]S. Chandrasekhar, Rev. Mod. Phys. **15,** 1 (1943).
[61]X. Michalet, Phys. Rev. E **82**, 041914 (2010).
[62]X. Michalet and A. J. Berglund, Phys. Rev. E **85**, 061916 (2012).
[63]D. S. Martin, M. B. Forstner, and J. A. Käs, Biophys. J. **83**, 2109 (2002).
[64]L. Weimann, K. A. Ganzinger, J. McColl, K. L. Irvine, S. J. Davis, N. J. Gay, C. E. Bryant, and D. Klenerman, PLoS One **8**, e64287 (2013).
[65]N. Monnier, S. M. Guo, M. Mori, J. He, P. Lénárt, and M. Bathe, Biophys. J. **103**, 616 (2012).
[66]P. J. Slator and N. J. Burroughs, Biophys. J. **115**, 1741 (2018).
[67]F. Persson, M. Lindén, C. Unoson, and J. Elf, Nat. Methods **10**, 265 (2013).
[68]A. J. Berglund, Phys. Rev. E **82**, 011917 (2010).

Biointerphases
A Journal of Biomaterials and Biological Interfaces
TUTORIAL
avs.scitation.org/journal/bip

[69]S. Block, V. P. Zhdanov, and F. Höök, Nano Lett. **16**, 4382 (2016).
[70]P. G. Saffman and M. Delbrück, Proc. Natl. Acad. Sci. U.S.A. **72**, 3111 (1975).
[71]E. Evans and E. Sackmann, J. Fluid Mech. **194**, 553 (1988).
[72]H. A. Stone and A. Ajdari, J. Fluid Mech. **369**, 151 (1998).
[73]S. Block, Biomolecules **8**, 30 (2018).
[74]D. Montiel, H. Cang, and H. Yang, J. Phys. Chem. B **110**, 19763 (2006).
[75]S. Wieser, M. Axmann, and G. J. Schütz, Biophys. J. **95**, 5988 (2008).
[76]C. Yoshina-Ishii and S. G. Boxer, Langmuir **22**, 2384 (2006).
[77]S. R. Tabaei, J. J. J. Gillissen, S. Block, F. Höök, and N. J. Cho, ACS Nano **10**, 8812 (2016).
[78]H. Li, B. Au, J. Rentsch, S. Block, and H. Ewers, Biophys J. **118**, 313a (2020).
[79]Albert Einstein, Ann. Phys. **322**, 549 (1905).
[80]A. Gunnarsson, P. Jönsson, V. P. Zhdanov, and F. Höök, Nucleic Acids Res. **37**, e99 (2009).
[81]A. Gunnarsson, L. Dexlin, P. Wallin, S. Svedhem, P. Jönsson, C. Wingren, and F. Höök, J. Am. Chem. Soc. **133**, 14852 (2011).
[82]O. Wahlsten, A. Gunnarsson, L. S. Nyström, H. Pace, S. Geschwindner, and F. Höök, Langmuir **31**, 10774 (2015).
[83]A. Kunze, M. Bally, F. Höök, and G. Larson, Sci. Rep. **3**, 1452 (2013).
[84]A. Guzman, M. Zelman-Femiak, J. H. Boergermann, S. Paschkowsky, P. A. Kreuzaler, P. Fratzl, G. S. Harms, and P. Knaus, J. Biol. Chem. **287**, 39492 (2012).
[85]J. Schindelin, I. Arganda-Carreras, E. Frise, V. Kaynig, M. Longair, T. Pietzsch, S. Preibisch, C. Rueden, S. Saalfeld, B. Schmid, J. Tinevez, D. White, V. Hartenstein, K. Eliceiri, P. Tomancak, and A. Cardona, Nat Methods **9**, 676 (2012).
[86]N. Perry, J. Y. Tinevez, J. Schindelin, G. M. Hoopes, G. D. Reynolds, E. Laplantine, S. Y. Bednarek, S. L. Shorte, and K. W. Eliceiri, Methods **115**, 80 (2017).
[87]K. Jaqaman and G. Danuser, Cold Spring Harb. Protoc. **2009**, pdb top65 (2009).

4.4 Microfluidics-based force spectroscopy enables to perform high-throughput force measurements with sub-nm resolution and sub-pN sensitivity

---

Yannic Kerkhoff, Latifeh Azizi, Vasyl Mykuliak Vesa P. Hytönen, and Stephan Block

Submitted to Small (October **2022**)

Short summary

Within this work, a new highly parallelized microfluidics-based single-molecule force spectroscopy method with sub-nm resolution and sub-pN sensitivity was developed [172]. It is based on the combination of microfluidics, TIRF microscopy, and single-particle tracking and its performance was tested on well-studied model systems (stretching of PEG-linkers and biotin-NeutrAvidin complex dissociation). It was used to quantify the energy barriers in biotin-NeutrAvidin complexes and the unfolding force of the third rod domain R3 of the force-bearing protein talin.

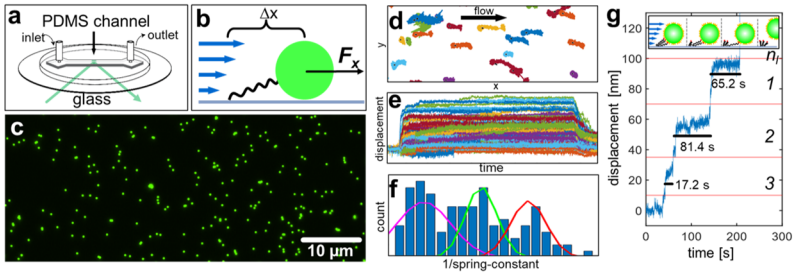

Figure 23: Scheme of the technical setup of the new hydrodynamic single-molecule force measurement method (a). Scheme of the relation of flow (blue arrows), shear force (F_x), and displacement (△x) of fluorescent beads (b). Crop of the microscopy field of view shows the parallelization of the method by the abundance of surface-linked beads (c). Sample of representative tracks show a displacement in flow direction (d). The force-dependent displacement in flow direction shows a broad distribution (e) which can be explained by the number of linkers engaged in bead immobilization, shown by distinct populations with different spring-constants (f). Sequential unbinding of biotin-NeutrAvidin complexes allows for the probing of residence time of specific bond valency's (g).

Author contributions

Yannic Kerkhoff performed all experiments, analyzed most of the experimental data, and wrote the manuscript. Latifeh Azizi cloned, expressed, and purified protein constructs and reviewed and edited the manuscript. Vasyl Mykuliak performed MD simulations of R3 unfolding and reviewed and edited the manuscript. Vesa P. Hytönen planned and supervised protein production and simulations and and reviewed and edited the manuscript. Stephan Block supervised the project, designed the method and data analysis workflow, implemented the cluster analysis, did deeper analyses of the experimental data, wrote part of the manuscript, and reviewed and edited the manuscript.

Microfluidics-based force spectroscopy enables high-throughput force experiments with sub-nm resolution and sub-pN sensitivity

*Yannic Kerkhoff, Latifeh Azizi, Vasyl V. Mykuliak, Vesa P. Hytönen, Stephan Block**

Y. Kerkhoff, S. Block

Department of Chemistry and Biochemistry, Freie Universität Berlin, Arnimallee 22, 14195 Berlin, Germany

E-mail: stephan.block@fu-berlin.de

L. Azizi, V. V. Mykuliak, V. P. Hytönen

Faculty of Medicine and Health Technology, Tampere University, Arvo Ylpön katu 34, FI-33520 Tampere, Finland

V. P. Hytönen

Fimlab Laboratories, Biokatu 4, FI-33520 Tampere Finland

Keywords: single-molecule force spectroscopy, microfluidics, TIRF microscopy, high-throughput measurements

Several techniques have been established to quantify the mechanicals of single molecules. However, most of them show only limited capabilities of parallelizing the measurement by performing many individual measurements simultaneously. Herein, we present a microfluidics-based single-molecule force spectroscopy method, which achieves sub-nm spatial resolution and sub-pN sensitivity and is capable of simultaneously quantifying hundreds of single-molecule targets in parallel. It relies on a combination of TIRF microscopy and microfluidics, in which monodisperse fluorescent beads are immobilized on the bottom of a microfluidic channel by macromolecular linkers. Application of a flow generates a well-defined shear force acting on the beads, whereas the nanomechanical linker response is quantified based on the force-induced displacement of individual beads. To handle the high amount of data generated by this method, we implemented a cluster analysis which is capable of a semi-automatic identification of measurement artifacts and molecular populations. We validated our method by probing the mechanical response PEG-linkers and binding strength of biotin-NeutrAvidin

complexes. With this new technique, we resolve 2 energy barriers (at 3 Å and 5.7 Å, respectively) in the biotin-NeutrAvidin interaction and probe the unfolding behavior of talin's rod domain R3 in the force range between 1 pN to ~ 10 pN.

1. Introduction

Over the past decades, several techniques have been established, which allow to apply forces on nanometer-sized biological objects, such as macromolecules, proteins or DNA, and to study biologically important processes, such as macromolecular interactions or force-induced changes in the conformation/structure of macromolecules, with single-molecule resolution.[1] The most prominent of these techniques are atomic force microscopy (AFM), optical tweezers (OT), and magnetic tweezers (MT), which use different approaches for force generation but have in common that they are capable of providing mechanical data originating from individual molecules.[2] In this way, they allow to learn how mechanical force modulated structure and function of molecule, for example by opening cryptic binding sites within proteins.[3] Single-molecule methods also enable to probe for heterogeneities, such as rare events or transient states, in the mechanical response of an ensemble, which can be important features for biological systems, but are averaged out and therefore lost when applying ensemble-averaging approaches. Hence, the introduction of single-molecule force techniques like AFM, OT, and MT enabled for completely new biophysical measurement schemes and allowed to study the force-related biological processes in unprecedented detail.[1] Nevertheless, as they probe response of individual macromolecules, which is typically subject to notable, thermally driven fluctuations, it is necessary to probe this response multiple times in order to gain sufficiently measurement statistics to make meaningful statements.[4] For AFM and OT, which are very limited in their capability to probe multiple individual interactions in parallel (low degree of parallelization), this is solved by repeating the measurement process, which may result in long measurement times. In contrast, the force generation in MT is compatible with a significant parallelization of the measurement process and implementations, in which hundreds of interactions have been simultaneously probed using MT have been described.[5] This concept has the advantage that significant amount of data is generated already in a single experimental run and also offers additional strategies to cope with heterogeneous samples, in which certain properties (such as the composition of interaction partners) show a notable distribution across the ensemble.

Such features are very interesting for investigations on complex biological systems, such as studies on how cells are able to transduce mechanical forces into biochemical signals.[6] It is known that mechanical forces have great effect on cellular behavior like adhesion, growth,

maturation and migration.[7][8][3][9][10][11] One of the many mechanosensors and mechanotransducers in cells is the force-bearing protein talin.[12][13][14][15] Talin is a force-sensitive protein consisting of 13 rod domains, which unfold at different forces (ranging between 5 and ~40 pN) and therefore lead to complex unfolding patterns of the full-length proteins. Application of the before mentioned force spectroscopy methods (OT,[16] MT,[11][17][18] and AFM [3][19]) allowed to investigate this process in great detail, whereas an assessment of the unfolding of rod domain R3 remains challenging, which sets in at forces being comparable to the force resolution of OT and MT (~ 1 pN) and out of the measurable range of AFM.

Inspired by these works, we aimed for designing a single-molecule force spectroscopy method, which combines the ability to apply very low to sub pN forces (like in OT), while extending the high throughput capability of parallel MT, to meet the before mentioned criteria of sensitivity and statistical power. In principle, this is fulfilled by setups, in which microfluidics is used to generate hydrodynamic shear forces on interface-linked nanoparticles. One recent example was introduced by Block *et al.,*[20] in which fluorescent nanoparticles with defined sizes were linked to a fluid phase supported lipid bilayer (SLB) in a microfluidic channel. Application of total internal reflection fluorescence (TIRF) microscopy allowed to track the force-induced motion of SLB-linked nanoparticles with single-nanoparticle resolution. Analyzing this motion provided a new means to determine the shear force acting on a nanoparticle directly from its trajectory and hence to determine the impact of nanoparticle size and channel flow rate on the generated shear force. In this way, the authors demonstrated that this setup enables to generate very small forces (ranging between fN to pN) and allows to sensitively probe the action of such small forces on hundreds of individual nanoparticles in parallel, providing a high parallelization of the force sensing process.

In this work, we aim to translate this setup to nanoparticles that have been stably linked to the bottom of the microfluidic channel, as this should allow for highly parallelized force measurements (addressing up to thousands of interactions in parallel) with an outstanding sub-pN force sensitivity. As in our previous study, we use a combination of TIRF-based optical video microscopy and a PDMS-based microfluidic channel (width: 150 µm; height: 100 µm), which was bonded to a thin glass slide (forming the bottom of the microfluidic channel; **Figure 1**a). To test our hypothesis, we attached fluorescent beads of known size to the glass surface by a linker and studied bead displacement and bead detachment as a function of the applied shear forces. This data provided information on the nanomechanical properties of the linker (bead displacement) or the binding strength between bead and interface (bead detachment), which

will be discussed in detail in the following paragraphs. We applied these two measurement modalities to two well-established model systems (nanomechanics of polyethylene glycol, PEG, and binding strength of the ligand-receptor interactions biotin-NeutrAvidin), which formed the basis for an assessment on the performance of this flow-based force spectroscopy approach. Finally, we applied this new tool to investigate the unfolding of talin's rod domain R3, further demonstrating the benefits offered by combining high force resolution (< pN) with high parallelization of the measurement process.

2. Results & Discussion

2.1. Stretching of PEG-Polymer

In a first set of experiments, we studied the nanomechanics of PEG-based linkers (**Figure 1**c), which allowed to evaluate our approach using a well-studied system. To this end, we functionalized the bottom of the microfluidic channel using block-copolymers consisting of a 20 kDa poly-L-lysine chain (PLL) coupled to a 3.4 kDa PEG chain, which bind via electrostatic interactions of the positively charged PLL to the negatively charged glass surface. As a very small fraction of the PEG chains were equipped with a biotin moiety (see Materials and Methods for details), it was possible to stably link monodisperse, NeutrAvidin-coated fluorescent polystyrene beads (diameter: 200 nm) to the interface using the highly specific biotin-NeutrAvidin interaction. In this way, thousands of fluorescent beads were immobilized in the field of view (FoV) of our microscope (135 x 135 μm²) and subjected to flow-induced shear forces, which allowed for a high parallelization of the measurement process.

This is demonstrated in **Figure 1**d, which represents ~ 7% of the microscope's FOV and shows 80 beads out of a sample carrying approximately 1100 beads per FoV. The high brightness of the beads enables to achieve single shot localization accuracies below 1 nm (see Supporting Information S1. Drift Compensation) and hence to detect sub-nm bead displacements as function of the applied flow rate (**Figure 1**e), provided that drifts of the sample surface (*e.g.*, caused by changes in the flow conditions) are correctly compensated (see Supporting Information S1. Drift Compensation for more details on the drift compensation procedure).

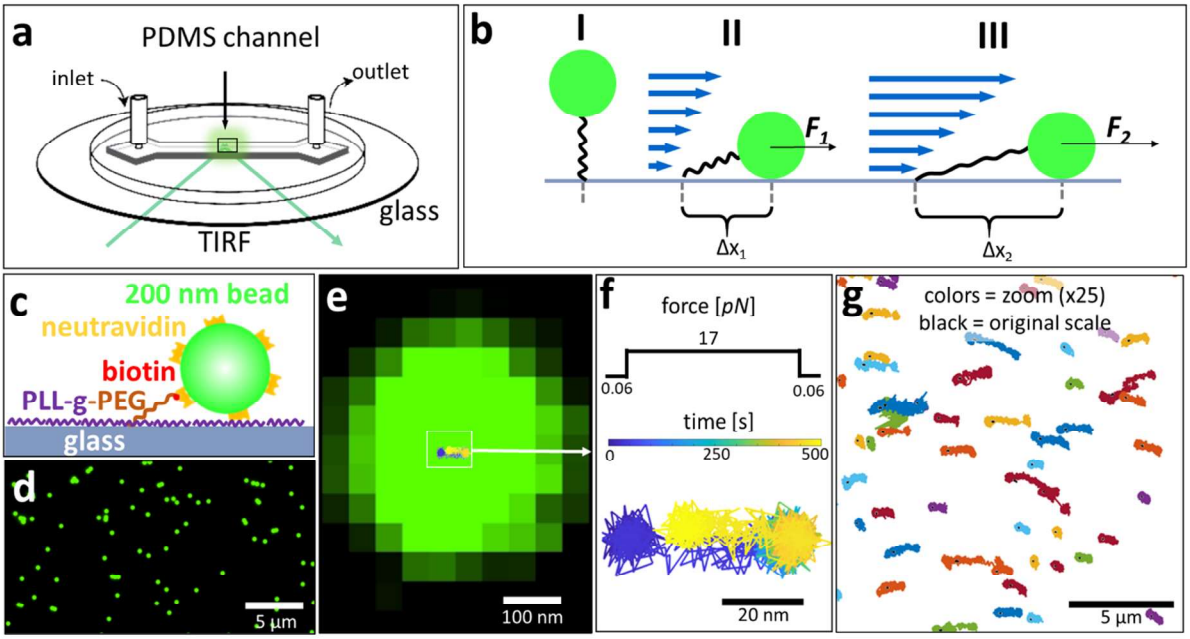

Figure 1: Scheme of the microfluidics-based force spectroscopy method. A 150 µm wide microfluidic channel with in- and outlet is embedded in a PDMS stamp, bonded on a glass slide, and mounted on a TIRF microscope (a). In general, fluorescent beads (green) are attached to a linker (black) which is bound to the glass (b), hovering in neutral position over the surface if no flow is applied (b, I). Low flow rates generate a low force (F_1), and the bead is pushed in flow direction (Δx_1) and towards the surface (b, II). High flow rates apply a high force (F_2), and push the bead further (Δx_2), resulting in a stretching of the linker (b, III), which can be quantified based on the bead displacement. To probe the nanomechanics of PEG (c), the glass surface is coated with block copolymers of poly-L-lysine (purple) and PEG (brown), a small fraction of which presents biotin moieties at the PEG chain (red) and can be used to link NeutrAvidin-coated 200 nm fluorescent bead (green). A zoom in the field of view (FoV) of the TIRF microscope of a sample having about 1100 linked beads in total per FoV (d). An overlay of the intensity distribution of one representative bead with its displacement trajectory (generated by application of a block-shaped force profile: 0.06→17→0.06 pN, see also f) indicates that the high localization accuracy of our approach allows to follow even very small bead displacements (e). In this representative displacement trajectory (f), the blue color shows the initial position of the bead center at the low force of 0.06 pN, followed by a displacement of the bead of about 40 nm upon application of 17 pN shear force (color shift from cyan to green and orange). Afterwards, the bead returns near its initial position due to the reduction of the shear force to 0.06 pN (yellow). As thousands of beads can be tracked per FoV, such measurements lead to thousands of force-induced displacement trajectories, a small fraction of which is shown in (g). For visualization reasons, these trajectories were sized up by the factor of 25, whereas their central position was preserved.

The application of a block-shaped force profile, for example, also leads as expected to a block-shaped displacement response of the beads (**Figure 1**f). In this example, the measurement started with the application of a very low shear force (0.06 pN) to the bead, which is so small

that the bead's center position (x- and y-coordinates in the image) fluctuates around the attachment point of the linker. After 50 seconds, the force was increased to 17 pN, leading to a 40 nm displacement of the bead in flow direction (cyan to orange). After application of this force for 400 seconds, the shear force was reduced again to 0.06 pN for 50 seconds, allowing the bead to return near its initial position (yellow, deviation ~ 13 nm). This almost fully reversible response indicates that the bead is indeed linked to glass surface via an elastic linker, which is a finding that is representative for nearly all of the 1100 analyzed beads (a fraction of 50 tracks from a randomly chosen part of the FoV is shown in **Figure 1**g).

Obviously, all beads given in **Figure 1**g showed a force-induced displacement in flow direction, whereas the extent of the displacement varies between the beads. This means that some of the beads showed a larger displacement, while others seemed to be nearly immobile. To quantify this effect, we calculated a density map of observed bead displacements from block-wise stretched linkers (**Figure 1**c-g). As a notable number of displacements curves terminated before the end of the experimental run (indicative for force-induced detachment of the corresponding bead), we restricted this analysis to all displacements curves, which covered the entire experimental run and which followed the block-wise force response (i.e., showed return to the initial position). Calculating the density map of these displacements curves (**Figure 2**b) shows that the displacement values are not evenly distributed, but exhibited only specific values (~ 22, 55, and 80 nm). These distinct populations are also clearly visible in the histogram of bead displacement values (**Figure 2**c) and indicate that the different bead displacement populations are caused by differences in the nanomechanical response of the linker (*i.e.*, by differences in the number of linkers engaged by the beads, as will be shown below).

In order to accurately quantify the nanomechanical response, one has to take into account that while all beads experience the same shear flow-based force (F_x, **Figure 2**a), the actual force acting in direction of the linker(s), F, depends on the angle between the linker(s) and the horizontal (*i.e.*, the surface). This means that only a fraction of the full shear force (that acts on the bead) will be applied to the linker(s) and that this fraction increases with increasing bead displacement (Δx), as this process will reduce the angle between the linker(s) and the surface. As shown in Supporting Information S2. Extension and Force Calculation, the force acting in direction of the linker, F, as well as the extension of the linker due to this force can be calculated from the bead displacement, Δx, under the assumption that the bead always touches the surface.

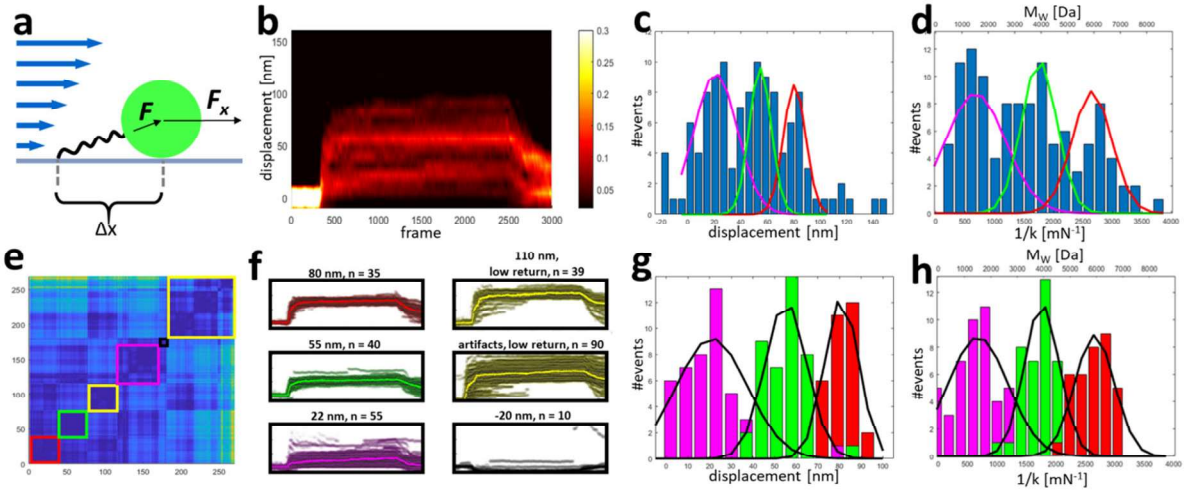

Figure 2: Stretching of PEG-linkers revealed linker valency indicated by distinct populations in displacement, molecular weight, and spring-constant. The bulk flow applies a shear force on the bead in flow direction, F_x, which loads the linker with the loading force F and results in a bead displacement Δx (a). A density map of 113 bead displacement curves (b) shows accumulations of curves (red) in distinct regions (approximately at displacements of 22, 55, and 80 nm, respectively). The histogram of these displacements at saturation (c) as well as of the corresponding values for linker spring constant and apparent linker molecular weight (d, see main text for details) shows three distinct populations. The solid lines in (c) and (d) give Gaussian fits that originate from the data analysis summarized in (e-h). In this data analysis, the beads have been automatically assigned to distinct populations based on a cluster analysis applied to the observed bead displacement curves. This procedure (described in detail in Supporting Information 3) yields a symmetric 2D similarity map (e), which provides the similarity of two displacement curves (given by their ID values on the x- and y-axis, respectively) based on the calculation of the standard deviation of their displacement difference. This similarity measure is color coded in (e), in which high to low similarity is indicated by colors ranging from blue to yellow. Applied to all 260 displacement curves from a representative experiment, the cluster analysis identified six distinct cluster groups (red, green, yellow, purple, black squares in e), whereas the assigned displacement curves indeed behave very similar within the corresponding cluster as shown in (f), which provides an overlay of all assigned displacement curves and their ensemble average as thick solid curve. (Enlarged version of (e) and (f) are given in the Supporting Information.) This analysis provides three populations showing the displacement behavior already observed in (b) and (c), but also three additional populations, the curves of which either contain obvious measurement artefacts (such as lack of return to the initial position at very low flow rates, yellow population) or indicate immobile beads (showing no notable displacement upon application of a force, black population). Histogram of the median displacement value (g, taken at the saturation regime of the displacement curves from the red, green and purple populations) as well as the corresponding values of linker spring constant and apparent linker molecular weight (h) are well described by Gaussian fits and yield distributions consistent with (c) and (d). Hence, the cluster analysis enables to decompose the full data set into individual bead populations based on their nanomechanical behavior and to efficiently identify artefact-bearing displacement curves within the data.

This assumption is plausible, as a shear force acting on "hovering" beads (not touching the surface) will generate a torque that pushes the beads towards the interface until contact has been achieved. We will revisit this assumption at the end of this section. Applying the model discussed in Supporting Information 2 allows to calculate for each bead the force acting in direction of the linker(s), F, and the force-induced extension of the linker(s), L, from the measured bead displacement. The ratio of both quantities gives the stiffness of the linker(s) in terms of the spring constant, $k = F/L$. Assuming that the PEG linkers are well described by the freely jointed chain model,[21] an assumption that has been validated for PEG chains in aqueous solutions in a variety of studies,[22][23] it is possible to relate the observed spring constant k to the molecular weight of the linker, M_w, via the relationship[21]

$$M_w = \frac{3 \cdot k_B \cdot T}{\kappa_K} \cdot k \cdot \frac{M_{EG}}{L_{EG}} \quad (1)$$

in which k_B denotes Boltzmann's constant, T the temperature (in Kelvin), and κ_K the Kuhn length of PEG (=0.7 nm)[22][23], while M_{EG} and L_{EG} denote the molecular weight and physical length of a PEG monomer (44 Da and 0.3 nm, respectively). A histogram of observed (theoretical) molecular weights of the linker (**Figure 2**d) also exhibits distinct populations with average weights of 1.5, 3.1, and 6.1 kDa. The calculated molecular weight of the softest (red) population (approximately 6.1 kDa) is higher than the molecular weight of the PEG target (3.4 kDa) and indicates that application of a shear force does not only stretch the 3.4 kDa PEG chain but also part of 20 kDa PLL chain. The green and the purple population show apparent molecular weights of ~ 3.5 and ~ 1.5 kDa respectively. This observation suggests that these populations correspond to beads linked with 2 and 3 linkers, as this will increase the (overall) linker spring constant by a factor of 2 and 3, respectively, and lead to apparent molecular weights being only one half and one third of the true molecular weight of a single linker (see Eq. 1). We therefore conclude that the distinct molecular populations observed in the histograms of bead displacement and spring constant/apparent molecular weights can be explained by differences in the number of linkers engaged by the respective beads.

Although this analysis workflow allowed to address the nanomechanics of PEG chains, the analysis of the obtained data turned out to be challenging (despite the simplicity of this system), as the difference in the binding stoichiometry of the beads caused broad distributions and complex morphology of the derived displacement curves. Furthermore, visual inspection of the displacement curves showed that a notable fraction of these curves contained obvious measurement artefacts and had to be (manually) removed from the data analysis. Owing to the high data throughput of the method, which allows to quickly perform many experimental runs

providing hundreds to thousands of displacement curves per run, this manual inspection turned out to be the bottle neck of the analysis. To address this limitation, we developed an automated cluster analysis, which enabled to automatically define and classify the distinct molecular populations as well as artifacts-bearing or non-responsive curves (**Figure 2**e, for details see Supporting Information S3. Cluster Analysis). In short, this analysis picks all possible pairs of 2 displacement curves from the data and calculates for each pair the standard deviation *sd* of the difference of their displacement curves. This information is stored in a two-dimensional matrix (in which the *x*- and *y*-dimension correspond to the IDs of the two displacement curves of a particular pair) and afterwards, displacement curves with high similarity (indicated by low *sd* values) are grouped together.

The grouping result can be visualized in a 2D color map (**Figure 2**e), indicating similar displacement curves in blue and distinct ones in yellow. This cluster map visualizes the distinct populations (indicated by red, green, yellow, purple, and black squares in **Figure 2**e) and therefore provides an assignment of displacement curves into populations of similar behavior that can be quickly validated by manual inspection. This tool turned out to be very valuable, as it allowed an almost automatic identification of artefact-bearing displacement curves and as it correctly decomposed the complex displacement distributions of **Figure 2**c into individual populations differing in the nanomechanical behavior (red, green, and purple populations in **Figure 2**f and **Figure 2**g). This showed that the cluster analysis allows for an automated reliable classification of molecular populations in such complex data sets, which was further validated by correct reconstruction of simulated FEC populations (for details see Supporting Information 3.2. Cluster Analysis Validation).

2.2. Binding strength of biotin-NeutrAvidin interaction

Beside the displacement curves covered above, which showed a constant displacement during force application and return afterwards, we also observed displacement curves that terminated before the end of an experimental run (caused by bead detachment) and/or showed sudden increases in the displacement value without any change in the applied shear force (**Figure 3**a,b). These features can be explained by a decrease in the number of linkers engaged by the corresponding bead, as some of the biotin-NeutrAvidin interactions, which are used to connect the beads to the linkers, can unbind due to the applied force.[24][25][26] If the bead is linked to n_l linkers, the generated loading force (F in Figure 2a) is distributed over several linkers. Each linker will be loaded (on average) by the reduced force F/n_l, which results in a bead displacement that increases with decreasing number of engaged linkers (n_l). Hence, if one linker

detaches, the bead will not completely rip from the surface but will show a step towards larger values in the displacement curve, as long as the bead is linked to at least one linker. If the last linker detaches, the bead will detach from the surface, causing the displacement curve to terminate before the end of the experimental run. This results in displacement curves, which show transitions between distinct displacement plateaus (**Figure 3**a) that can be assigned to the number of remaining linkers (n_l) based on the defined populations of **Figure 2**g. The length of these plateaus represents the residence time of each of the linking state and thus contains information on the force-dependent stability of the biotin-NeutrAvidin interaction.

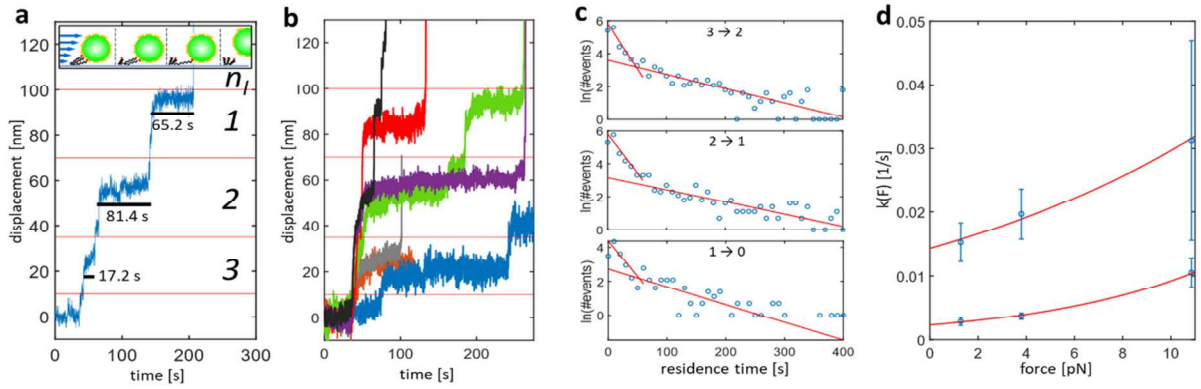

Figure 3: Detachment kinetics of multivalent biotin-NeutrAvidin complexes. A representative bead displacement curve showing three distinct displacement plateaus (a), which caused by a sequential detachment of three PEG-linkers. This detachment requires rupture of individual biotin-NeutrAvidin interactions, as schematically indicated in the inset. Measuring the duration of individual rupture processes (black bars in a) allows to determine the residence time associated for transitions from n_l = 3 to 2 (3→2), from 2 to 1 (2→1) as well as for release of the final interaction (1→0). The sequential detachment of linkers was observed in many displacement curves, as indicated by a sample of 7 representative curves shown in (b). Extracting the residence times (as shown in a) from all such curves allowed to determine the residence time distributions for the different transitions (3→2, 2→1, and 1→0), which typically showed two distinct exponential decays and therefore indicates that each these processes decays with 2 transition rates (c). These transition rates increase with increasing loading force per linker (d), which can be well-described by the Bell model (solid line). Application of this model revealed two energy barriers for the energy landscape of the biotin-NeutrAvidin interaction, having potential widths of 5.7 Å and 3.0 Å and zero-force off-rates of 2.3×10^{-3} s^{-1} and 14.3×10^{-3} s^{-1}, respectively.

Applying this analysis to all displacement curves showing transition allowed to extract the residence time distribution for each of the 3 transitions: n_l = 3 to 2, 2 to 1, and 1 to 0 (bead detachment). For random detachment processes (*i.e.*, for transition that are statistically uncorrelated), the residence time distributions are expected to show an exponential decay, the decay rate of which would correspond to the transition rate. Plotting the 3 residence time

distributions with a semi logarithmic scale (**Figure 3**c) indeed revealed exponential decays (indicated by straight lines in this representation), but in fact two distinct decay rates for each of the 3 transitions. Hence, the biotin-NeutrAvidin interaction decays in our experiments with 2 transition rates, which can be determined by linear fits of the residence time distributions (red lines in **Figure 3**c).

In order to determine the impact of the loading force on the failure rate of unbinding of the biotin-NeutrAvidin interaction, one has to account for the difference in the number of acting interactions of the 3 transition processes. If the transition starts with n_l linkers, one has to take into account that only the fraction F/n_l of the total loading force acts on a single linker (i.e., on a single biotin-NeutrAvidin interaction). Furthermore, since n_l interactions are present, the observed transition rate is n_l times larger than the rate of rupture (off-rate) of a single biotin-NeutrAvidin interaction. Accounting for these effects enabled to determine the impact of loading force on the off-rate of a single biotin-NeutrAvidin interaction (**Figure 3**d). As two transition rates were observed in the residence time distribution, this plot contained two force-dependent off-rates, each of which is well described by Bell's theory.[27] This analysis suggests an energy landscape that consists of at least two energy barriers, having potential widths of 5.7 Å and 3.0 Å and zero-force (equilibrium) off-rates of 2.3×10^{-3} s^{-1} and 14.3×10^{-3} s^{-1}, respectively. The energy barrier at 3.0 Å is consistent with AFM-based force spectroscopy experiments,[26][28] whereas the outer barrier at 5.7 Å was to our knowledge not observed in experiments before. The existence of such an outer barrier was, however, suggested by steered molecular dynamics simulations as well as by discrepancies observed in the off-rates obtained from non-equilibrium and equilibrium measurements.[29][30][31]

2.3. Nanomechanics of talin's rod domain R3

After evaluating the performance of our microfluidics-based force spectroscopy approach, we set out to apply it to study the nanomechanics of proteins, which start to unfold already if subject to pN forces. In particular, we aimed for probing the unfolding behavior of talin's rod domain R3, the characterization of which proved to be very challenging even for highly sensitive force sensing techniques such as OT and MT. To this end, we integrated into our assay a recently described fragment containing talin's rod domains R1 to R3,[19] which has been intensively characterized using MT and AFM in the past and showed unfolding of R3 for forces being on the order of 5 pN.[19][17] In our measurements, we employed the construct introduced by Haining *et al*. (termed R1-3 in the following),[19] in which the rod domains R1 to R3 are integrated between two repeats of titin's I27 domain (which generated a nanomechanical signature in their

AFM measurements), whereas the N- and C-termini of the whole construct were functionalized with a HaloTag and cysteine residue, respectively. Hence, the R1-3 construct can be understood as the following polyprotein: HaloTag-$(I27)_2$-R1-R2-R3-$(I27)_2$-His-Cys. Furthermore, a variant of this construct was available for our measurements (termed I27 in the following), which consists only of the I27 domain repeats: HaloTag-$(I27)_4$-His-Cys. As unfolding of I27 requires forces exceeding 50 pN [32], the construct I27 cannot be unfolded with the forces achievable in our setup (~ 20 pN) and therefore serves as negative control in our unfolding measurements. Furthermore, R1 and R2 unfolding has been reported to occur for loading forces well beyond 10 pN, [17] making unfolding of these two rod domains in our experiments a possible yet unlikely process.

Both constructs were integrated into our assay by coupling the constructs to monodisperse, fluorescent beads (diameter: 200 nm) via the HaloTag moiety, whereas the cysteine residue was used to link functionalized beads to maleimide groups attached to the bottom of a microfluidic channel (as described in the Materials and Methods section). The displacement of these beads was recorded using a flow profile that generated the following sequence of loading forces: 0.3 pN, 0.7 pN, 1.3 pN, 2.8 pN, 6.0 pN, 0.3 pN (**Figure 4**a). As in our stretching experiments involving PEG chains, we again observed a broad distribution of bead displacement responses, which required the application of the above-mentioned cluster analysis to identify populations of similar nanomechanical behavior as well as artifact-containing displacement curves. We typically observed 4 populations, which reproduced well between independent measurement runs and which were attributed to beads being linked to the surface by one, two, three or more constructs (**Figure 4**a showing the ensemble-averaged displacement curves of the individual populations). This interpretation is supported by the observed spring constants being consistent with a recent investigation.[17] To simplify the analysis, we will restrict the following assessment to the population corresponding to a single construct linking the bead to the surface. Comparing the individual displacement curves of this population with the ensemble-averaged response yields several candidate curves, which exhibit significantly larger displacements (*i.e.*, potential unfolding events) in comparison to the enable answer. We therefore continued to extract for each displacement curve the linker extensions (using the model described in Supporting Information 2) as a function of the applied shear force and compared these distributions for the R1-3 and the I27 construct (**Figure 4**b and **Supporting Figure S**6).

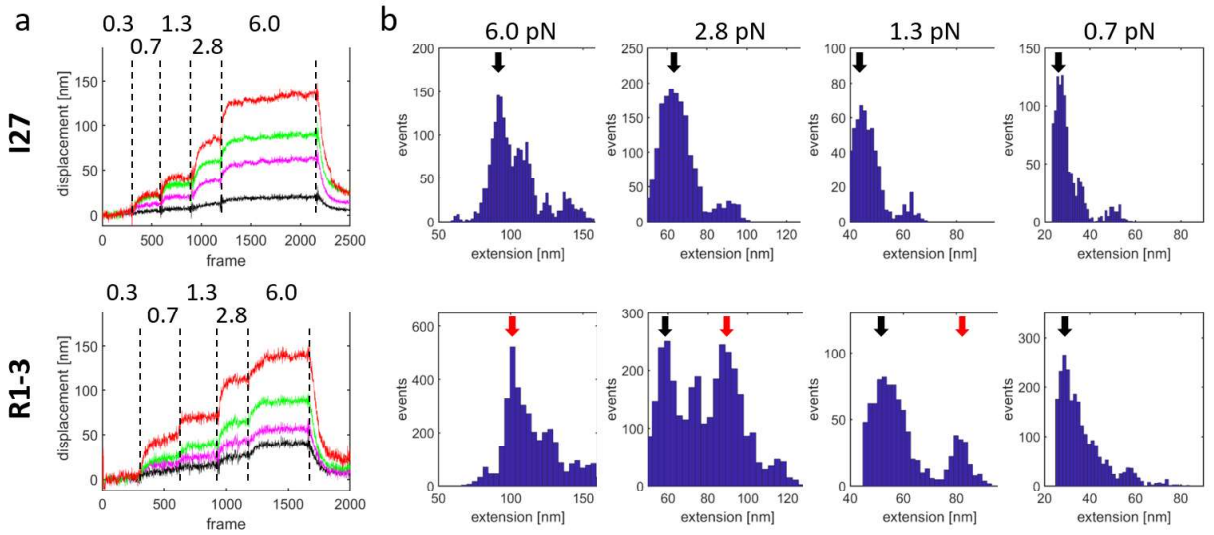

Figure 4: Unfolding of talin's rod domain R3. Linking the beads using protein constructs containing (talin rod domains R1 to R3; R1-3) or lacking (I27) talin's rod domain inserts yielded shear force-induced displacement curves that showed a broad distribution of displacement values. As in the case of PEG-linker stretching (Figure 2), application of the cluster analysis yielded distinct populations (a, showing the ensemble-averaged displacement curve), which correspond to beads that are linked by one (red), two (green), three (purple) or more (black) constructs to the surface. Analyzing all displacement curves of beads being linked by a single construct (red in a), yielded information on the extension of the constructs (b) as a function of applied loading force (as indicated in b). While the extension distributions of I27 typically showed only one major peak (black arrow), which is consistent with a construct that cannot be unfolded below loading forces of 50 pN, an additional peak is observed for the R3-containing construct (R1-3, red arrows), which is attributed to unfolded R3 (as discussed in the main text).

The extension distributions obtained from the I27 construct are mainly given by a single peak, which indicates the extension value of a fully folded construct (black arrows in **Figure 4**b). In addition, the I27 distributions also show few minor peaks, which contribute less than 10% of the observed events and are attributed to minor errors in the determination of the displacement. The extension distributions obtained from the R1-3 construct show, however, a much more complex structure. While for loading forces of 0.7 pN and 6 pN only one peak is observed, at least one additional population is observed for loading forces of 1.3 pN and 2.8 pN (red arrows in **Figure 4**b), which is missing for the I27 construct. The change in extension between the two populations is 27.8 and 31.8 nm (at 1.3 and 2.8 pN, respectively), which matches very well with the expected increase in construct extension upon unfolding of the rod domain R3 (as determined in steered molecular dynamics simulations) and is close to experimentally observed values (~ 25 nm).[17] Hence, this population is attributed to fully unfolded R3.

This analysis reveals that 21% and 64% of the R1-3 constructs started to unfold at 1.3 and 2.8 pN, respectively, indicating that notable R3 unfolding can already be observed for loading forces at the 1 pN scale. At 6 pN, we observe, as for the I27 construct, only a single population, which we attribute to fully unfolded R1-3 construct. This interpretation is supported by the trend in the unfolding at 1.3 and 2.8 pN as well as by a notable shift in the peak position between the I27 and the R1-3 construct (~ 20 nm).

3. Conclusion

In our study, we introduced a microfluidics-based force spectroscopy technique, which allowed to quantify the nanomechanical behavior of polymers and protein constructs as well as the binding strength of a ligand-receptor interaction. The performance of this technique was evaluated by quantifying the molecular spring constant of PEG-containing linkers, which allowed to validate the measurement and data analysis procedure using a well-studied system. This assessment indicated that the technique combines high parallelization of the measurement process (following the response of up to thousand beads in parallel) with outstanding spatial resolution (sub-nm localization accuracy) and sub-pN force sensitivity. Nevertheless, it also revealed that the close vicinity of the beads to the surface of the microfluidic channel causes a notable fraction of displacement curves to contain artifacts, which have to be identified and excluded from further data analysis. To address this problem, we integrated a cluster analysis, which assigned the recorded displacement curves into populations according to similarities in their displacement behavior. This procedure did not only enable to semi automatically identify artifact-containing displacement curves but also to identify populations that differ in their nanomechanical response (due to difference in the number of engaged linkers), which was key to analyze the complex data sets obtained by this technique. As an application of this new technique, we probed the dynamics of force-induced bond failure of the ligand-receptor interaction biotin-NeutrAvidin, which revealed one already known and one yet unobserved energy barrier, therefore highlighting the additional information obtainable by our constant force spectroscopy setup. Furthermore, we used this technique to study the unfolding behavior of a talin's rod domain R3, which indicated notable unfolding to occur at smaller forces (1 pN scale) than previously believed. These experiments clearly demonstrate the potential of this microfluidics-based force spectroscopy technique, especially for the characterization of even more complex systems than covered in this study.

Evaluation of this technique showed, however, that the non-covalent immobilization strategy currently used in the experiments is, contrary to our initial expectations, not strong enough even

for force in the 5 pN range. Although this allowed us to study the bond failure of a ligand-receptor interaction, this immobilization strategy causes a notable fraction of tracked beads to detach before the end of an experimental run, thereby significantly lowering the data throughput and making the data analysis more complex. In future experiments, we will therefore switch to covalent immobilization strategies in order to avoid this problem.

4. Experimental Section/Methods

Chemicals: PDMS (Polydimethylsiloxane), Biotin-maleimide, TCEP (Tris(2-carboxyethyl) phosphin-hydrochlorid), and DMSO (Dimethylsulfoxid) were obtained from Sigma Aldrich (Steinheim, Germany). Poly-L-lysine(20)-g[3.5]-PEG(2) and PLL(20)-g[3.5]-PEG(3.4)-biotin were obtained from SuSoS (Dübendorf, Switzerland). NeutrAvidin, 200 nm NeutrAvidin-labelled, and amine-modified polystyrene beads were obtained from Thermo Fisher Scientific (Massachusetts, USA). Sodium acetate (>98.5 %), acetic acid (100 %), and phosphate-buffered saline (PBS, pH = 7.4) were obtained from Carl Roth (Karlsruhe, Germany). HaloTag NHS ligand was obtained from Promega (Wisconsin, USA). The constructs denotes as I27 (containing 4 titin I27 domains) and R1-3 (containing talin's rod domains R1 to R3) were expressed and purified as previously described (see next paragraph).[19] PBS buffer was created by diluting 10x PBS concentrate according to the manufacturer's instructions. Sodium acetate buffer (pH = 5) was created by mixing 67 ml of sodium acetate stock (10 mM) with 33 ml acetic acid stock (10 mM). PBS|TCEP buffer was created by adding 1 mM TCEP to the PBS buffer. Sodium acetate|TCEP buffer was created by adding 1 mM TCEP to the sodium acetate buffer. PLL-g-PEG|Biotin solution was created by mixing $2.6x10^{-1}$ g/L PLL-g-PEG and $3.4x10^{-6}$ g/L PLL-g-PEG-biotin in PBS|TCEP buffer. NeutraAvidin solution was created by preparing 10^{-3} g/L NeutrAvidin in PBS|TCEP buffer. The construct solution was created by preparing $4.2x10^{-2}$ g/L I27 or R1-3 and $8.5x10^{-4}$ g/L biotin-maleimide in sodium acetate|TCEP buffer. The NeutrAvidin-bead solution was prepared by diluting the NeutrAvidin-bead stock solution 1:200 in 1x PBS. The amine-bead solution was prepared by diluting the amine-bead stock solution 1:100 in PBS|TCEP buffer and adding $5x10^{-6}$ g/L HaloTag NHS ligand.

Protein expression and purification: Halo-(I27)x2-R1-R2-R3-(I27)x2-His-Cys construct was expressed using target protein encoding DNA subcloned into a customized pET-based plasmid, [19] which included a C-terminal hexahistidine tag following by a Cys. The plasmids were introduced into *E. coli* BL21-Star cells (ThermoFisher Scientific). Bacterial were pre-cultured in LB-medium containing 100 µg/mL ampicillin at 37°C overnight in a shaker. The larger production (1 L) was done in LB-medium containing 100 µg/mL ampicillin. To induce protein

expression at optical density (OD~600) of 0.4, 1 mM IPTG was used. Cells were incubated for 12h at 18°C after which they were harvested by centrifugation. The Emulsiflex C3 was used for homogenization in 20 mM $NaPO_4$, 500 mM NaCl, 20 mM imidazole pH 7.4 buffer. The homogenized *E. coli* suspension was centrifuged to get clarified lysate, which then applied to HisTrap FF (5 mL) affinity column (GE healthcare) using chromatography Äkta prime P100. The Halo-(I27)x2-R1-R3-(I27)x2-His-Cys was eluted from column using 20 mM $NaPO_4$, 500 mM NaCl PH 7.4 buffer with gradually increasing imidazole concentration (20 – 500 mM). Fractions were directly eluted into Eppendorf tubes containing 1mM EDTA, 1mM DTT.

Eluted fractions were analysed by SDS-PAGE and Coomassie staining. Furthermore, Halo-(I27)x2-R1-R3-(I27)x2-His-Cys construct was purified and buffer exchanged into 1x PBS (containing 1 mM EDTA, 1 mM TCEP) using P-10 column. The homogeneity of the purified protein was evaluated by SDS-PAGE and Western blot (using a-His HRP 1:4000 antibody) up to 90%. In addition, the purity of protein also confirmed by dynamic light scattering (DLS), Malvern ZetaSizer ZS, which indicated that protein was pure and homogenize. For long-term storage, sample was aliquoted and performed flash freezing for -80°C storage.

Microfluidic channel preparation and functionalization: Microfluidic channels have been formed using PDMS-based soft lithography and plasma-based bonding of the PDMS-channel on silica cover glasses (#1.5 coverslips, 15 mm; Menzel, Germany) as previously reported.[20][33] Directly before bonding, the cover glasses were cleaned using the RCA-1 procedure.

For the stetching experiments involving PLL-g-PEG linkers, the microfluidic channel was equilibrated by washing with 1x PBS buffer at 25 µL/min for 10 minutes. Afterwards, the PLL-g-PEG|Biotin solution was incubated at 17 µL/min for 30 minutes and then washed with 1x PBS buffer at 25 µL/min for 10 minutes. Subsequently, NeutrAvidin-beads were incubated at 17 µL/min for several minutes until sufficient coverage (approximately 1000 - 2000 beads per FoV) was reached and then washed with 1x PBS buffer at 25 µL/min for 12 minutes.

For the stetching experiments involving the I27 and R1-3 protein constructs, the microfluidic channel was equilibrated by washing with PBS|TCEP buffer at 25 µL/min for 10 minutes. Afterwards, PLL-g-PEG|Biotin solution was incubated at 17 µL/min for 30 minutes and then washed with PBS|TCEP buffer at 25 µL/min for 10 minutes. Subsequently, NeutrAvidin was incubated at 17 µL/min for 15 minutes and again washed as mentioned previously. Then the respective construct (I27 or R1-3) was incubated at 17 µL/min for 30 minutes and then washed as mentioned previously. Finally, the amine-beads were incubated at 10 µL/min for several

minutes until sufficient coverage (approximately 1000 beads per FoV) was reached and then washed with PBS|TCEP buffer at 10 µl/min for 5 minutes.

Microfluidics-based force experiments: All measurements were performed on a Nikon Eclipse Ti-E microscope (Nikon, Düsseldorf, Germany) equipped with a 100× Plan-Apo oil immersion objective (NA 1.45), a Lumen 200 (Prior Scientific, Cambridge, UK) white light source and an Andor Zyla 4.2 sCMOS camera (2048 × 2048 pixels; Oxford Instruments, Oxford, UK). The measurements were done using a ND4 neutral density intensity filter, 1 × 1 binning of the sCMOS camera and using a dichroic filter set optimized for green fluorescent protein (GFP; excitation: 482 nm ± 9 nm, dichroic filter: 495 nm, emission: 520 nm ± 14 nm). For the stetching experiments involving PLL-g-PEG linkers, an additional 1.5x relay lens was used, resulting in a pixel size of 43.3 nm with a field of view (FoV) of ~ 90 x 90 µm², and images were recorded with an acquisition rate of 10 Hz (*i.e.*, 100 ms time lag between two frames) and an exposure time of 50 ms. Measurements involving the I27 and R1-3 constructs were done without adding the relay lens (*i.e.*, at a pixel size of 65 nm and a FoV of ~ 135 x 135 µm²) and at an acquisition rate of 4 Hz (*i.e.*, 250 ms time lag between two frames; 20 ms exposure time). Flow rates between 5 and 300 µl/min or 50 and 1500 µl/min (as indicated in the main manuscript), applied in a block- or stepwise profile, were generated by syringe pumps (WPI, #AL1000-2202) using 1 ml syringe (HSV, #4200.000V0) for functionalization reagent injection and 20 ml syringe (HSV, #4200.000V0) filled with buffer (1x PBS or PBS|TCEP) for washing and flow-based force generation. Bead displacement curves were extracted from these measurements using a previously described, custom-made single-particle tracking library.[33] This library was extended by additional procedures, which corrected the measurement for the drift of the sample (see Supporting Information section S1), extracted force and extension information with single-bead resolution (using the model described in Supporting Information section S2), and enabled for a semi automatic analysis of the obtained data sets using a cluster analysis (Supporting Information section S3).

Steered molecular dynamics simulations: R1-R3 construct was prepared using 1SJ8 and 2L7A PDB structures. The simulations were performed with Gromacs software [34] using supercomputing facilities provided by CSC, Finland. The CHARMM36m force field [35] and TIP3P water model in 0.15 M NaCl solution were used. The system was energy minimized and then equilibrated using harmonic position restraints on all heavy atoms of the protein. The temperature and pressure of the system was maintained at 310 K and 1 bar using Berendsen algorithm.[36] Integration time step of 2 fs was used in all the simulations.

The protein construct was first equilibrated for 100 ns, and then subject to unfolding in steered molecular dynamics by the end-to-end distance extension using constant velocity pulling at 2 nm/ns. Three independent replicas were performed for the unfolding using steered molecular dynamics.

Supporting Information
Supporting Information is available from the Wiley Online Library or from the author.

Acknowledgements
S.B. acknowledges funding by the Deutsche Forschungsgemeinschaft (DFG, German Research Foundation) within project BL1514/1. V.P.H. thanks Academy of Finland, Cancer Foundation Finland and Sigrid Jusélius Foundation for financial support and Biocenter Finland for infrastructure support. V.V.M. acknowledges support by the Academy of Finland (grant 323021). We gratefully acknowledge assistance from the Core Facility BioSupraMol (Freie Universität Berlin) supported by the DFG, the CSC – IT Center for Science for computational resources as well as support by Prof. Armando del Rio, who shared material that was used for generating the talin-based constructs investigated in this study.

Received: ((will be filled in by the editorial staff))
Revised: ((will be filled in by the editorial staff))
Published online: ((will be filled in by the editorial staff))

References

[1] E. Evans, "Probing the relation between force—lifetime—and chemistry in single molecular bonds," Annual review of biophysics and biomolecular structure, 30 (1), pp. 105-128, 2001.
[2] K. Neuman and A. Nagy, "Single-Molecule Force Spectroscopy: Optical Tweezers, Magnetic Tweezers And Atomic Force Microscopy," Nature Methods, 5 (6), pp. 491-505, 2008.
[3] A. del Rio, R. Perez-Jimenez, R. Liu, P. Roca-Cusachs, J. Fernandez and M. Sheetz, "Stretching Single Talin Rod Molecules Activates Vinculin Binding," Science, 323 (5914), pp. 638-641, 2009.

[4] Y. F. Dufrêne, E. Evans, A. Engel, J. Helenius, H. E. Gaub and D. J. Müller, "Five challenges to bringing single-molecule force spectroscopy into living cells," Nature Methods, 8 (2), pp. 123-127, 2011.

[5] I. De Vlaminck, T. Henighan, M. van Loenhout, I. Pfeiffer, J. Huijts, J. Kerssemakers, A. Katan, A. van Langen-Suurling, E. van der Drift, C. Wyman and C. Dekker, "Highly Parallel Magnetic Tweezers By Targeted DNA Tethering," Nano Letters, 11 (12), pp. 5489-5493, 2011.

[6] J. Eyckmans, T. Boudou, X. Yu and C. Chen, "A Hitchhiker's Guide To Mechanobiology," Developmental Cell, 21, pp. 35-47, 2011.

[7] S. Lee, R. Kamm and M. Mofrad, "Force-Induced Activation Of Talin And Its Possible Role In Focal Adhesion Mechanotransduction," Journal of Biomechanics, 40 (9), pp. 2096-2106, 2007.

[8] V. Hytönen and V. Vogel, "How Force Might Activate Talin's Vinculin Binding Sites: SMD Reveals A Structural Mechanism," PLoS Computational Biology, 4 (2), p. e24, 2008.

[9] M. Paszek, C. DuFort, O. Rossier, R. Bainer, J. Mouw, K. Godula, J. Hudak, J. Lakins, A. Wijekoon, L. Cassereau, M. Rubashkin, M. Magbanua, K. Thorn, M. Davidson, H. Rugo, J. Park, D. Hammer, G. Giannone, C. Bertozzi and V. Weaver, "The Cancer Glycocalyx Mechanically Primes Integrin-Mediated Growth And Survival," Nature, 511 (7509), pp. 319-325, 2014.

[10] C. Ciobanasu, B. Faivre and C. Le Clainche, "Actomyosin-Dependent Formation Of The Mechanosensitive Talin–Vinculin Complex Reinforces Actin Anchoring," Nature Communications, 5, 2014.

[11] M. Yao, B. Goult, H. Chen, P. Cong, M. Sheetz and J. Yan, "Mechanical Activation Of Vinculin Binding To Talin Locks Talin In An Unfolded Conformation," Scientific Reports, 4, 2014.

[12] K. Burridge, "Mangeat, P. An Interaction Between Vinculin And Talin," Nature, 308, pp. 744-746, 1984.

[13] H. Chen, P. Appeddu, J. Parsons, J. Hildebrand, M. Schaller and J. Guan, "Interaction Of Focal Adhesion Kinase With Cytoskeletal Protein Talin," Journal of Biological Chemistry, 270, pp. 16995-16999, 1995.

[14] D. Critchley and A. Gingras, "Talin At A Glance," Journal of Cell Science, 121, pp. 1345-1347, 2008.

[15] D. Critchley, "Biochemical And Structural Properties Of The Integrin-Associated Cytoskeletal Protein Talin," Annual Review of Biophysics, 38, pp. 235-254, 2009.

[16] K. Austen, P. Ringer, A. Mehlich, A. Chrostek-Grashoff, C. Kluger, C. Klingner, B. Sabass, R. Zent, M. Rief and C. Grashoff, "Extracellular Rigidity Sensing By Talin Isoform-Specific Mechanical Linkages," Nature Cell Biology, 17, pp. 1597-1606, 2015.

[17] M. Yao, B. Goult, B. Klapholz, X. Hu, C. Toseland, Y. Guo, P. Cong, M. Sheetz and J. Yan, "The Mechanical Response Of Talin," Nature Communications, 7, 2016.

[18] R. Tapia-Rojo, Á. Alonso-Caballero and J. Fernández, "Talin Folding As The Tuning Fork Of Cellular Mechanotransduction," Proceedings of the National Academy of Sciences, 117, pp. 21346-21353, 2020.

[19] A. Haining, M. von Essen, S. Attwood, V. Hytönen and A. del Río Hernández, "All Subdomains Of The Talin Rod Are Mechanically Vulnerable And May Contribute To Cellular Mechanosensing," ACS Nano, 10 (7), pp. 6648-6658, 2016.

[20] S. Block, B. Fast, A. Lundgren, V. Zhdanov and F. Höök, "Two-Dimensional Flow Nanometry Of Biological Nanoparticles For Accurate Determination Of Their Size And Emission Intensity," Nature Communications, 7, 2016.

[21] R. R. Netz and D. Andelman, "Neutral and charged polymers at interfaces," Physics Reports, 380 (1-2) , pp. 1-95, 2003.

[22] F. Oesterhelt, M. Rief and H. E. Gaub, "Single molecule force spectroscopy by AFM indicates helical structure of poly (ethylene-glycol) in water," New Journal of Physics, 1 (1), p. 6, 1999.

[23] S. Liese, M. Gensler, S. Krysiak, R. Schwarzl, A. Achazi, B. Paulus, T. Hugel, J. Rabe and R. R. Netz, "Hydration Effects Turn a Highly Stretched Polymer from an Entropic into an Energetic Spring," ACS Nano, 11 (1), pp. 702-712, 2017.

[24] C. Yuan, A. Chen, P. Kolb and V. Moy, "Energy Landscape Of Streptavidin−Biotin Complexes Measured By Atomic Force Microscopy," Biochemistry, 39,, pp. 10219-10223, 2000.

[25] F. Pincet and J. Husson, "The Solution To The Streptavidin-Biotin Paradox: The Influence Of History On The Strength Of Single Molecular Bonds," Biophysical Journal, 89, pp. 4374-4381, 2005.

[26] V. Tabard-Cossa, M. Wiggin, D. Trivedi, N. Jetha, J. Dwyer and A. Marziali, "Single-Molecule Bonds Characterized By Solid-State Nanopore Force Spectroscopy," ACS Nano, 3, pp. 3009-3014, 2009.

[27] G. I. Bell, "Models for the specific adhesion of cells to cells," Science 200, p. 618–627, 1978.

[28] F. Rico and V. T. Moy, "Energy landscape roughness of the streptavidin–biotin interaction," Journal of Molecular Recognition: An Interdisciplinary Journal, 20 (6), pp. 495-501, 2007.

[29] S. Izrailev, S. Stepaniants, M. Balsera, Y. Oono and K. Schulten, "Molecular dynamics study of unbinding of the avidin-biotin complex," Biophysical Journal, 72 (4), pp. 1568-1581, 1997.

[30] O. H. Laitinen, V. P. Hytönen, H. R. Nordlund and M. S. Kulomaa, "Genetically engineered avidins and streptavidins," Cellular and Molecular Life Sciences CMLS, 63 (24), pp. 2992-3017, 2006.

[31] F. Rico, A. Russek, L. Gonzalez, H. Grubmüller and S. Scheuring, "Heterogeneous and rate-dependent streptavidin–biotin unbinding revealed by high-speed force spectroscopy and atomistic simulations," Proceedings of the National Academy of Sciences, 116 (14), pp. 6594-6601, 2019.

[32] S. B. Fowler, R. B. Best, J. L. T. Herrera, T. J. Rutherford, A. Steward, E. Paci, M. Karplus and J. Clarke, "Mechanical unfolding of a titin Ig domain: structure of unfolding intermediate revealed by combining AFM, molecular dynamics simulations, NMR and protein engineering," Journal of Molecular Biology, pp. 841-849, 2002.

[33] P. Jönsson, A. Gunnarsson and F. Höök, "Accumulation And Separation Of Membrane-Bound Proteins Using Hydrodynamic Forces," Analytical Chemistry, 83 (2), pp. 604-611, 2010.

[34] M. J. Abraham, T. Murtola, R. Schulz, S. Páll, J. C. Smith, B. Hess and E. Lindahl, "Gromacs: High Performance Molecular Simulations through Multi-Level Parallelism from Laptops to Supercomputers," SoftwareX, 1-2, p. 19–25, 2015.

[35] J. Huang, S. Rauscher, G. Nawrocki, T. Ran, M. Feig, B. L. de Groot, H. Grubmüller and A. D. MacKerell, "CHARMM36M: An Improved Force Field for Folded and Intrinsically Disordered Proteins," Nature Methods, 14, p. 71–73, 2016.

[36] H. J. Berendsen, J. P. Postma, W. F. van Gunsteren, A. DiNola and J. R. Haak, "Molecular Dynamics with Coupling to an External Bath," The Journal of Chemical Physics, 81, p. 3684–3690, 1984.

WILEY-VCH

Supporting Information

Microfluidics-based force spectroscopy enables high-throughput force experiments with sub-nm resolution and sub-pN sensitivity

*Yannic Kerkhoff, Latifeh Azizi, Vasyl V. Mykuliak, Vesa P. Hytönen, Stephan Block**

S1. Drift Compensation

Single-particle tracking was performed using previously described, home-made MATLAB scripts.[1] This analysis provided for each bead a two-dimensional trajectory, indicating the position of the bead on the surface of the microfluidic channel over the course of the measurement. Inspection of these tracks (**Figure S1**) showed the expected shear force-induced displacement of the bead (in direction of the flow) but also the presence of notable drifts and vibrations of the sample, which have to be compensated before a meaningful assessment of the bead displacement is possible. We compensated for such vibrations and drifting effects (**Figure S1**a) by a two-step drift compensation procedure.

In a first correction step, the procedure calculated for all tracks, which covered the entire measurement run and showed sufficient localization quality (estimated by the quality of Gaussian fit to the bead's intensity distribution), the frame-by-frame displacement in x- and y-direction, followed by calculating for each frame an initial estimator of the median displacement (in x- and y-direction, respectively) from the corresponding frame-by-frame displacements. In order to reject outliers (caused, for example, by transient bead detachment or errors in the tracking procedure), this initial estimator was refined by also calculating the standard deviation of the corresponding frame-by-frame displacement distribution, by rejecting all values that were outside the range given by the initial estimator ± 2x the corresponding standard deviation, and by calculating again the median value of the remaining frame-by-frame displacement values. In a first correction step, these frame-dependent median displacement values (in x- and y-direction) were subtracted from all tracks.

The so-obtained tracks showed the expected block-wise displacement profile, but also tracks with negative displacement values (**Figure S1**b), which formally correspond to beads being displaced against the flow. Control experiments using flow-profiles, in which only half of the

beads were exposed to the flow (and hence subject to a shear force) indicated that this population is generated by immobile beads, which apparently move against the flow as the median displacement of the first compensation step was calculated using all tracks (*i.e.*, immobile as well as displaced beads). We therefore assigned the beads, which showed the strongest negative displacement (**Figure S1**b, green FEC) after the first correction step, to be immobile beads and repeated the procedure of the first compensation step (described above) using these tracks as input for the determination of the final frame-dependent median displacement values. These median displacement values were then subtracted from all tracks to correct for sample drift (**Figure S1**c), which formed the basis for all further calculations.

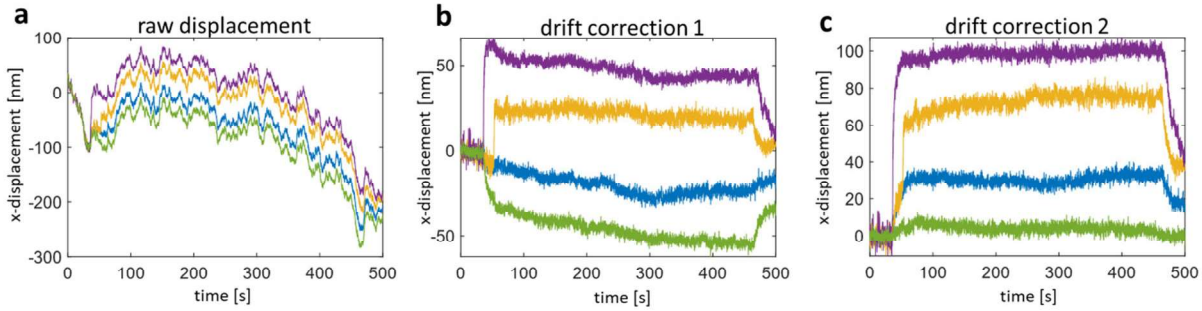

Figure S1: Overview of the two-step drift compensation. The raw x-displacement (in flow direction) of four displacement curves, generated by applying a block-shaped force profile to the PLL-g-PEG-linked beads, shows notable distortion by stage vibrations (high frequency oscillations) and drift of the sample (a). The vibrations typically show amplitudes on the nm-scale and are indicative for sub-nm single shot localization accuracy, reflecting the high spatial accuracy achievable when using bright fluorescent beads. To compensate for such distortions a two-step compensation procedure is used (see text for more details), with (b) and (c) showing the results after the first (b) and second compensation step (c), respectively.

S2. Extension and Force Calculation

In our microfluidics-based force spectroscopy method, we monitor the x-displacement of beads, Δx, as function of the applied shear force, F_x. Hence, to quantify the nanomechanical properties of the linker, which connects the bead with the surface of the microfluidic channel, it is necessary to model the process of bead displacement (**Figure S2**). Input values of this model are parameters, which are either set by the user (applied flow rate f) or extracted from the measurement (bead displacement in flow direction, Δx, and bead intensity I). Output values are (as will be detailed below), the shear force applied to bead F_x and the part of F_x, which acts in direction of the linker (F), the linker length ΔL, and the bead's distance to the surface, Δz, of the microfluidic channel.

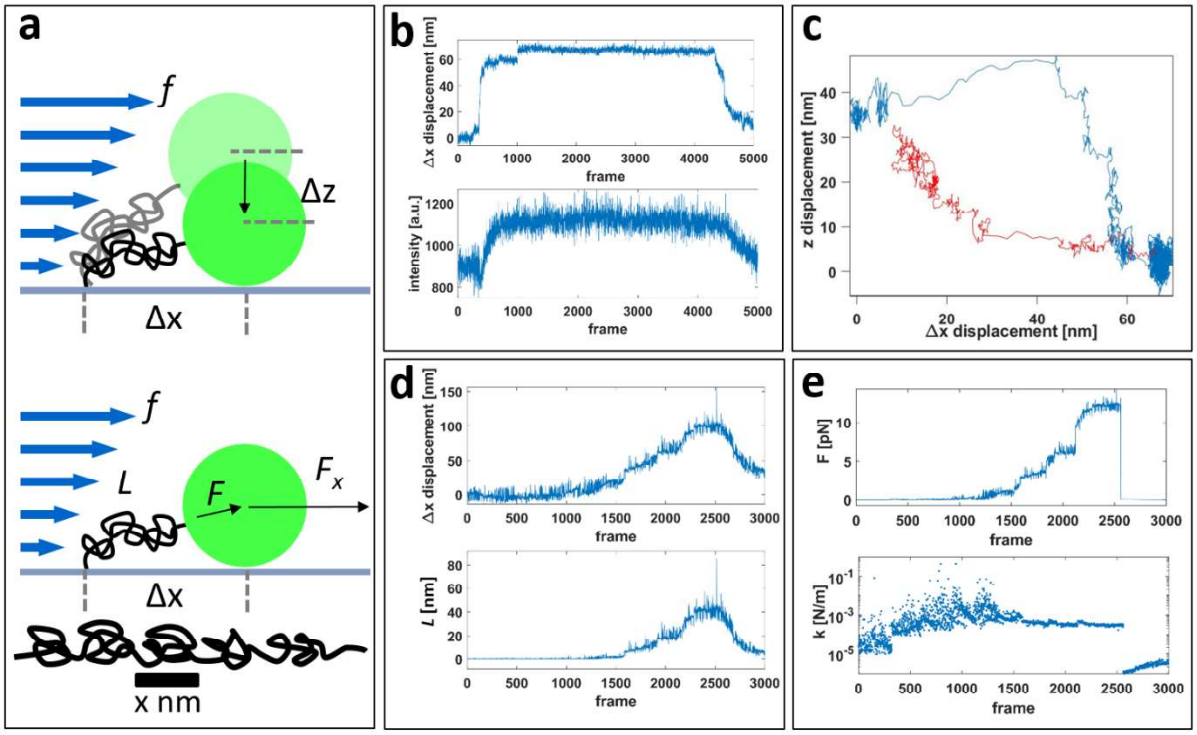

Figure S2: Overview of the relationship between the experimentally determined values (applied flow rate *f*, bead displacement in flow direction, Δ*x*, and bead intensity) and the properties extracted from these values (force applied to bead F_x and linker *F*, linker length Δ*L*, and distance to the surface, z, of the microfluidic channel). (a) In absence of a flow, the bead is only subject to random forces and its time-averaged center position (projected on the surface) will coincide with the anchoring point of the linker to the surface. The bead distance to the surface will, however, not average out but depends on the type of linker (see text for details). As a consequence, application of a shear force to the bead will generate a torque that tilts the bead towards the surface. The bead will be in contact with the surface, if the shear force exceeds a threshold value, which depends on the nanomechanical properties of the linker. After touching the surface, the linker length *L* as well as the part of F_x, which acts in direction of the linker (*F*), that can be directly calculated knowing bead radius *r* and displacement Δ*x* (a, bottom). (b, c) The tilting process can be captured using TIRF illumination, in which the fluorescence intensity of the bead decays exponentially with distance to the surface (b). Application of a block-wise shear force profile (0.06→17→0.06 pN) also generates a block-wise shape of bead displacement and intensity. Estimating the bead's surface separation based on the change of its intensity allows to extract the 3-dimensional bead displacement, the x- and z-component of which is shown in (c). The initial position and force-dependent displacement is indicated in blue, whereas the return after force-release is indicated in red. (d) The bead tilt can be neglected in the data analysis, if the shear rate is large enough to ensure that the bead is always in contact with the surface. This is demonstrated in (e), which gives bead displacement Δ*x* (top) and linker length *L* (bottom) for application of a step-wise shear force profile: 0.06→0.58→1.15→2.88→5.75→8.63→11.50→17→0.06 pN. The linker's spring constant *k* derived using this data (f) saturates for shear force exceeding 2.88 pN. At this shear force, the bead starts to touch the surface and reproducible *k*-values are extracted.

The shear force acting on the bead F_x directly follows by multiplying the applied flow rate f with the channel- and bead-specific shear force coefficient, $\tau = 0.0115$ pN/(μL/min), which was derived by recently performed calibration experiments:[2]

$$F_x = f \cdot \tau. \quad \text{(S1)}$$

In absence of a flow, the bead is only subject to random forces and its center position (projected on the surface) will fluctuate around the point, at which the linker contacts the surface. As the temporal resolution is far below the timescale of these fluctuations, our experiments will record a time-averaged center position, which provides information on the contact point of the linker. As such confines conformational fluctuations can take place only above the surface, the bead distance to the surface will, however, not vanish in the time average but adopt a non-zero value, which depends on the type of linker. For a polymer in a good solvent (such as PEG chains in PBS), the length scale of his distance will be given by the polymer's radius of gyration (~ 8 nm for a PEG chain of ~ 80 monomers).[3] For proteins, the length scale of his distance is given by the distance of the N- and C-termini (~ 12 nm for the protein constructs I27 and R1-3).
As a consequence, application of a shear force will generate a torque, which pushes the bead towards the glass surface (**Figure S2**a,top). Owing to the TIRF illumination used in our experiments, which generates an evanescent excitation wave at the surface and causes the bead's fluorescence intensity I to be a function of the bead's surface separation z, this motion along the z-axis can be followed based on recording changes to the bead's intensity (**Figure S2**b). Based on the penetration depth of the evanescent wave z_{EV} (~ 150 nm) in TIRF microscopy, the the bead's surface separation z is estimated from the intensity I according to

$$z = -\log(I/I_0) \cdot z_{EV}, \quad \text{(S2)}$$

in which I_0 denotes the intensity of the bead if it touches the surface ($z = 0$). A representative example for this analysis is given in **Figure S2**b and c, which shows the stretching of a PLL-g-PEG chain by application of a block-wise shear force profile (0.06→17→0.06 pN). As expected, this leads to block-wise profiles of the bead's displacement and intensity, which enables to plot the bead's displacement in the xz-plane using Eq. S2 (**Figure S2**c). Initially, the bead hovers ~ 35 nm above the surface at a force of 0.06 pN. This value is much larger than the one expected based on the radius of gyration of a 3.4 kDa PEG chain (~ 8 nm), which is attributed to an overestimation of the penetration depth of the evanescent wave. When the shear force is

increased to 17 pN, the bead is displaced in x-direction by 50 nm and then pushed to the surface (blue course), while relaxation to 0.06 pN causes the bead to return almost completely to its initial position (red course).

The tilting motion of the bead makes it challenging to quantify linker length L and force F acting on the linker solely from the observed bead displacement. These relationships, however, become simple, if the bead touches the surface. In this case, it is possible to calculate the linker length L by simple geometric considerations, which lead to

$$L = \sqrt{\Delta x^2 + r^2} - r. \quad \text{(S3)}$$

(with r denoting the radius of the bead, which is 100 nm in our experiments). Furthermore, the force acting on the linker F can be calculated by multiplying the shear force F_x with the angle of the linker:

$$F = F_x \cdot \cos(\text{atan}(r/\Delta x)). \quad \text{(S4)}$$

Using these equations, it is possible to extract linker length L and force F acting on the linker from the observed shear force-dependent bead displacement (**Figure S2**d) and hence to translate displacement curves into force-extension curves (**Figure S2**d,e). Knowing the force-dependent linker extension allows to calculate the linker's spring constant k based on:

$$k = F/L. \quad \text{(S5)}$$

A representative example for this analysis is given in **Figure S2**d and e, which shows the stretching of a PLL-g-PEG chain by application of a step-wise shear force profile (0.06→0.58→1.15→2.88→5.75→8.63→11.50→17→0.06 pN). Inspection of the linker's spring constant k (**Figure S2**e) indicates that this quantity increases for small shear forces and saturates for shear force exceeding 2.88 pN. This behavior is attributed to bead tilting, which leads to an underestimation of the spring constant. For shear forces exceeding 2.88 pN, the bead is in contact with the surface and reproducible k-values can be extracted. Note that in our experiments on PEG chain stretching, rupture of biotin-NeutrAvidin interactions or the unfolding of talin's rod domain, all characterizations have been done in the limit of a surface-touching bead.

S3. Cluster Analysis

S3.1. Cluster Analysis Procedure

In the first step of the cluster analysis, all possible pairs of 2 displacement curves (Δx_i, Δx_j) from one experimental run are taken. The indices *i* and *j* ranging between 1 and the number of recorded displacement curves, *N*. Furthermore, the curve IDs have been sorted such that the median value of the bead displacement at highest shear force increases with increasing index (*i.e.*, the curves with the smallest displacements have small values of i and j, respectively, and vice versa). For each of these pairs, the standard deviation of the difference of the displacement curves is calculated:

$$sd(i,j) = \mathrm{std}(\Delta x_\mathrm{i} - \Delta x_\mathrm{j}). \quad \text{(S6)}$$

This information is stored in a two-dimensional matrix (in which the x- and y-dimension correspond to the IDs of the two displacement curves of a particular pair). Inspecting this matrix as heat map of log(*sd*) (**Figure S2**a,top) showed the occurrence of patterns in the *sd*-values of displacement curves, indicating that curves, which are similar to each other, are also similar in their similarity to other curves. In order to group displacement curves according to these similarity patterns, the cluster algorithm calculates a second similarity map by calculating the variance of the log(sd)-values:

$$si(i,j) = 1/\mathrm{N} \cdot \sum_{n=1}^{N} (\log(sd(i,n)) - \log(sd(j,n)))^2. \quad \text{(S7)}$$

A small value of *si*(*i*,*j*) therefore indicates that the displacement curves *i* and *j* have similar displacement behavior with respect to all other curves. The cluster analysis automatically groups displacement curves into populations of similar *si*-values, by applying a permutation π to the displacement curve IDs, which maximizes the areas of low si-values along the diagonal of the *si* matrix. The result of this procedure is shown in **Figure S2**a,bottom, which displays the heat map of *si*(π(*i*),π(*j*)) (*i.e.*, of the *si*-map after application of the permutation π to the displacement curve IDs). In this representation, displacement curves of similar displacement behavior form blue "blocks" along the diagonal, which strongly simplifies the identification of the corresponding populations (**Figure S2**b). Blue areas (small *si*-values) in off-diagonal entries indicate a certain overlap in the similarity between curves of the different populations and can be used to refine the automatic assignment done by the cluster analysis. In any case, the populations identified by the cluster analysis were always manually confirmed before being included in follow up analyses.

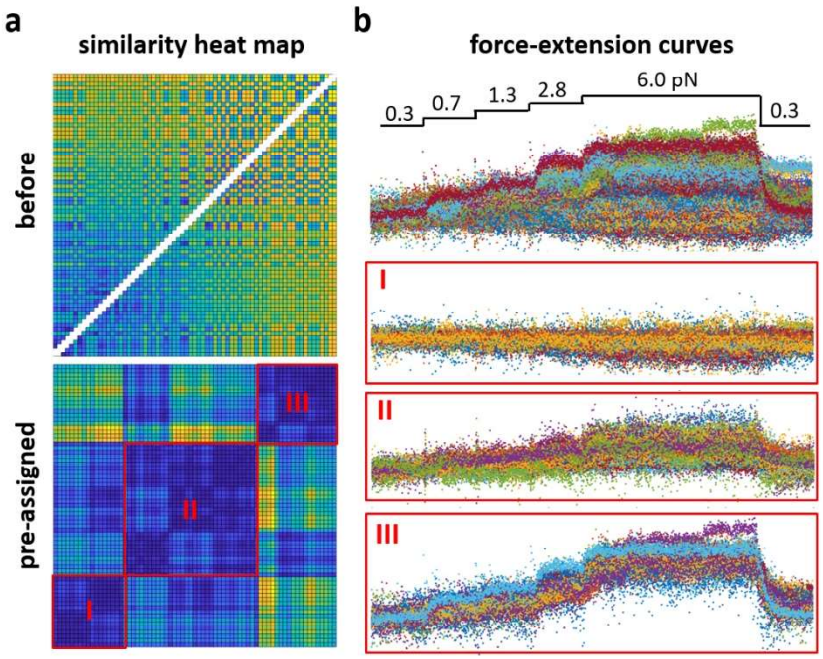

Figure S3: Pre-assignment of displacement curves by a cluster analysis. (a) The cluster analysis first calculates for each recorded force curve the mean squared difference to all other force curves, yielding a heat map (blue = high similarity, yellow = low similarity). These heat maps exhibit patterns, which can be used to automatically pre-assign the force curves into subpopulations. (b) The top-most plot gives an overlay of all force curves of an I27 stretching experiment (at loading forces as indicated). It exhibits a broad distribution of different behaviors, caused here by differences in the molecular configuration of the particular beads. Application of the cluster analysis (left) pre-assigns these curves into 3 populations I – III (for this particular measurement), in which the force curves show high similarity in their force-dependent extension behavior.

3.2. Cluster Analysis Validation

The cluster analysis was validated by simulation of 500 displacement curves (**Figure S**a) with five defined input populations (**Figure S**b) and comparison to the automatically defined output populations (Figure S4d-h) extracted from the cluster analysis-based color map (**Figure S**c). The simulated displacement curves (**Figure S**a) show a hysteresis-bearing block-wise profile with a displacement scattering around 0 for the first 500 values (furthermore denoted as frames) and then a steep linear increase for 100 frames, a flat increase for 400 frames. The displacement curves then show a stable displacement according to their population (0, 0.5, 1.0, 1.5 pixel) with a random scattering around this value for 2300 frames. Afterwards the values show a steep decrease for 100 frames and a lower decrease for 400 frames and then stabilize at 0 with a small random offset for the last 200 frames.

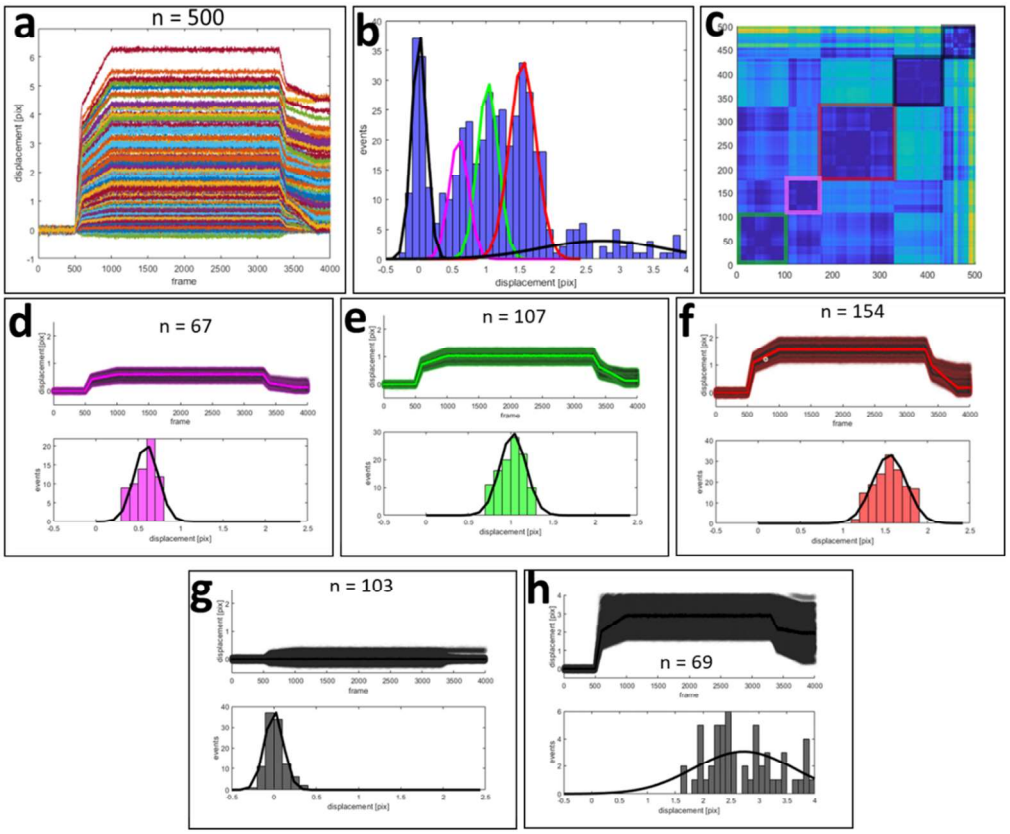

Figure S4: Overview of the cluster analysis validation by classification of defined input populations of simulated FECs. A set of 500 displacement curves was simulated, consisting of five defined populations (0, 0.5, 1.0, 1.5 pixel displacement and artifact-bearing displacement curves, showing a high displacement and no sufficient return) with 100 displacement curves each (a). The median displacement histogram of the 500 simulated displacement curves with Gaussian fits gained from classified populations after cluster analysis shows the distinct simulated populations (b). The color map after cluster analysis (c) also shows five defined cluster groups (green, purple, red, 2x black). The purple cluster group contains 67 displacement curves (d) with a peak at 0.6. The green cluster group contains 107 displacement curves (e) with a peak at 1.0, and the he purple cluster group contains 154 displacement curves (f) with a peak at 1.5. The two black cluster groups contain 103 immobile (g) and 69 artifact-bearing (h) displacement curves.

The artifact-bearing displacement curves show a high random offset, resulting in a high displacement and no sufficient return in the last 200 frames. The median displacement histogram of the 500 simulated displacement curves shows four distinct peaks representing the simulated populations (**Figure S**b). The four peaks of the defined populations (0, 0.5, 1.0, and 1.5) as well as some artifacts (at more than 2 pixel displacement) are clearly visible and highlighted by Gaussian fits which were generated based on the defined populations of the

cluster analysis (**Figure S**c-g). The color map of the cluster analysis (**Figure S**c) shows distinct cluster groups, which are highlighted with rectangles in green, purple, red, and two times black. The extracted displacement curves and median displacement histogram of the purple cluster group (**Figure S**d) is revealed to be the simulated population with a 0.5 displacement. While the input population was correctly defined, only 67 of 100 input displacement curves are classified in this group. As the immobile populations (**Figure S**g) was correctly defined with 103 displacement curves, we attribute the difference in input and output displacement curves of the 0.5 population to a loss of displacement curves to the green population (**Figure S**e). The green population contains 107 displacement curves with a displacement around 1.0 and is therefore correctly defined. The red population (**Figure S**f) contains 154 displacement curves with a displacement around 1.5. This shows that also this input population is correctly defined despite having 54 more displacement curves than the simulated 100 ones.

We attribute this to the fact, that by chance the simulated artifact-bearing curves can have a very small offset and thus being quite similar to the displacement curves of the defined input populations. This is supported by **Figure S**h, as only 69 of 100 simulated artifact-bearing displacement curves are classified as artifacts. However, the displacement curves with are strong offset are reliably grouped together and could in real experiments therefore be excluded from the further analysis. Conclusively, the validation simulation shows, that while the input ratios of simulated displacement curves are not necessarily correct conserved, at least the displacement profile of the three input populations as well as immobile and intense artifact-bearing displacement curves are correctly identified, demonstrating the utility and reliability of the automated cluster analysis.

WILEY-VCH

S4. Supporting Displacement Curves

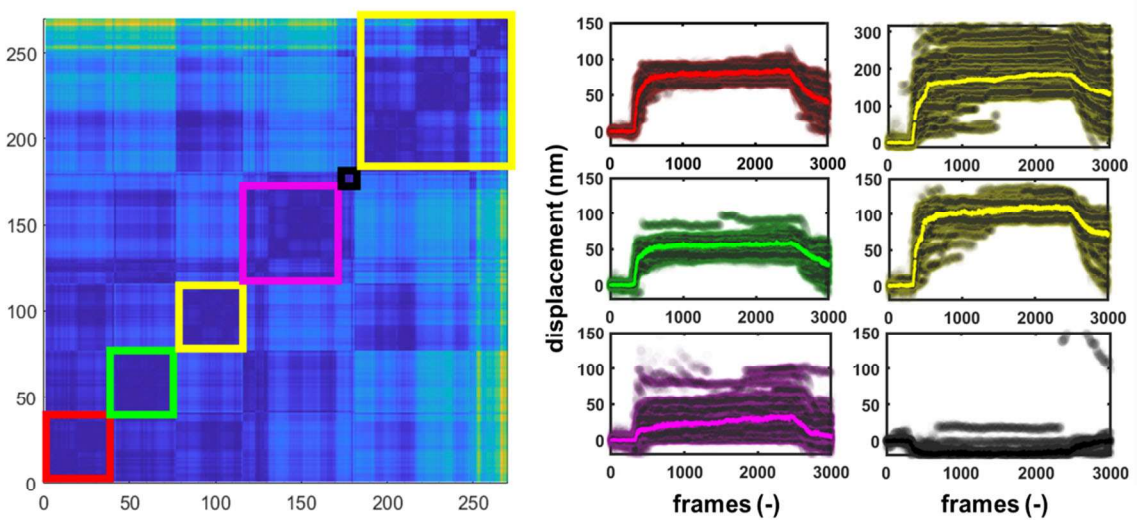

Figure S5: Enlarged versions of Figure 2e and 2f of the main manuscript.

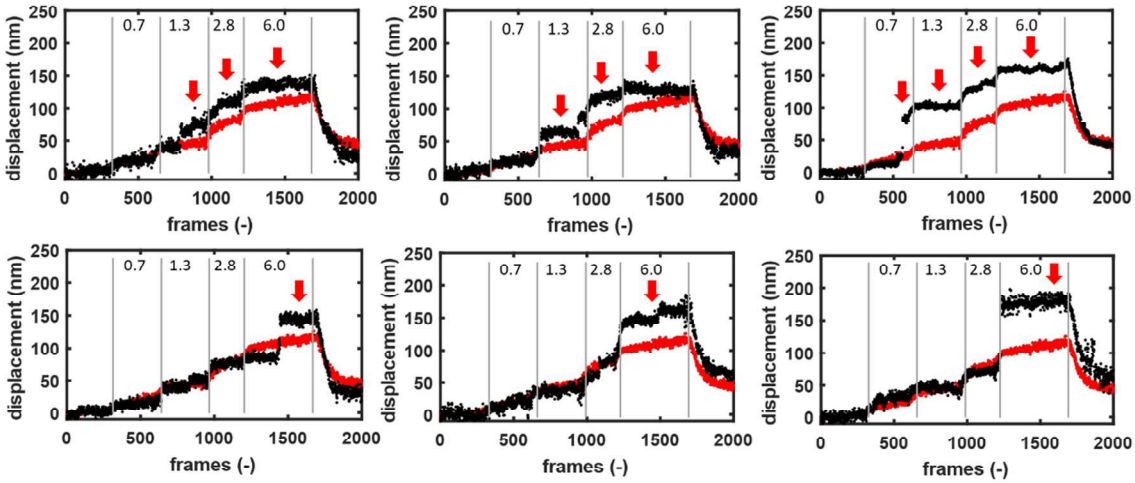

Figure S6: Six representative displacement curves of the R13 construct (black) show a force dependent R3 unfolding. The median displacement of all displacement curves of beads being linked by a single construct are shown in red and the forces acting on the protein constructs (0.7, 1.3, 2.8, and 6.0 pN) are shown on top of the curves. Unfolding events are indicated by red arrows.

References

[1] S. Block, V. Zhdanov and F. Höök, "Quantification Of Multivalent Interactions By Tracking Single Biological Nanoparticle Mobility On A Lipid Membrane," Nano Letters, 16 (7), pp. 4382-4390, 2016.

[2] S. Block, B. Fast, A. Lundgren, V. Zhdanov and F. Höök, "Two-Dimensional Flow Nanometry Of Biological Nanoparticles For Accurate Determination Of Their Size And Emission Intensity," Nature Communications, 7, 2016.

[3] S. Liese, M. Gensler, S. Krysiak, R. Schwarzl, A. Achazi, B. Paulus, T. Hugel, J. P. Rabe and R. R. Netz, "Hydration Effects Turn a Highly Stretched Polymer from an Entropic into an Energetic Spring," ACS Nano, 11, p. 702–712, 2016.

5. Discussion & conclusion

The focus of this work was the development of new high-throughput single-entity analysis methods to allow for the investigation of biomembrane-associated interactions from the cellular to the molecular scale. These interactions, which include e.g., the binding of pathogens to host cells, the binding of polymer-based inhibitors to viruses, and the response of biopolymers (such as proteins) to mechanical forces, are often very delicate and complex due to weak multivalent interactions. Getting new insights into those processes is thus very interesting for the screening of new antiviral agents [173] [174] [175], the understanding of transmembrane signaling based diseases [47], as well as basic research e.g., in the field of mechanobiology [176]. New methods to study these biochemical events must be easy to use to enable a wide application in the scientific field, very sensitive to detect distinct cellular or molecular populations, and generate a large amount of data to assure statistical power. While to this date, there is a variety of methods already available to address these requirements, only few methods combine them all. This is especially true for the most common single-molecule force spectroscopy methods, namely atomic force microscopy, optical tweezers, and magnetic tweezers, as these methods are usually designed for high sensitivity or high throughput applications. However, to study weak multivalent membrane-associated interactions, such as protein unfolding or the dissociation of receptor-ligand complexes, it is essential to address both aspects. To tackle the shortcomings of current methods, it was thus necessary to establish new approaches in order to monitor the response of delicate biological systems to external stimuli, with single-cell and single-molecule resolution.

In the first project, a fast, yet sensitive, and easy to use Fiji-macro was developed [38] to segment densely packed cells in a two-dimensional monolayer, and quantify the intensity of a fluorescent reporter with single-cell resolution. Plotting the single-cell intensity in a logarithmic scale allowed for a clear visualization of cellular populations, representing cells with or without a fluorescence signal, higher than the background intensity. This allowed for an automatic determination of fluorescent and non-fluorescent fraction of the cells, which (depending on the reporter system) provided information about the transfection efficiency using different amounts and ratios of DNA and PEI, or the amount of virus infected cells. This method was used to screen the inhibition potency of hyperbranched polymer-based virus binding inhibitors against HSV-1 [168], based on the IC_{50} value. A main goal of this project was to establish a method which is as easy to use as possible, which was achieved by implementing an option for the automatic estimation of analysis parameters (i.e., background thresholding, segmentation sensitivity, and intensity cutoff of cellular populations), leading to a reduction in manual work and need for expertise in handling single-cell segmentation methods. A correlation of the analysis results with manually and automatically chosen analysis parameters showed an excellent correlation of (R^2 >= 0.98) for widefield and confocal imaged fluorescent cells.

This single-cell segmentation approach was then extended in the second project, where a method was developed to estimate the number of clustered fluorescent nanoparticles below the diffraction limit, on confocal imaged cells, with single-cell resolution [81]. The aim of this project was to establish a new method, which is able to quantify the number of virus-like particles bound to cells, but at a resolution

where tens of cells can be imaged in parallel to assess the cell-to-cell heterogeneity in particle binding. This is especially challenging as the nanoparticles (~ 200 nm) and the PSF of their emitted light (~300 – 400 nm) are near the pixel-size (180 – 360 nm) of the confocal imaged cells, which leads them being displayed as blurred spots with increased intensity, without the possibility to resolve them individually. To overcome this resolution-based limitation, an approach of parallel single-cell and single-nanoparticle analysis was developed, where the cells were segmented and the local intensity maxima per cell were identified and a subsequent application of a low-pass filter and intensity correlation allowed for an estimation of the number of clustered fluorescent nanoparticles within each local intensity maximum. The accuracy of the estimation was validated by the simulation of fluorescent nanoparticles of different densities and at different resolutions and was found to be in the range of ~ 80 – 100 %, compared to the number of simulated nanoparticles. An early version of this method was used to quantify the amount of SARS-CoV-2 particles bound to Vero E6 cells under treatment with negatively charged polysulfates [169].

Within the third project, the quantification of nanoparticles was extended from static images to dynamic image series, using single-particle tracking. For this, a tutorial for the analysis and refinement of single-particle tracking experiments was developed [53], which focuses on the quality assessment of such analysis approaches, and especially gives advice for choosing a suitable maximal linking distance, to ensure the quality of derived single-particle tracks. It was initially intended to probe for the ligand dependent change in diffusion due to different oligomerization states of GM1 in SLBs (see 7.1.1 Multivalent GM1 binding of choleratoxin subunit B) and BMPRs in hybrid supported lipid bilayer systems, but instead revealed some mobility-based limitations in setting up this system (see 7.1.2 Hybrid lipid bilayer formation). However, the SPT method was then used to quantify the BMP2 induced immobilization of BMPR2 on endothelia tip-cells [170], to track IAVs binding on hybrid lipid bilayers containing red blood cell membrane material [71], and also to track the displacement of 200 nm sized fluorescent beads in a microfluidic setup, which was used in project four.

Within the fourth project, a new sensitive high-throughput single-molecule force spectroscopy method based on hydrodynamic forces [172] was developed. To this end, TIRF microscopy was combined with microfluidics and SPT to exert low to sub-pN forces on single molecular targets, bound to fluorescent beads and immobilized on the glass surface of a microfluidic channel and to observe their mechanical response (i.e., stretching, unfolding, and dissociation) with sub-nm resolution. This combination of several techniques allowed for a massive parallelization of measurements, due to the high surface coverage of fluorescent beads in the microscopy FoV (1000+ beads each). The flow-based force calibration of the microfluidic architecture based on the 2D flow nanometry approach from Block *et al.* [86], also allowed for the calculation of acting forces, without the need for assumptions based on the parabolic flow profile in the channel. Also, the beads used to apply forces on molecular targets were 200 nm in size, while other approaches used micrometer sized beads, which allowed to apply especially low forces (down to rang of approximately 0.01 pN) as the flow-based shear force is scaling with the size of the used beads. This method was validated by successfully reconstructing the mechanical properties and the valency of PEG-linkers and was then used to probe for the energy barriers of the dissociation of multivalent biotin-

NeutrAvidin complexes which were found to be at 3 Å and 5.7 Å and to study the unfolding of the third rod domain (R3) of talin at such low forces, previously not achieved by any other method.

To conclude, this work expands the repertoire of suitable biochemical and biophysical methods for the high-throughput investigation of the properties and interactions of cells, nanoparticles, and molecules with single-entity resolution, and is therefore a valuable contribution to the scientific community.

6. Outlook

This work demonstrated the establishment of several high-throughput single-entity analysis methods from the cellular to the molecular scale. While these methods were mainly applied to well-studied model systems, such as quantifying GFP expression in cellular monolayers or investigating the mechanical response of PEG linkers, to assess their sensitivity and high-throughput capabilities, they are intended to be used in further applications.

The automated single cell segmentation and parallel nanoparticle quantification methods could be combined and established as a platform to characterize virus binding and inhibition, as they allow precise quantification of virus infection and attachment to cells under different conditions. Since the nanoparticle quantification method has only been used with polystyrene beads and virus-like particles, further testing with real viruses such as IAV, HSV-1, or SARS-CoV-2, in combination with binding inhibitors, would be a suitable next step. The refined single particle tracking could be used on a larger scale to quantify the oligomerization processes of transmembrane receptors such as BMPRs and their responses to ligands and co-receptors on living cells or in hybrid lipid bilayers. This will first require overcoming the current limitations of incorporating membrane material into synthetic lipid bilayers (such as uniform fusion and distribution of native lipids and proteins), but if successful, this hybrid system would be a valuable addition to measurements performed on cells. The newly established method of single-molecule hydrodynamic force measurement could be used to further study the mechanical response of talin under sub-pN forces, e.g., to determine the transient folding and refolding of intermediate states or the influence of vinculin binding after talin unfolding. It could also be used to study the energy barriers of receptor-ligand of the viruses mentioned above, allowing for a multi-scale investigation of these membrane-associated interactions.

7. Appendix

This chapter contains additional data and information which do not belong to the main body of the thesis. This is namely unpublished data (7.1 Supplementary data) and the abbreviations (7.2 List of abbreviations) used in the main text.

7.1 Supplementary data

The unpublished data presented and discussed in this section regards the successful reconstruction of the multivalent GM1 binding of choleratoxin subunit B by refined single-particle tracking [53] and the challenges in the preparation of hybrid lipid bilayers [68] e.g., used for virus binding studies [171].

7.1.1 Multivalent GM1 binding of choleratoxin subunit B

To test whether the SPT approach of [53] is sensitive enough to detect different oligomerization states based on the diffusion coefficient (which according to the Evans-Sackmann model should depend on the hydrodynamic radius of the diffusing object [108] embedded in the SLB) Alexa Fluor 488 (AF488)-labeled CTxB was incubated in SLBs containing GM1 at different concentrations (Supplemental figure 1a) and tracked (Supplemental figure 1b) to quantify the GM1-dependent diffusion coefficient profile (Supplemental figure 1c) of CTxB.

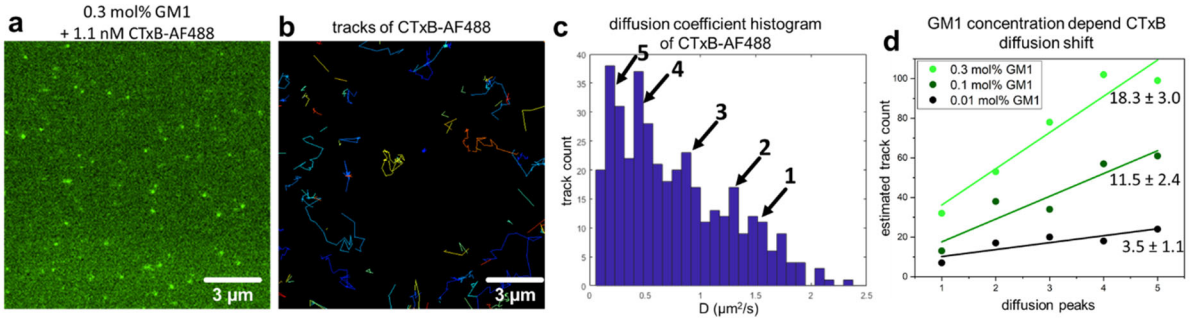

Supplemental figure 1: Quantification of multivalent GM1 binding of CTxB by refined SPT. AF488 labelled CTxB was incubated on POPC SLBs containing GM1 in different concentrations and imaged via TIRF microscopy (a). The derived images series were tracked (b) and the extraction of the diffusion coefficients of the tracks revealed distinctive histogram peaks (c). The tracks were attributed to the diffusion peaks and their counts for the different GM1 concentrations in the SLB (0.01, 0.1, and 0.3 mol %) plotted and linear fits were applied (d). With increasing GM1 concentration the slope of the fits also increases (3.5 ± 1.1, 11.5 ± 2.4, and 18.3 ± 3.0).

As expected, the histogram of the diffusion coefficients of the tracked CTxB-AF488 incubated on SLBs containing 0.3 mol% GM1, shows distinct peaks, which are interpreted as CTxBs multivalently bound to different numbers of GM1, where slower peaks indicate higher valency. The five most prominent peaks were determined, where the peak with the lowest *D* at about 0.1 µm^2/s was attributed to CTxB with the lowest binding valency, and the peak with the highest *D* at about 1.5 µm^2/s was attributed to CTxB with the highest valency. The number of tracks within the five peaks was then plotted for the different concentrations of GM1 contained in the SLBs and linear fits were applied (Supplemental figure 1d). As expected, the higher the amount of GM1 in the SLB was, the higher was the total number of derived tracks, as more GM1 allows for more binding of CTxB. However, the ratio of the peaks seems to be constant for all concentrations, indicating that a higher GM1 concentration does not lead to a shift to higher binding valencies.

7.1.2 Hybrid lipid bilayer formation

The SPT-based oligomerization quantification approach was initially intended to be used on BMPRs imbedded into hybrid supported lipid bilayers, but the tracking revealed some mobility-based limitations in setting up this system. Firstly, it was intended to use red labelled receptors (e.g., mCherry fusion proteins and atto-565 dyes) but the pure POPC SLBs already contained a significant amount of mobile red particles (Supplemental figure 2a) which are mainly attributed to dye residues form other experiments. Tracking of these mobile events in the red channel (Supplemental figure 2b) revealed that also here distinct diffusion based populations are present (Supplemental figure 2c), and thus there is a high risk of confusing the labeled receptors with the dye residues, which would presumably corrupt the results.

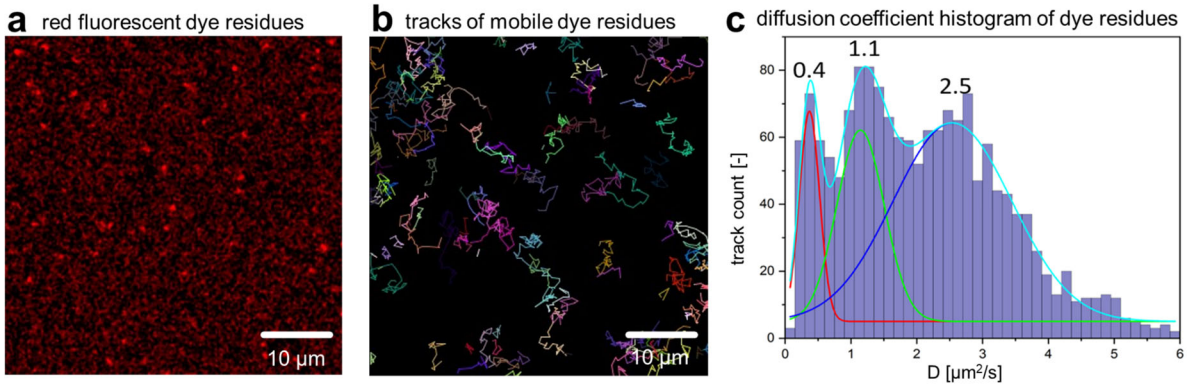

Supplemental figure 2: Presence of red dye residues in hSLBs. When preparing and imaging hSLBs at high intensites, an unspecific mobile population of red dye resiudes was found (a). When tracked (b) these dye residues showed three unexplained distict diffusion coefficient histogram peaks (c).

To avoid this problem, it was decided to change the color of the receptor labels to the green channel (e.g., GFP fusion proteins and Atto-488 dyes) as there were no prominent mobile dye residues in the POPC lipids detected here. The labelling specificity of Atto-488 labelled benzylguanine to SNAP-tagged receptors was tested by confocal imaging of HEK cells, transfected with ß-galactosidase (control, no labelling expected) and transfected with SNAP-tagged BR2-TC1 (target receptor, specific labelling expected) (Supplemental figure 2a, top). The confocal images of the ß-galactosidase transfected cells, showed no specific fluorescence signal while the cells transfected with SNAP-tagged BR2-TC1 showed a high fluorescence signal, indicating a high specificity of the SNAP-labelling system. When preparing native membrane vesicles from both labelled cells and fusing them with synthetic vesicles to build hSLBs, TIRF imaging on the other hand revealed the presence of many immobile fluorescent particles in both samples (Supplemental figure 2a, bottom). While the confocal images indicate a high level of labelling specificity, the single-molecule resolution by TIRF imaging shows that there are still dye residues left in the sample, even after intense washing. This carries the risk of confusing these dye residues with immobile receptors. However, the sample with SNAP-tagged BR2-TC1 transfected cells, also contains large fluorescent vesicles, which are suspected to be unruptured NMVs, contain the specific labelled BR2-TC1 receptors. Transfection, cultivation, labelling, and imaging of HEK cells as well as preparation of native membrane vesicles was performed by Christian Hiepen, Jerome Jatzlau, and Michael Trumpp according to the protocol found in [68].

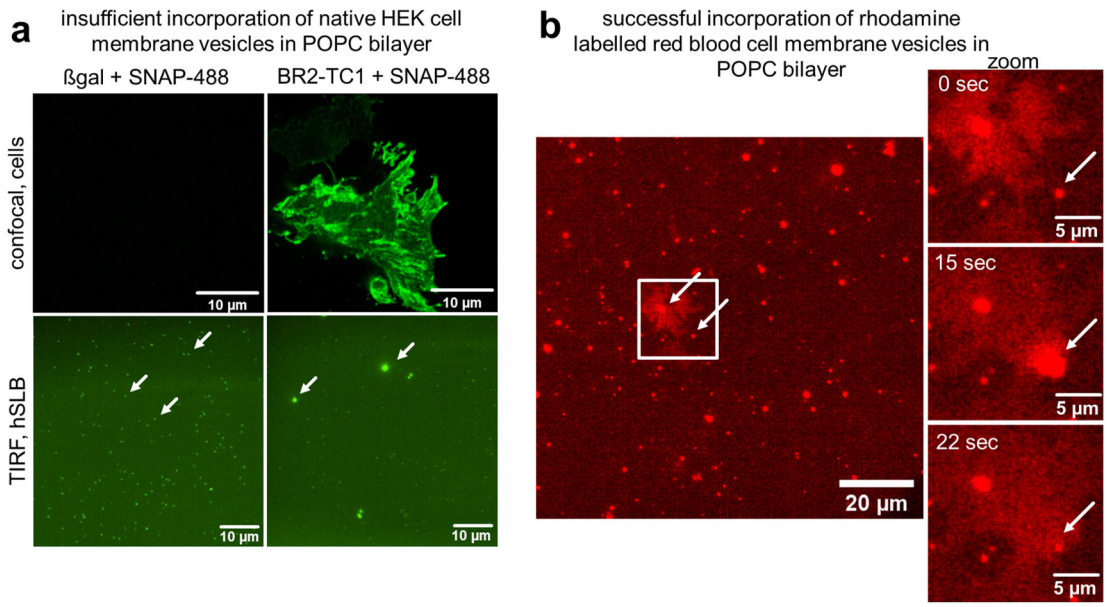

Supplemental figure 3: Preparation of hSLBs with native cell membrane material derived from HEK and red blood cells. Native cell membrane vesicles derived from HEK cells transfected with ßgal or labelled BR2-TC1 receptors showed no homogenious incorporation of native material into the synthetic SLB (a). Also immobile dye residues remained in the sample, which can be resolved by TIRF but not by confocal microscopy. Rhodamine labelled red blood cell membrane (RBCm) vesicles successfully fused into a synthetic POPC SLB (b) building a hybdrid lipid bilayer.

In a similar approach used in [171] a hSLB was formed by fusing rhodamine labelled RBCm vesicles into a POPC SLB (Supplemental figure 2b) to allow for transient virus binding studies. Red blood cell membrane vesicles were prepared by Chuanxiong Nie according to the protocol found in [171] and tracking of IAVs on the RBCm containing hSLB was performed by Matthias Wallert and Stephan Block.

Similar to hSLBs made with NMVs from HEK cells, large, non-fused vesicles with labeled material were observed. However, many of these vesicles showed clear fusion and distribution into the surrounding POPC-SLB (three zoomed inlets of Supplemental figure 2b). This fusion could not be observed in NMVs from HEK cells, leading to the assumption that the effectiveness of the fusion process is dependent on the source of membrane vesicles. Thus, for the continuation of this project, it would first be necessary to systematically study the fusion of native and synthetic vesicles to obtain a uniform hybrid lipid layer. If the membrane receptors incorporated into such a homogenous hSLB then show mobility, it would be possible to apply a SPT-based approach (like with the CTxB and GM1 system of 7.1.1) to study the ligand dependent oligomerization of BMPRs.

7.2 List of abbreviations

µl	micro liter
2D	two dimensional
ACE2	angiotensin converting enzyme 2
AF488	Alexa Fluor 488 dye
AFM	atomic force microscopy
APD	avalanche photodiode
BMP	bone morphogenetic protein
BMPR	bone morphogenetic protein receptor
CCD	charge-coupled device
CLSM	confocal laser scanning microscopy
CTxB	cholera toxin subunit B
D	diffusion coefficient
F	force
fN	femto newton
FOP	fibrodysplasia ossificans progressiva
FOV	field of view
FRAP	fluorescence recovery after photobleaching
Fs	shear force
GFP	green fluorescent protein
GM1	monosialotetrahexosylganglioside
h	hour
HEK	human embryonic kidney
HSPG	hyperbranched polyglycerol sulfate
HSV-1	herpes simplex virus
HVEM	herpes virus entry mediator
IAV	influenza A virus
IC_{50}	average 50 % inhibitory-concentration
k_B	Boltzmann constant
LED	light emitting diode
min	minute
MT	magnetic tweezers
nm	nanometer
NP	nanoparticle
OT	optical tweezers
PDMS	polydimethylsiloxane
PEG	polyethylene glycol
PLL	poly-L-lysine
PMT	photoelectron multiplier tube

pN	pico newton
POPC	phosphatidylcholine
PSF	point spread function
r	radius
RBCm	red blood cell membrane
ROI	region of interest
SA	sialic acid
SARS-CoV-2	severe acute respiratory syndrome coronavirus 2
sd	standard deviation
SLB	supported lipid bilayer
SMAD	suppressor of mothers against decapentaplegic
SNAP-tag	a self-labeling protein tag
SPT	single-particle tracking
T	temperature
TIRFM	total internal fluorescence reflection microscopy
v	velocity
WFM	widefield fluorescence microscopy

8. References

[1] N. Yang and M. Hinner, „Getting Across The Cell Membrane: An Overview For Small Molecules, Peptides, And Proteins," *Site-Specific Protein Labeling,* pp. 29-53, 2014.

[2] D. Dou, R. Revol, H. Östbye, H. Wang and R. Daniels, „Influenza A Virus Cell Entry, Replication, Virion Assembly And Movement," *Frontiers in Immunology,* p. 9, 2018.

[3] P. Spear, „Herpes Simplex Virus: Receptors And Ligands For Cell Entry," *Cellular Microbiology, 6 (5),* pp. 401-410, 2004.

[4] J. Shang, Y. Wan, C. Luo, G. Ye, Q. Geng, A. Auerbach and F. Li, „Cell Entry Mechanisms Of SARS-Cov-2," *Proceedings of the National Academy of Sciences, 117 (21),* pp. 11727-11734, 2020.

[5] Z. Razinia, T. Mäkelä, J. Ylänne and D. Calderwood, „Filamins In Mechanosensing And Signaling," *Annual Review of Biophysics, 41 (1),* pp. 227-246, 2012.

[6] M. Yao, B. Goult, B. Klapholz, X. Hu, C. Toseland, Y. Guo, P. Cong, M. Sheetz and J. Yan, „The Mechanical Response Of Talin," *Nature Communications, 7 (1),* p. 11966, 2016.

[7] J. Yan, M. Yao, B. Goult and M. Sheetz, „Talin Dependent Mechanosensitivity Of Cell Focal Adhesions," *Cellular and Molecular Bioengineering , 8 (1),* pp. 151-159, 2014.

[8] L. Schermelleh, A. Ferrand, T. Huser, C. Eggeling, M. Sauer, O. Biehlmaier and G. Drummen, „Super-Resolution Microscopy Demystified," *Nature Cell Biology, 21 (1),* pp. 72-84, 2019.

[9] B. Alberts, D. Bray, J. Lewis, M. Raff, K. Roberts and J. D. Watson, Molecular Biology of the Cell, New York: Garland Publishing, Inc, 1994 .

[10] M. Vert, Y. Doi, K. Hellwich, M. Hess, P. Hodge, P. Kubisa, M. Rinaudo and F. Schué, „Terminology For Biorelated Polymers And Applications (IUPAC Recommendations 2012)," *Pure and Applied Chemistry, 84 (2),* pp. 377-410, 2012.

[11] N. Ji, H. Shroff, H. Zhong and E. Betzig, „Advances In The Speed And Resolution Of Light Microscopy," *Current Opinion in Neurobiology, 18 (6) ,* Nr. 605-616, 2008.

[12] B. Rothen-Rutishauser, D. Kuhn, Z. Ali, M. Gasser, F. Amin, W. Parak, D. Vanhecke, A. Fink, P. Gehr and C. Brandenberger, „Quantification Of Gold Nanoparticle Cell Uptake Under Controlled Biological Conditions And Adequate Resolution," *Nanomedicine, 9 (5),* pp. 607-621, 2014.

[13] M. Hink, R. Griep, J. Borst, A. van Hoek, M. Eppink, A. Schots and A. Visser, „Structural Dynamics Of Green Fluorescent Protein Alone And Fused With A Single Chain Fv Protein," *Journal of Biological Chemistry, 275 (23),* pp. 17556-17560, 2000.

[14] S. Dimopoulos, C. Mayer, F. Rudolf and J. Stelling, „ Accurate Cell Segmentation In Microscopy Images Using Membrane Patterns," *Bioinformatics, 30 (18),* pp. 2644-2651, 2014.

[15] D. Vanhecke, L. Rodriguez-Lorenzo, M. D. Clift, F. Blank, A. Petri-Fink and B. Rothen-Rutishauser, „Quantification Of Nanoparticles At The Single-Cell Level: An Overview About State-Of-The-Art Techniques And Their Limitations," *Nanomedicine, 9 (12),* pp. 1885-1900, 2014.

[16] K. Neuman and A. Nagy, „Single-Molecule Force Spectroscopy: Optical Tweezers, Magnetic Tweezers And Atomic Force Microscopy," *Nature Methods, 5 (6),* pp. 491-505, 2008.

[17] R. Kotani, S. Yokoyama, S. Nobusue, S. Yamaguchi, A. Osuka, H. Yabu and S. Saito, „Bridging Pico-To-Nanonewtons With A Ratiometric Force Probe For Monitoring Nanoscale Polymer Physics Before Damage," *Nature Communications, 13 (1),* p. 27972, 2022.

[18] S. Singer and G. Nicolson, „The Fluid Mosaic Model Of The Structure Of Cell Membranes.," *Science, 175 (4023),* pp. 720-731, 1972.

[19] J. O'Brien, „Cell Membranes—Composition: Structure: Function," *Journal of Theoretical Biology, 15 (3),* pp. 307-324, 1967.

[20] K. Boesze-Battaglia and R. Schimmel, „Cell Membrane Lipid Composition And Distribution: Implications For Cell Function And Lessons Learned From Photoreceptors And Platelets," *Journal of Experimental Biology, 200 (23),* pp. 2927-2936, 1997.

[21] E. Sezgin, I. Levental, S. Mayor and C. Eggeling, „The Mystery Of Membrane Organization: Composition, Regulation And Roles Of Lipid Rafts," *Nature Reviews Molecular Cell Biology, 18 (6),* pp. 361-374, 2017.

[22] A. Lee, „Lipid–Protein Interactions In Biological Membranes: A Structural Perspective," *Biochimica et Biophysica Acta (BBA) - Biomembranes, 1612 (1),* pp. 1-40, 2003.

[23] M. Berridge, „The Molecular Basis Of Communication Within The Cell," *Scientific American, 253 (4),* pp. 142-152, 1985.

[24] J. Holmgren, „Actions Of Cholera Toxin And The Prevention And Treatment Of Cholera," *Nature, 292 (5822),* pp. 413-417, 1981.

[25] A. Hartung, K. Bitton-Worms, M. Rechtman, V. Wenzel, J. Boergermann, S. Hassel, Y. Henis and P. Knaus, „Different Routes Of Bone Morphogenic Protein (BMP) Receptor Endocytosis Influence BMP Signaling," *Molecular and Cellular Biology, 26 (20),* pp. 7791-7805, 2006.

[26] L. Zakin and E. De Robertis, „Extracellular Regulation Of BMP Signaling," *Current Biology, 20 (3),* pp. 89-92, 2010.

[27] C. da Silva Madaleno, J. Jatzlau and P. Knaus, „BMP Signalling In A Mechanical Context – Implications For Bone Biology," *Bone, 137,* p. 115416, 2020.

[28] C. Hiepen, P. Mendez and P. Knaus, „It Takes Two To Tango: Endothelial Tgfβ/BMP Signaling Crosstalk With Mechanobiology," *Cells, 9 (9),* p. 1965, 2020.

[29] J. Liu and S. Thorp, „Cell Surface Heparan Sulfate And Its Roles In Assisting Viral Infections," *Medicinal Research Reviews, 22 (1),* pp. 1-25, 2001.

[30] V. Cagno, E. Tseligka, S. Jones and C. Tapparel, „Heparan Sulfate Proteoglycans And Viral Attachment: True Receptors Or Adaptation Bias?," *Viruses, 11 (7),* p. 596, 2019.

[31] F. Scialo, A. Daniele, F. Amato, L. Pastore, M. Matera, M. Cazzola, G. Castaldo and A. Bianco, „ACE2: The Major Cell Entry Receptor For SARS-Cov-2," *Lung, 198 (6),* pp. 867-877, 2020.

[32] C. Sieben, E. Sezgin, C. Eggeling and S. Manley, „Influenza A Viruses Use Multivalent Sialic Acid Clusters For Cell Binding And Receptor Activation," *PLOS Pathogens, 16 (7),* p. e1008656, 2020.

[33] A. Nahmias and S. Kibrick, „Inhibitors effect of heparin on herpes simplex virus," *Journal of Bacteriology, 87 (5),* pp. 1060-1066, 1964.

[34] M. Holodniy, S. Kim, D. Katzenstein, M. Konrad, E. Groves and T. Merigan, „Inhibition Of Human Immunodeficiency Virus Gene Amplification By Heparin," *Journal of Clinical Microbiology, 29 (4),* pp. 676-679, 1991.

[35] C. Hao, H. Xu, L. Yu and L. Zhang, „Heparin: An Essential Drug For Modern Medicine," *Progress in Molecular Biology and Translational Science, 163,* pp. 1-19, 2019.

[36] T. Whitehead, A. Chevalier, Y. Song, C. Dreyfus, S. Fleishman, C. De Mattos, C. Myers, H. Kamisetty, P. Blair, I. Wilson and D. Baker, „Optimization Of Affinity, Specificity And Function Of Designed Influenza Inhibitors Using Deep Sequencing," *Nature Biotechnology, 30 (6),* pp. 543-548, 2012.

[37] N. Zhu, D. Zhang, W. Wang, X. Li, B. Yang, J. Song, X. Zhao, B. Huang, W. Shi, R. Lu, P. Niu, F. Zhan, X. Ma, D. Wang, W. Xu, G. Wu, G. Gao and W. Tan, „A Novel Coronavirus From Patients With Pneumonia In China, 2019," *New England Journal of Medicine, 382 (8),* pp. 727-733, 2020.

[38] Y. Kerkhoff, S. Wedepohl, C. Nie, V. Ahmadi, R. Haag and S. Block, „A Fast Open-Source Fiji-Macro To Quantify Virus Infection And Transfection On Single-Cell Level By Fluorescence Microscopy," *MethodsX, 9,* p. 101834, 2022.

[39] M. Cohen, X. Zhang, H. Senaati, H. Chen, N. Varki, R. Schooley and P. Gagneux, „Influenza A Penetrates Host Mucus By Cleaving Sialic Acids With Neuraminidase," *Virology Journal, 10 (1),* 2013.

[40] H. Ribi, D. Ludwig, K. Mercer, G. Schoolnik and R. Kornberg, „Three-Dimensional Structure Of Cholera Toxin Penetrating A Lipid Membrane," *Science, 239 (4845),* pp. 1272-1276, 1988.

[41] A. Kabbani, K. Raghunathan, W. Lencer, A. Kenworthy and C. Kelly, „Structured Clustering Of The Glycosphingolipid GM1 Is Required For Membrane Curvature Induced By Cholera Toxin," *Proceedings of the National Academy of Sciences, 117 (26),* pp. 14978-14986, 2020.

[42] A. Kenworthy, S. Schmieder, K. Raghunathan, A. Tiwari, T. Wang, C. Kelly and W. Lencer, „Cholera Toxin As A Probe For Membrane Biology," *Toxins, 13 (8),* p. 543, 2021.

[43] D. Ingber, „Mechanobiology And Diseases Of Mechanotransduction," *Annals of Medicine, 35 (8),* pp. 564-577, 2003.

[44] J. Wang, „Mechanobiology Of Tendon," *Journal of Biomechanics, 39 (9),* pp. 1563-1582, 2006.

[45] D. Mohammed, M. Versaevel, C. Bruyère, L. Alaimo, M. Luciano, E. Vercruysse, A. Procès and S. Gabriele, „ Innovative Tools For Mechanobiology: Unraveling Outside-In And Inside-Out Mechanotransduction," *Frontiers in Bioengineering and Biotechnology, 7,* p. 162, 2019.

[46] F. Kaplan, M. Le Merrer, D. Glaser, R. Pignolo, R. Goldsby, J. Kitterman, J. Groppe and E. Shore, „Fibrodysplasia Ossificans Progressiva," *Best Practice & Research Clinical Rheumatology, 22 (1),* pp. 191-205, 2008.

[47] R. Wang, J. Green, Z. Wang, Y. Deng, M. Qiao, M. Peabody, Q. Zhang, J. Ye, Z. Yan, S. Denduluri, O. Idowu, M. Li, C. Shen, A. Hu, R. Haydon, R. Kang, J. Mok, M. Lee, H. Luu and L. Shi, „Bone Morphogenetic Protein (BMP) Signaling In Development And Human Diseases," *Genes & Diseases, 1 (1),* pp. 87-105, 2014.

[48] T. Kobayashi, K. Lyons, A. McMahon and H. Kronenberg, „BMP Signaling Stimulates Cellular Differentiation At Multiple Steps During Cartilage Development," *Proceedings of the National Academy of Sciences, 102 (50),* pp. 18023-18027, 2005.

[49] K. Galvin, M. Donovan, C. Lynch, R. Meyer, R. Paul, J. Lorenz, V. Fairchild-Huntress, K. Dixon, J. Dunmore, M. Gimbrone, D. Falb and D. Huszar, „A Role For Smad6 In Development And Homeostasis Of The Cardiovascular System," *Nature Genetics, 24 (2),* pp. 171-174, 2000.

[50] F. Milano, J. van Baal, N. Buttar, A. Rygiel, F. de Kort, C. DeMars, W. Rosmolen, J. Bergman, J. van Marle, K. Wang, M. Peppelenbosch and K. Krishnadath, „Bone Morphogenetic Protein 4 Expressed In Esophagitis Induces A Columnar Phenotype In Esophageal Squamous Cells," *Gastroenterology, 132 (7),* pp. 2412-2421, 2007.

[51] K. Lee, M. Mendelsohn and T. Jessell, „Neuronal Patterning By Bmps: A Requirement For GDF7 In The Generation Of A Discrete Class Of Commissural Interneurons In The Mouse Spinal Cord," *Genes & Development, 12 (21),* pp. 3394-3407, 1998.

[52] A. Guzman, M. Femiak, J. Boergermann, S. Paschkowsky, P. Kreuzaler, P. Fratzl, G. Harms and P. Knaus, „SMAD Versus Non-SMAD Signaling Is Determined By Lateral Mobility Of Bone Morphogenetic Protein (BMP) Receptors," *Journal of Biological Chemistry, 287 (47),* pp. 39492-39504, 2012.

[53] Y. Kerkhoff and S. Block, „Analysis And Refinement Of 2D Single-Particle Tracking Experiments," *Biointerphases, 15 (2),* p. 021201, 2020.

[54] J. Seong, N. Wang and Y. Wang, „Mechanotransduction At Focal Adhesions: From Physiology To Cancer Development," *Journal of Cellular and Molecular Medicine, 17 (5),* pp. 597-604, 2013.

[55] S. Lee, R. Kamm and M. Mofrad, „Force-Induced Activation Of Talin And Its Possible Role In Focal Adhesion Mechanotransduction," *Journal of Biomechanics, 40 (9),* pp. 2096-2106, 2007.

[56] A. del Rio, R. Perez-Jimenez, R. Liu, P. Roca-Cusachs, J. Fernandez and M. Sheetz, „Stretching Single Talin Rod Molecules Activates Vinculin Binding," *Science , 323 (5914),* pp. 638-641, 2009.

[57] M. Yao, B. Goult, H. Chen, P. Cong, M. Sheetz and J. Yan, „Mechanical Activation Of Vinculin Binding To Talin Locks Talin In An Unfolded Conformation," *Scientific Reports , 4 (1),* p. 4610, 2014.

[58] B. Hoffman, C. Grashoff and M. Schwartz, „Dynamic Molecular Processes Mediate Cellular Mechanotransduction," *Nature, 475 (7356),* pp. 316-323, 2011.

[59] K. Saini and D. Discher, „Forced Unfolding Of Proteins Directs Biochemical Cascades," *Biochemistry, 58 (49),* pp. 4893-4902, 2019.

[60] C. Turner, „Paxillin Interactions," *Journal of Cell Science, 113 (23),* pp. 4139-4140, 2000.

[61] K. Austen, P. Ringer, A. Mehlich, A. Chrostek-Grashoff, C. Kluger, C. Klingner, B. Sabass, R. Zent, M. Rief and C. Grashoff, „Extracellular Rigidity Sensing By Talin Isoform-Specific Mechanical Linkages," *Nature Cell Biology, 17,* pp. 1597-1606, 2015.

[62] R. Tapia-Rojo, Á. Alonso-Caballero and J. Fernández, „Talin Folding As The Tuning Fork Of Cellular Mechanotransduction," *Proceedings of the National Academy of Sciences, 117,* pp. 21346-21353, 2020.

[63] A. Haining, M. von Essen, S. Attwood, V. Hytönen and A. del Río Hernández, „All Subdomains Of The Talin Rod Are Mechanically Vulnerable And May Contribute To Cellular Mechanosensing," *ACS Nano, 10,* pp. 6648-6658, 2016.

[64] V. Mykuliak, A. Haining, M. von Essen, A. del Río Hernández and V. Hytönen, „Mechanical Unfolding Reveals Stable 3-Helix Intermediates In Talin And A-Catenin," *PLOS Computational Biology, 14 (4),* p. e1006126, 2018.

[65] E. Tan, E. Ooi, C. Lin, H. Tan, A. Ling, B. Lim and L. Stanton, „Inhibition Of SARS Coronavirus Infection In Vitro With Clinically Approved Antiviral Drugs," *Emerging Infectious Diseases, 10 (4),* pp. 581-586, 2004.

[66] A. Douglass and R. Vale, „Single-Molecule Microscopy Reveals Plasma Membrane Microdomains Created By Protein-Protein Networks That Exclude Or Trap Signaling Molecules In T Cells," *Cell 121 (6),* pp. 937-950, 2005.

[67] P. Tinnefeld and M. Sauer, „Branching Out Of Single-Molecule Fluorescence Spectroscopy: Challenges For Chemistry And Influence On Biology," *Angewandte Chemie International Edition, 44 (18),* pp. 2642-2671, 2005.

[68] H. Pace, L. Simonsson Nyström, A. Gunnarsson, E. Eck, C. Monson, S. Geschwindner, A. Snijder and F. Höök, „Preserved Transmembrane Protein Mobility In Polymer-Supported Lipid Bilayers Derived From Cell Membranes," *Analytical Chemistry, 87 (18),* pp. 9194-9203, 2015.

[69] H. Pace, J. Hannestad, A. Armonious, M. Adamo, B. Agnarsson, A. Gunnarsson, S. Micciulla, P. Sjövall, Y. Gerelli and F. Höök, „Structure And Composition Of Native Membrane Derived Polymer-Supported Lipid Bilayers," *Analytical Chemistry, 90 (21),* pp. 13065-13072, 2018.

[70] N. Peerboom, E. Schmidt, E. Trybala, S. Block, T. Bergström, H. Pace and M. Bally, „Cell Membrane Derived Platform To Study Virus Binding Kinetics And Diffusion With Single Particle Sensitivity," *ACS Infectious Diseases, 4 (6),* pp. 944-953, 2018.

[71] M. Müller, D. Lauster, H. Wildenauer, A. Herrmann and S. Block, „Mobility-Based Quantification Of Multivalent Virus-Receptor Interactions: New Insights Into Influenza A Virus Binding Mode," *Nano Letters, 19 (3),* pp. 1875-1882, 2019.

[72] D. Verardo, B. Agnarsson, V. Zhdanov, F. Höök and H. Linke, „Single-Molecule Detection With Lightguiding Nanowires: Determination Of Protein Concentration And Diffusivity In Supported Lipid Bilayers," *Nano Letters , 19 (9),* pp. 6182-6191, 2019.

[73] Y. Chen, W. Cao, J. Zhou, B. Pidhatika, B. Xiong, L. Huang, Q. Tian, Y. Shu, W. Wen, I. Hsing and H. Wu, „Poly(L-Lysine)-Graft-Folic Acid-Coupled Poly(2-Methyl-2-Oxazoline) (PLL-G-PMOXA-C-FA): A Bioactive Copolymer For Specific Targeting To Folate Receptor-Positive Cancer Cells," *ACS Applied Materials & Interfaces, 7 (4),* pp. 2919-2930, 2015.

[74] F. Schenk, H. Boehm, J. Spatz and S. Wegner, „Dual-Functionalized Nanostructured Biointerfaces By Click Chemistry," *Langmuir, 30 (23),* pp. 6897-6905, 2014.

[75] M. Fricker, „Optical Microscopy: Emerging Methods And Applications," *FEBS Letters, 335 (1),* pp. 145-145, 1993.

[76] Y. Garini, B. Vermolen and I. Young, „From Micro To Nano: Recent Advances In High-Resolution Microscopy," *Current Opinion in Biotechnology, 16 (1),* pp. 3-12, 2005.

[77] J. R. Lakowicz, Principles of fluorescence spectroscopy: Introduction to fluorescence, Boston, MA: Springer, 1-23, 1999.

[78] J. White, W. Amos and M. Fordham, „An Evaluation Of Confocal Versus Conventional Imaging Of Biological Structures By Fluorescence Light Microscopy," *The Journal of Cell Biology, 105 (1),* pp. 41-48, 1987.

[79] E. Stelzer, „Contrast, Resolution, Pixelation, Dynamic Range And Signal-To-Noise Ratio: Fundamental Limits To Resolution In Fluorescence Light Microscopy," *Journal of Microscopy, 189 (1),* pp. 15-24, 1998.

[80] R. Webb, „Confocal Optical Microscopy," *Reports on Progress in Physics, 59 (3),* pp. 427-471, 1996.

[81] Y. Kerkhoff, C. Nie, S. Wedepohl and K. G. Hugentobler, „Bridging cellular- and nanoscale: Accurate quantification of clustered nano-particles on monolayered confocal imaged cells“.*In preparation.*

[82] E. Ambrose, „A Surface Contact Microscope For The Study Of Cell Movements,“ *Nature, 178 (4543),* pp. 1194-1194, 1956.

[83] K. Fish, „Total Internal Reflection Fluorescence (TIRF) Microscopy,“ *Current Protocols in Cytometry, 50 (1),* 2009.

[84] A. Mattheyses, S. Simon and J. Rappoport, „Imaging With Total Internal Reflection Fluorescence Microscopy For The Cell Biologist,“ *Journal of Cell Science, 123 (21),* pp. 3621-3628, 2010.

[85] D. Owen, D. Williamson, C. Rentero and K. Gaus, „Quantitative Microscopy: Protein Dynamics And Membrane Organisation,“ *Traffic, 10 (8),* pp. 962-971, 2009.

[86] S. Block, B. Fast, A. Lundgren, V. Zhdanov and F. Höök, „Two-Dimensional Flow Nanometry Of Biological Nanoparticles For Accurate Determination Of Their Size And Emission Intensity,“ *Nature Communications, 7 (1),* p. 12956, 2016.

[87] C. Beh, D. Pan, J. Lee, X. Jiang, K. Liu, H. Mao and T. Wang, „Direct Interrogation Of DNA Content Distribution In Nanoparticles By A Novel Microfluidics-Based Single-Particle Analysis,“ *Nano Letters, 14 (8),* pp. 4729-4735, 2014.

[88] J. Meng, J. You, G. Arends, H. Hao, X. Tan and X. Zhang, „Microfluidic Device Coupled With Total Internal Reflection Microscopy For In Situ Observation Of Precipitation,“ *The European Physical Journal E, 44 (4),* p. 57, 2021.

[89] K. Huang and R. Murphy, „From Quantitative Microscopy To Automated Image Understanding,“ *Journal of Biomedical Optics, 9 (5),* p. 893, 2004.

[90] J. Caicedo, S. Cooper, F. Heigwer, S. Warchal, P. Qiu, C. Molnar, A. Vasilevich, J. Barry, H. Bansal, O. Kraus, M. Wawer, L. Paavolainen, M. Herrmann, M. Rohban, J. Hung, H. Hennig, J. Concannon, I. Smith, P. Clemons, S. Singh, P. Rees, P. Horvath, R. Linington and A. Carpenter, „Data-Analysis Strategies For Image-Based Cell Profiling,“ *Nature Methods, 14 (9),* pp. 849-863, 2017.

[91] B. Sankur, „Survey Over Image Thresholding Techniques And Quantitative Performance Evaluation,“ *Journal of Electronic Imaging, 13 (1),* p. 146, 2004.

[92] F. Meyer and S. Beucher, „Morphological Segmentation,“ *Journal of Visual Communication and Image Representation, 1 (1),* pp. 21-46, 1990.

[93] J. Schindelin, I. Arganda-Carreras, E. Frise, V. Kaynig, M. Longair, T. Pietzsch, S. Preibisch, C. Rueden, S. Saalfeld, B. Schmid, J. Tinevez, D. White, V. Hartenstein, K. Eliceiri, P. Tomancak and A. Cardona, „Fiji: An Open-Source Platform For Biological-Image Analysis," *Nature Methods, 9 (7),* pp. 676-682, 2012.

[94] E. Fröhlich, „The Role Of Surface Charge In Cellular Uptake And Cytotoxicity Of Medical Nanoparticles," *International Journal of Nanomedicine,* p. 5577, 2012.

[95] S. Salatin, S. Maleki Dizaj and A. Yari Khosroushahi, „Effect Of The Surface Modification, Size, And Shape On Cellular Uptake Of Nanoparticles," *Cell Biology International, 39 (8),* pp. 881-890, 2015.

[96] S. Behzadi, V. Serpooshan, W. Tao, M. Hamaly, M. Alkawareek, E. Dreaden, D. Brown, A. Alkilany, O. Farokhzad and M. Mahmoudi, „Cellular Uptake Of Nanoparticles: Journey Inside The Cell," *Chemical Society Reviews, 46 (14),* pp. 4218-4244, 2017.

[97] A. Vanderplasschen and G. Smith, „A Novel Virus Binding Assay Using Confocal Microscopy: Demonstration That The Intracellular And Extracellular Vaccinia Virions Bind To Different Cellular Receptors," *Journal of Virology, 71 (5),* pp. 4032-4041, 1997.

[98] A. Vanderplasschen and G. Smith, „Using Confocal Microscopy To Study Virus Binding And Entry Into Cells," *Confocal Microscopy,* pp. 591-607, 1999.

[99] R. Newton, M. Delguste, M. Koehler, A. Dumitru, P. Laskowski, D. Müller and D. Alsteens, „Combining Confocal And Atomic Force Microscopy To Quantify Single-Virus Binding To Mammalian Cell Surfaces," *Nature Protocols, 12 (11),* pp. 2275-2292, 2017.

[100] A. Torrano, J. Blechinger, C. Osseforth, C. Argyo, A. Reller, T. Bein, J. Michaelis and C. Bräuchle, „A Fast Analysis Method To Quantify Nanoparticle Uptake On A Single Cell Level," *Nanomedicine, 8 (11),* pp. 1815-1828, 2013.

[101] R. Parthasarathy, „Rapid, Accurate Particle Tracking By Calculation Of Radial Symmetry Centers," *Nature Methods, 9 (7),* pp. 724-726, 2012.

[102] R. Thompson, D. Larson and W. Webb, „Precise Nanometer Localization Analysis For Individual Fluorescent Probes," *Biophysical Journal, 82 (5),* pp. 2775-2783, 2002.

[103] S. Wieser and G. Schütz, „Tracking Single Molecules In The Live Cell Plasma Membrane—Do'S And Don't's," *Methods, 46 (2),* pp. 131-140, 2008.

[104] D. Krapf, „Mechanisms Underlying Anomalous Diffusion In The Plasma Membrane," *Lipid Domains,* pp. 167-207, 2015.

[105] R. Metzler, J. Jeon and A. Cherstvy, „Non-Brownian Diffusion In Lipid Membranes: Experiments And Simulations," *Biochimica et Biophysica Acta (BBA) - Biomembranes, 1858 (10),* pp. 2451-2467, 2016.

[106] H. Berry and H. Chaté, „Anomalous Diffusion Due To Hindering By Mobile Obstacles Undergoing Brownian Motion Or Orstein-Ulhenbeck Processes," *Physical Review E, 89 (2),* p. 022708, 2014.

[107] G. Campagnola, K. Nepal, B. Schroder, O. Peersen and D. Krapf, „Superdiffusive Motion Of Membrane-Targeting C2 Domains," *Scientific Reports, 5 (1),* p. 17721, 2015.

[108] E. Evans and E. Sackmann, „Translational and rotational drag coefficients for a disk moving in a liquid membrane-associated with a rigid substrate," *J. Fluid Mech, 194,* p. 553–561, 1988.

[109] A. Kusumi, C. Nakada, K. Ritchie, K. Murase, K. Suzuki, H. Murakoshi, R. Kasai, J. Kondo and T. Fujiwara, „Paradigm Shift Of The Plasma Membrane Concept From The Two-Dimensional Continuum Fluid To The Partitioned Fluid: High-Speed Single-Molecule Tracking Of Membrane Molecules," *Annual Review of Biophysics and Biomolecular Structure, 34 (1),* pp. 351-378, 2005.

[110] H. Joensson and H. Andersson Svahn, „Droplet Microfluidics-A Tool For Single-Cell Analysis," *Angewandte Chemie International Edition, 51 (49),* pp. 12176-12192, 2012.

[111] R. Walder, M. Kastantin and D. Schwartz, „High Throughput Single Molecule Tracking For Analysis Of Rare Populations And Events," *The Analyst, 137 (13),* p. 2987, 2012.

[112] Z. Yao and R. Carballido-López, „Fluorescence Imaging For Bacterial Cell Biology: From Localization To Dynamics, From Ensembles To Single Molecules," *Annual Review of Microbiology, 68 (1),* pp. 459-476, 2014.

[113] S. Dorsch, K. Klotz, S. Engelhardt, M. Lohse and M. Bünemann, „Analysis Of Receptor Oligomerization By FRAP Microscopy," *Nature Methods, 6 (3),* pp. 225-230, 2009.

[114] A. Clayton, „Fluorescence-Based Approaches For Monitoring Membrane Receptor Oligomerization," *Journal of Biosciences, 43 (3),* pp. 463-469, 2018.

[115] A. Payne, I. Binduga-Gajewska, E. Kauffman and L. Kramer, „Quantitation Of Flaviviruses By Fluorescent Focus Assay," *Journal of Virological Methods, 134 (1-2),* pp. 183-189, 2006.

[116] M. Cebecauer, M. Amaro, P. Jurkiewicz, M. Sarmento, R. Šachl, L. Cwiklik and M. Hof, „Membrane Lipid Nanodomains," *Chemical Reviews, 118 (23),* pp. 11259-11297, 2018.

[117] J. Kure, C. Andersen, K. Mortensen, P. Wiseman and E. Arnspang, „Revealing Plasma Membrane Nano-Domains With Diffusion Analysis Methods," *Membranes, 10 (11),* p. 314, 2020.

[118] S. Wharton, „An Analysis Of The Effects Of Sample Size On Classification Performance Of A Histogram Based Cluster Analysis Procedure," *Pattern Recognition, 17 (2),* pp. 239-244, 1984.

[119] L. Davies, U. Gather, D. Nordman and H. Weinert, „A Comparison Of Automatic Histogram Constructions," *ESAIM: Probability and Statistics, 13,* pp. 181-196, 2009.

[120] D. Scott, „Averaged Shifted Histogram," *Wiley Interdisciplinary Reviews: Computational Statistics, 2 (2),* pp. 160-164, 2010.

[121] L. Loo, L. Wu and S. Altschuler, „Image-Based Multivariate Profiling Of Drug Responses From Single Cells," *Nature Methods, 4 (5),* pp. 445-453, 2007.

[122] G. Hummer and A. Szabo, „Free Energy Surfaces From Single-Molecule Force Spectroscopy," *Accounts of Chemical Research, 38 (7),* pp. 504-513, 2005.

[123] D. Rugar and P. Hansma, „Atomic Force Microscopy," *Physics Today , 43 (10),* pp. 23-30, 1990.

[124] E. Meyer, „Atomic Force Microscopy," *Progress in Surface Science, 41 (1),* pp. 3-49, 1992.

[125] R. García, „Dynamic Atomic Force Microscopy Methods," *Surface Science Reports, 47 (6-8),* pp. 197-301, 2002.

[126] F. Giessibl, „Advances In Atomic Force Microscopy," *Reviews of Modern Physics, 75 (3),* pp. 949-983, 2003.

[127] R. Lal and S. John, „Biological Applications Of Atomic Force Microscopy," *American Journal of Physiology-Cell Physiology, 266 (1),* pp. C1-C21, 1994.

[128] Y. Shi, M. Cai, L. Zhou and H. Wang, „The Structure And Function Of Cell Membranes Studied By Atomic Force Microscopy," *Seminars in Cell & Developmental Biology 73,* pp. 31-44, 2018.

[129] D. Alsteens, M. Garcia, P. Lipke and Y. Dufrêne, „Force-Induced Formation And Propagation Of Adhesion Nanodomains In Living Fungal Cells," *Proceedings of the National Academy of Sciences, 107 (48),* pp. 20744-20749, 2010.

[130] C. Formosa and E. Dague, „Imaging Living Yeast Cells And Quantifying Their Biophysical Properties By Atomic Force Microscopy," *Fungal Biology,* pp. 125-141, 2015.

[131] M. Cebecauer, M. Amaro, P. Jurkiewicz, M. Sarmento, R. Šachl, L. Cwiklik and M. Hof, „Membrane Lipid Nanodomains," *Chemical Reviews, 118 (23),* pp. 11259-11297, 2018.

[132] L. Wang, Y. Qian, Y. Sun, B. Liu and G. Wei, „Single-Molecule Force Spectroscopy: A Facile Technique For Studying The Interactions Between Biomolecules And Materials Interfaces," *Reviews in Analytical Chemistry , 39 (1),* pp. 116-129, 2020.

[133] B. Yang, Z. Liu, H. Liu and M. Nash, „Next Generation Methods For Single-Molecule Force Spectroscopy On Polyproteins And Receptor-Ligand Complexes," *Frontiers in Molecular Biosciences 7,* p. 85, 2020.

[134] P. Frederix, P. Bosshart and A. Engel, „Atomic Force Microscopy Of Biological Membranes," *Biophysical Journal, 96 (2),* pp. 329-338, 2009.

[135] A. Ashkin, „Acceleration And Trapping Of Particles By Radiation Pressure," *Physical Review Letters, 24 (4),* pp. 156-159, 1970.

[136] J. Killian, F. Ye and M. Wang, „Optical Tweezers: A Force To Be Reckoned With," *Cell, 175 (6),* pp. 1445-1448, 2018.

[137] S. Smith, Y. Cui and C. Bustamante, „Overstretching B-DNA: The Elastic Response Of Individual Double-Stranded And Single-Stranded DNA Molecules," *Science, 271 (5250),* pp. 795-799, 1996.

[138] C. Riesenberg, C. Iriarte-Valdez, A. Becker, M. Dienerowitz, A. Heisterkamp, A. Ngezahayo and M. Torres-Mapa, „Probing Ligand-Receptor Interaction In Living Cells Using Force Measurements With Optical Tweezers," *Frontiers in Bioengineering and Biotechnology, 8,* 2020.

[139] C. Arbore, L. Perego, M. Sergides and M. Capitanio, „Probing Force In Living Cells With Optical Tweezers: From Single-Molecule Mechanics To Cell Mechanotransduction," *Biophysical Reviews, 11 (5),* pp. 765-782, 2019.

[140] K. Svoboda, C. Schmidt, B. Schnapp and S. Block, „Direct Observation Of Kinesin Stepping By Optical Trapping Interferometry," *Nature, 365 (6448),* pp. 721-727, 1993.

[141] K. Neuman, E. Chadd, G. Liou, K. Bergman and S. Block, „Characterization Of Photodamage To Escherichia Coli In Optical Traps," *Biophysical Journal, 77 (5),* pp. 2856-2863, 1999.

[142] L. Sacconi, I. Tolić-Nørrelykke, C. Stringari, R. Antolini and F. Pavone, „Optical Micromanipulations Inside Yeast Cells," *Applied Optics, 44 (11),* p. 2001, 2005.

[143] D. Cherney, T. Bridges and J. Harris, „Optical Trapping Of Unilamellar Phospholipid Vesicles: Investigation Of The Effect Of Optical Forces On The Lipid Membrane Shape By Confocal-Raman Microscopy," *Analytical Chemistry, 76 (17),* pp. 4920-4928, 2004.

[144] J. Curtis, B. Koss and D. Grier, „Dynamic Holographic Optical Tweezers," *Optics Communications, 207 (1-6),* pp. 169-175, 2002.

[145] K. Neuman, T. Lionnet and J. Allemand, „Single-Molecule Micromanipulation Techniques," *Annual Review of Materials Research, 37 (1),* pp. 33-67, 2007.

[146] H. Itoh, A. Takahashi, K. Adachi, H. Noji, R. Yasuda, M. Yoshida and K. Kinosita, „Mechanically Driven ATP Synthesis By F1-Atpase," *Nature, 427 (6973),* pp. 465-468, 2004.

[147] G. Charvin, T. Strick, D. Bensimon and V. Croquette, „Tracking Topoisomerase Activity At The Single-Molecule Level," *Annual Review of Biophysics and Biomolecular Structure, 34 (1),* pp. 201-219, 2005.

[148] A. Bausch, W. Möller and E. Sackmann, „Measurement Of Local Viscoelasticity And Forces In Living Cells By Magnetic Tweezers," *Biophysical Journal, 76 (1),* pp. 573-579, 1999.

[149] M. Keller, J. Schilling and E. Sackmann, „Oscillatory Magnetic Bead Rheometer For Complex Fluid Microrheometry," *Review of Scientific Instruments, 72 (9),* pp. 3626-3634, 2001.

[150] A. Bharde, R. Palankar, C. Fritsch, A. Klaver, J. Kanger, T. Jovin and D. Arndt-Jovin, „Magnetic Nanoparticles As Mediators Of Ligand-Free Activation Of EGFR Signaling," *PLoS ONE, 8 (12),* 2013.

[151] J. Li, P. Santos-Otte, B. Au, J. Rentsch, S. Block and H. Ewers, „Directed Manipulation Of Membrane Proteins By Fluorescent Magnetic Nanoparticles," *Nature Communications, 11 (1),* p. 4259, 2020.

[152] I. De Vlaminck, T. Henighan, M. van Loenhout, I. Pfeiffer, J. Huijts, J. Kerssemakers, A. Katan, A. van Langen-Suurling, E. van der Drift, C. Wyman and C. Dekker, „Highly Parallel Magnetic Tweezers By Targeted DNA Tethering," *Nano Letters, 11 (12),* pp. 5489-5493, 2011.

[153] S. Monismith, „Stokes Drift: Theory And Experiments," *Journal of Fluid Mechanics,* p. 884, 2019.

[154] J. Zhang, S. Yan, D. Yuan, G. Alici, N. Nguyen, M. Ebrahimi Warkiani and W. Li, „Fundamentals And Applications Of Inertial Microfluidics: A Review," *Lab on a Chip, 16 (1),* pp. 10-34, 2016.

[155] G. Zocchi, „Force Measurements On Single Molecular Contacts Through Evanescent Wave Microscopy," *Biophysical Journal, 81 (5),* pp. 2946-2953, 2001.

[156] J. Liang, J. Li, Z. Zhong, T. Rujiralai and J. Ma, „Quantifying The Force In Flow-Cell Based Single-Molecule Stretching Experiments," *Nanoscale, 13 (37),* pp. 15916-15927, 2021.

[157] A. van Oijen, P. Blainey, D. Crampton, C. Richardson, T. Ellenberger and X. Xie, „Single-Molecule Kinetics Of λ Exonuclease Reveal Base Dependence And Dynamic Disorder," *Science, 301 (5637),* pp. 1235-1238, 2003.

[158] J. Lee, R. Hite, S. Hamdan, X. Sunney Xie, C. Richardson and A. van Oijen, „DNA Primase Acts As A Molecular Brake In DNA Replication," *Nature, 439 (7076),* pp. 621-624, 2006.

[159] N. Tanner, S. Hamdan, S. Jergic, K. Loscha, P. Schaeffer, N. Dixon and A. van Oijen, „Single-Molecule Studies Of Fork Dynamics In Escherichia Coli DNA Replication," *Nature Structural & Molecular Biology, 15 (2),* pp. 170-176, 2008.

[160] K. Duderstadt, H. Geertsema, S. Stratmann, C. Punter, A. Kulczyk, C. Richardson and A. van Oijen, „Simultaneous Real-Time Imaging Of Leading And Lagging Strand Synthesis Reveals The Coordination Dynamics Of Single Replisomes," *Molecular Cell, 64 (6),* pp. 1035-1047, 2016.

[161] M. Urbanska, A. Lüdecke, W. Walter, A. Oijen, K. Duderstadt and S. Diez, „Highly-Parallel Microfluidics-Based Force Spectroscopy On Single Cytoskeletal Motors," *Small, 17 (18),* p. 2007388, 2021.

[162] A. Einstein, „Über die von der molekularkinetischen Theorie der Wärme geforderte Bewegung von in ruhenden Flüssigkeiten suspendierten Teilchen," *Annalen der Physik 322,* p. 549–560, 1905.

[163] F. Schwabl, Quantum mechanics, Berlin: Springer, 2005.

[164] L. Loo, L. Wu and S. Altschuler, „Image-Based Multivariate Profiling Of Drug Responses From Single Cells," *Nature Methods, 4 (5), ,* pp. 445-453, 2007.

[165] A. Carpenter, „Image-Based Chemical Screening," *Nature Chemical Biology, 3 (8),* pp. 461-465, 2007.

[166] N. Hooper, „Detergent-Insoluble Glycosphingolipid/Cholesterol-Rich Membrane Domains, Lipid Rafts And Caveolae (Review)," *Molecular Membrane Biology, 16 (2),* pp. 145-156, 1999.

[167] H. Wu, Y. Lin, T. Yen and C. Hsieh, „Nanoscopic Substructures Of Raft-Mimetic Liquid-Ordered Membrane Domains Revealed By High-Speed Single-Particle Tracking," *Scientific Reports, 6 (1),* p. 20542, 2016.

[168] V. Ahmadi, C. Nie, E. Mohammadifar, K. Achazi, S. Wedepohl, Y. Kerkhoff, S. Block, K. Osterrieder and R. Haag, „One-Pot Gram-Scale Synthesis Of Virucidal Heparin-Mimicking Polymers As HSV-1 Inhibitors," *Chemical Communications, 57 (90),* pp. 11948-11951, 2021.

[169] C. Nie, P. Pouyan, D. Lauster, J. Trimpert, Y. Kerkhoff, G. Szekeres, M. Wallert, S. Block, A. Sahoo, J. Dernedde, K. Pagel, B. Kaufer, R. Netz, M. Ballauff and R. Haag, „Polysulfates Block SARS-CoV-2 Uptake through Electrostatic Interactions**," *Angewandte Chemie International Edition, 60 (29),* pp. 15870-15878, 2021.

[170] C. Hiepen, M., M. Benamar, J. Barrasa Fano, M. Cóndor Salgado, M. Ilhan, J. Münch, N. Hastar, Y. Kerkhoff, G. S. Harms, T. Mielke, B. Koenig, S. Block, S. Abdelilah-Seyfried, H. Van Oosterwyck and P. Knaus, „Endothelial tip-cell filopodia formation and pulling forces require BMPR2 expression and signaling". *in preparation.*

[171] C. Nie, M. Stadtmüller, B. Parshad, M. Wallert, V. Ahmadi, Y. Kerkhoff, S. Bhatia, S. Block, C. Cheng, T. Wolff and R. Haag, „Heteromultivalent Topology-Matched Nanostructures As Potent And Broad-Spectrum Influenza A Virus Inhibitors," *Science Advances, 7 (1),* p. eabd3803, 2021.

[172] Y. Kerkhoff, L. Azizi, V. Mykuliak, V. Hytönen and S. Block, „Microfluidics-based force spectroscopy enables to perform high-throughput force measurements with sub-nm resolution and sub-pN sensitivity".*submitted to Small.*

[173] J. Chen, L. Dai, A. Goldstein, H. Zhang, W. Tang, J. Forrest, S. Post, X. Chen and Z. Qin, „Identification Of New Antiviral Agents Against Kaposi'S Sarcoma-Associated Herpesvirus (KSHV) By High-Throughput Drug Screening Reveals The Role Of Histamine-Related Signaling In Promoting Viral Lytic Reactivation," *PLOS Pathogens, 15 (12),* p. e1008156, 2019.

[174] X. Xiao, C. Wang, D. Chang, Y. Wang, X. Dong, T. Jiao, Z. Zhao, L. Ren, C. Dela Cruz, L. Sharma, X. Lei and J. Wang, „Identification Of Potent And Safe Antiviral Therapeutic Candidates Against SARS-Cov-2," *Frontiers in Immunology 11,* 2020.

[175] J. Rietdijk, M. Tampere, A. Pettke, P. Georgiev, M. Lapins, U. Warpman-Berglund, O. Spjuth, M. Puumalainen and J. Carreras-Puigvert, „A Phenomics Approach For Antiviral Drug Discovery," *BMC Biology, 19 (1),* 2021.

[176] J. Eyckmans, T. Boudou, X. Yu and C. Chen, „A Hitchhiker's Guide To Mechanobiology," *Developmental Cell, 21 (1),* pp. 35-47, 2011.

9. List of publications, manuscripts, and conference contributions

9.1 Publications and manuscripts

1) Hiepen, C., Benamar, M., Fano, J. B., Salgado, M. C., Ilhan, M., Münch, J., Hastar, N., Kerkhoff, Y., Harms, G. S., Mielke, T., Koenig, B., Block, S., Abdelilah-Seyfried, S., Van Oosterwyck, H., Knaus, P., **Endothelial tip-cell filopodia formation and pulling forces require BMPR2 expression and signaling**. *In preparation*.

2) Kerkhoff, Y., Nie, C., Wedepohl, S., and Hugentobler, K. G., **Bridging cellular- and nanoscale: Accurate quantification of clustered nanoparticles on monolayered confocal imaged cells.** *In manuscript.*

3) Kerkhoff, Y., Azizi, L., Mykuliak, V., Hytönen, V. P., and Block, S., **Microfluidics-based force spectroscopy enables to perform high-throughput force measurements with sub-nm resolution and sub-pN sensitivity**. *Submitted to Small (invited contribution)*.

4) Kerkhoff, Y., Wedepohl, S., Nie, C., Ahmadi, V., Haag, R., and Block, S., (2022). **A fast open-source Fiji-macro to quantify virus infection and transfection on single-cell level by fluorescence microscopy.** MethodsX 9, 101834.

5) Ahmadi, V., Nie, C., Mohammadifar, E., Achazi, K., Wedepohl, S., Kerkhoff, Y., Block, S., Osterrieder, K. and Haag, R., (2021). **One-pot gram-scale synthesis of virucidal heparin-mimicking polymers as HSV-1 inhibitors**. Chemical Communications 57, 11948.

6) Nie, C., Pouyan, P., Lauster, D., Trimpert, J., Kerkhoff, Y., Szekeres, G., Wallert, M., Block, S., Sahoo, A., Dernedde, J., Pagel, K., Kaufer, B., Netz, R., Ballauff, M. and Haag, R., (2021). **Polysulfates Block SARS-CoV-2 Uptake through Electrostatic Interactions**. Angewandte Chemie International Edition 60, 15870.

7) Nie, C., Stadtmüller, M., Parshad, B., Wallert, M., Ahmadi, V., Kerkhoff, Y., Bhatia, S., Block, S., Cheng, C., Wolff, T. and Haag, R., (2021). **Heteromultivalent topology-matched nanostructures as potent and broad-spectrum influenza A virus inhibitors**. Science Advances 7(1), eabd3803.

8) Kerkhoff, Y. and Block, S., (2020). **Analysis and refinement of 2D single-particle tracking experiments**. Biointerphases 15, 021201 (invited contribution).

9) Kulka, M., Nie, C., Nickl, P., Kerkhoff, Y., Garg, A., Salz, D., Radnik, J., Grunwald, I. and Haag, R., (2020). **Surface-Initiated Grafting of Dendritic Polyglycerol from Mussel-Inspired Adhesion-Layers for the Creation of Cell-Repelling Coatings**. Advanced Materials Interfaces 7 (24), 2000931.

10) Kulka, M., Smatty, S., Hehnen, F., Bierewirtz, T., Silberreis, K., Nie, C., Kerkhoff, Y., Grötzinger, C., Friedrich, S., Dahms, L., Dernedde, J., Grunwald, I., Schirner, M., Kertzscher, U., Affeld, K. and Haag, R., (2020). **The Application of Dual-Layer, Mussel-Inspired, Antifouling Polyglycerol-Based Coatings in Ventricular Assist Devices**. Advanced Materials Interfaces 7 (21), 2000272.

11) Nie, C., Parshad, B., Bhatia, S., Cheng, C., Stadtmüller, M., Oehrl, A., Kerkhoff, Y., Wolff, T. and Haag, R., (2020). **Topology-Matching Design of an Influenza-Neutralizing Spiky Nanoparticle-Based Inhibitor with a Dual Mode of Action**. Angewandte Chemie International Edition 59 (36), 15532.

12) Parshad, B., Yadav, P., Kerkhoff, Y., Mittal, A., Achazi, K., Haag, R. and Sharma, S. (2019). **Dendrimer-based Micelles as Cyto-compatible Nanocarriers**. New Journal of Chemistry 43, 11984.

9.2 Conference contributions

07/2021 Talk: Yannic Kerkhoff & Stephan Block. **Microfluidics-based force measurements with sub-nm resolution and sub- pN sensitivity**. 13th European Biophysics Conference, Vienna, Austria

12/2019 Poster: Yannic Kerkhoff, Matthias Wallert, Chuanxiong Nie, Rainer Haag, and Stephan Block. **Incorporating Native Plasma Membrane Material into Supported Lipid Bilayers for Equilibrium Fluctuation Analysis**. Biomembrane Days 2019, Berlin, Germany

11/2019 Poster: Yannic Kerkhoff, Christian Hiepen, Jerome Jatzlau, Petra Knaus, and Stephan Block. **Single Particle Tracking of Transmembrane Receptor Proteins in Supported Lipid Bilayers Containing Native Membrane Material.** Live Cell Single Molecule Tracking Symposium, Ulm, Germany